University of Southampton

Faculty of Physical Sciences and Engineering

Optoelectronics Research Centre

Adaptive Graphene Electronics and Plasmonics

By

Jon Gorecki

March 2020

Thesis submitted for the degree of
Doctor of Philosophy

Abstract

University of Southampton
Optoelectronics Research Centre
Doctor of Philosophy

Adaptive Graphene Electronics and Plasmonics

Jon Gorecki

Graphene, the world's first two dimensional material, has attracted great interest in the scientific community due to its unique behaviours such as the dramatic tunability of its electronic and optical properties, strong light-matter interactions, and high values of carrier mobility which render graphene as a fascinating material for photodetection, plasmonic devices, and modulation of terahertz frequency radiation. To realise the next generation of graphene devices we must find new ways to adaptively control the electronic and optical properties of graphene and other two dimensional materials.

In this thesis I propose a method to optically control the electronic properties of graphene in a spatially resolved, non-volatile, yet reversible manner via the use of photorefractive lithium niobate. The method I propose relies on the ability of lithium niobate to sustain optically defined charge distributions which result in large electrostatic fields at the surface of the crystal.

By transferring graphene onto lithium niobate crystals I show that the optically defined electrostatic surface charges in the substrate are capable of tuning the DC electrical conductivity of graphene in a behaviour which is non-volatile yet reversible under thermal annealing.

Further, I utilise this effect in a plasmonic device consisting of a hybrid graphene-metal metasurface on lithium niobate where the optical tuning effect is capable of altering the transmissive properties of the device at terahertz frequencies.

Finally, I show through simulations that by spatially patterning charge distributions it is possible to create optically defined plasmonic devices on graphene on lithium niobate. Such devices would not need permanent lithographic patterning of metasurfaces, yet instead would rely on optically defined regions of high and low conductivity graphene to sustain a plasmonic resonance. If such devices can be experimentally achieved this would allow for rewritable yet non-volatile plasmonic structures in graphene and open the doors to a truly reconfigurable plasmonic platform for two dimensional materials.

Research Thesis: Declaration of Authorship

Print name: Jon Gorecki

Title of thesis: Adaptive Graphene Electronics and Plasmonics

I declare that this thesis and the work presented in it are my own and has been generated by me as the result of my own original research.

I confirm that:

1. This work was done wholly or mainly while in candidature for a research degree at this University;
2. Where any part of this thesis has previously been submitted for a degree or any other qualification at this University or any other institution, this has been clearly stated;
3. Where I have consulted the published work of others, this is always clearly attributed;
4. Where I have quoted from the work of others, the source is always given. With the exception of such quotations, this thesis is entirely my own work;
5. I have acknowledged all main sources of help;
6. Where the thesis is based on work done by myself jointly with others, I have made clear exactly what was done by others and what I have contributed myself;
7. Parts of this work have been published as:

   J. Gorecki, V. Apostolopoulos, J-Y. Ou, S. Malis, N. Papasimakis, "Optical Gating of Graphene on Photoconductive Fe:$LiNbO_3$" ACS Nano, 12, 6, 5940-5945, (2018)

   J. Gorecki, N. Klokkou, L. Piper, S. Mailis, N. Papasimakis, V. Apostolopoulos, "High-precision THz-TDS via self-referenced transmission

echo method" Appl. Opt. 59, 6744-6750 (2020)

J. Gorecki, L. Piper, A. Noual, S. Mailis, N. Papasimakis, V. Apostolopoulos, "Optically Reconfigurable Graphene/Metal Metasurface on Fe:$LiNbO_3$ for Adaptive THz Optics" ACS Appl. Nano Mater. 3, 9, 9494-9501, (2020)

Signature: .....Date: .....

Contents

List of Figures

To create a little flower is the labour of ages...

William Blake

Chapter 1

Physical Background

1.1 Preface

The world around us has changed drastically in the last century. Technological advances have pushed us further and further into a science fiction reality, from the microprocessor powering your smart phone, to the optical communication devices connecting us globally across the internet, ideas once unimaginable are now common place. For the most part this technological revolution has come from our ability to control the manner in which electricity and light pass through objects at ever smaller scales, patterning structures of increasing complexity into materials to embed new levels of functionality.

Around the turn of the millennium we again took a new step forward into the unknown, creating a material which had never been seen in nature before. The world's first two dimensional material had been produced, with many unique and extraordinary properties. Now, over 15 years after this initial discovery scientists have found that graphene is not alone in its two dimensional world, there are thousands of other thin materials waiting to be explored, each as bizarre as the next, yet bursting with new technological opportunities. We stand at the cusp of a new technological revolution, however if we are to realise the unexplored possibilities offered by this new class of materials then it is vital to develop new methods to control their electronic and optical properties to embed them with structure and functionality.

Two dimensional materials are generally controlled via electrostatic gating in a 'field effect' configuration however this method offers limited reconfigurability, and therefore it is advantageous to look towards optical methods which could allow for spatially resolved patterning. In this thesis I propose that iron doped lithium niobate can be a platform for reconfigurable and spatially resolved tuning of 2D materials which may open the doors towards rewritable electronic interconnects and reconfigurable plasmonic devices defined simply by optical illumination without the need for permanent patterning of structures.

1.2 Graphene

1.2.1 A Brief History of Graphene

The discovery of graphene is commonly mis-attributed to Geim and Novoselov et al. [1] for their seminal 2004 publication for which they jointly received

the Nobel prize in 2010. In truth the history of graphene predates this publication by over a century when in 1896 the American chemist Acheson patented a method of creating graphitic layers by liquid exfoliation of silicon carbide. Many people point to this discovery as the root of graphene production, however as this event predated modern crystallographic characterisation techniques such as x-ray diffraction it was impossible for anyone at the time to realise the 2 dimensional nature of the material that had been created. In the century after Acheson there followed sporadic research into graphene production techniques with limited success. In 1947 a theoretical framework of the electrical properties of graphene was laid out by Wallace [2], however it was widely believed at the time that due to the atomic thinness of graphene it would be impossible for such a structure to exist in nature, and therefore Wallace had developed the band structure equations merely as a stepping stone towards calculating those for graphite. Finally in 2004, over 100 years after the work of Acheson, graphene entered the mainstream when Geim and Novoselov developed the 'scotch tape method' which allowed them to easily create flakes of high quality exfoliated graphene on silicon wafers. At last this discovery enabled the team to experimentally demonstrate the long-theorised-at extraordinary electrical properties of graphene, and therefore in 2010 the pair were awarded the Nobel Prize in Physics *"for groundbreaking experiments regarding the two-dimensional material graphene".* Now the floodgates have opened, and new monolayers beyond graphene are being demonstrated at a staggering rate, creating a family of 2D materials with a rich diversity in unique optical and electronics properties, of whose prospective applications surely we are only beginning to scrape the surface [3].

1.2.2 Electronic Properties of Graphene

Graphene is a 2D allotrope of carbon in which the atoms sit in a hexagonal lattice each bound to three neighbours by covalent π bonds with one unbound π orbital pointed out of the atomic plane [4]. The hexagonal graphene lattice can be described mathematically by two triangular sub-lattices each containing three carbon atoms as depicted in Figure 1.1(a). By using a tight binding model and the assumption that electrons in graphene can jump to either their nearest or next nearest neighbouring atom an analytical solution for the energy dispersion relation was proposed in 1947 by Wallace [2]. The solution of this model for the first Brillouin zone predicts that there are certain points at which the valence and conduction bands meet, referred to as the Dirac

point; around this point the graphene Fermi level is given by Equation 1.1 where n is the number of charge carriers (either electrons or holes), v_F is the graphene Fermi velocity, and $\hbar$ is the reduced plank constant.

$$E_F = \hbar v_F \sqrt{\pi |n|} \tag{1.1}$$

Due to the linear dispersion relation (depicted in Figure 1.1c) the density of states in graphene vanishes at the Dirac point. An implication of the vanishing density of states is that close to the Dirac point a small injection of charge carriers can dramatically shift the Fermi level and increases the electrical conductivity; an injection of electrons increases the Fermi level and electrons become the dominant mechanism for electronic charge transport, while a decrease in electrons will lower the Fermi level and holes become dominant for charge transport [5]. This description of the dispersion relation provides an intuitive understanding of Figure 1(b) which shows that at zero charge carrier density the resistivity is at a maximum value of $\rho_{max} = 1 / \sigma_{min}$ while either injection or removal of charge carriers causes a decrease in resistivity resulting in a bell-shaped curve. The maximum value of resistivity has been shown experimentally around $\sigma_{min} = 4e^2/h\pi$ which is believed to be caused by rippling deformations in the graphene sheet which alter π bond overlaps [6].

1.2.3 Plasmonics in Graphene

The optical conductivity of graphene is determined by interband and intraband transitions. Interband refers to charge carriers transitioning from the valence to the conduction band (or vice versa) while intraband refers to charge carriers transitioning to different energy state while staying within the valence or conduction band (Figure 1.1c). Due to Pauli blocking the number of charge carriers occupying a band is limited, therefore to achieve an interband transition from valence to conduction band an electron must be excited to an available state above those which are fully occupied. A lower limit is therefore placed on the excitation energy required for an interband transition of $\omega\hbar = 2E_F$, while below this limit intraband transitions will dominate. Based on the Drude model a theoretical solution for two dimensional plasma frequency in graphene can be obtained however due to the massless nature of charge carriers in graphene the result is different from that of noble metals in that the plasma frequency of graphene depends on the Fermi level E_F,

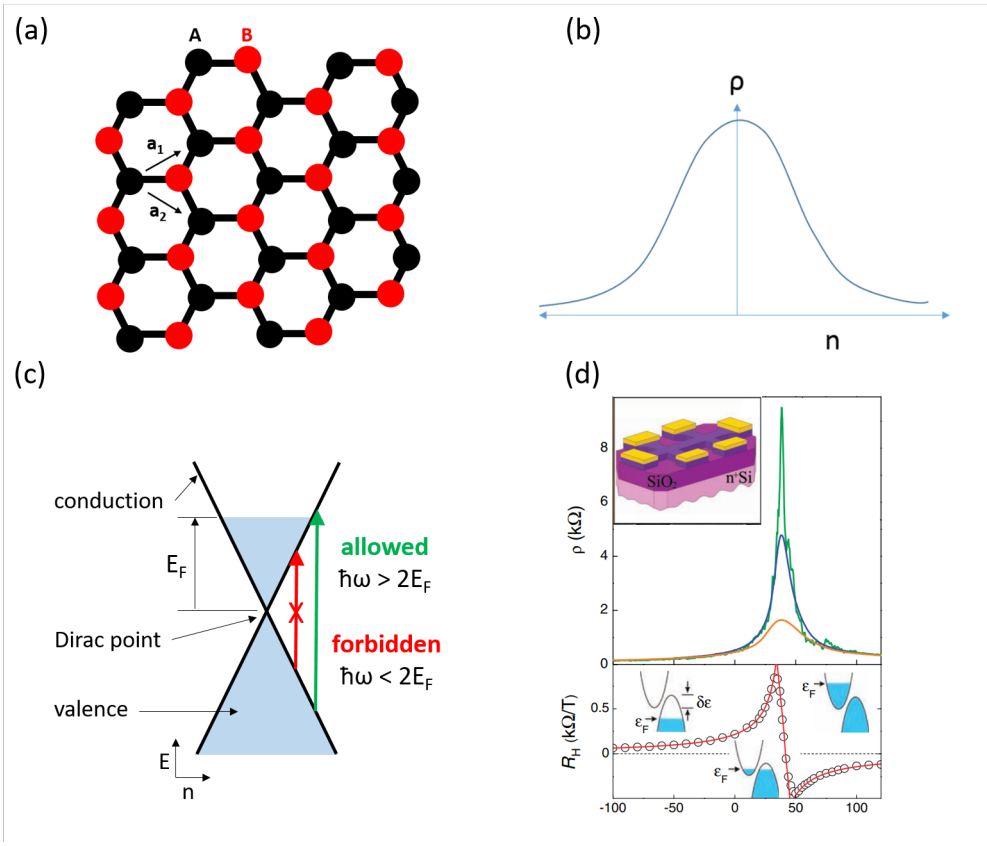

Figure 1.1: ***(a)*** *Diagram of graphene hexagonal lattice with carbon atoms depicted by circles. The two repeating triangular lattices are denoted in red and black with the unit vectors for the A sublattice shown by arrows a_1 and a_2.* ***(b)*** *Example of typical bell shaped curve for resistivity ρ against carrier number n for graphene.* ***(c)*** *Schematic of linear dispersion relation showing valence and conduction bands intersecting at Dirac point, with example of forbidden and allowed inter-band transitions.* ***(d)*** *Measurements of graphene [1] (FET device depicted in inset figure) showing resistivity and Hall coefficient plotted against gate voltage.*

in other words the plasma frequency can be tuned by controlling the Fermi level through gating the graphene as shown in Figure 1.2(a) [7]. Due to high mobility values in graphene, plasmonic resonances can reach into terahertz frequencies [8] (Figure 1.2a) and beyond into the infra-red region [9, 10, 11]. Dirac plasmons in graphene can couple to free-space light provided a sufficiently sharp object to compensate for the momentum mismatch such as an AFM tip [12] (Figure 1.2b), a periodic grating [13], or nanoscale defects in the graphene lattice [9]. Due to the relatively low optical absorption of graphene ($\sim$2.3 %) its application for optical modulation is currently limited however by combining graphene with noble metals it is possible to form hybrid plasmonic devices in which the metals act to enhance the plasmonic resonance effects while the graphene allows for tuning the resonance behaviour of the device (shown in Figure 1.2c) [14, 15, 16].

1.2.4 Graphene Fabrication Methods

There are a range of methods available for producing graphene sheets, each with distinct advantages and disadvantages. Improving the production methods of graphene is an important area of research which will be vital to the future utilisation of graphene in a range of technological applications [17]. Currently the main methods for producing graphene are exfoliation [1], Chemical Vapour Deposition (CVD) [18], and the less common epitaxial growth on SiC [19]. Exfoliated graphene starts with high quality graphite crystals and separates the layers to form monolayer graphene. The first demonstrated method of separation was by peeling layers from the graphite with an adhesive tape [1], however chemical exfoliation [20] and ball milling [21] have also been shown to produce monolayer graphene. The crystals produced by exfoliation are the highest quality graphene; they are single crystal domains and therefore there are no crystal domain boundaries for charge carriers to scatter on and so can exhibit carrier mobilities >200,000 cm^2/Vs measured at a temperature of 5 K [22]. The main drawback to exfoliated graphene is that the crystals usually have a size of 10-20 μm which limits use of exfoliated graphene in many applications [23]. Chemical Vapour Deposition (CVD) graphene begins with a substrate of highly polished metal (usually copper) placed in a high temperature vacuum chamber; a mixture of hydrocarbon vapours are fed into the chamber which thermally decompose on the metallic surface forming a graphene monolayer. The metallic substrate is then dissolved away via a chemical etchant to leave a floating layer of graphene

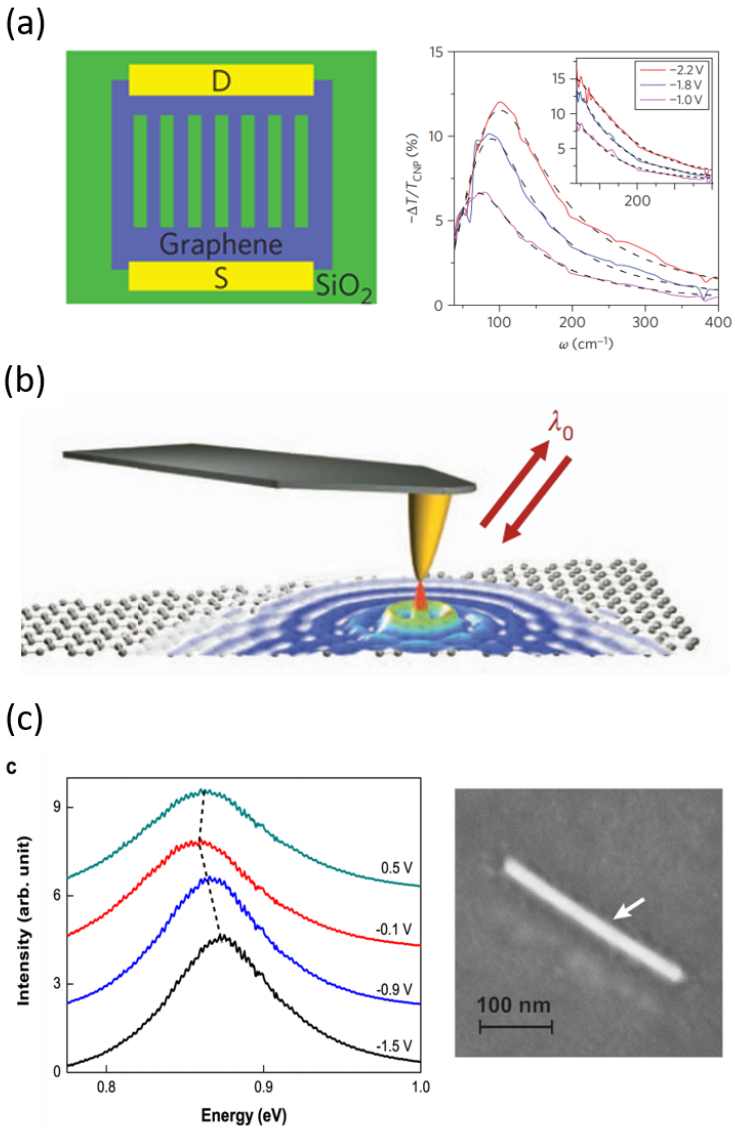

Figure 1.2: ***(a)*** *Tuneable plasmonic device by patterning graphene into ribbons [8]* ***(b)*** *Coupling of light to graphene plasmon by AFM tip [12]* ***(c)*** *Hybrid metal nano-rod with graphene device where resonance frequency is tuned by graphene conductivity [14].*

which can be transferred to a desired substrate. The CVD method is able to produce large area graphene films (several tens of square centimetres) which makes it an attractive method for practical applications however CVD graphene has poorer electrical properties than exfoliated sheets [24]. The CVD method produces graphene of multiple crystalline domains and often once removed from the metallic substrates still experiences some residual contamination of metallic particles and polymers due to the fabrication process [25]. Due to the multi-crystalline nature of the graphene there is increased charge scattering from domain boundaries which reduces the carrier mobility to $\sim$10,000 cm^2/Vs, while the residual contamination often results in a graphene layer which is intrinsically p-doped (excess of holes) and therefore requires a positive gate voltage to bring the sheet towards the Dirac point [26].

1.2.5 Optoelectronic Applications of Graphene

Due to the 2D confinement charge carriers in graphene experience low scattering loss and therefore can exhibit extremely high values of carrier mobility of hundreds of thousands cm^2/Vs [22] (for ballpark-comparison μ silicon $\sim$ 1000 cm^2/Vs) allowing for graphene to sustain confined plasmonic resonances at low frequencies into infra-red (IR) and Terahertz (THz) regions [8, 27, 28, 29], which allows the realisation of miniaturised tuneable devices [30]. In combination with the inherent high values of charge carrier mobility, the tuneable electronic properties render graphene an appealing material for applications such as MEMS [31], flexible touch-screen electrodes [32, 33], chemical sensing [34, 35], membranes [16], and especially optoelectronic applications [36, 37]. including photodetection [38].

One of the most exciting applications for graphene is as the active element in photodetector devices as graphene allows for the broadband absorption over a wide range of wavelengths from UV to IR with a flat spectral response [39]. The response time of graphene photodetectors has been demonstrated to reach ultra-fast timescales of few picoseconds [40], however there is an apparent trade-off between response time and current responsivity which is highlighted by Wang et al. in Figure 1.3 [41]. This figure reveals that although graphene can respond on ultra-fast timescales the currents generated in the photodetectors are generally low in comparison to those demonstrated with other 2D materials. In efforts to overcome this flaw of graphene photodetectors it has been demonstrated that the current reponsivity can be

increased by integration with QDs [42], semiconductor substrates [43], and layered heterostructures [44].

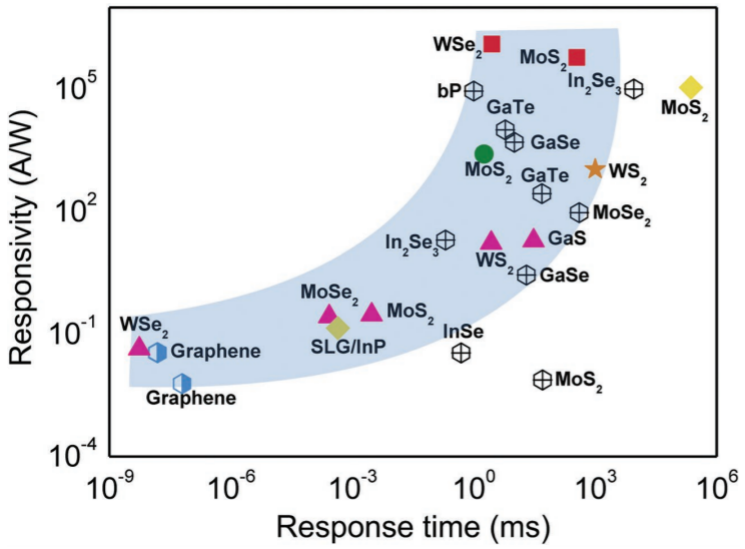

Figure 1.3: *Infographic showing response times plotted against current responsivity of 2D material photodetectors, reproduced from Wang et al. [41].*

1.2.6 2D Materials Beyond Graphene

Since the initial demonstration of graphene by Geim and Novoselov et al. [1] the study of 2D materials has grown rapidly into a thriving field [45, 46] yielding materials with unique properties especially of interest in optoelectronics [47] such as molybdenum disulphide [48], silicene [49] and black phosphorus [38]. A big advantage over graphene which many of these materials exhibit is that they have an electronic bandgap which could allow for high on/off ratio transistors and optical elements with a large degree of tuneability. In Figure 3 I have reproduced a chart of 2D material bandgaps [41] to show the large variation in material properties offered by just a small selection of 2D materials.

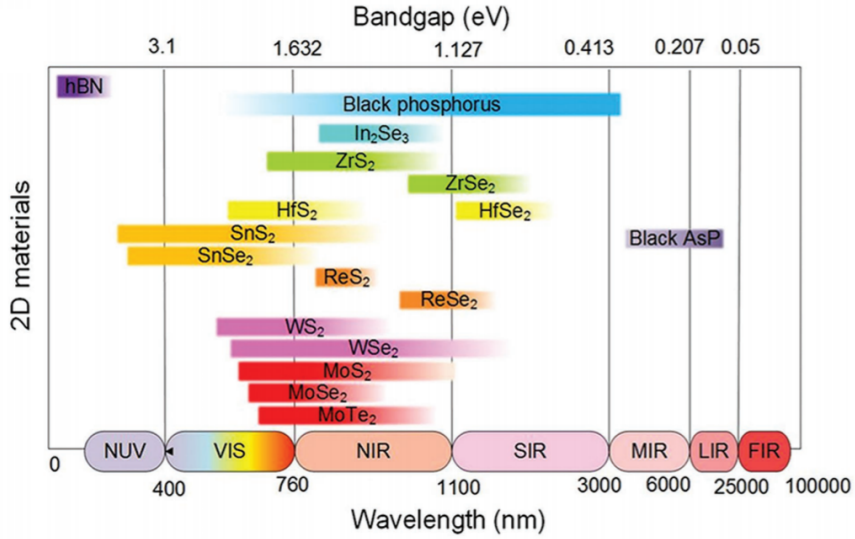

Figure 1.4: *Infographic showing electronic bandgaps of popular 2D materials varying from visible to infra-red frequencies [41].*

1.3 Controlling Electronic Properties of Graphene

Many mechanisms for controlling the electronic properties of graphene have been put forward, such as electrical backgating [1], chemical doping [50], permanent structuring into ribbons [51, 52, 53], or by combination with other 2D lattices [54] such as hexagonal boron nitride (hBN) [55], and transition metal dichalcogenides (TMD's) [56, 57].

1.3.1 Chemical Doping

There are a wide range of publications on chemical doping on graphene [58], and in fact it has been noted that contamination with almost any chemical species will alter the electronic properties of graphene [59]. There are generally two approaches which fall under the umbrella of chemical doping, which can be categorised as surface adsorption of a chemical species, or lattice substitution. In the first case surface adsorption happens when chemical species such as gasses [60], metals [61], or organic molecules [62] are attracted to the surface of the graphene layer via electrostatic interactions and modify the graphene Fermi level [63, 64, 65]. In the second case lattice replacement refers to a graphene surface in which a portion of the carbon atoms have been replaced by another atom such as nitrogen [66], boron [67, 68], and phosphorus [69], where it is believed that lattice replacement doping could open large bandgaps in the graphene sheet [70, 71].

1.3.2 2D Material Heterostuctures

By creating heterostructures consisting of layers of graphene with various 2D monolayers it is possible to drastically alter the properties of the graphene sheet. To this end various researchers have reported devices combining graphene with MoS_2 [72, 73], WS_2 [74], WSe_2 [75], phosphorene [76], and many many other 2D materials [77, 78, 79].

Another interesting application of heterostrucutres to mention is the encapsulation of graphene with hexagonal boron nitride [80, 81]. This has proved extremely useful in creating graphene devices as it has shown to dramatically improve the graphene charge carrier mobility, and protect the graphene from atmospheric adsorption. The increases to carrier mobility are thought to come from the matching of the hexagonal boron nitride layer lattice structure to that of the graphene, providing a near-perfectly matched

lattice layer for the graphene to sit on and therefore minimising out-of-plane structural deformations in the graphene and electrically insulating the graphene from its surrounding environment.

Finally, it should be mentioned that graphene heterostructures do not have to consist of materials other than graphene, in fact it has been shown that by layering pristine graphene crystals on top of each other at specific angular orientations reveals bizarre electronic effects which are not observed in single layers [82, 83, 84].

1.3.3 Electrostatic Control

In the case of electrostatic gating [1, 85], a field effect (FET) is usually employed, in which an electrically conductive substrate (shielded from the graphene by a thin insulator layer) is held at a voltage bias with respect to the graphene, thereby setting up an electrostatic field between the graphene and the substrate (also known as the gate). In response to the electrostatic field charge carriers will move within the graphene sheet (either injected or ejected from the electric ground) in order to counteract the electric field created by the gate. Graphene FET's are often comprised of a graphene monolayer on a conductive silicon substrate insulated by a thin silica layer $\sim$ 100 - 300 nm, with applied gate voltages $\sim \pm$ 100 V achieving charge injections on the order of $10^{13} cm^{-2}$ charge carriers with Fermi level modulation of hundreds of meV.

The electrostatic field created by the gate is determined by the dielectric permittivity and the thickness of the insulator, where a low relative permittivity and a high thickness result in weak electrostatic fields imposed on the graphene. To enhance the gating effect and thereby reduce the operating voltages of the device there have been various attempts reported to use extremely thin insulating layers with high values of relative permittivity, such as Al_2O_3 [91, 92] and HfO_2 [93] by atomic layer deposition which can achieve few nanometer thick layers.

The FET configuration has proved extremely useful for investigating fundamental properties of graphene [1] such as the quantum Hall effect and the observation of the Berry phase [94] however there are a number of limitations to this approach. Firstly the shape and size of the electric gate must be permanently patterned during fabrication process which removes the ability for reconfiguration of the device. Secondly, if multiple gates were required each gate must be individually contacted to a voltage source, which requires empty

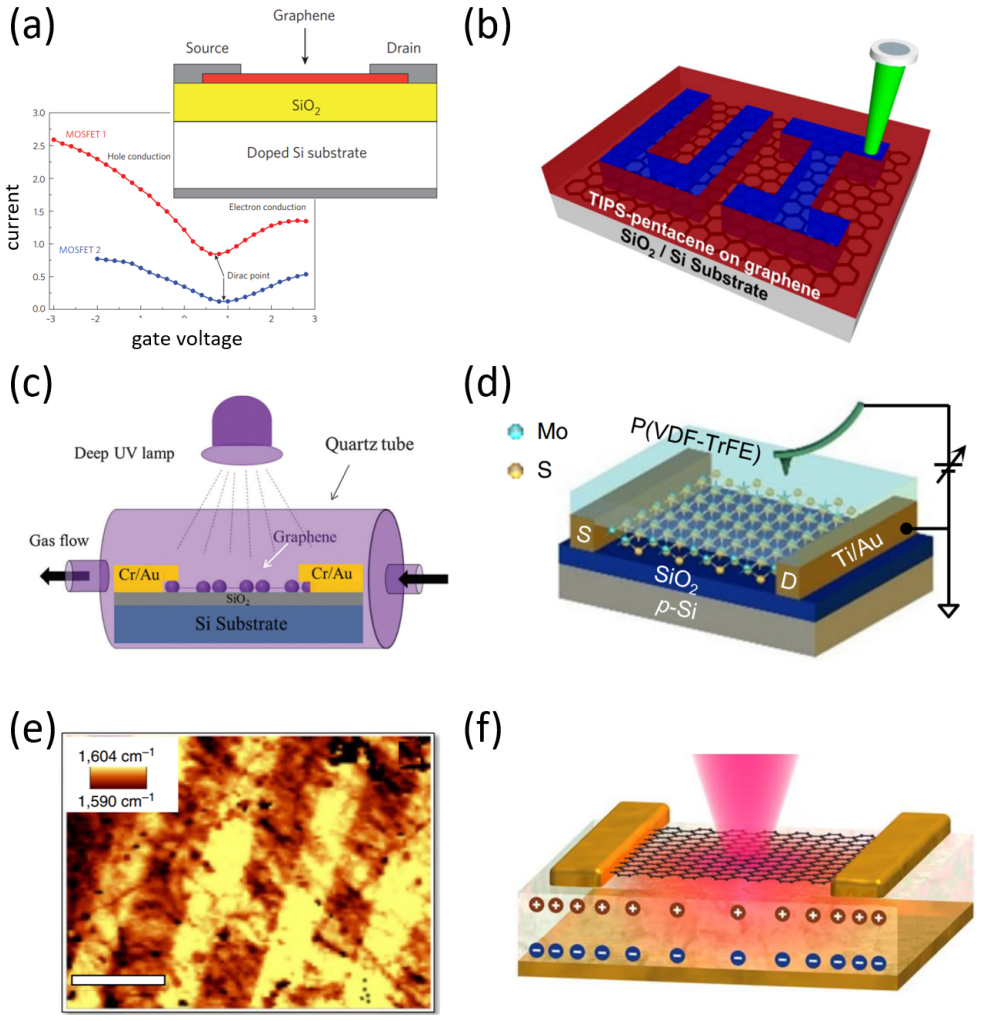

Figure 1.5: ***(a)*** *Representation of graphene on Si/SiO_2 field effect transistor with characteristic gate/current measurement [85].* ***(b)*** *Laser written photo-oxidation of pentacene leading to charge exchange with graphene sheet [86].* ***(c)*** *Optically induced chemical doping of graphene from gasseous environment [87].* ***(d)*** *Writing of ferroelectric domains via AFM tip to spatially tune MoS_2 layer [88].* ***(e)*** *Raman spectroscopy map of graphene on periodically poled $LiNbO_3$ revealing spatial variation in Fermi level [89].* ***(f)*** *Optically induced volatile doping of graphene via pyroelectric effect in $LiNbO_3$ [90].*

space left between the gates to pattern a complicated design of interconnecting conductive tracks. Thirdly the field effect is volatile, therefore requiring a persistent voltage which requires a continuous power source for the device operation. Furthermore, the gate devices are often optically opaque due to being comprised of metallic materials which hinders their use in optically transmissive graphene based tuning elements. To overcome some of the limitations of FET gating a number of light-assisted approaches have been put forward.

1.3.4 Optical Control

Optical doping methods are in their infancy and are largely confined to laboratory based demonstrations rather than practical applications. Many optical methods have been presented, such as photo-oxidation of organic layers resulting in non-reversible charge transfer [86] (Figure 1.5b). In this case Seo et al. [86] demonstrate that their graphene sample starts as p-doped and can be altered to n-doped by the chemical by-products of the photo-oxidation of a pentacene layer. They demonstrate spatial resolution and write features of a few microns in width. The charge carrier injection to the graphene is large ($7\times10^{12}cm^{-2}$) and measured to be stable over a 30 day period however the effect is non-reversible and always results in n-doping.

Photochemical effects have also been demonstrated [87, 95] (Figure 1.5c), where irradiation leads to exchange of dopants between the atmosphere and graphene. The mechanism reported in these references is similar in both cases, where graphene in a gasseous environment is chemically doped by irradiation with a UV laser. By exposing the graphene to a nitrogen rich environment and UV exposure the graphene can become n-doped, which can then be reversed by a similar process in an oxygen rich environment. Both publications report relatively long process times around 1 hour, however it is not mentioned whether these times could be decreased by higher illumination intensities. Iqbal et al. [87] mention their process is capable of injecting $3\times10^{12}cm^{-2}$ carriers and the effect is non-volatile, however for Wang et al. [95] they mention only that their doping effect is stable when the graphene is held in the gas environment. While this type of photochemical effect is advantageous as it offers reversible behaviour it is a rather cumbersome technique as it requires atmospheric control over process gasses which limits the functionality of the device for remote actuation, and exhibits rather long processing times.

In addition, it has been shown that combining light illumination with an electrostatic gate can lead to charge exchange between graphene and the substrate [96, 97, 98]. The doping mechanisms here rely on photoexcitation of charge carriers within the dielectric which under the applied gate voltage can be pushed over the potential barrier of the dielectric and be transferred to the graphene. Once the carriers are on the graphene they no longer have enough energy to re-cross the potential barrier and leave a net positive charge in the substrate interface. Such processes are non-volatile yet can be reversed by suitable application of the gate voltage to allow charges to overcome the potential barrier and travel between the graphene and the substrate. These photoexcitation mechanisms have been reported to create large carrier modulation of $1 \times 10^{13}\text{cm}^{-2}$ with graphene on titanium oxide [96] and $3 \times 10^{12}\text{cm}^{-2}$ with graphene on boron nitride [97]. While these mechanisms are reversible and do not require gasseous environments to operate they still utilise electronic back-gates which can cause additional fabrication issues. Further, the dielectric layers demonstrated in these devices are of nanometer thickness and as such they have a limited available charge capacity for their doping mechanism as they rely on the graphene/dielectric interface rather than bulk effects.

1.3.5 Ferroelectric Control

There have been various reports of attempts to use bulk ferroelectric substrates to control the electronic properties of graphene. There are a number of advantages to using ferroelectric substrates; the fields persist without the application of a voltage bias which therefore reduces operational power consumption; the ferroelectric dipole can be switched in direction allowing for a bi-stable tuning of the graphene; ferroelectric domains can be spatially patterned; ferroelectric dipoles often respond to external stimuli such as change in temperature or pressure which allows for additional actuation methods. In 2011 Song et al. [99] demonstrated graphene on a ferroelectric substrate (lead zirconium titanate) where the ferroelectric dipole could be flipped by application of a back-gate voltage, altering the conductivity of the graphene to create a bi-stable memory device. Manipulation of ferroelectric substrates via a biased AFM tip to create ferroelectric domains of arbitrary shape has been demonstrated to locally control the electronic properties of graphene [100] and MoS_2 [88] (Figure 1.5d); this method is useful as it allows for spatially resolved domains to be written but is rather slow due to the scanning

speed of the AFM tips. Periodically poled lithium niobate has also been demonstrated to induce a periodic variation in the Fermi level of graphene as revealed by mapping Raman spectroscopy [89, 101] (Figure 1.5e). By placing graphene on lithium niobate electrical tuning by an optically induced strain effect has been demonstrated which is attributed to the mismatch in expansion coefficients of the graphene and substrate [102]. Further, by exploiting the pyroelectric effect in which a temperature change causes a transient change in the magnitude of the ferroelectric dipole the electronic properties of a graphene layer can be tuned in a volatile manner [103, 90, 104] (Figure 1.5f).

* Here I pause the discussion of graphene and 2D materials for the moment to introduce lithium niobate, a synthetic crystal with many interesting optical properties.

1.4 Lithium Niobate

1.4.1 A Brief History of Lithium Niobate

Since the first demonstration of the ruby laser in 1960 [105] there has been significant interest in the use of ferroelectric crystals for beam modulation via electro-optic effects. In the search for appropriate materials many novel crystalline compounds were investigated, however few of these have had such a great impact on the field of optoelectronics as the synthesis of lithium niobate due to its combination of ferroelectric, pyroelectric, piezoelectric, electro-optic, photo-elastic, and photo-conductive effects [106]. The first growth of lithium niobate is sometimes reported to come from Matthias and Remeika in 1949 [107] however this publication only appears to mention $LiTaO_3$ growth and its ferroelectric behaviour. Regardless of this slight mystery, by the 1960's the knowledge of $LiNbO_3$ as a promising material for electro-optics had lead to a multitude of groups growing and investigating the crystal, with two well cited reports of large crystal growth emerging in 1965 from Fedulov [108] in Russia and Ballman [109] in the United States. Since the early days of research into lithium niobate a parasitic effect known as 'photo-damage' was observed in which the crystals would experience a non-volatile change in local refractive index in response to optical illumination intensity causing unwanted defocusing and distortion of the beam [110]. Many attempts were made to suppress the photo-damage effect by growing crystals with a range of dopants such as Mg, Zn, In, and Sc [111], however instead of viewing the effect as an unwanted phenomena some researchers looked for ways to use the photo-damage as a platform for optically written charge distributions which has lead to success in holography [112, 113, 114], nano-particle trapping [115, 116], and liquid crystal alignment [117].

1.4.2 Physical Fundamentals of Lithium Niobate

The ferroelectric effect of $LiNbO_3$ is caused by a charge separation between the lithium and niobium ions which creates a permanent electric dipole aligned along a crystalline polar-axis denoted as the z axis (also referred to as c axis) [106] as shown in Figure 1.6(a) [118]. Due to the symmetry of the crystal lattice the z axis is also the optic axis; the lattice is uniaxial with the remaining two orthogonal directions referred to as x and y axis which are identical to each other in optical properties. Due to the direction of the

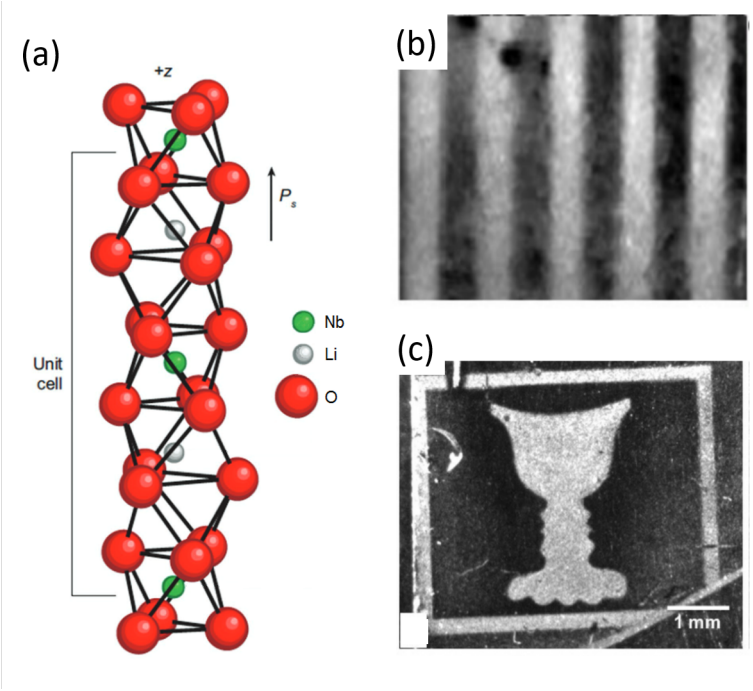

Figure 1.6: ***(a)*** *Unit cell of lithium niobate showing z axis orientation determined by Li position within the lattice [118]. (b & c) Photorefractive effect used for patterning of nanoparticles by creation of surface electric fields in lithium niobate [119].*

ferroelectric dipole the z faces are labelled +z and –z where the +z (-z) face exhibits a net positive (negative) surface charge density when in the absence of adsorbed atmospheric particles which tend to neutralise the net charge. The direction of the ferroelectric domains can be reversed via application of a large voltage difference between the two z faces to produce an electric field higher than the coercive field which acts to shift the positions of lithium and niobium ions within the crystal lattice. Spatially selective domain reversal can be achieved by covering one of the polar faces with photolithographically patterned photoresist to spatially modulate the applied electric field. In this way the $LiNbO_3$ can be poled into multiple domains of arbitrary shape even with sub-millimetre resolution [120]. $LiNbO_3$ exhibits a pyroelectric effect in which the ferroelectric polarisation changes in magnitude as a function of temperature due to thermal expansion of the lattice leading to an increase in Li-Nb ion separation. $LiNbO_3$ also exhibits an electro-optic effect in which an applied electric field creates an asymmetric electrostatic potential which affects the motion of electrons in the lattice creating a change in refractive index.

1.4.3 Origin of the Photo-Damage Effect

$LiNbO_3$ suffers from a photo-damage effect (also known as photo-refractive and photo-conductive effect) in which Fe ion impurities in the crystal act as photo-excitation centres, exciting electrons from interband defect states to the conduction band, which then become free to migrate in the lattice [110]. Depending on their valence state these Fe impurities can act as donors or acceptors of charge thus allowing for the recording of photo-induced charge distributions in this material. The effect is capable of producing charge distributions of arbitrary shape, which are non-volatile yet able to be reversed by further illumination or thermal annealing that equally redistributes the separated charge carriers. The effect is not unique to Fe dopants; other transition metals such as molybdenum and hafnium can be used [121], alternatively undoped crystals can also be used with UV or high intensity visible illumination to access Nb antisites. Generally out of all these methods Fe dopants are the most used as it is generally agreed Fe results in the largest photo-induced electric fields. This charge migration effect is well documented in Fe:$LiNbO_3$ and can produce space charge distributions that are stable in the dark for long periods of time (years) [122]. The response time of charge migration is a function of illumination intensity [123] and can reach sub-ps

time scales under pulsed illumination [124, 125]. Furthermore, the charge migration effect can create charge distributions of sub-micron dimensions [122].

1.4.4 Electron Migration Mechanisms

In the absence of an externally applied electric field there can be defined two electron migration mechanisms, termed as drift and diffusion [126].

Drift The drift mechanism refers to motion of electrons in response to electric fields. When an electron is excited into the conduction band within the crystal it will experience a force along the ferroelectric dipole of the lithium niobate which will drive the electron along the $+\hat{z}$ direction. The drift effect is usually used to create surface electric fields for the manipulation of nano-object and liquids [115].

Diffusion The diffusion mechanism is the result of non-uniform illumination of the crystal which creates a non-uniform distribution of free electrons which through random scattering motion will diffuse within the crystal, becoming trapped in 'dark' regions of the crystal. The diffusion effect is normally employed with illumination gratings and interference patterns to create structured charge distributions within the bulk crystal for holography [112].

1.4.5 Electric Fields in $LiNbO_3$

Despite the relatively long duration of research into photorefractive effects in lithium niobate the surface profile of the electric fields produced are still not fully understood. The initial demonstrations of the photorefractive effect employed bulk charge distributions to create holographic gratings; volume charge densities create static electric fields between illuminated and dark regions within the crystal which induce a change of refractive index due to the electro-optic effect. This photorefractive behaviour is capable of creating refractive index changes of $\Delta n \sim 10^{-3}$ which corresponds to internal electric fields on the order of tens of kV/cm, and can be equated to internal volume charge densities of kC/m^3 [127]. Moving on from bulk to surface effects there have been attempts to investigate surface charge profiles via the use of atomic force microscopy (AFM). The AFM technique generally has had limited success due to the electrostatic 'sticking' of the tip to the substrate as a result of the large fields created by the ferroelectric dipole and the photorefractive effects, however there has been some achievements by measuring

in a liquid environment to screen the tip from the electrostatic fields, which allowed for imaging of the hexagonal lattice [128]. There are few publications on simulated photorefractive effects in Fe:$LiNbO_3$ however the group of Carrascossa have developed simulations of optically induced electron migration with lithium niobate which are coupled with experimental verification from particle trapping measurements [129, 130]. The photorefractive effect in Fe:$LiNbO_3$ has been shown experimentally to produce high strength electric fields in the 100 - 250 kV/cm range [131, 119, 132, 133].

1.5 Motivation - 2D Materials on Photorefractive $LiNbO_3$

In this thesis I propose the use of photorefractive lithium niobate as a platform for the reconfigurable optical control of 2D materials, with a view to creating adaptive electronic and plasmonic devices. Owing to the photorefractive effect I propose that lithium niobate can allow for optically created charge distributions which could electrostatically tune a monolayer on the surface of the crystal. This platform could have a number of advantageous properties such as: non-volatility which would reduce the need for a persistent voltage or illumination source; reversibility which would allow for any changes to the monolayer to be undone at will; repeatability which would allow for rewriting of the charge distributions, and the spatially defined nature of the effect allows for individual regions of the monolayer to be addressed by simply directing the optical illumination to a specific region of the substrate.

In this thesis I demonstrate graphene on lithium niobate as a proof-of-concept device and determine the strength of the doping effect and relevant incident light intensities involved. This platform is not limited simply to graphene as it may find richer application in 2D materials exhibiting a bandgap thereby allowing for optically defined electronic interconnects, non-volatile optical tuning of transistor devices and spatial control of spontaneous emission frequencies. Monolayer graphene sheets are transferred onto lithium niobate crystals. By illuminating the crystals with spatially non-uniform intensity light the photorefractive electron migration creates a non-uniform charge distribution in the $LiNbO_3$ substrate (Figure 6). Due to the electrostatic interaction of the substrate with the graphene there will be an injection of charge carriers (from an electric ground) into the graphene in or-

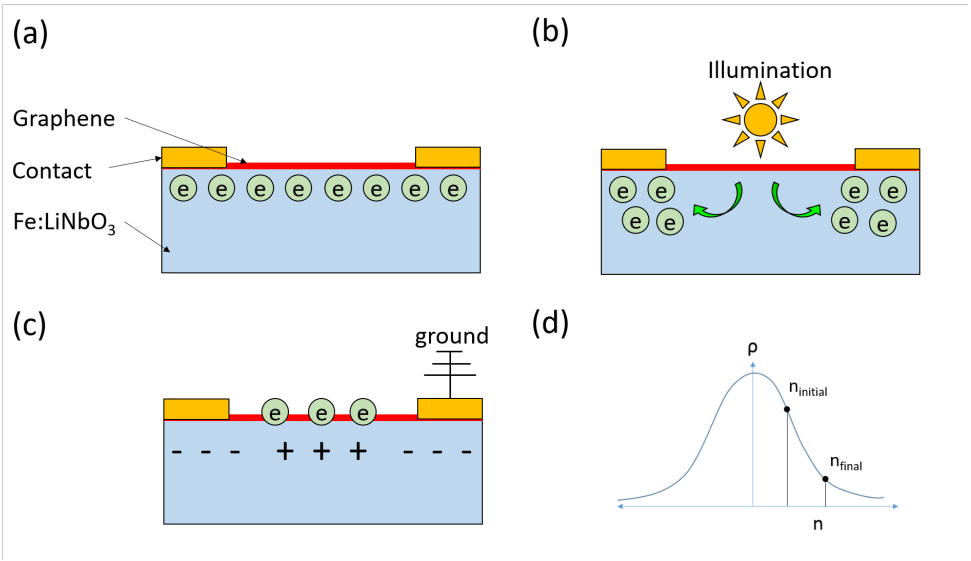

Figure 1.7: *Schematic of graphene on photorefractive lithium niobate.* ***(a)*** *Graphene monolayer with metallic contacts on Fe:$LiNbO_3$ where the Fe:$LiNbO_3$ beins with a uniform electron distribution.* ***(b)*** *Under optical illumination electrons are excited within the Fe:$LiNbO_3$ and migrate within the lattice; here I depict the diffusion mechanism in which electrons migrate away from regions of high illumination intensity.* ***(c)*** *Once the illumination source is removed the electrons with the Fe:$LiNbO_3$ are 'frozen' in position; in response to the electrostatic fields created by the Fe:$LiNbO_3$ substrate the graphene experiences an injection of electrons from the ground to compensate the fields.* ***(d)*** *Characteristic curve of resistivity against charge carrier number, depicting how an increase in electron numbers results in a decrease in electrical resistivity.*

der to counteract the photorefractive fields, which therefore alters the Fermi level of the graphene and its electrical conductivity. By thermal annealing of the lithium niobate it is possible to redistribute the charge carriers in the substrate, which should reverse the optical doping effect, and allow for subsequent optical charge domains to be rewritten. Further, by employing structured illumination such as a grating it may be possible to periodically tune the electrical properties of graphene in a spatially resolved manner. From these properties of the photorefractive effect it would seem as if lithium niobate is a tantalisingly versatile platform for controlling the electronic properties of 2D materials; this theme will be explored in the upcoming chapters of this thesis.

1.6 Thesis Structure

In this thesis I explore the use of lithium niobate to control the electronic properties of graphene. By optically patterning regions of electric charge density into lithium niobate the graphene experiences an electrostatic interaction which will modify the charge carrier number in graphene and therefore alter its Fermi level. I present a variety of research streams investigating the optical tuning of graphene to create adaptive electronic and plasmonic devices. The work comprises of experimental and numerical investigations. Due to the diverse nature of the research presented I leave an explanation of experimental methods to be self-contained in each chapter where necessary.

Chapter 2 experimentally demonstrates the optical doping effect of lithium niobate to tune the DC electrical resistivity of graphene. The optical doping effect is shown to increase the resistivity of graphene nearly 3 fold which is equated to a 0.3 eV shift in Fermi level and a charge carrier modification of $\Delta n \sim 5.5 \times 10^{12}\ cm^{-2}$. This effect is reversed with thermal annealing to return the graphene to its initial conditions, and the effect is shown to be repeatable with subsequent illumination cycles.

Chapter 3 utilises the optical doping effect in combination with a metallic metasurface which exhibits a plasmonic resonance at terahertz frequencies. It is shown the optical doping effect can tune the plasmonic resonance strength, achieving relative transmittance changes up to 35 % in an effect which is shown to be non-volatile once the illumination source is removed.

Chapter 4 further investigates plasmonic effects via simulations of monolayer graphene covering a lithium niobate substrate. Optically defined periodic regions of charge densities within the lithium niobate are used to define a structured variation in graphene Fermi level via the electrostatic gating effect. It is shown this periodic pattering is capable of sustaining plasmonic resonances at terahertz frequencies in an optically defined system without the need for permanent patterning of structures.

Chapter 5 provides a summary of the work presented and results obtained in this thesis. Further, there is a discussion of future work which could be undertaken to extend the research.

Appendix A: A novel method for extracting THz TDS data is presented in which internal reflections within a sample of lithium niobate are used to self-reference the transmitted intensity, thereby removing the need for additional calibration measurements in air. It is shown this method is capable of reducing the deviation in refractive index values as compared to the traditional air method.

Appendix B: Terahertz time domain spectroscopy measurements of lithium niobate.

Appendix C: Optically driven volatile tuning of THz transmission through lithium niobate.

Appendix D: Thermally driven volatile tuning of THz transmission through lithium niobate.

Bibliography

[1] Novoselov, K. S.; Geim, A. K.; Morozov, S. V.; Jiang, D.; Zhang, Y.; Dubonos, S. V.; Grigorieva, I. V.; Firsov, A. A. Electric Field Effect in Atomically Thin Carbon Films. *Science* **2004**, *306*, 666–669.

[2] Wallace, P. R. The Band Theory of Graphite. *Physical Review* **1947**, *71*, 622–634.

[3] Novoselov, K. S.; Mishchenko, A.; Carvalho, A.; Neto, A. H. C. 2D Materials and Van Der Waals Heterostructures. *Science* **2016**, *353*, Aac9439.

[4] Neto, A. H. C.; Guinea, F.; Peres, N. M. R.; Novoselov, K. S.; Geim, A. K. The Electronic Properties of Graphene. *Reviews of Modern Physics* **2009**, *81*, 109–162.

[5] Novoselov, K. S.; Geim, A. K.; Morozov, S. V.; Jiang, D.; Katsnelson, M. I.; Grigorieva, I. V.; Dubonos, S. V.; Firsov, A. A. Two-Dimensional Gas of Massless Dirac Fermions in Graphene. *Nature* **2005**, *438*, 197–200.

[6] Geim, A. K.; Novoselov, K. S. The Rise of Graphene. *Nature Materials* **2007**, *6*, 183–191.

[7] Grigorenko, A. N.; Polini, M.; Novoselov, K. S. Graphene Plasmonics. *Nature Photonics* **2012**, *6*, 749–758.

[8] Ju, L.; Geng, B.; Horng, J.; Girit, C.; Martin, M.; Hao, Z.; Bechtel, H. A.; Liang, X.; Zettl, A.; Shen, Y. R.; Wang, F. Graphene Plasmonics for Tunable Terahertz Metamaterials. *Nature Nanotechnology* **2011**, *6*, 630–634.

[9] Zhou, W.; Lee, J.; Nanda, J.; Pantelides, S. T.; Pennycook, S. J.; Idrobo, J.-C. Atomically Localized Plasmon Enhancement in Monolayer Graphene. *Nature Nanotechnology* **2012**, *7*, 161–165.

[10] Yan, H.; Li, X.; Chandra, B.; Tulevski, G.; Wu, Y.; Freitag, M.; Zhu, W.; Avouris, P.; Xia, F. Tunable Infrared Plasmonic Devices using Graphene/Insulator Stacks. *Nature Nanotechnology* **2012**, *7*, 330–334.

[11] Jablan, M.; Buljan, H.; Soljacic, M. Plasmonics in Graphene at Infrared Frequencies. *Physical Review B* **2009**, *80*, 245435.

[12] Chen, J.; Badioli, M.; Alonso-Gonzalez, P.; Thongrattanasiri, S.; Huth, F.; Osmond, J.; Spasenovic, M.; Centeno, A.; Pesquera, A.; Godignon, P.; Elorza, A. Z.; Camara, N.; Abajo, F. J. G. D.; Hillenbrand, R.; Koppens, F. H. L. Optical Nano-Imaging of Gate-Tunable Graphene Plasmons. *Nature* **2012**, *487*, 77–81.

[13] Brar, V. W.; Jang, M. S.; Sherrott, M.; Lopez, J. J.; Atwater, H. A. Highly Confined Tunable Mid-Infrared Plasmonics in Graphene Nanoresonators. *Nano Letters* **2013**, *13*, 2541–2547.

[14] Kim, J.; Son, H.; Cho, D. J.; Geng, B.; Regan, W.; Shi, S.; Kim, K.; Zettl, A.; Shen, Y.-R.; Wang, F. Electrical Control of Optical Plasmon Resonance With Graphene. *Nano Letters* **2012**, *12*, 5598–5602.

[15] Thackray, B.; Kravets, V. G.; Schedin, F.; Jalil, R.; Grigorenko, A. N. Resistive Coupling of Localized Plasmon Resonances in Metallic Nanostripes Through a Graphene Layer. *Journal of Optics* **2013**, *15*, 114002.

[16] Liu, P. Q.; Luxmoore, I. J.; Mikhailov, S. A.; Savostianova, N. A.; Valmorra, F.; Faist, J.; Nash, G. R. Highly Tunable Hybrid Metamaterials Employing Split-Ring Resonators Strongly Coupled to Graphene Surface Plasmons. *Nature Communications* **2015**, *6*, 8969.

[17] Bonaccorso, F.; Lombardo, A.; Hasan, T.; Sun, Z.; Colombo, L.; Ferrari, A. C. Production and Processing of Graphene and 2D Crystals. *Materials Today* **2012**, *15*, 564–589.

[18] Reina, A.; Jia, X.; Ho, J.; Nezich, D.; Son, H.; Bulovic, V.; Dresselhaus, M. S.; Kong, J. Large Area, Few-Layer Graphene Films On Arbitrary Substrates by Chemical Vapor Deposition. *Nano Letters* **2009**, *9*, 30–35.

[19] Heer, W. A. D.; Berger, C.; Wu, X.; First, P. N.; Conrad, E. H.; Li, X.; Li, T.; Sprinkle, M.; Hass, J.; Sadowski, M. L.; Potemski, M.; Martinez, G. Epitaxial Graphene. *Solid State Communications* **2007**, *143*, 92–100.

[20] Xia, Z. Y.; Pezzini, S.; Treossi, E.; Giambastiani, G.; Corticelli, F.; Morandi, V.; Zanelli, A.; Bellani, V.; Palermo, V. The Exfoliation of Graphene in Liquids by Electrochemical, Chemical, and Sonication-Assisted Techniques: A Nanoscale Study. *Advanced Functional Materials* **2013**, *23*, 4684–4693.

[21] Zhao, W.; Fang, M.; Wu, F.; Wu, H.; Wang, L.; Chen, G. Preparation of Graphene by Exfoliation of Graphite using Wet Ball Milling. *Journal of Materials Chemistry* **2010**, *20*, 5817.

[22] Bolotin, K.; Sikes, K.; Jiang, Z.; Klima, M.; Fudenberg, G.; Hone, J.; Kim, P.; Stormer, H. Ultrahigh Electron Mobility in Suspended Graphene. *Solid State Communications* **2008**, *146*, 351–355.

[23] Yi, M.; Shen, Z. A Review On Mechanical Exfoliation for the Scalable Production of Graphene. *Journal of Materials Chemistry A* **2015**, *3*, 11700–11715.

[24] Zhang, Y.; Zhang, L.; Zhou, C. Review of Chemical Vapor Deposition of Graphene and Related Applications. *Accounts of Chemical Research* **2013**, *46*, 2329–2339.

[25] Lupina, G. et al. Residual Metallic Contamination of Transferred Chemical Vapor Deposited Graphene. *ACS Nano* **2015**, *9*, 4776–4785.

[26] Mattevi, C.; Kim, H.; Chhowalla, M. A Review of Chemical Vapour Deposition of Graphene On Copper. *Journal of Materials Chemistry* **2011**, *21*, 3324–3334.

[27] Low, T.; Avouris, P. Graphene Plasmonics for Terahertz to Mid-Infrared Applications. *ACS Nano* **2014**, *8*, 1086–1101.

[28] Otsuji, T.; Popov, V.; Ryzhii, V. Active Graphene Plasmonics for Terahertz Device Applications. *Journal of Physics D: Applied Physics* **2014**, *47*, 094006.

[29] Jablan, M.; Buljan, H.; Soljacic, M. Plasmonics in Graphene at Infrared Frequencies. *Physical Review B* **2009**, *80*, 245435.

[30] Fei, Z.; Rodin, A. S.; Andreev, G. O.; Bao, W.; Mcleod, A. S.; Wagner, M.; Zhang, L. M.; Zhao, Z.; Thiemens, M.; Dominguez, G.;

Fogler, M. M.; Neto, A. H. C.; Lau, C. N.; Keilmann, F.; Basov, D. N. Gate-Tuning of Graphene Plasmons Revealed by Infrared Nano-Imaging. *Nature* **2012**, *487*, 82–85.

[31] Zang, X.; Zhou, Q.; Chang, J.; Liu, Y.; Lin, L. Graphene and Carbon Nanotube (CNT) in MEMS/NEMS Applications. *Microelectronic Engineering* **2015**, *132*, 192–206.

[32] Bae, S. et al. Roll-to-Roll Production of 30-Inch Graphene Films for Transparent Electrodes. *Nature Nanotechnology* **2010**, *5*, 574–578.

[33] Huang, X.; Zeng, Z.; Fan, Z.; Liu, J.; Zhang, H. Graphene-Based Electrodes. *Advanced Materials* **2012**, *24*, 5979–6004.

[34] Schedin, F.; Geim, A. K.; Morozov, S. V.; Hill, E. W.; Blake, P.; Katsnelson, M. I.; Novoselov, K. S. Detection of Individual Gas Molecules Adsorbed on Graphene. *Nature Materials* **2007**, *6*, 652–655.

[35] Shao, Y.; Wang, J.; Wu, H.; Liu, J.; Aksay, I. A.; Lin, Y. Graphene Based Electrochemical Sensors and Biosensors: A Review. *Electroanalysis* **2010**, *22*, 1027–1036.

[36] Bonaccorso, F.; Sun, Z.; Hasan, T.; Ferrari, A. C. Graphene Photonics and Optoelectronics. *Nature Photonics* **2010**, *4*, 611–622.

[37] Avouris, P.; Freitag, M. Graphene Photonics, Plasmonics, and Optoelectronics. *IEEE Journal of Selected Topics in Quantum Electronics* **2014**, *20*, 72–83.

[38] Liu, C.-H.; Chang, Y.-C.; Norris, T. B.; Zhong, Z. Graphene Photodetectors with Ultra-Broadband and High Responsivity at Room Temperature. *Nature Nanotechnology* **2014**, *9*, 273–278.

[39] Nair, R. R.; Blake, P.; Grigorenko, A. N.; Novoselov, K. S.; Booth, T. J.; Stauber, T.; Peres, N. M. R.; Geim, A. K. Fine Structure Constant Defines Visual Transparency of Graphene. *Science* **2008**, *320*, 1308–1308.

[40] Urich, A.; Unterrainer, K.; Mueller, T. Intrinsic Response Time of Graphene Photodetectors. *Nano Letters* **2011**, *11*, 2804–2808.

[41] Wang, J.; Fang, H.; Wang, X.; Chen, X.; Lu, W.; Hu, W. Recent Progress On Localized Field Enhanced Two-Dimensional Material Photodetectors from Ultraviolet-Visible to Infrared. *Small* **2017**, *13*, 1700894.

[42] Konstantatos, G.; Badioli, M.; Gaudreau, L.; Osmond, J.; Bernechea, M.; de Arquer, F. P. G.; Gatti, F.; Koppens, F. H. L. Hybrid graphene–quantum dot phototransistors with ultrahigh gain. *Nature Nanotechnology* **2012**, *7*, 363–368.

[43] Luo, F.; Zhu, M.; tan, Y.; Sun, H.; Luo, W.; Peng, G.; Zhu, Z.; Zhang, X.-A.; Qin, S. High responsivity graphene photodetectors from visible to near-infrared by photogating effect. *AIP Advances* **2018**, *8*, 115106.

[44] Liu, C.-H.; Chang, Y.-C.; Norris, T. B.; Zhong, Z. Graphene photodetectors with ultra-broadband and high responsivity at room temperature. *Nature Nanotechnology* **2014**, *9*, 273–278.

[45] Miro, P.; Audiffred, M.; Heine, T. An Atlas of Two-Dimensional Materials. *Chemical Society Reviews* **2014**, *43*, 6537–6554.

[46] Mas-Balleste, R.; Gomez-Navarro, C.; Gomez-Herrero, J.; Zamora, F. 2D Materials: To Graphene and Beyond. *Nanoscale* **2011**, *3*, 20–30.

[47] Ponraj, J. S.; Xu, Z.-Q.; Dhanabalan, S. C.; Mu, H.; Wang, Y.; Yuan, J.; Li, P.; Thakur, S.; Ashrafi, M.; Mccoubrey, K.; Zhang, Y.; Li, S.; Zhang, H.; Bao, Q. Photonics and Optoelectronics of Two-Dimensional Materials Beyond Graphene. *Nanotechnology* **2016**, *27*, 462001.

[48] Mak, K. F.; Lee, C.; Hone, J.; Shan, J.; Heinz, T. F. Atomically Thin MoS_2: A New Direct-Gap Semiconductor. *Physical Review Letters* **2010**, *105*, 136805.

[49] Vogt, P.; Padova, P. D.; Quaresima, C.; Avila, J.; Frantzeskakis, E.; Asensio, M. C.; Resta, A.; Ealet, B.; Lay, G. L. Silicene: Compelling Experimental Evidence for Graphenelike Two-Dimensional Silicon. *Physical Review Letters* **2012**, *108*, 155501.

[50] Wang, X.; Li, X.; Zhang, L.; Yoon, Y.; Weber, P. K.; Wang, H.; Guo, J.; Dai, H. N-Doping of Graphene through Electrothermal Reactions with Ammonia. *Science* **2009**, *324*, 768–771.

[51] Han, M. Y.; Oezyilmaz, B.; Zhang, Y.; Kim, P. Energy Band-Gap Engineering of Graphene Nanoribbons. *Physical Review Letters* **2007**, *98*, 206805.

[52] Son, Y.-W.; Cohen, M. L.; Louie, S. G. Energy Gaps in Graphene Nanoribbons. *Physical Review Letters* **2006**, *97*, 216803.

[53] Kosynkin, D. V.; Higginbotham, A. L.; Sinitskii, A.; Lomeda, J. R.; Dimiev, A.; Price, B. K.; Tour, J. M. Longitudinal Unzipping of Carbon Nanotubes to form Graphene Nanoribbons. *Nature* **2009**, *458*, 872–876.

[54] Das Sarma, S.; Adam, S.; Hwang, E. H.; Rossi, E. Electronic Transport in Two-Dimensional Graphene. *Reviews of Modern Physics* **2011**, *83*, 407–470.

[55] Dean, C. R.; Young, A. F.; Meric, I.; Lee, C.; Wang, L.; Sorgenfrei, S.; Watanabe, K.; Taniguchi, T.; Kim, P.; Shepard, K. L.; Hone, J. Boron Nitride Substrates for High-Quality Graphene Electronics. *Nature Nanotechnology* **2010**, *5*, 722–726.

[56] Britnell, L.; Ribeiro, R. M.; Eckmann, A.; Jalil, R.; Belle, B. D.; Mishchenko, A.; Kim, Y. J.; Gorbachev, R. V.; Georgiou, T.; Morozov, S. V.; Grigorenko, A. N.; Geim, A. K.; Casiraghi, C.; Castro Neto, A. H.; Novoselov, K. S. Strong Light-Matter Interactions in Heterostructures of Atomically Thin Films. *Science* **2013**, *340*, 1311–1314.

[57] Geim, A. K.; Grigorieva, I. V. Van Der Waals Heterostructures. *Nature* **2013**, *499*, 419–425.

[58] Liu, H.; Liu, Y.; Zhu, D. Chemical Doping of Graphene. *Journal of Materials Chemistry* **2011**, *21*, 3335–3345.

[59] Wang, L.; Sofer, Z.; Pumera, M. Will Any Crap We Put Into Graphene Increase its Electrocatalytic Effect? *ACS Nano* **2020**, *14*, 21–25.

[60] Schedin, F.; Geim, A. K.; Morozov, S. V.; Hill, E. W.; Blake, P.; Katsnelson, M. I.; Novoselov, K. S. Detection of Individual Gas Molecules Adsorbed on Graphene. *Nature Materials* **2007**, *6*, 652–655.

[61] Lupina, G. et al. Residual Metallic Contamination of Transferred Chemical Vapor Deposited Graphene. *ACS Nano* **2015**, *9*, 4776–4785.

[62] Chen, W.; Chen, S.; Qi, D. C.; Gao, X. Y.; Wee, A. T. S. Surface Transfer P-Type Doping of Epitaxial Graphene. *Journal of the American Chemical Society* **2007**, *129*, 10418–10422.

[63] Chen, J.-H.; Jang, C.; Adam, S.; Fuhrer, M. S.; Williams, E. D.; Ishigami, M. Charged-Impurity Scattering in Graphene. *Nature Physics* **2008**, *4*, 377–381.

[64] Chen, J.-H.; Jang, C.; Xiao, S.; Ishigami, M.; Fuhrer, M. S. Intrinsic and Extrinsic Performance Limits of Graphene Devices on SiO_2. *Nature Nanotechnology* **2008**, *3*, 206–209.

[65] Lee, G.; Cho, K. Electronic Structures of Zigzag Graphene Nanoribbons with Edge Hydrogenation and Oxidation. *Physical Review B* **2009**, *79*, 165440.

[66] Wei, D.; Liu, Y.; Wang, Y.; Zhang, H.; Huang, L.; Yu, G. Synthesis of N-Doped Graphene by Chemical Vapor Deposition and its Electrical Properties. *Nano Letters* **2009**, *9*, 1752–1758.

[67] Lherbier, A.; Blase, X.; Niquet, Y.-M.; Triozon, F.; Roche, S. Charge Transport in Chemically Doped 2D Graphene. *Physical Review Letters* **2008**, *101*, 036808.

[68] Panchakarla, L. S.; Subrahmanyam, K. S.; Saha, S. K.; Govindaraj, A.; Krishnamurthy, H. R.; Waghmare, U. V.; Rao, C. N. R. Synthesis, Structure, and Properties of Boron- and Nitrogen-Doped Graphene. *Advanced Materials* **2009**, *21*, 4726–4730.

[69] Zhang, C.; Mahmood, N.; Yin, H.; Liu, F.; Hou, Y. Synthesis of Phosphorus-Doped Graphene and its Multifunctional Applications for Oxygen Reduction Reaction and Lithium Ion Batteries. *Advanced Materials* **2013**, *25*, 4932–4937.

[70] Deifallah, M.; Mcmillan, P. F.; Cora, F. Electronic and Structural Properties of Two-Dimensional Carbon Nitride Graphenes. *The Journal of Physical Chemistry C* **2008**, *112*, 5447–5453.

[71] Wei, D.; Liu, Y.; Wang, Y.; Zhang, H.; Huang, L.; Yu, G. Synthesis of N-Doped Graphene by Chemical Vapor Deposition and its Electrical Properties. *Nano Letters* **2009**, *9*, 1752–1758.

[72] Yu, W. J.; Liu, Y.; Zhou, H.; Yin, A.; Li, Z.; Huang, Y.; Duan, X. Highly Efficient Gate-Tunable Photocurrent Generation in Vertical Heterostructures of Layered Materials. *Nature Nanotechnology* **2013**, *8*, 952–958.

[73] Cui, X. et al. Multi-Terminal Transport Measurements of MoS_2 Using a Van Der Waals Heterostructure Device Platform. *Nature Nanotechnology* **2015**, *10*, 534–540.

[74] Georgiou, T.; Jalil, R.; Belle, B. D.; Britnell, L.; Gorbachev, R. V.; Morozov, S. V.; Kim, Y.-J.; Gholinia, A.; Haigh, S. J.; Makarovsky, O.; Eaves, L.; Ponomarenko, L. A.; Geim, A. K.; Novoselov, K. S.; Mishchenko, A. Vertical Field-Effect Transistor Based On Graphene-WS_2 Heterostructures for Flexible and Transparent Electronics. *Nature Nanotechnology* **2012**, *8*, 100–103.

[75] Shim, J. et al. Extremely Large Gate Modulation in Vertical Graphene/WSe_2 heterojunction Barristor Based an a Novel Transport Mechanism. *Advanced Materials* **2016**, *28*, 5293–5299.

[76] Padilha, J. E.; Fazzio, A.; Silva, A. J. R. D. Van Der Waals Heterostructure of Phosphorene and Graphene: Tuning the Schottky Barrier and Doping by Electrostatic Gating. *Physical Review Letters* **2015**, *114*, 066803.

[77] Liu, J.-J.; Li, R.-J.; Li, H.; Li, Y.-F.; Yi, J.-H.; Wang, H.-C.; Zhao, X.-C.; Liu, P.-Z.; Guo, J.-J.; Liu, L. Graphene-Based In-Plane Heterostructures for Atomically Thin Electronics. *New Carbon Materials* **2018**, *33*, 481–492.

[78] Li, C.; Zhou, P.; Zhang, D. W. Devices and Applications of Van Der Waals Heterostructures. *Journal of Semiconductors* **2017**, *38*, 031005.

[79] Liang, S.-J.; Cheng, B.; Cui, X.; Miao, F. Van Der Waals Heterostructures for High-Performance Device Applications: Challenges and Opportunities. *Advanced Materials* **2019**, 1903800.

[80] Siskins, M.; Mullan, C.; Son, S.-K.; Yin, J.; Watanabe, K.; Taniguchi, T.; Ghazaryan, D.; Novoselov, K. S.; Mishchenko, A. High-Temperature Electronic Devices Enabled by hBN-Encapsulated Graphene. *Applied Physics Letters* **2019**, *114*, 123104.

[81] Yankowitz, M.; Xue, J.; Leroy, B. J. Graphene On Hexagonal Boron Nitride. *Journal of Physics: Condensed Matter* **2014**, *26*, 303201.

[82] Cao, Y.; Fatemi, V.; Fang, S.; Watanabe, K.; Taniguchi, T.; Kaxiras, E.; Jarillo-Herrero, P. Unconventional Superconductivity in Magic-Angle Graphene Superlattices. *Nature* **2018**, *556*, 43–50.

[83] Cao, Y.; Fatemi, V.; Demir, A.; Fang, S.; Tomarken, S. L.; Luo, J. Y.; Sanchez-Yamagishi, J. D.; Watanabe, K.; Taniguchi, T.; Kaxiras, E.; Ashoori, R. C.; Jarillo-Herrero, P. Correlated Insulator Behaviour at Half-Filling in Magic-Angle Graphene Superlattices. *Nature* **2018**, *556*, 80–84.

[84] Tarnopolsky, G.; Kruchkov, A. J.; Vishwanath, A. Origin of Magic Angles in Twisted Bilayer Graphene. *Physical Review Letters* **2019**, *122*, 106405.

[85] Schwierz, F. Graphene Transistors. *Nature Nanotechnology* **2010**, *5*, 487–496.

[86] Seo, B. H.; Youn, J.; Shim, M. Direct Laser Writing of Air-Stable P-N Junctions in Graphene. *ACS Nano* **2014**, *8*, 8831–8836.

[87] Iqbal, M. Z.; Iqbal, M. W.; Khan, M. F.; Eom, J. Ultraviolet-Light-Driven Doping Modulation in Chemical Vapor Deposition Grown Graphene. *Physical Chemistry Chemical Physics* **2015**, *17*, 20551–20556.

[88] Xiao, Z.; Song, J.; Ferry, D. K.; Ducharme, S.; Hong, X. Ferroelectric-Domain-Patterning-Controlled Schottky Junction State in Monolayer MoS_2. *Physical Review Letters* **2017**, *118*, 236801.

[89] Baeumer, C.; Saldana-Greco, D.; Martirez, J. M. P.; Rappe, A. M.; Shim, M.; Martin, L. W. Ferroelectrically Driven Spatial Carrier Density Modulation in Graphene. *Nature Communications* **2015**, *6*, 6136.

[90] Gopalan, K. K.; Janner, D.; Nanot, S.; Parret, R.; Lundeberg, M. B.; Koppens, F. H. L.; Pruneri, V. Mid-Infrared Pyroresistive Graphene Detector On $LiNbO_3$. *Advanced Optical Materials* **2016**, *5*, 1600723.

[91] Wang, X.; Tabakman, S. M.; Dai, H. Atomic Layer Deposition of Metal Oxides On Pristine and Functionalized Graphene. *Journal of the American Chemical Society* **2008**, *130*, 8152–8153.

[92] Lee, B.; Park, S.-Y.; Kim, H.-C.; Cho, K.; Vogel, E. M.; Kim, M. J.; Wallace, R. M.; Kim, J. Conformal AL_2O_3 Dielectric Layer Deposited by Atomic Layer Deposition for Graphene-Based Nanoelectronics. *Applied Physics Letters* **2008**, *92*, 203102.

[93] Mcdonnell, S.; Brennan, B.; Azcatl, A.; Lu, N.; Dong, H.; Buie, C.; Kim, J.; Hinkle, C. L.; Kim, M. J.; Wallace, R. M. HfO_2 On MoS_2 by Atomic Layer Deposition: Adsorption Mechanisms and Thickness Scalability. *ACS Nano* **2013**, *7*, 10354–10361.

[94] Zhang, Y.; Tan, Y.-W.; Stormer, H. L.; Kim, P. Experimental Observation of the Quantum Hall Effect and Berrys Phase in Graphene. *Nature* **2005**, *438*, 201–204.

[95] Wang, H. I.; Braatz, M.-L.; Richter, N.; Tielrooij, K.-J.; Mics, Z.; Lu, H.; Weber, N.-E.; Muellen, K.; Turchinovich, D.; Klaeui, M.; Bonn, M. Reversible Photochemical Control of Doping Levels in Supported Graphene. *Journal of Physical Chemistry C* **2017**, *121*, 4083–4091.

[96] Wang, X.-J.; Zou, L.; Li, D.; Zhang, Q.; Wang, F.; Zhang, Z. Photo-Induced Doping in Graphene/Silicon Heterostructures. *Journal of Physical Chemistry C* **2015**, *119*, 1061–1066.

[97] Ho, P.-H.; Chen, C.-H.; Shih, F.-Y.; Chang, Y.-R.; Li, S.-S.; Wang, W.-H.; Shih, M.-C.; Chen, W.-T.; Chiu, Y.-P.; Li, M.-K.; Shih, Y.-S.; Chen, C.-W. Precisely Controlled Ultrastrong Photoinduced Doping at Graphene-Heterostructures Assisted by Trap-State-Mediated Charge Transfer. *Advanced Materials* **2015**, *27*, 7809–7815.

[98] Jun, L.; Velasco, J., Jr.; Huang, E.; Kahn, S.; Nosiglia, C.; Tsai, H.-Z.; Yang, W.; Taniguchi, T.; Watanabe, K.; Zhang, Y.; Zhang, G.; Crommie, M.; Zettl, A.; Wang, F. Photoinduced Doping in Heterostructures of Graphene and Boron Nitride. *Nature Nanotechnology* **2014**, *9*, 348–352.

[99] Song, E. B. et al. Robust Bi-Stable Memory Operation in Single-Layer Graphene Ferroelectric Memory. *Applied Physics Letters* **2011**, *99*, 042109.

[100] Yusuf, M. H.; Gura, A.; Du, X.; Dawber, M. Local Control of the Resistivity of Graphene through Mechanically Induced Switching of a Ferroelectric Superlattice. *2D Materials* **2017**, *4*, 021022.

[101] Zelenovskii, P.; Romanyuk, K.; Vidyasagar, R.; Akhmatkhanov, A.; Zhao, P.; Shur, V. Y.; Kholkin, A. L. Effect of Ferroelectric Domains On Electric Properties of Single Layer Graphene. *Ferroelectrics* **2019**, *542*, 93–101.

[102] Papasimakis, N.; Mailis, S.; Huang, C. C.; Al-Saab, F.; Hewak, D. W.; Luo, Z.; Shen, Z. X. Strain Engineering in Graphene by Laser Irradiation. *Applied Physics Letters* **2015**, *106*, 061904.

[103] Sassi, U.; Parret, R.; Nanot, S.; Bruna, M.; Borini, S.; Fazio, D. D.; Zhao, Z.; Lidorikis, E.; Koppens, F.; Ferrari, A. C.; Colli, A. Graphene-Based Mid-Infrared Room-Temperature Pyroelectric Bolometers with Ultrahigh Temperature Coefficient of Resistance. *Nature Communications* **2017**, *8*, 14311.

[104] Shimatani, M.; Ogawa, S.; Fukushima, S.; Okuda, S.; Kanai, Y.; Ono, T.; Matsumoto, K. Enhanced Photogating via Pyroelectric Effect Induced by Insulator Layer for High-Responsivity Long-Wavelength Infrared Graphene-Based Photodetectors Operating at Room Temperature. *Applied Physics Express* **2019**, *12*, 025001.

[105] Maiman, T. H. Stimulated Optical Radiation in Ruby. *Nature* **1960**, *187*, 493–494.

[106] T. Volk, M. W. *Lithium Niobate*; Springer Berlin Heidelberg, 2008.

[107] B. T. Matthias, J. P. R. Ferroelectricity in the Ilmenite Structure. *Physical Review* **1949**, *76*, 1886–1887.

[108] Fedulov, S. A.; Ladyzhenskii, P. B.; Shapiro, Z. I. *Kristallografiya* **1965**, *10*, 268.

[109] Ballman, A. A. Growth of Piezoelectric and Ferroelectric Materials by the Czochraiski Technique. *Journal of the American Ceramic Society* **1965**, *48*, 112–113.

[110] Buse, K. Light-Induced Charge Transport Processes in Photorefractive Crystals I: Models and Experimental Methods. *Applied Physics B: Lasers and Optics* **1997**, *64*, 273–291.

[111] Volk, T.; Rubinina, N.; Wohlecke, M. Optical-Damage-Resistant Impurities in Lithium Niobate. *Journal of the Optical Society of America B* **1994**, *11*, 1681.

[112] Chen, F. S.; Lamacchia, J. T.; Fraser, D. B. Holographic Storage in Lithium Niobate. *Applied Physics Letters* **1968**, *13*, 223–225.

[113] Buse, K.; Adibi, A.; Psaltis, D. Non-Volatile Holographic Storage in Doubly Doped Lithium Niobate Crystals. *Nature* **1998**, *393*, 665–668.

[114] Mok, F. H. Angle-Multiplexed Storage of 5000 Holograms in Lithium Niobate. *Optics Letters* **1993**, *18*, 915–917.

[115] Carrascosa, M.; Garcia-Cabanes, A.; Jubera, M.; Ramiro, J. B.; Agullo-Lopez, F. $LiNbO_3$: A Photovoltaic Substrate for Massive Parallel Manipulation and Patterning of Nano-Objects. *Applied Physics Reviews* **2015**, *2*, 040605.

[116] Grilli, S.; Ferraro, P. Dielectrophoretic Trapping of Suspended Particles by Selective Pyroelectric Effect in Lithium Niobate Crystals. *Applied Physics Letters* **2008**, *92*, 232902.

[117] Habibpourmoghadam, A.; Lucchetti, L.; Evans, D. R.; Reshetnyak, V. Y.; Omairat, F.; Schafforz, S. L.; Lorenz, A. Laser-Induced Erasable Patterns in A N* Liquid Crystal on an Iron Doped Lithium Niobate Surface. *Optics Express* **2017**, *25*, 26148.

[118] Bartasyte, A.; Margueron, S.; Baron, T.; Oliveri, S.; Boulet, P. Toward High-Quality Epitaxial $LiNbO_3$ and $LiTaO_3$ Thin Films for Acoustic and Optical Applications. *Advanced Materials Interfaces* **2017**, *4*, 1600998.

[119] Puerto, A.; Munoz-Martin, J. F.; Mendez, A.; Arizmendi, L.; Garcia-Cabanes, A.; Agullopez, F.; Carrascosa, M. Synergy Between Pyroelectric and Photovoltaic Effects for Optoelectronic Nanoparticle Manipulation. *Optics Express* **2019**, *27*, 804.

[120] Broderick, N. G. R.; Ross, G. W.; Offerhaus, H. L.; Richardson, D. J.; Hanna, D. C. Hexagonally Poled Lithium Niobate: A Two-Dimensional Nonlinear Photonic Crystal. *Physical Review Letters* **2000**, *84*, 4345–4348.

[121] Zhu, L.; Zheng, D.; Saeed, S.; Wang, S.; Liu, H.; Kong, Y.; Liu, S.; Chen, S.; Zhang, L.; Xu, J. Photorefractive Properties of Molybdenum and Hafnium Co-Doped $LiNbO_3$ Crystals. *Crystals* **2018**, *8*, 322.

[122] Arizmendi, L.; Lopez-Barbera, F. J. Lifetime of Thermally Fixed Holograms in $Linbo_3$ Crystals Doped With Mg and Fe. *Applied Physics B* **2007**, *86*, 105–109.

[123] Chen, F. S. Optically Induced Change of Refractive Indices in $LiNbO_3$ and $LiTaO_3$. *Journal of Applied Physics* **1969**, *40*, 3389–3396.

[124] Hsieh, H.; Psaltis, D.; Beyer, O.; Maxein, D.; Von Korff Schmising, C.; Buse, K.; Sturman, B. Femtosecond Holography in Lithium Niobate Crystals. *Optics Letters* **2005**, *30*, 2233–2235.

[125] Paipulas, D.; Buivydas, R.; Juodkazis, S.; Mizeikis, V. Local Photorefractive Modification in Lithium Niobate using Ultrafast Direct Laser Write Technique. *Journal of Laser Micro/Nanoengineering* **2016**, *11*, 246–252.

[126] Ohmori, Y.; Yasojima, Y.; Inuishi, Y. Photoconduction, Thermally Stimulated Luminescence, and Optical Damage in Single Crystal of $LiNbO_3$. *Japanese Journal of Applied Physics* **1975**, *14*, 1291–1300.

[127] Chen, F. S. Optically Induced Change of Refractive Indices in $LiNbO_3$ and $LiTaO_3$. *Journal of Applied Physics* **1969**, *40*, 3389–3396.

[128] Rode, S.; Holscher, R.; Sanna, S.; Klassen, S.; Kobayashi, K.; Yamada, H.; Schmidt, W. G.; Kuhnle, A. Atomic-Resolution Imaging of the Polar $000\bar{1}$ Surface of $LiNbO_3$ in Aqueous Solution by Frequency Modulation Atomic Force Microscopy. *Physical Review B* **2012**, *86*, 075468.

[129] Arregui, C.; Ramiro, J. B.; Alcazar, A.; Mendez, A.; Munoz-Martinez, J. F.; Carrascosa, M. Comparative Theoretical Analysis Between Parallel and Perpendicular Geometries for 2D Particle Patterning in Photovoltaic Ferroelectric Substrates. *Journal of the European Optical Society: Rapid Publications* **2015**, *10*, 15026.

[130] Arregui, C.; Ramiro, J. B.; Alcazar, A.; Mendez, A.; Burgos, H.; Garcia-Cabanes, A.; Carrascosa, M. Optoelectronic Tweezers Under Arbitrary Illumination Patterns: Theoretical Simulations and Comparison to Experiment. *Optics Express* **2014**, *22*, 29099.

[131] Miguel, E. M. D.; Limeres, J.; Carrascosa, M.; Arizmendi, L. Study of Developing Thermal Fixed Holograms in Lithium Niobate. *Journal of the Optical Society of America B* **2000**, *17*, 1140.

[132] Kalkum, F.; Peithmann, K.; Buse, K. Dynamics of Holographic Recording with Focused Beams in Iron-Doped Lithium Niobate Crystals. *Optics Express* **2009**, *17*, 1321.

[133] Calamiotou, M.; Chrysanthakopoulos, N.; Papaioannou, G.; Baruchel, J. Dynamics of Photodeformations and Space Charge Field in Photorefractive Fe:$LiNbO_3$ Studied with Synchrotron Area Diffractometry. *Journal of Applied Physics* **2007**, *102*, 083527.

Chapter 2

Optical Tuning of Graphene Electronics

2.1 Introduction

Two dimensional materials offer great prospects for tuneable optoelectronic devices however there currently exists a lack of methods to control the electronic properties of these materials in a spatially resolved and non-volatile manner. Here I investigate the use of photorefractive iron doped lithium niobate (Fe:$LiNbO_3$) as a platform for the optical control of two dimensional materials. As a proof-of-concept device I transfer graphene to lithium niobate crystals and show how optical illumination can result in charge distributions within the substrate which electrostatically interact with the graphene monolayer, resulting in a substantial 0.3 eV shift in Fermi level, which is shown to be reversed under thermal annealing yet repeatable by subsequent illumination cycles. Based on the reported properties of the photorefractive effect in lithium niobate this platform is expected to allow for spatial control where individual regions of the 2D material can be locally addressed, and to be optically reversible under uniform illumination. Despite testing the proof-of-concept on graphene it is expected that this platform can be utilised with a wide range of 2D materials, where the incorporation of materials such as MoS_2 which exhibit an electronic bandgap could pave the way towards optically controlled transistors or even optically written electronic interconnects.

2.2 Graphene Electronics

Due to the unique electronic band structure of graphene [1] the linear dispersion relation centred around the Dirac point implies the density of states will vanish at the Dirac point, or in other words the number of free charge carriers will tend towards zero. As a result of this the Fermi level is extremely sensitive to number of carriers [2], therefore by making small adjustments to the number of carriers can create a large change in Fermi level (for example: adding 10^{12} cm^{-2} carriers can change E_F on the order of 100's of meV). To adjust the carrier numbers in graphene a field effect is usually employed, in which a substrate (separated from the graphene by a thin insulator layer) is held at a voltage bias with respect to the graphene, thereby setting up an electrostatic field between the graphene and the substrate (also known as the gate). In response to the electrostatic field charge carriers will move within the graphene sheet (either injected or ejected from the electric ground) in order to counteract the electric field created by the gate.

Gating of 2D materials in such a manner has a number of drawbacks as: the gate is usually a uniform slab of material and therefore offers no spatial resolution unless patterned into a complicated structure of individual gates with individual electrical interconnects; the gate is not reconfigurable as its geometry must be structured during fabrication of the device; the gate materials are often not optically transparent which limits the operation of the device as optical tuning elements. Further, gating with an electrical back-gate is a volatile effect which does not remain once the voltage source is removed and therefore requires persistent voltages in order to operate. To this end it is advantageous to look for optically actuated non-volatile mechanisms to spatially control the properties of 2D materials.

2.3 Graphene on Fe:$LiNbO_3$ Mechanism

Here, I present an approach to optically control the electronic properties of graphene in a non-volatile yet reversible manner by use of a photorefractive iron doped lithium niobate substrate. $LiNbO_3$ exhibits a photorefractive effect [3] in which Fe impurities in the crystal act as photo-excited charge centres, supplying electrons to the conduction band which are free to migrate in the lattice. Depending on their valence state these impurities can act as donors or acceptors, thus by non-uniform illumination of the substrate photoexcited electrons are free to migrate within the crystal lattice where they become trapped in acceptor Fe^{+3} sites creating a non-uniform charge distribution which is stable at room temperature over long periods of time (years) [4]. As described in Chapter 1 there are generally considered to be two mechanisms responsible for inducing the migration of photoexcited electrons which are the drift and diffusion effects. A schematic representation of the device is shown in Figure 2.1 consisting of Fe:$LiNbO_3$ substrate covered with monolayer CVD graphene and patterned with an array of metallic electrodes. Upon illumination the substrate will experience a photorefractive effect in which electrons migrate within the crystal, defining a non-uniform charge distribution. In response to the fields created in the substrate a graphene top layer will experience an electrostatic interaction in which the number of charge carriers will be altered to compensate any electrostatic fields created by the substrate.

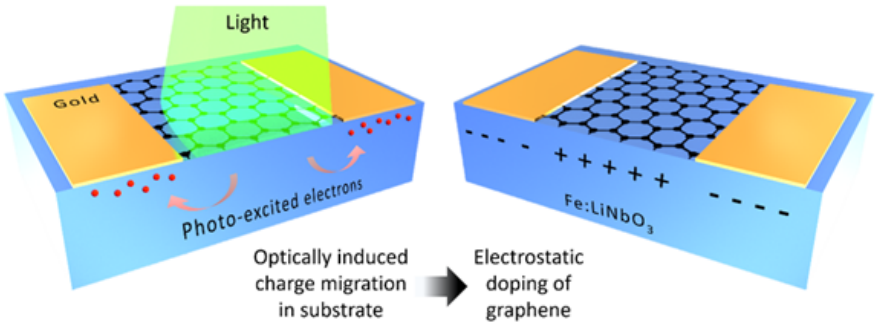

Figure 2.1: *Diagram of optical doping mechanism depicts photoexcited electrons in Fe:$LiNbO_3$ migrating away from the illuminated region to become trapped in dark regions of the crystal resulting in non-uniform charge distribution. In response to the electrostatic fields of the substrate the graphene will experience an injection/ejection of charge carriers from the electric ground.*

2.4 Experimental Methods

To demonstrate the optical gating of graphene requires fabrication of a device which in the simplest case includes a graphene monolayer in contact with a lithium niobate surface to induce a doping effect, and metallic electrodes with which to electrically probe the graphene (depicted in Figure 2.1). Further to this it is customary to pattern the graphene into strips to define a conductive channel of known dimensions, and to pattern an array of electrodes into either a '4 point' or 'transition line method' (TLM) configuration in order to decouple the contact resistance and sheet resistance. By measuring the electrical current across the graphene channel after successive illumination periods I determine the change in graphene resistivity as a function of fluence. Once the graphene shows negligible change in resistivity I conclude that the photorefractive effect has saturated and I reset the device by thermal annealing to restore a uniform charge distribution. I repeat this cycle a total of three times to investigate the repeatability of the mechanism. In fact literature suggests the photorefractive behaviour of Fe:$LiNbO_3$ can be repeated indefinitely [5].

2.4.1 Device Fabrication

Monolayer CVD graphene grown on a copper substrate and transferred to sacrificial polymer substrate is obtained commercially from Graphenea. The supplier of the graphene states the graphene monolayer is inherently p-type with a typical resistivity of 450 Ω/sq and mobility of 3760 cm^2/Vs measured for a graphene monolayer on silica-on-silicon wafer. From these parameters it can be deduced that the nominal charge carrier density of the p-doped graphene is 3.7 $\times 10^{12} cm^{-2}$. The graphene was transferred onto -z cut Fe:$LiNbO_3$ (Fe content 0.1 weight %) in a wet transfer process as shown in Figure 2.2. Metallic electrodes were fabricated via thermal resistance evaporation of a Cr/Au layer (5/100 nm) with a shadow mask to partially obscure sections of the substrate to create an array of electrode pads as shown in Figure 2.3.

The metallic electrodes were patterned with a varying inter-electrode distance as required by TLM to decouple the contact and sheet resistivity. The crystal was a square of 10 mm side length with 1 mm thickness. The shadow mask utilised the full 10 mm square area, patterning an array of 8 electrode pairs with inter-electrode spacing (L) from 100 up to 450 μm. The width of the electrodes (W) was 1 mm. It should be noted that a shadow mask was used for this procedure instead of the traditional photolithography route as the graphene is very sensitive to chemical contamination which can cause chemical doping of the graphene, or even detachment of the graphene and metal from the substrate due to aggressive solvents used in the photoresist development process (see Figure 2.4a and b). The graphene was not patterned into channels; this was attempted however it provided many issues during fabrication such as damage and detachment of the graphene. For future experiments the device was mounted in a printed circuit board with electrical contacts as shown in Figure 2.4(d) to allow electrical probing of the graphene remotely and therefore reduced chances of damage to the graphene, however for the experiments presented in this chapter the mounting technique had not been developed.

Before illumination devices were thermally annealed in a convection oven at 100°C for 24 hours. By heating the substrate electrons which are bound at Fe^{+2} sites are released and become free to migrate within the substrate, thereby reversing the optically induced fields and creating a uniform charge distribution within the Fe:$LiNbO_3$ substrate.

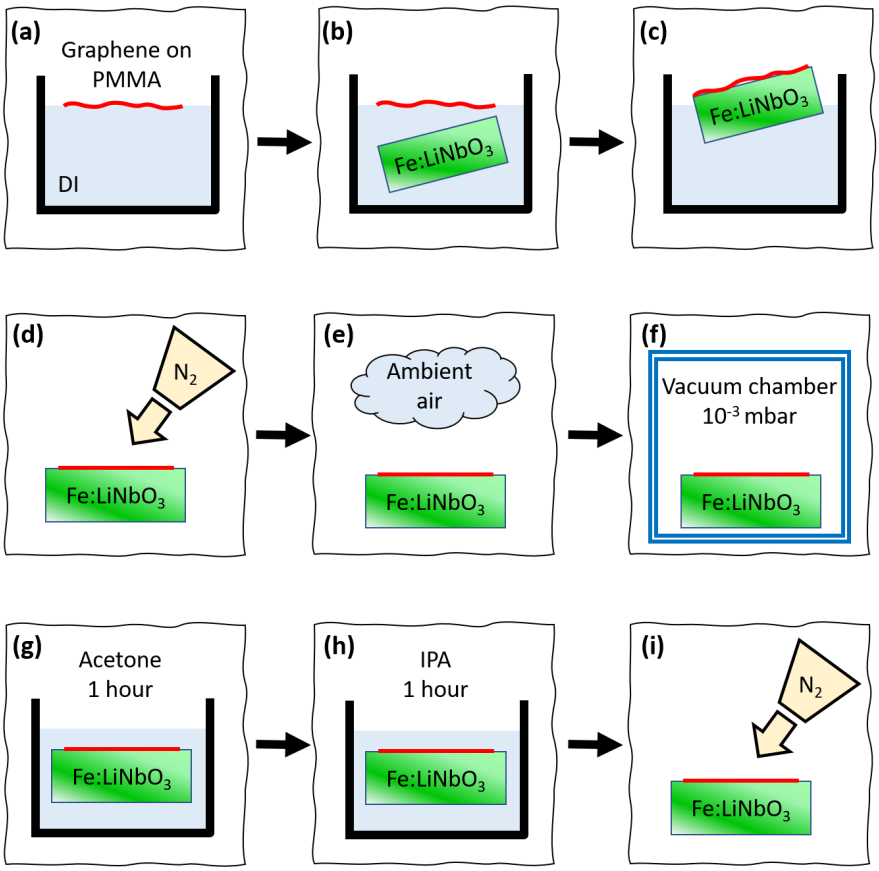

Figure 2.2: *Depiction of the graphene transfer process from sacrificial polymer substrate to lithium niobate.* ***(a)*** *The graphene on PMMA substrate is floated in a beaker of water,* ***(b)*** *the lithium niobate substrate held with tweezers is introduced from beneath,* ***(c)*** *and scooped from underneath to catch the graphene on the substrate surface.* ***(d)*** *Excess water is removed via the dry nitrogen gun,* ***(e)*** *then the substrate is left to dry completely in ambient air for 2 hours.* ***(f)*** *To promote adhesion the device is then held in a vacuum chamber for 24 hours.* ***(g)*** *To remove the protective polymer coating the graphene is soaked in acetone for 1 hour,* ***(h)*** *then IPA for 1 hour,* ***(i)*** *and finally dried in nitrogen.*

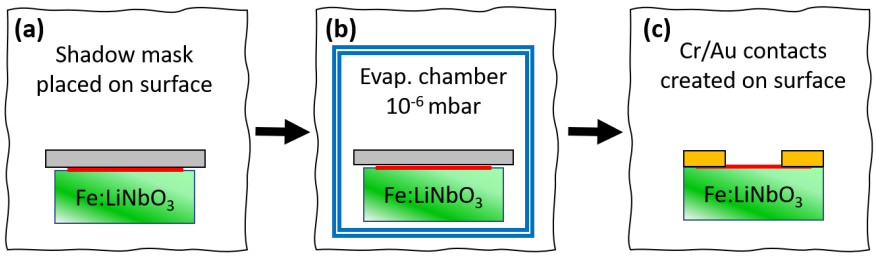

Figure 2.3: *Process flow chart for the creation of metallic contacts.* ***(a)*** *The metallic shadow mask is placed onto graphene on lithium niobate substrate.* ***(b)*** *The assembly is placed into the vacuum chamber of the evaporation chamber and pumped down to 10^{-6} mbar.* ***(c)*** *Evaporated chromium and gold are deposited onto the substrate surface in the pattern defined by the shadow mask, creating an array of contacts.*

2.4.2 Raman characterisation

Raman spectroscopy reveals many insights into the chemical and structural properties of graphene sheets. Figure 2.5(a) reproduced from Ferrari et al. [6] shows the Raman spectrum for pristine and defected monolayer graphene. For the pristine monolayer there were two main peaks observed, the G peak around 1600 cm^{-1} and the 2D peaks around 2700 cm^{-1}, where the 2D peak is roughly twice the height of the G peak. The 2D peak is an overtone of the D peak, where the D peak is activated by defects however the 2D peak is activated by phonons and therefore does not signify the presence of defects. The G peak corresponds to an in-plane vibrational mode in the graphene. For the defected graphene there are many extra peaks which are caused by the defects. In Figure 2.5(b) reproduced from [6] the 2D peak is shown for various number of graphene layers. It can be seen here that as the number of layers increases the 2D peak becomes a convolution of multiple components and forms a more complex shape. Therefore from the shape of the 2D peak one can infer the number of graphene layers.

Raman spectroscopy was performed by Adam Lewis to characterise the graphene layer after transfer onto the lithium niobate substrates, using a 632 nm laser source to probe the graphene with a 50x objective lens. The Raman spectrum is shown in Figure 2.5(c) where the ratio of heights of the 2D:G peak and the shape of the 2D peak is a characteristic sign of

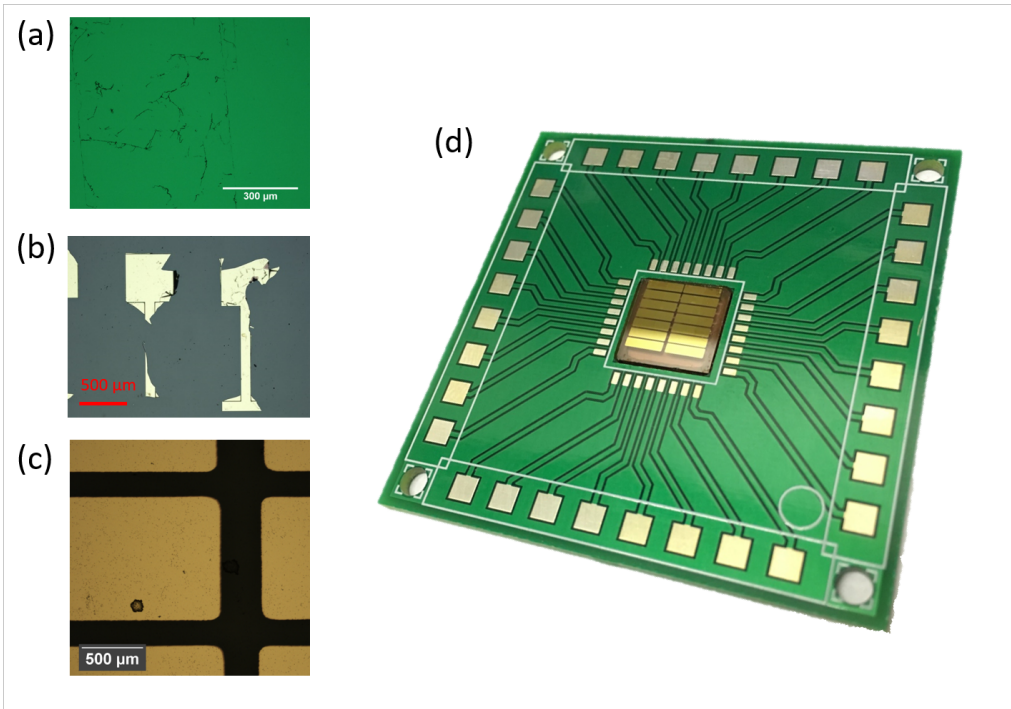

Figure 2.4: ***(a)*** *Graphene surface after photoresist development reveals detachment from surface.* ***(b)*** *Patterning of metallic contacts after lift-off procedure show poor adhesion of metal to graphene surface.* ***(c)*** *Contacts defined by shadow mask reveal no damage and good adhesion.* ***(d)*** *Photograph of device (graphene on Fe:$LiNbO_3$ patterned with contacts via shadow mask method) mounted into printed circuit board.*

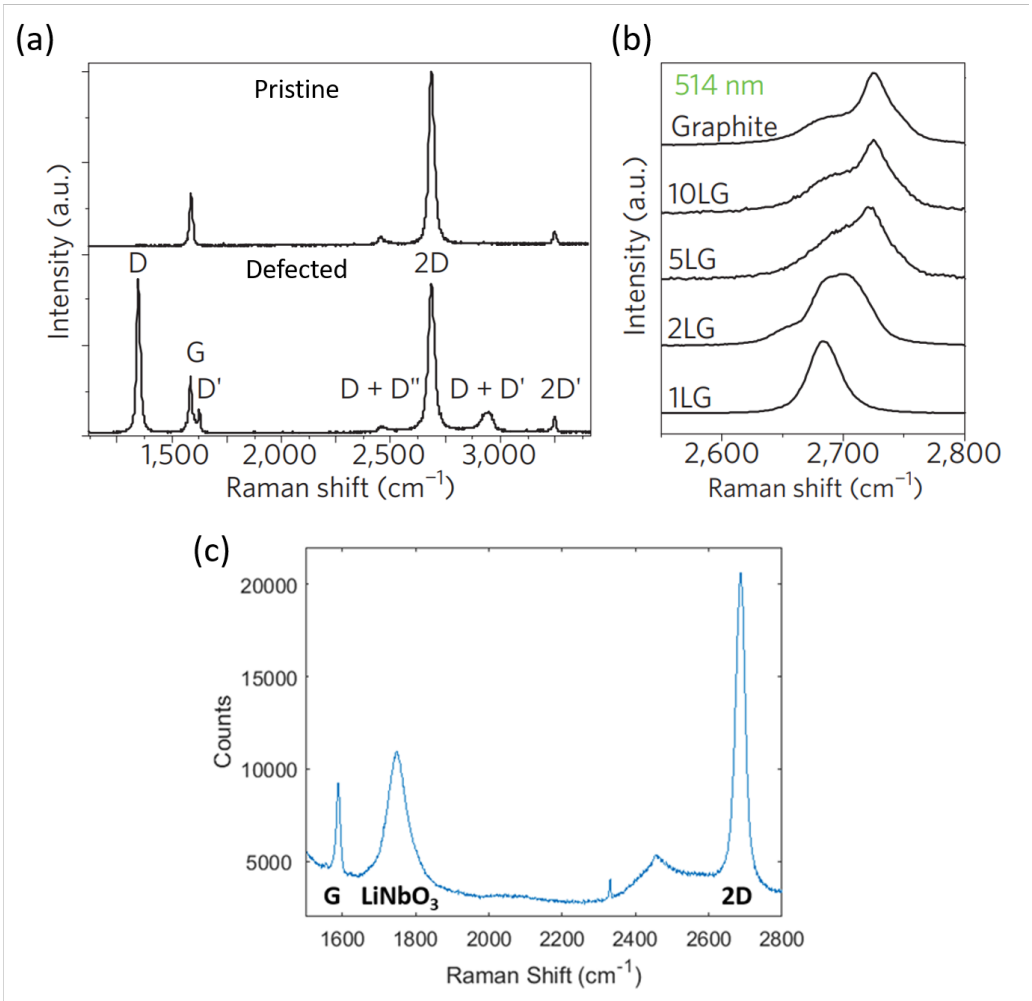

Figure 2.5: ***(a)*** *Raman spectrum of pristine and defected graphene showing presence of defect activated D peak and overtones [6].* ***(b)*** *Comparison of 2D peak for varying number of graphene layers, where for multiple layers the 2D peak becomes a convolution of multiple components [6].* ***(c)*** *Raman spectrum of graphene purchased from Graphenea and transferred onto lithium niobate, suggesting low-defect monolayer graphene.*

monolayer graphene [6]. The broad peak centred around 1750 cm^{-1} is due to photoluminescence of the Fe:$LiNbO_3$ substrate in response to illumination by the Raman spectrometer laser. Further it can be inferred from this spectrum that the graphene purchased from Graphenea was relatively free of defects.

2.4.3 Electrical characterisation

An Agilent 4155c electrical parameter analyser is used in a two probe configuration to pass a voltage (sweeping from -0.1V to +0.1V in 200 steps) while measuring the current passing through the circuit. The transition line method (TLM) [7, 8, 9] is used to determine sheet resistivity; the method requires an array of electrodes with varying inter-electrode spacing (each assumed to have identical contact resistance R_c). By measuring resistance across a pair of electrodes (as shown in Figure 2.6a) the total resistance in the circuit is the sum of two contact resistances and a graphene resistance equal to the sheet resistivity ρ multiplied by electrode gap length L divided by electrode width W.

$$R = 2R_c + \rho L/W$$

By plotting the total resistance R against electrode gap length L the sheet and contact resistances can be decoupled, where contact resistance is half the value of the Y axis intercept and sheet resistivity is the gradient multiplied by channel width W. A linear regression analysis is used to calculate the line of best fit; the standard error of the gradient multiplied by W is used as an estimate of the error in the sheet resistivity. All measurements are performed in a cleanroom environment to ensure stable control over temperature and humidity conditions.

2.4.4 Optical Illumination

To induce a photoresponsive effect in the Fe:$LiNbO_3$ substrate an illumination from the top surface of the device is provided by a broadband white light source, delivering a power of 1 mW/cm^2 as measured at the surface of the sample, in the wavelength range 400 - 800 nm. In Figure 2.7 I present the emission spectra of the lamp measured with an OceanOptics spectrometer (OceanOptics USB4000-VIS-NIR) overlaid with an absorption spectra of Fe:$LiNbO_3$ reproduced from [10]. It can be seen that the lamp emits a broad

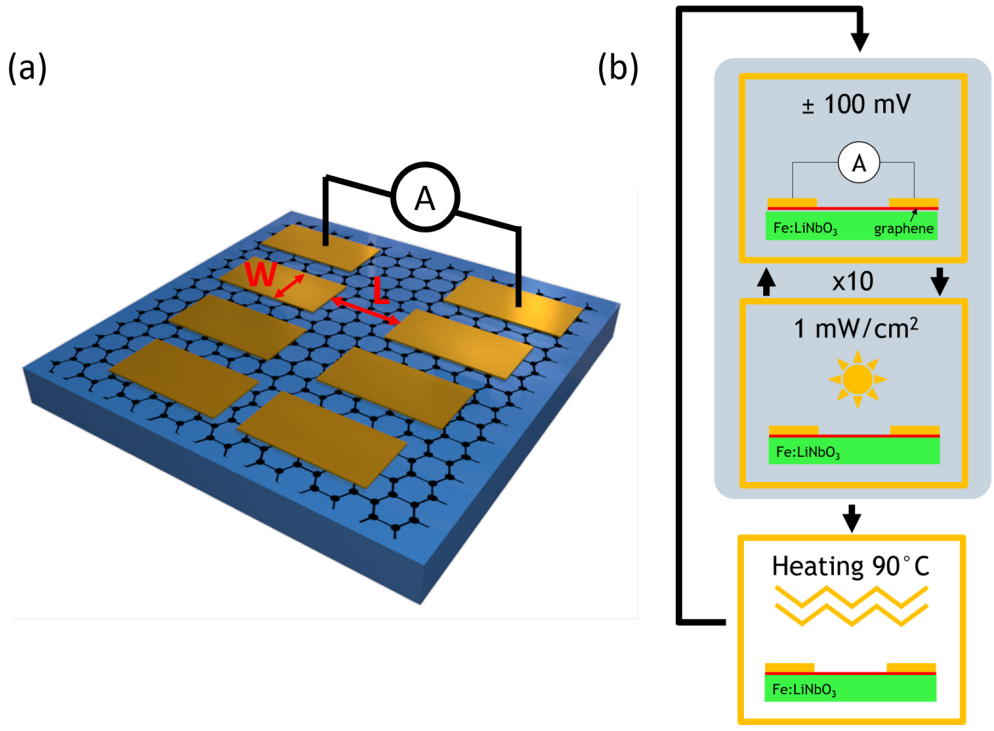

Figure 2.6: ***(a)*** *Transition line method where metallic contacts with width W are placed at increasing separation distances L for electrical current measurements of graphene* ***(b)*** *Experimental procedure where graphene current is measured in the dark with applied voltages of $\pm$ 0.1 V to determine resistivity. After measurement the graphene is illuminated for a 30 minute period at 1 mW/cm^2. This process of measurement and then illumination is repeated a total of 10 times at which point the optical effect has saturated and the device is thermally annealed to return the substrate to a uniform charge distribution.*

range of visible frequencies centred around 600 nm while the Fe:$LiNbO_3$ crystal is mainly sensitive to wavelengths below 450 nm, so although a large portion of the deposited energy will be ineffective ($\lambda > 600$ nm) there is still a significant portion of the emitted light which will induce a photorefractive effect.

The device is illuminated for 30 minute periods, then with the illumination source switched off the electrical characteristics are measured in the dark. This cycle of illumination followed by measurement is repeated until there is negligible change measured in graphene electrical properties at which point the photorefractive effect is assumed to have reached saturation, and there should be no further electron migration in response to continued illumination. This procedure is depicted in Figure 2.6(b).

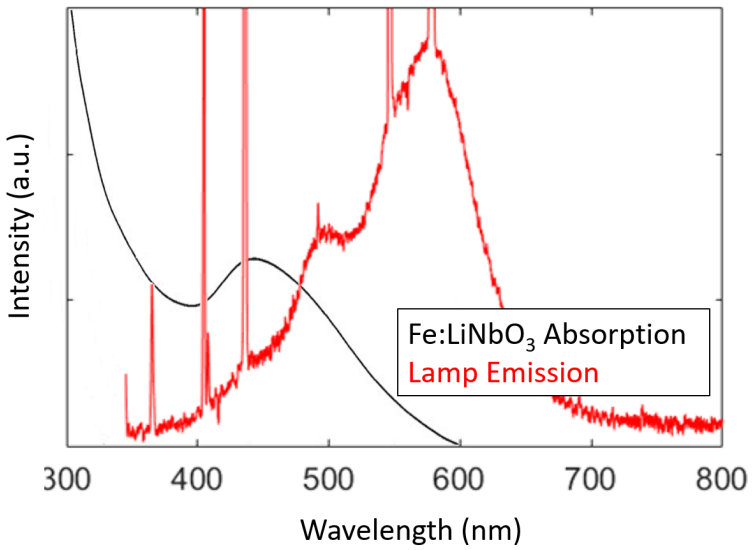

Figure 2.7: *Optical absorption of Fe:$LiNbO_3$ substrate reproduced from [10] overlaid with emission spectra of lamp used for illumination of graphene on Fe:$LiNbO_3$ devices.*

2.5 Results and Discussion

To illustrate the optical gating of graphene on Fe:$LiNbO_3$ the device was illuminated and then measured intermittently, consisting of 30 minute illumination periods followed by electrical measurement in the dark. After 10 periods of illumination and measurement the device is thermally annealed and the whole cycle is repeated 3 times; this procedure is shown graphically in Figure 2.6(b). By illuminating the device from the top surface the opaque metallic electrodes act as an illumination mask which can create a non-uniform illumination pattern in the substrate and therefore drive the photorefractive electron migration effect. The device is not illuminated while voltage is applied to exclude any effects from voltage induced drift of the electrons within the substrate.

2.5.1 Resistance Measurements

The measured resistance is plotted against the inter-electrode spacing L and a straight line is fitted to the data, as shown in Figure 2.8(a) for three values of electrode spacing. It can be seen that the current and voltage have a linear relationship which suggests an Ohmic contact between the graphene and metal stack. Further it can be seen that as the electrode spacing L decreases the current increases. The resistance of the circuit is given by the inverse of the gradient of the current-voltage line.

In Figure 2.8(b) the resistance is plotted against electrode spacing for various illumination conditions. It is possible to decouple the contact and sheet resistances from each other by using a least squares method to fit a straight line to the data points, where the sheet resistance is given by the gradient of the fitted lines multiplied by the width of the electrodes W. The uncertainty in the contact resistance and sheet resistance is provided by the uncertainty in the intercept divided by two and the uncertainty of the gradient multiplied by W, as provided by the least squares method. The graph shows that with each successive illumination period the gradient of the line is increased, which suggests an increase of graphene resistivity, while the vertical axis intercept is close to the zero point for each fitted line suggesting the contact resistance is relatively small and unchanged by illumination.

Graphene resistivity is presented in Figure 2.8(c) plotted against fluence delivered to the device. It can be seen from the figure the resistivity starts

around 200 Ω/sq and increases with each illumination period, finally reaching a value of ∼600 Ω/sq. The initial change in resistivity is rapid however the rate of change decreases as fluence increases. After a total fluence dose of 18 J/cm^2 the changes in resistivity are negligible and the photorefractive behaviour is assumed to have saturated.

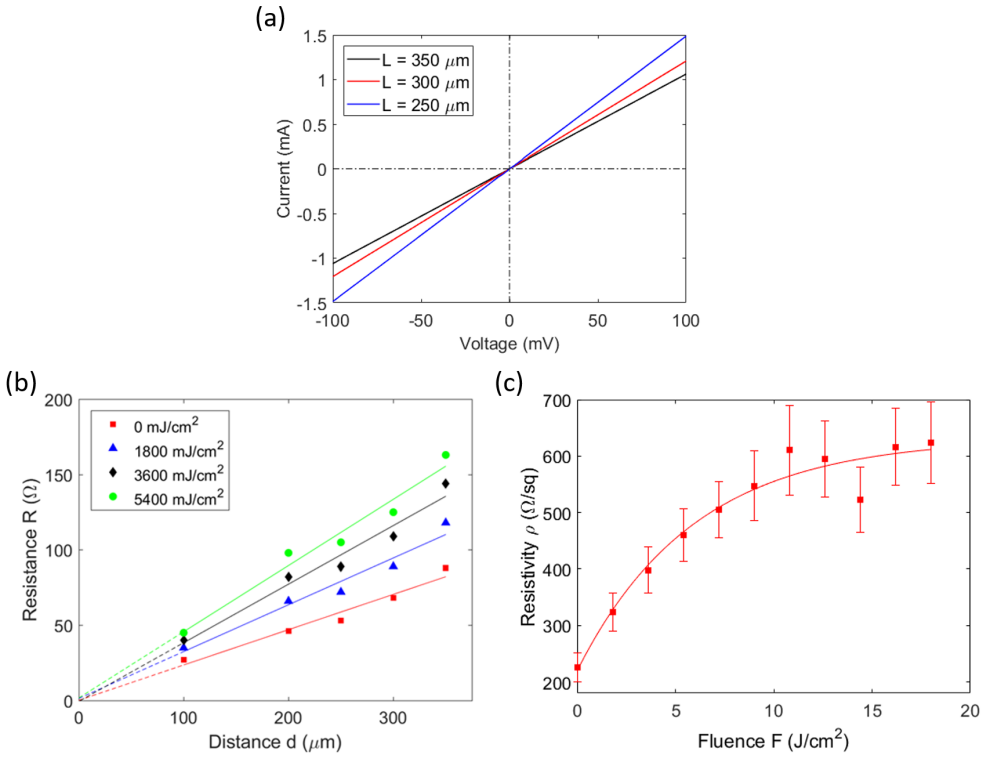

Figure 2.8: ***(a)*** *Current against voltage plots taken for three electrode distances L, where the resistance can be deduced from the gradient of the line.* ***(b)*** *Resistance plotted against electrode distance for four fluence doses. It can be seen that after each illumination the gradient of the fitted line increases suggesting an increase in resistivity.* ***(c)*** *Resistivity plotted against fluence for 10 illumination and measurement cycles showing optically induced increase in resistivity.*

2.5.2 Resistivity Cycles

Once the device has been illuminated to saturation (a dose of 18 J/cm^2) the device is reset by thermal annealing for 24 hours at 100 °C to redistribute the charge carriers within the substrate. After the thermal annealing the experiment is repeated by illuminating and measuring the device. A total of 3 complete cycles are shown in Figure 2.9(a). The first cycle (consisting of 10 illumination and measurement stages) is shown in red. After this first cycle the device is thermally annealed to reset the charge distribution and remeasured as shown in blue. It can be seen that after thermal annealing the device returns to similar resistivity as the pre-illuminated values, and upon further illumination the repeat cycles show a similar behaviour to each other. For the third cycle there can be seen more fluctuation in the data and perhaps some level of degradation due to damage of the gold contacts and the graphene monolayer due to electrically contacting the device with needle probes for every electrical measurement. Average resistivity of the three illumination cycles is taken at each fluence dose and the errors propagated forward as shown by the error bars in Figure 2.9(b). The resistivity ρ follows an inverse exponential increase as a function of illumination fluence F which can be fitted by $\rho = a(1 - exp^{(-F/F_0)}) + c$, where $a = 373\ \Omega/sq$, $F_0 = 6.32$ J/cm^2, and $c = 231\ \Omega/sq$. This dependence suggests that the effect saturates to a resistivity value of 604 Ω/sq reaching e^{-1} of saturation value at a fluence of 6.32 J/cm^2 ($\sim$ 2.6 fold increase from initial pre-illumination values). The secondary vertical axis, to the right, in the plot of Figure 2.9(b) provides the corresponding values for charge carrier density calculated from the measured resistivity values, electron charge, and using a mobility value of 3760 cm^2/Vs as characterised by the supplier of the graphene. Carrier Number n is calculated from $n = 1/e\mu\rho$. The graph indicates that the carrier density decreases by a factor of $\sim$3 (corresponding to a modulation of carrier density $\sim 5.5 \times 10^{12}$ cm^{-2}) with increasing illumination.

2.5.3 Contact Resistance

Contact resistance is measured by the TLM results shown in Figure 2.8(b) in which the contact resistance is given by half the y axis intercept of the fitted line (using a least squares method) which also provides an estimate of the uncertainty of the intercept value. Contact resistance is plotted against fluence dose in Figure 2.10 which show no discernible relationship to each other.

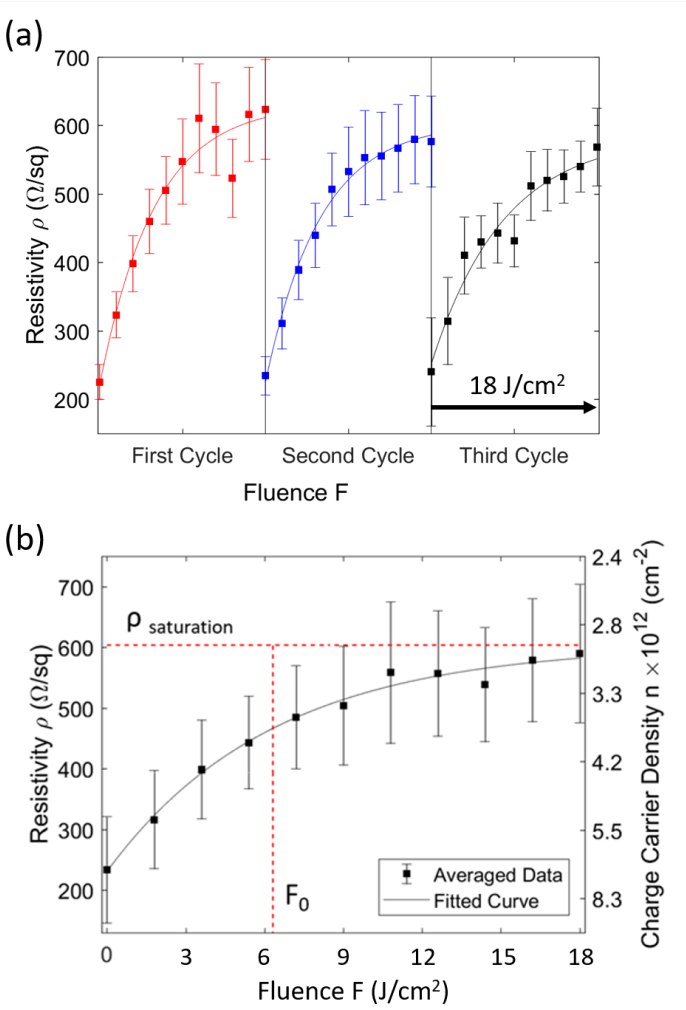

Figure 2.9: *(a) Resistivity measured against illumination for a total received dose of 18 J/cm^2. After this cycle the device is thermally annealed to return the substrate towards a uniform charge distribution. A total of 3 cycles of illumination and annealing are presented. (b) Resistivity measurements for all three cycles are averaged and fitted with an inverse exponential equation to estimate the saturation value and time scale of the effect.*

The mean value of contact resistance is calculated to be 1.7 Ω. From this result I can conclude that the resistance measured along the graphene/contact circuit is largely attributed to the graphene (typical circuit resistance around 100 Ω) and that any change in this value which shows a relationship with illumination can be attributed to changes in the graphene electrical properties and not due to changes in the contact resistance.

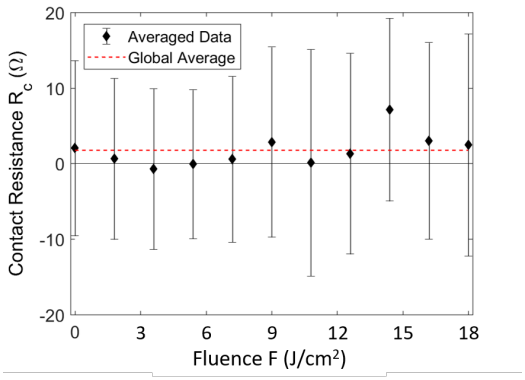

Figure 2.10: *Contact resistance extracted from TLM measurements plotted against fluence averaged over 3 illumination/anneal cycles. It can be seen there is negligible change except due to noise and that these variation are all within the uncertainty of the measurement as shown by the error bars.*

2.5.4 Thermal Annealing

The thermal annealing of the device is investigated to determine the timescales involved in the annealing process to reverse the photorefractive doping mechanism. The device is mounted onto a printed circuit board (PCB) which allows for permanent electrical contact to one electrode pair. A thermocouple is mounted onto the PCB close to the device to record temperature. The device is placed into the oven which starts at room temperature, and then quickly heated to 100 °C. The electrical conductivity of the graphene channel and the temperature of the thermocouple are continually measured for the duration of the annealing cycle.

Figure 2.11(a) presents the graphene channel resistance as a function of time during the annealing cycle. It can be seen that the resistance starts around 200 Ω and over the duration of the anneal cycle it tends towards a

final resistance of 340 Ω, reaching this final value after around 12 hours of annealing, after which there is negligible change in resistance.

It can also be seen that at the start of the cycle there is a dramatic resistance spike once the oven is switched on. This behaviour may be explained by Figure 2.11(b) which shows the resistance during the first hour, overlaid with the oven temperature, and the rate of change of the oven temperature (both plotted in arbitrarily scaled units for ease of comparison). The oven temperature data sets are also shifted by 6 minutes delay to aid comparison, which can be accounted for by the slow thermal response of the lithium niobate which will lag behind that of the thermocouple. It can be seen that the peak in graphene resistance mimics the rate of change of temperature in the oven which suggests a transient temperature driven effect such as the pyroelectric response in lithium niobate is the reason for the resistance spike [11] in which electrostatic fields on the surface of the lithium niobate build up in response to temperature changes, and slowly fade away once the temperature has stabilised.

It is important to note here that the annealing behaviour appears in opposite magnitude to the results presented in Figure 2.9(a) in which it can be seen that illumination increases the resistance and thermal annealing returns the resistance is its pre-illuminated values, however in Figure 2.11(a) I show that annealing also has the effect of increasing the resistance. This apparent contradiction may be explained by the fact that the measurements were performed at high temperature so it is natural to assume resistance has increased as compared to room temperature (according to a positive thermal coefficient of resistance as has been observed [12]), and that once returned to ambient conditions the graphene resistivity would again decrease.

2.5.5 Control Measurement

To determine that the optically induced resistance change observed here is indeed due to the lithium niobate substrate a control measurement is performed in which a device consisting of graphene on silicon substrate with insulating silica layer and identical electrode geometry is optically illuminated. Figure 2.12 presents results from this experiment in which it can be seen that while indeed there is some variation in the graphene resistivity on silicon this effect is far smaller than the changes observed on lithium niobate. The mechanism responsible to the change in graphene resistivity on silica may be from either thermally induced heating by the illumination lamp or from a charge mi-

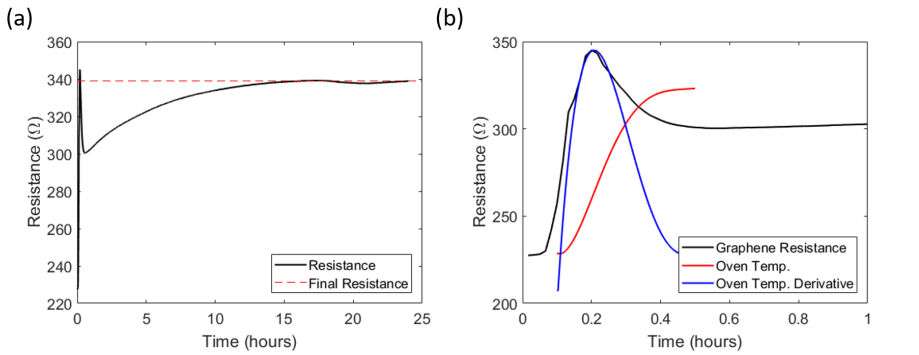

Figure 2.11: *(a) Graphene resistance plotted against time while heated in oven at 100 °C for 24 hours. (b) Graphene resistance during the first hour of annealing overlaid with oven temperature and rate of change of oven temperature in arbitrary units. The oven temperature and rate of change of temperature measurements are shifted forward by 6 minutes to aid comparison.*

gration effect within the substrate. Indeed it has been reported that optical illumination of graphene on silica and other substrates can result in charge migration from interface trap sites and defects which result in electrostatic doping of the graphene [13, 14, 15]. The measurements presented here reveal that the photoinduced changes to graphene on Fe:$LiNbO_3$ are ten times greater than can are achieved on a silica on silicon substrate.

2.5.6 Error Analysis

There are a range of elements to discuss in this chapter which can contribute to errors in the measured change in electrical properties. To determine resistivity the TLM method is used in which an array of graphene channels with varying length are measured and the graphene resistivity can be decoupled from the contact resistance.

Current Measurements: The channel resistance is measured by applying a 0.1 V bias between two contacts with an Agilent 4155c parameter analyser. Channel resistances were typically 100 Ω or smaller, which would impose a lower current limit of 0.2 μA, which is well within the measurement range of the equipment which is rated to measure down to the pA scale.

Illumination Intensity: The device is illuminated with a broadband

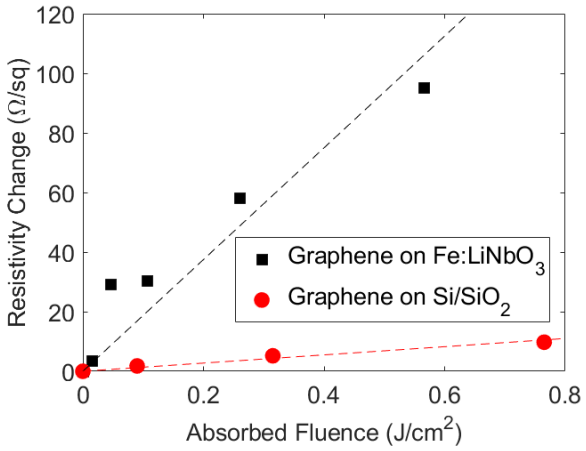

Figure 2.12: *Control test in which graphene on Fe:$LiNbO_3$ and graphene on Si/SiO_2 are both illuminated and change in resistivity is measured, and plotted against the absorbed fluence of the device. Linear fits are added to both data sets, where the gradient for the lithium niobate device is around ten times greater than that of the control device.*

white light source which is measured to emit a power of 1 mW/cm^2 at a distance equal to that of the substrate surface. A wavelength spectrum of the lamp (Figure 2.7) reveals a wide range of frequencies emitted however the photorefractive effect is mostly responsive to wavelengths at and below 450 nm (blues and greens [16]) so a large part of the energy released by the lamp is ignored by the lithium niobate. Therefore the actual energy deposited into the crystal will be somewhat lower than the quoted values.

Graphene and Contact Uniformity: The TLM method relies on the assumption that the graphene is uniform over the entirety of its surface, and that all the contacts have identical resistance. Both these questions are generally quite difficult to answer individually and it has been shown that large area CVD graphene can indeed have non-negligible variations in electrical properties over the surface [17]. If both these assumptions were correct then when one plots the channel resistance against channel length there should be a linear relationship. Indeed when these are plotted for example in Figure 2.8(a) it can be seen that generally there is a high degree of linearity to the data, with some small variation. To quantify the variation here a least squares method is used to fit a straight line to the data, where the

uncertainty in the slope of the fitted line is used to determine the uncertainty of the resistivity value. These uncertainties are carried forward into the resistivity plots in Figure 2.8(a) and Figure 2.9 where it can be seen that the measured change in resistivity is far larger than the uncertainty. The average uncertainty in sheet resistance is 106 Ω/sq, where the uncertainty value at each fluence dose and at each repeat cycle is added and divided by the total number of data points which is 30 (10 fluence doses with 3 repeats), while the measured change in sheet resistivity is $\sim$ 400 Ω/sq.

2.6 Discussion of Photorefractive Mechanism

The experiments in this chapter have shown there is a clear relationship between illumination of the device and the resistivity of the graphene, in an effect which is non-volatile yet reversible and repeatable. This effect is attributed to the photorefractive charge migration in the lithium niobate which creates electric fields capable of inducing an electrostatic doping effect within the graphene and alter the graphene charge carrier numbers.

Figure 2.13 depicts the influence of charge distributions in the lithium niobate surface on the monolayer graphene. The figure presents an electrically grounded graphene layer on the top surface of a lithium niobate substrate which initially has a uniform charge distribution in the substrate. Upon illumination if the central top surface of the substrate electrons migrate away from the illuminated region and become trapped in dark regions, leaving behind a positive charge distribution below the graphene sheet. In response to this positively charged domain in the substrate the graphene will experience an injection of electrons from the electric ground to compensate for the electrostatic field of the lithium niobate. Graphically, this increase in the number of electrons in graphene can be depicted on the Dirac cone diagram which plots Fermi level on the y axis with density of states (D.O.S) on the x axis, which corresponds to the available number of charge carriers in the material. As the graphene is assumed to be inherently p-doped (which means holes are the dominant charge transport mechanism) an increase in electron number means the number of charge carriers is reduced, which correlates to a reduction in electrical conductivity of the graphene sheet.

From these experiments it is unclear what is the main driving force behind the electron migration within the substrate (drift or diffusion). It is possible the effect is caused by diffusion (Figure 2.14a) in which electrons migrate

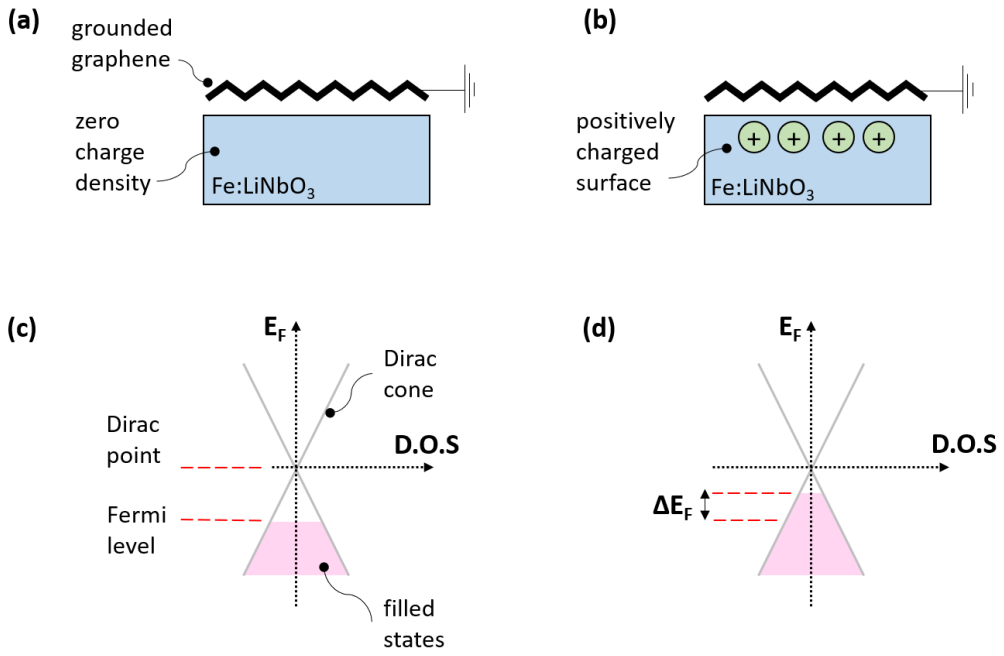

Figure 2.13: ***(a)*** *Depiction of the initial state of the device consisting of a lithium niobate substrate with an electrically grounded graphene layer on the top surface. The lithium niobate initially has zero charge density.* ***(b)*** *As electrons move away from the top surface of the lithium niobate in response to optical illumination the top surface has a net positive electric charge. In response to the positive electrostatic field created by the substrate the graphene will experience an injection of electrons from the electric ground.* ***(c)*** *The initial Dirac cone of the graphene layer is depicted for P-doped graphene.* ***(d)*** *The final Dirac cone of the graphene shows that as the electron number increases the D.O.S (density of states) is reduced, thereby increasing the electrical resistivity.*

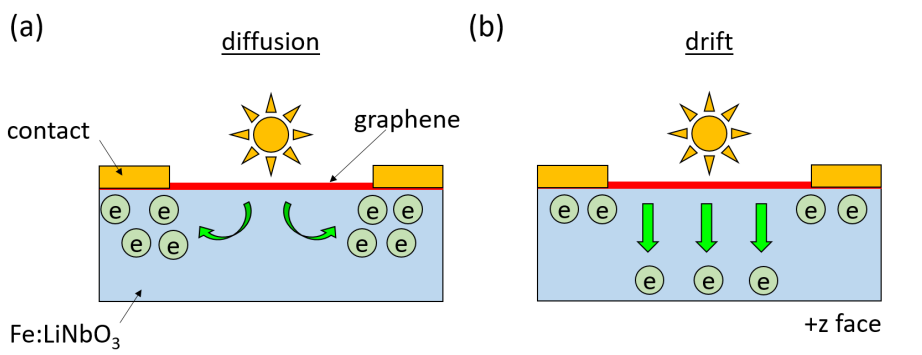

Figure 2.14: ***(a)*** *Diffusion mechanism in which electrons diffuse away from regions of high illumination intensity.* ***(b)*** *Drift mechanism in which electrons migrate towards +z polar face of lithium niobate due to the internal ferroelectric dipole.*

towards dark regions; in this case the electrons would migrate away from the channel towards the dark regions underneath electrodes, which should create a net positive field under the graphene channel. Another candidate is the drift mechanism (Figure 2.14b) in which electrons are excited preferentially along the +z axis. As the graphene is on the -z face this would also result in a net positive charge under the graphene channel. Assuming the graphene is initially p doped (excess holes) then creating a positive electric field in the substrate would attract excess electrons to the graphene from electric ground which would have a net effect of reducing charge carrier numbers and increase resistivity as is seen in the experiments here. Both mechanisms (diffusion and drift) therefore fit with this theory so it is unclear from this chapter which mechanism is dominant. In Chapter 3 I investigate this further by creating devices on both +z and -z faces of lithium niobate which suggests the drift mechanism is dominant.

2.7 Conclusions

In this chapter I have investigated the use of photorefractive iron doped lithium niobate as a platform for the optical doping of 2D materials. Graphene on Fe:$LiNbO_3$ was illuminated via a broadband white light source achieving a maximum increase in resistivity of $\sim$370 Ω/sq ($\sim$ 2.6 fold increase) which cor-

responds to charge carrier density modulation on the order of $5.5 \times 10^{12}/cm^2$ in the graphene sheet. The effect is shown to be reversed under thermal annealing of the device however the doping effect can be repeated by subsequent illumination cycles. By performing a control test in which a device consisting of graphene on Si/SiO_2 it is shown that the doping effect on lithium niobate is ten times greater than measured on the control device.

The experiments performed here utilise a broadband white light source with low power, and as such the illumination times are rather long (hours) however it it expected that the speed of this effect will scale with illumination power. Also, here a thermal anneal is used to reverse the optically induced charge distributions however literature suggests that this effect can be optically reversed by uniform illumination. Further, by replacing the graphene with other 2D materials which exhibit an electronic band-gap it is expected that such a doping effect could effectively switch a material from insulating to metallic and thereby realise high on/off ratio optically actuated transistors and electrical interconnects.

Bibliography

[1] Wallace, P. R. The Band Theory Of Graphite. *Physical Review* **1947**, *71*, 622–634.

[2] Castro Neto, A. H.; Guinea, F.; Peres, N. M. R.; Novoselov, K. S.; Geim, A. K. The Electronic Properties Of Graphene. *Reviews Of Modern Physics* **2009**, *81*, 109–162.

[3] Gunter, P., Huignard, J.-P., Eds. *Photorefractive Materials And Their Applications 2*; Springer New York, 2007.

[4] Arizmendi, L.; Lopez-Barbera, F. J. Lifetime Of Thermally Fixed Holograms In $LiNbO_3$ Crystals Doped With Mg And Fe. *Applied Physics B-Lasers And Optics* **2007**, *86*, 105–109.

[5] Buse, K.; Adibi, A.; Psaltis, D. Non-Volatile Holographic Storage In Doubly Doped Lithium Niobate Crystals. *Nature* **1998**, *393*, 665–668.

[6] Ferrari, A. C.; Basko, D. M. Raman Spectroscopy As A Versatile Tool For Studying The Properties Of Graphene. *Nature Nanotechnology* **2013**, *8*, 235–246.

[7] Xia, F.; Perebeinos, V.; Lin, Y.-M.; Wu, Y.; Avouris, P. The Origins And Limits Of Metal-Graphene Junction Resistance. *Nature Nanotechnology* **2011**, *6*, 179–184.

[8] Venugopal, A.; Colombo, L.; Vogel, E. M. Contact Resistance In Few And Multilayer Graphene Devices. *Applied Physics Letters* **2010**, *96*, 013512.

[9] Smith, J. T.; Franklin, A. D.; Farmer, D. B.; Dimitrakopoulos, C. D. Reducing Contact Resistance In Graphene Devices Through Contact Area Patterning. *Acs Nano* **2013**, *7*, 3661–3667.

[10] Ciampolillo, M. V.; Zaltron, A.; Bazzan, M.; Argiolas, N.; Sada, C. Quantification Of Iron (Fe) In Lithium Niobate By Optical Absorption. *Applied Spectroscopy* **2011**, *65*, 216–220.

[11] Gopalan, K. K.; Janner, D.; Nanot, S.; Parret, R.; Lundeberg, M. B.; Koppens, F. H. L.; Pruneri, V. Mid-Infrared Pyroresistive Graphene Detector On $LiNbO_3$. *Advanced Optical Materials* **2016**, *5*, 1600723.

[12] Davaji, B.; Cho, H. D.; Malakoutian, M.; Lee, J.-K.; Panin, G.; Kang, T. W.; Lee, C. H. A Patterned Single Layer Graphene Resistance Temperature Sensor. *Scientific Reports* **2017**, *7*, 8811.

[13] Wang, X.-J.; Zou, L.; Li, D.; Zhang, Q.; Wang, F.; Zhang, Z. Photo-Induced Doping In Graphene/Silicon Heterostructures. *Journal Of Physical Chemistry C* **2015**, *119*, 1061–1066.

[14] Ho, P.-H.; Chen, C.-H.; Shih, F.-Y.; Chang, Y.-R.; Li, S.-S.; Wang, W.-H.; Shih, M.-C.; Chen, W.-T.; Chiu, Y.-P.; Li, M.-K.; Shih, Y.-S.; Chen, C.-W. Precisely Controlled Ultrastrong Photoinduced Doping At Graphene-Heterostructures Assisted By Trap-State-Mediated Charge Transfer. *Advanced Materials* **2015**, *27*, 7809–7815.

[15] Jun, L.; Velasco, J., Jr.; Huang, E.; Kahn, S.; Nosiglia, C.; Tsai, H.-Z.; Yang, W.; Taniguchi, T.; Watanabe, K.; Zhang, Y.; Zhang, G.; Crommie, M.; Zettl, A.; Wang, F. Photoinduced Doping In Heterostructures Of Graphene And Boron Nitride. *Nature Nanotechnology* **2014**, *9*, 348–352.

[16] Furukawa, Y.; Kitamura, K.; Ji, Y.; Montemezzani, G.; Zgonik, M.; Medrano, C.; Gunter, P. Photorefractive Properties Of Iron-Doped Stoichiometric Lithium Niobate. *Optics Letters* **1997**, *22*, 501.

[17] Boggild, P.; Mackenzie, D. M. A.; Whelan, P. R.; Petersen, D. H.; Buron, J. D.; Zurutuza, A.; Gallop, J.; Hao, L.; Jepsen, P. U. Mapping The Electrical Properties Of Large-Area Graphene. *2d Materials* **2017**, *4*, 042003.

Chapter 3

Optical Tuning of Graphene-Metal Metasurface

3.1 Introduction

Terahertz frequencies show potential for technological applications in a wide range of areas such as spectroscopy of biological samples [1, 2, 3, 4], detection of concealed drugs and explosives [5, 6, 7], imaging of astronomical objects [8, 9], industrial quality control of semiconductor manufacturing [10, 11], and broad bandwidth telecommunications systems [12, 13]. Despite this wide array of applications there is currently a lack of optoelectronic devices for the tuning of phase, amplitude, and polarisation of terahertz radiation. A variety of techniques based on optical [14, 15, 16], thermal [17, 18], electronic [19, 20, 21], and mechanical [22, 23] actuation have been developed for the modulation of Terahertz radiation. Optical actuation methods generally offer an advantage over other approaches in that they readily allow for individual regions of the modulation device to be addressed locally, although such mechanisms are typically volatile and therefore require constant illumination of the active devices. To this end it is advantageous to investigate routes towards non-volatile optical control of THz tuning devices.

Here I present photorefractive iron doped lithium niobate (Fe:$LiNbO_3$) as a platform for optically controlled non-volatile tuning of terahertz plasmonic devices. By combining a metallic metasurface with a graphene layer and photorefractive substrate I demonstrate that tuning of the terahertz transmission through the device can be controlled by optical illumination. The effect is non-volatile in the dark however it can be reversed by thermal annealing and repeated by further illumination. Owing to the properties of the photorefractive substrate it should be possible to locally address individual regions of the device optically, and also to allow for optical reversal of the effect via uniform illumination, thereby creating an all-optical non-volatile spatially resolved terahertz transmission tuning device.

3.2 Modulation of Terahertz Radiation

Optical: Early demonstrations of optical modulation relied on optically excited charge carriers in bulk semiconductors [14, 15, 16, 24]. Under illumination with a pump laser, electrons are excited from the valence to the conduction band and consequently act as a free-carrier plasma interacting strongly with THz radiation. Optical modulation by this method has been demonstrated in silicon [14, 15, 16] and GaAs [16] where the resul-

tant amplitude modulation is a broad band effect which decays on the order of the charge recombination time of the semiconductor material (τ_{Si} ∼100 ns, τ_{GaAs} ∼1 ns). The effect has also been employed in combination with structured illumination for wavefront shaping [24] (Figure 3.1a) and tunable plasmonic gratings [25]. Semiconductors have been combined with 2D materials to enhance the photo-absorption effects, where photoexcited carriers within the semiconductor diffuse into the 2D material where they experience a significantly higher mobility and therefore interact more strongly to absorb the terahertz radiation [26, 27]. **Plasmonic:** Metamaterials fabricated on semi-insulating GaAs [28, 29], silicon [30, 31, 32, 33, 34] (Figure 3.1b), and ErAs/GaAs [35], have been demonstrated where tuning of the substrate dielectric properties affects the plasmonic resonance of the metamaterial array. Further, the combination of 2D materials with metamaterials allows one to tune metamaterial resonance through optical doping of the 2D material [36, 37] (Figure 3.1c). Phase change materials have also been demonstrated as a platform for optically tunable plasmonic devices by tuning the dielectric properties of the material, where the crystalline to amorphous transition can be optically driven by a short intense pulse to raise the temperature above the melt temperature, or reversed by a lower intensity long duration pulse to reverse the phase change, however costly pulsed laser systems are often required, and phase change mechanisms suffer from degradation due to the repeated melt/quenching of the material which negatively impacts the repeatability of the device [38, 39] (Figure 3.1d). None of the mechanisms presented here are non-volatile except for the phase change materials; however the authors note their device suffers from degradation due to repeated cycles [38, 39]. To this end it is advantageous to look for optically actuated mechanisms which are non-volatile yet repeatable to tune transmission of terahertz frequencies. Owing to the photorefractive properties of lithium niobate which is able to sustain optically induced charge distributions in a non-volatile yet rewriteable fashion I propose here that lithium niobate incorporated with graphene and a metallic metasurface can create an optically tuneable device to control transmission of terahertz frequencies.

3.3 Experimental Methods

The device consists of Fe:$LiNbO_3$ substrate patterned with metallic resonator array and covered with a sheet of monolayer chemical vapour deposition

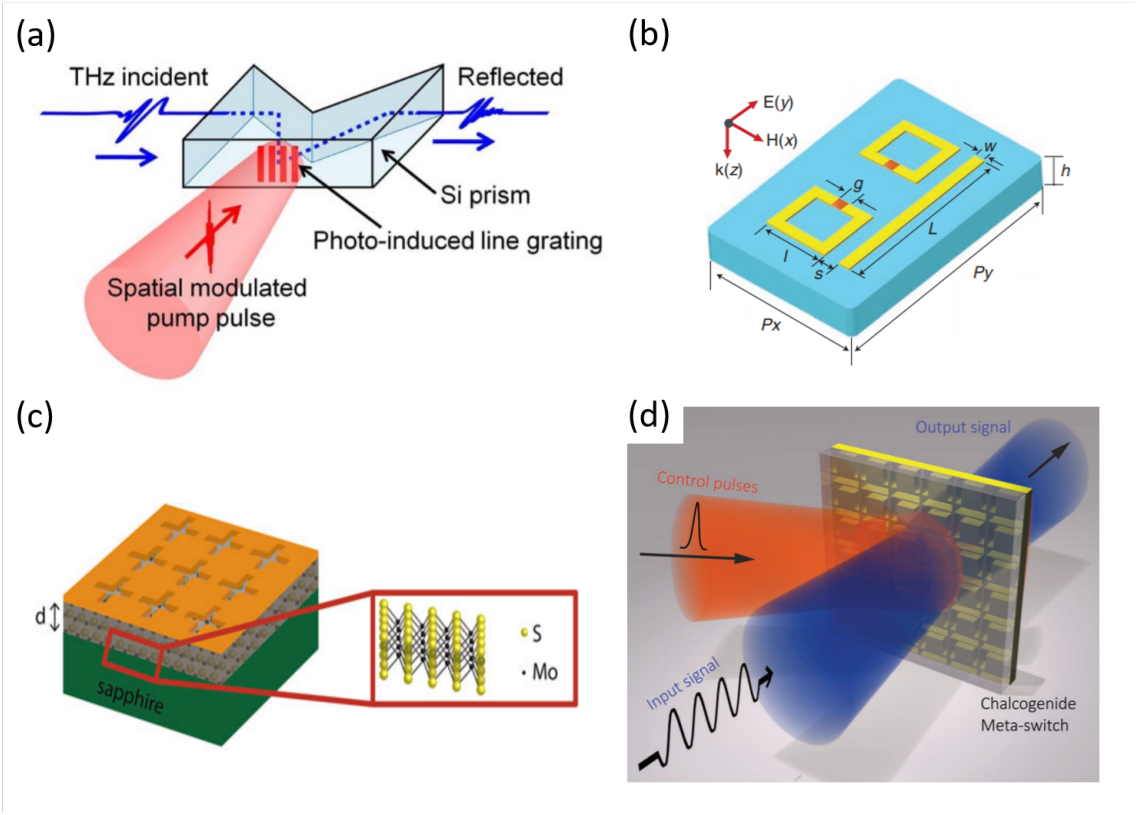

Figure 3.1: ***Controlling Terahertz Radiation:*** ***(a)*** *Photo-induced grating on silicon [24].* ***(b)*** *Metamaterial with semiconductor patch (red) in SRR gap [32].* ***(c)*** *Metamaterial combined with MoS_2 [37].* ***(d)*** *Phase change material coating on patterned metal surface [39].*

(CVD) graphene (Figure 3.2). Upon illumination it is expected that the photorefractive effect in the substrate will modify the graphene electrical properties which therefore will alter the electrical losses in the plasmonic system. The transmittance properties of the device were measured via terahertz time domain spectroscopy (THz TDS) while under optical illumination. Experimental results were compared to finite element simulations where the Fermi level (E_F) of the graphene is tuned to fit to experimental results, thereby gauging the optically induced modification to the graphene sheet achieved by the Fe:$LiNbO_3$ substrate.

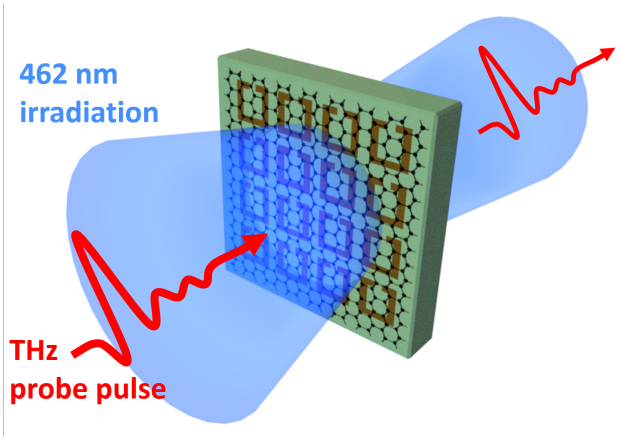

Figure 3.2: *Schematic of device consisting of metallic metasurface on Fe:$LiNbO_3$ with graphene monolayer. Upon illumination from the blue laser the photorefractive effect creates non-uniform charge distributions within the substrate which electrostatically dope the graphene, thereby altering the losses in the plasmonic system.*

3.3.1 Fabrication

A range of devices were fabricated on iron doped lithium niobate crystal substrates (Fe content 0.01 weight %) with a processing flow chart depicted in Figure 3.3. The process of transferring the graphene to lithium niobate substrates is identical to the explanation provided in the previous chapter. An array of metallic resonators were defined by photolithography of AZ2070 photoresist followed by electron beam evaporation deposition of a Cr/Au stack (5/100 nm). The geometry of the resonators was designed by Lewis

Piper. Excess material was removed in a lift-off process in acetone to remove any metal deposited on top of the photoresist. Care must be taken during the photolithography procedure to achieve a good adhesion of the metal to the substrate; Figure 3.4(a) reveals a low adhesion due to a poorly cleaned and dried substrate surface. Once the process parameters (such as exposure and development time) have been optimised a high quality geometry can be achieved (Figure 3.4b), which provides large scale coverage (Figure 3.4c). Commercially supplied CVD graphene (grown on copper foil) was transferred via sacrificial polymer substrate and layered on top of the resonator array in a wet transfer process. After transfer of the graphene the device was held under vacuum (10^{-3} mbar) for 24 hours to remove moisture under the graphene layer and promote adhesion before the removal of the protective PMMA layer via washing in acetone followed by isopropyl alcohol. Due to the photo-responsive nature of the substrate, the devices were thermally annealed in a convection oven at 100°C for 24 hours prior to any measurements in order to thermally erase any non-uniform charge distributions within the substrate.

3.3.2 THz Time Domain Spectroscopy

THz Time Domain Spectroscopy was used to characterise the transmission spectrum of the devices in the frequency range 0.1 to 1 THz. THz pulses are created by the optical excitation of a voltage biased photo-conductive antenna (PCA) via a pulsed femtosecond laser at 800 nm (Figure 3.5). The laser (Spectra Physics Tsunami) is a Ti-sapphire laser which creates short optical pulses with a typical length around 100 fs at a repetition rate of 80 MHz. The THz emitter used is Laser Quantum GMBH's Tera-SED, and for the detector a Menlo GMBA Tera8 detector is used. Due to the voltage bias in the emitter the optically excited charge carriers are accelerated, creating a transient current which evolves over picosecond timescales and therefore emits a pulse of electromagnetic radiation at terahertz frequencies. The detector works on a similar principle however instead of relying on a voltage bias the incident THz pulse accelerates the optically excited charge carriers which are measured by a lock-in amplifier as a current. The charge carriers generated in the detector are short lived and so rely on the incoming optical pulse to overlap in time with the incoming THz pulse. This is achieved by use of an optical delay stage. Further, by oscillating the position of the optical delay stage it is possible to intersect the short optical pulse with different sections of the longer duration THz pulse to build up a temporal map of the

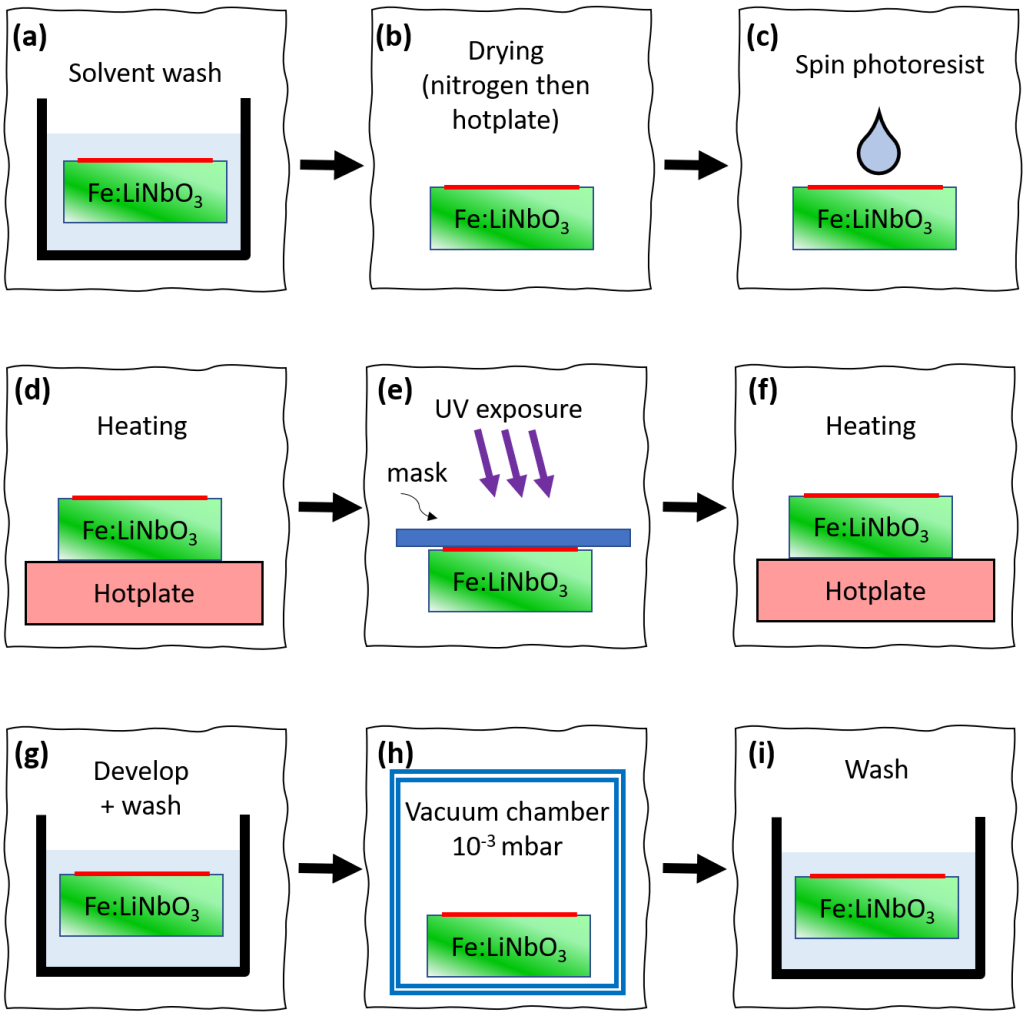

Figure 3.3: *Processing flow diagram of fabrication steps.* ***(a)*** *The graphene covered substrate is washed in acetone, then IPA, then de-ionised water.* ***(b)*** *the substrate is dried with nitrogen and then placed on a hotplate at 100 C for 5 minutes to remove any remaining moisture.* ***(c)*** *Photoresist (AZ 2070) is spin-coated on the substrate by dropping with a pipette and ramping over 5 seconds to a speed of 6000 rpm and holding for 40 seconds.* ***(d)*** *the substrate is heated on a hotplate at 100 °C for 1 minute.* ***(e)*** *3.5 second exposure (75 mJ/cm^2) in mask aligner.* ***(f)*** *Heating on hotplate at 100 °C for 1 minute.* ***(g)*** *Develop in AZ762 for 80 sec.* ***(h)*** *Deposit metal in evaporation chamber.* ***(i)*** *Remove excess material with acetone wash followed by IPA.*

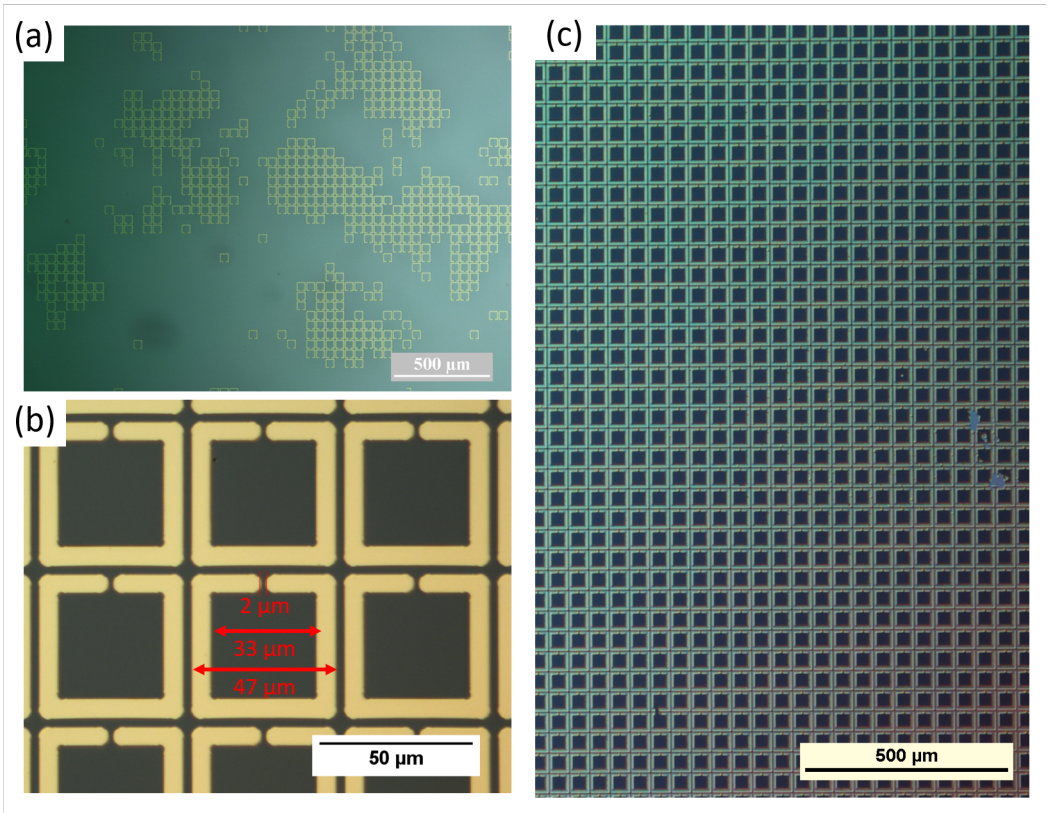

Figure 3.4: ***Fabrication of THz Metamaterials:*** ***(a)*** *Poor adhesion of metal to lithium niobate after lift-off.* ***(b)*** *Optimised fabrication procedure results in high quality geometry of structures, with geometry dimensions noted in red, where the resonators are in a repeating square grid of 50 µm.* ***(c)*** *Large area coverage of resonators achieved with optimised process conditions.*

THz pulse.

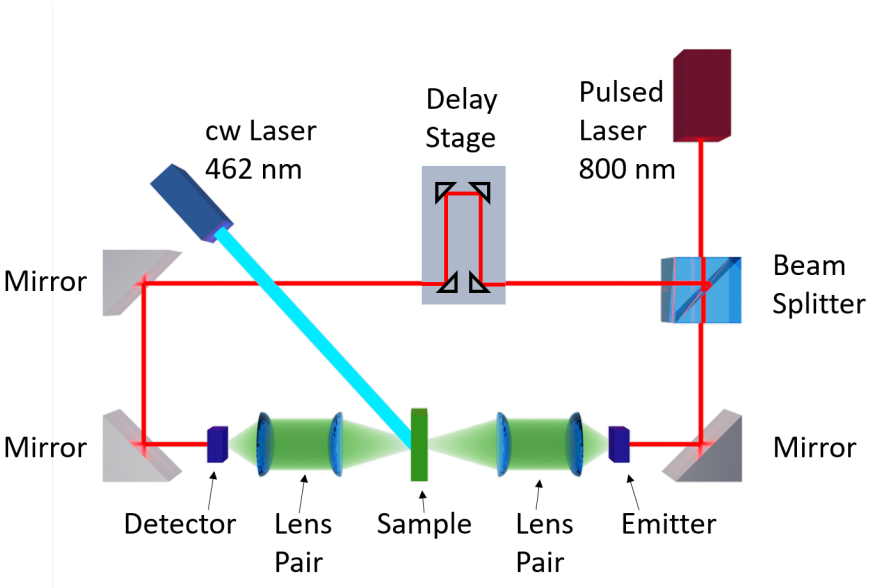

Figure 3.5: *Diagram of THz TDS setup. A femtosecond pulse is emitted by the 800 nm Ti:Sapphire laser which is split by the beam-splitter. One pulse is sent to the emitter which creates a pulse of terahertz radiation, while the other optical pulse is sent to the detector via the delay stage. The terahertz pulse is collimated and focused onto the lithium niobate sample and then focused into the detectors. The lithium niobate is illuminated by the 462 nm blue laser to induce the photorefractive effect.*

The components of the THz spectrometer are rated to emit and detect radiation with a bandwidth from $\sim$ 0.1 - 4 THz however in reality this is prevented by the practicalities of alignment, laser pulse length, and atmospheric absorption of the THz pulse. The strongest signals can be achieved through air (in the absence of a sample in the beam path) which can generally achieve a band-width from 0.1 -2.5 THz before falling to the noise floor, with a peak signal-to-noise ratio around 50 dB. Once a crystal of lithium niobate is placed in the beam path the THz pulse is strongly attenuated at high frequencies, and the pulse has a band-width around 0.1 - 1.0 THz before hitting the noise floor.

The devices are measured before, during, and after illumination, then

the frequency domain spectra are normalised with respect to a reference spectrum taken on with a lithium niobate substrate without metal array or graphene. The normalisation process removes the effects of frequency dependent emission of the PCA, propagation in air, propagation in lithium niobate, and Fresnel reflections from the air/Fe:$LiNbO_3$ interfaces.

In Figure 3.6 the raw, non-normalised, transmission spectra are plotted for scans taken in air, through lithium niobate, and through lithium niobate patterned with metallic resonators. It can be seen that for the transmission through air the signal extends beyond 2 THz, however once the lithium niobate is introduced into the beam path the signal is attenuated at high frequencies, reaching the noise floor around 1.4 THz. Due to the high absorption of frequencies above 1 THz in lithium niobate the resonantor geometry was designed to such dimensions that the first three resonances all occur below 1 THz and therefore can all be measured in the spectral region of highest measurable signal.

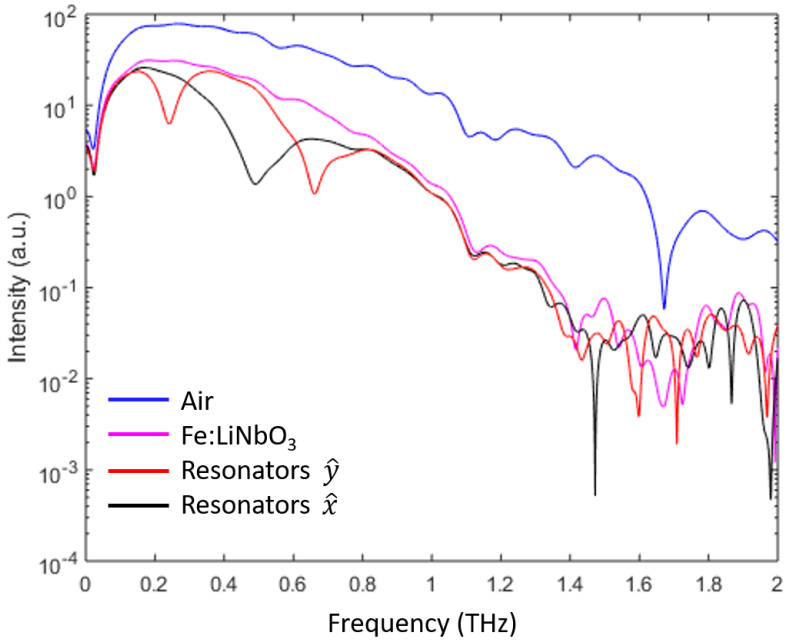

Figure 3.6: *THz transmission spectra measured for air, lithium niobate substrate, and resonators in two orthogonal orientations without graphene. The transmission intensities do not include any normalisation factor. It can be seen that for the transmission in air the THz signal extends beyond 2 THz however once the lithium niobate is placed in the beam path the signal is strongly attenuated and the bandwidth limited to 1.4 THz. For the two orientations of the resonator structures there is the clear presence of three absorption features between 0.2 and 0.6 THz.*

3.3.3 Device Illumination

The devices are illuminated from the top surface, which is covered with the resonator array and graphene by a 462 nm fibre coupled diode laser at 25 mW cm^{-2} collimated at the fibre output by an aspheric lens resulting in a 10 mm beam diameter as shown in Figure 3.2. The laser is aligned on the device to ensure the beam completely covers the region of the focused THz pulse; this is achieved by using a metallic aperture of 3 mm diameter placed on the rear surface of the device which is placed at the THz focus and visually overlapping the laser beam with the aperture. For the duration of all experiments the emitter, detector, and metasurface device are held in a light-proof box to avoid ambient illumination of the device. Before illumination THz scans are taken over a 20 minute period to gauge the drift in the THz system. The device is then illuminated continuously for a 70 minute period while measuring the THz transmission. The illumination source is then switched off and the scans continue in the dark to observe whether any optically induced transmission change is non-volatile.

3.3.4 Finite Element Analysis

A finite element analysis is performed in Comsol to investigate the effect of varying the graphene Fermi level on the transmission spectrum of the resonator structures. The model consists of a unit cell 50 x 50 μm in the x-y direction; linearly polarised electromagnetic radiation is excited from a port on the upper plane of the unit cell propagating downwards through 300 μm of air then into a 1 mm thick slab of lithium niobate (depicted in Figure 3.7a). The incoming port on the top surface of the air has an electric field wave excitation wave which emits an electric field of 1 V/m uniformly over the entirely measured frequency range. The choice of port excitation field strength is arbitrary as, similar to the experimental measurements using the THz-TDS, all transmitted fields are normalised to either transmission through an unpatterned lithium niobate substrate, or a non-illuminated metasurface device. Experimental values of the frequency dependent complex refractive index of the substrate are used for the material properties as measured on my $LiNbO_3$ crystals via THz TDS as presented in Appendix B. A gold resonator structure is created on the air/lithium niobate interface and modelled to the 2 dimensional geometry of the photolithography mask (Figure 3.7b). The permittivity values of the gold are taken from a Drude model [40]. Trans-

mitted power is normalised against a simulation in the absence of graphene and gold through a $LiNbO_3$ slab. The simulation is first performed in the absence of the graphene layer to compare to experimental spectra before graphene transfer. The graphene layer is then added to the simulated model and the Fermi level of the graphene is modified in a parametric sweep to find convergence with experimental results.

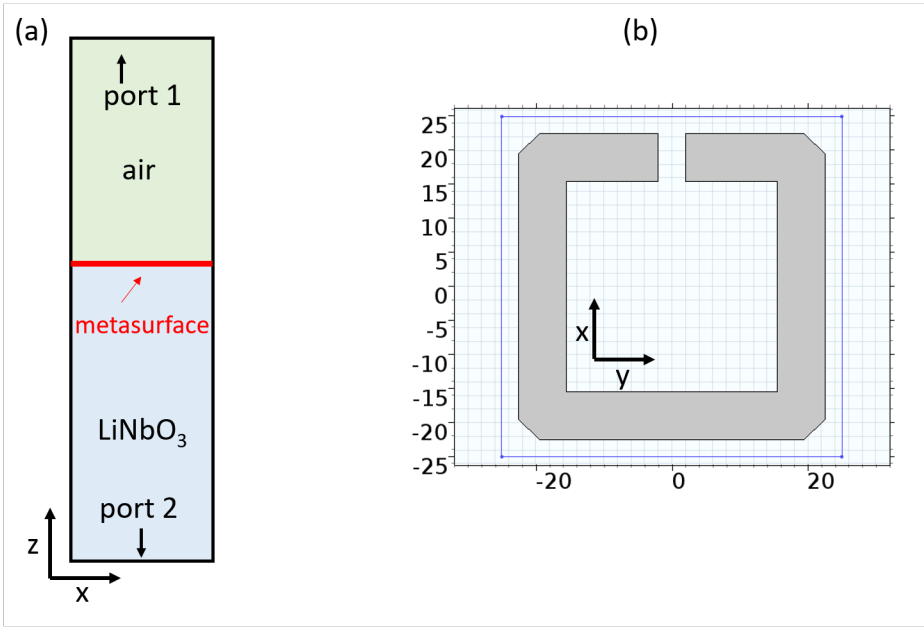

Figure 3.7: ***(a)*** *Side-view of unit cell showing air and lithium niobate slab.* ***(b)*** *Top-view of unit cell with metallic resonator structure.*

Modelling Graphene: Graphene is modelled as a 3D sheet of 5 nm thickness covering the entire unit cell on top of the gold resonator, which is similar to the fabricated geometry. A 3D wave equation model is applied to the graphene domain with the graphene material parameters defined by permittivity. The frequency dependent conductivity and permittivity of graphene can be represented by Equations 3.1 and 3.2 respectively, as a function of Fermi level E_f [41], where τ is the electron relaxation time given by Equation 3.3, μ is the charge carrier mobility (3760 cm^2/Vs), e is the electron charge, t is the graphene thickness (5 nm), and V_f is the Fermi velocity (10^8 cm/s).

$$\sigma = \frac{ie^2}{\pi\hbar}\frac{E_f}{\omega + i\tau^{-1}} \tag{3.1}$$

$$\epsilon = 1 + \frac{i\sigma}{\epsilon_0 \omega t} \tag{3.2}$$

$$\tau = \frac{\mu E_f}{e v_f^2} \tag{3.3}$$

The DC conductivity is obtained by multiplying the frequency dependent conductivity by (1 - i$\omega\tau$). The carrier number n is then simply given by dividing the DC conductivity by electron charge and mobility. The formalisation of the frequency dependent conductivity in Equation 3.1 takes into account only the intra-band conductivity, while the inter-band conductivity is ignored. This can be justified when one considers that for inter-band absorption the incident energy must be greater than $2E_f$ where the energy of a THz photon is $\sim$4 meV ($<2E_f$) and therefore the inter-band transition is forbidden at such low frequencies.

3.4 Results and Discussion

3.4.1 Resonators Before Transfer of Graphene

Transmittance:

The THz transmittance of the metallic metasurface on Fe:$LiNbO_3$ is measured before the transfer of the graphene layer. The device is measured with the metasurface at two orientations relative to the polarisation of the THz electric field, either along ($\vec{E} \parallel \hat{y}$) or normal ($\vec{E} \parallel \hat{x}$) to the split ring gap. It can be seen that for the $\hat{y}$ orientation there is a pronounced resonance peak at 0.22 THz followed by a broader peak around 0.65 THz which corresponds to the fundamental and third-order resonance, respectively (Figure 3.8a). In this orientation the system responds as a split ring resonator. For the horizontal polarisation ($\vec{E} \parallel \hat{x}$) there is a single resonance peak centred around 0.45 THz which has a much broader resonance (Figure 3.8b). In this configuration the system responds as a ring resonator.

Overlaid in the dashed lines are simulated transmittance spectra for an identical metamaterial unit cell on lithium niobate substrate. It can be seen that for both orientations there is good agreement between experiment and simulation however for the $\hat{y}$ orientation there is some deviation in transmittance away from the resonance frequencies. The simulated results expect sharper resonance peaks, which may be attributed to imperfections in the geometry and quality of the metamaterial array which is produced during fabrication.

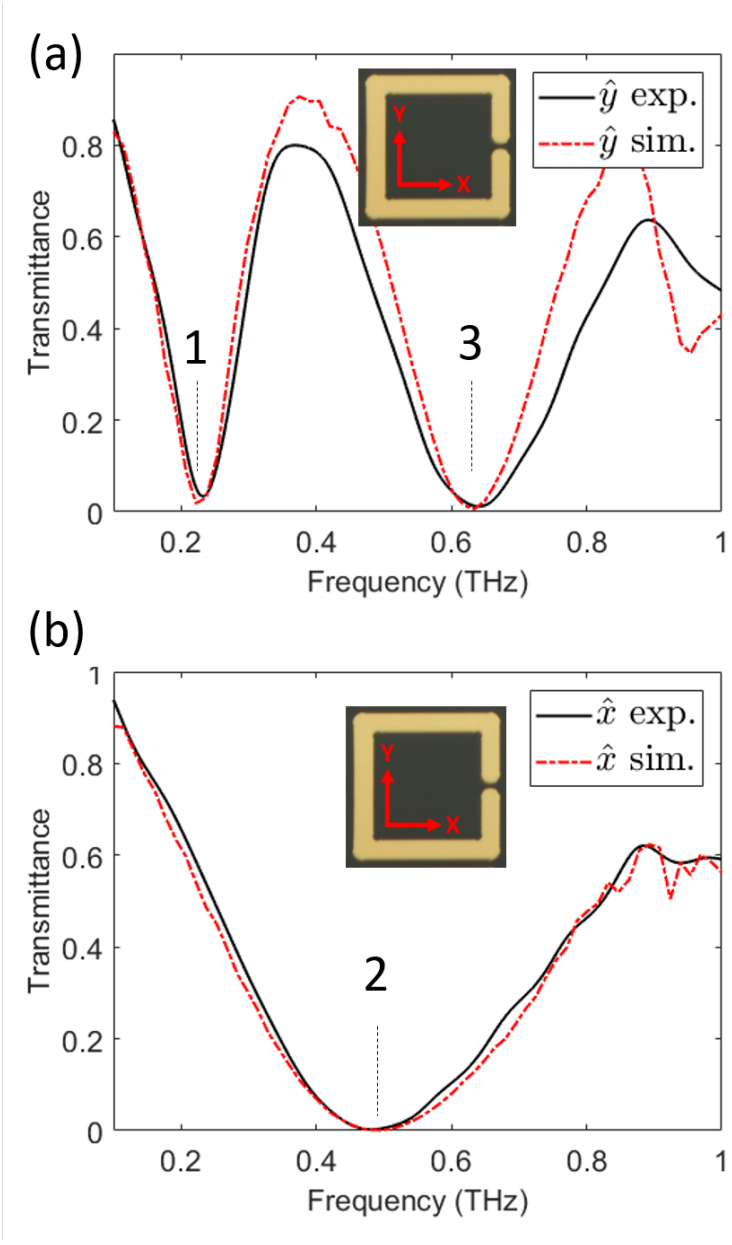

Figure 3.8: ***(a)*** *Experimental and simulated transmittance spectra of resonators without graphene in $\hat{y}$ orientation, with resonances labelled* ***(1)*** *at 0.22 THz and* ***(3)*** *at 0.64 THz.* ***(b)*** *Experimental and simulated transmittance spectra of resonators without graphene in $\hat{x}$ orientation, with resonance labelled* ***(2)*** *at 0.48 THz.*

Simulated Field Maps:

Figures 3.9, 3.10 and 3.11 show simulated electric and magnetic field maps at a plane 5 μm above the metasurface without graphene. Figure 3.9 investigates resonance **1** in the $\hat{y}$ orientation at 0.22 THz, Figure 3.10 investigates resonance **2** in the $\hat{x}$ orientation at 0.48 THz, and Figure 3.11 investigates resonance **3** in the $\hat{y}$ orientation at 0.64 THz.

The absolute electric field $|E|$ is the absolute value of the $\hat{x}$, $\hat{y}$, and $\hat{z}$ components of the electric field which reveals where the regions of high electric field exist. In the case of Figure 3.9(a) it can be seen that there is strong electric field in the gap of the split ring. The absolute of the $\hat{z}$ component of the electric field $|E_Z|$ relates to regions of high charge density in the metasurface, where regions of high charge density result in electric field lines pointing in the $\hat{z}$ direction. From Figure 3.9(b) it can be seen that the regions of high charge density exist at each side of the split ring gap and are largely confined to within the metallic resonator. The confinement here is expected as the material surrounding the metallic resonator is not conductive and therefore should not contain significant charge densities.

To further investigate the regions of charge density it is useful to plot the real part of the $\hat{z}$ component of the electric field E_Z. As the real part of E_Z oscillates in time it must be multiplied by an arbitrary imaginary component in order to see how the signs of the charge densities vary over the cycle. In Figure 3.9(c) it can be seen the charge densities have similar magnitude to the absolute values however the lobes on each side of the split ring gap have opposite signs. This can be understood as two regions of high charge density with opposite signs (i.e. a positive and negative lobe) which will oscillate between positive and negative sign. These regions of charge density with opposite sign will create electric fields between them which will result in currents between the lobes of the electric field.

To infer the electric currents in the metasurface the absolute parts of the magnetic field are plotted. In Figure 3.9(d) I plot the absolute part of the $\hat{y}$ component of the magnetic field $|H_Y|$ which is related to electric currents travelling in the $\hat{x}$ direction. From this map it can be understood there is a region of high current density travelling in the $\hat{x}$ direction along the lower arm of the resonator structure. A similar analysis can be performed with the $\hat{x}$ component of the magnetic field with corresponds to electric currents travelling in the $\hat{x}$ direction as shown in Figure 3.9(e). From there field maps of magnetic field it can be understood that electric currents run down the sides and along the lower arm of the resonator structure, confined to

within the metallic region. The direction of the currents matches to the interpretation of the charge density regions which confirms that this is the fundamental resonance mode.

Similar analysis can be understood for resonances **2** in Figure 3.10 and **3** in Figure 3.11, which reveal they do indeed correspond to the second and third order resonances respectively.

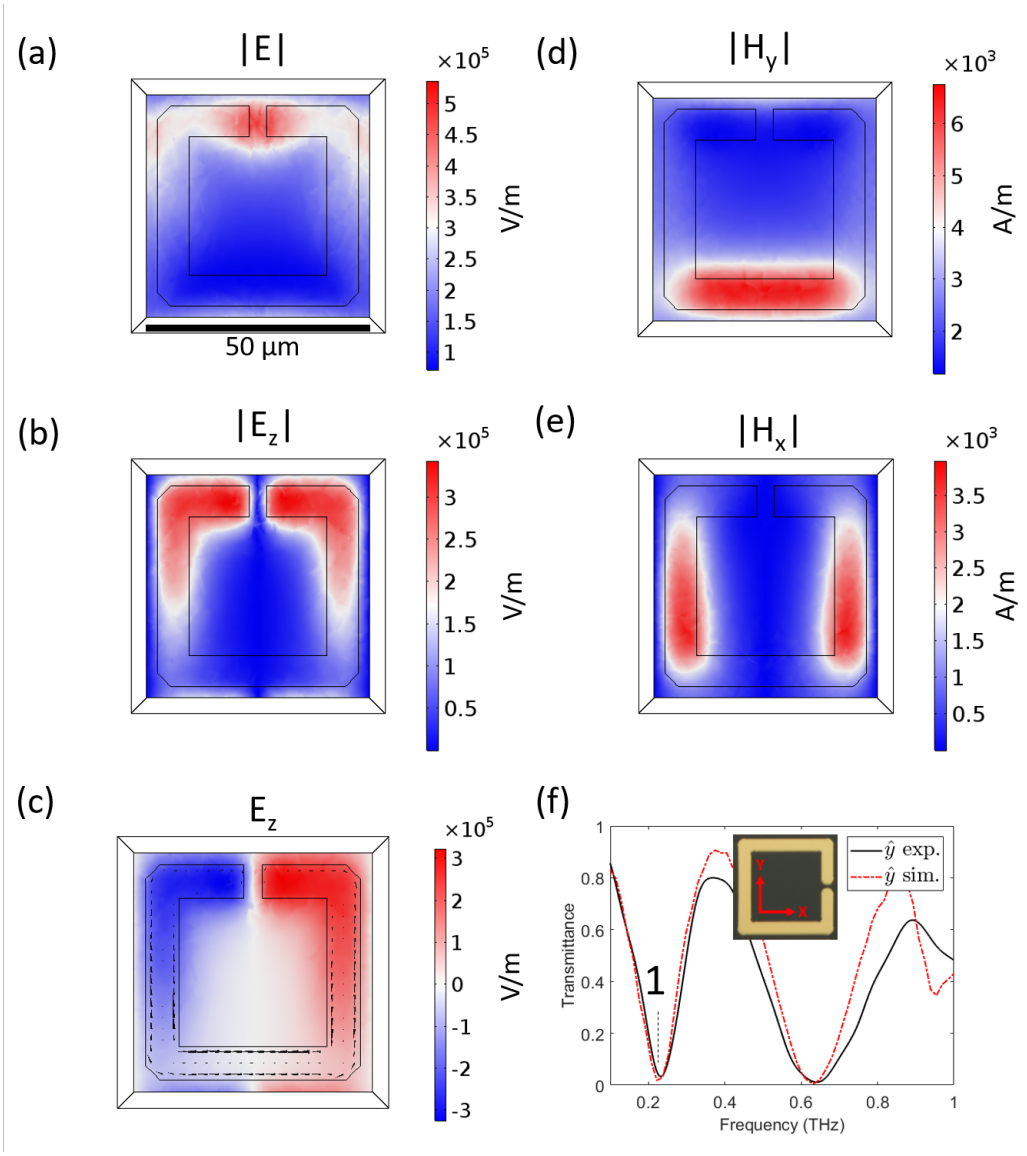

Figure 3.9: ***(a-e)*** *Simulated field maps for resonance **1** in $\hat{y}$ orientation at 0.22 THz which reveal two regions of high charge density connected by one region of current, therefore demonstrating the first order resonance mode.* ***(f)*** *Experimental and simulated resonance spectra.*

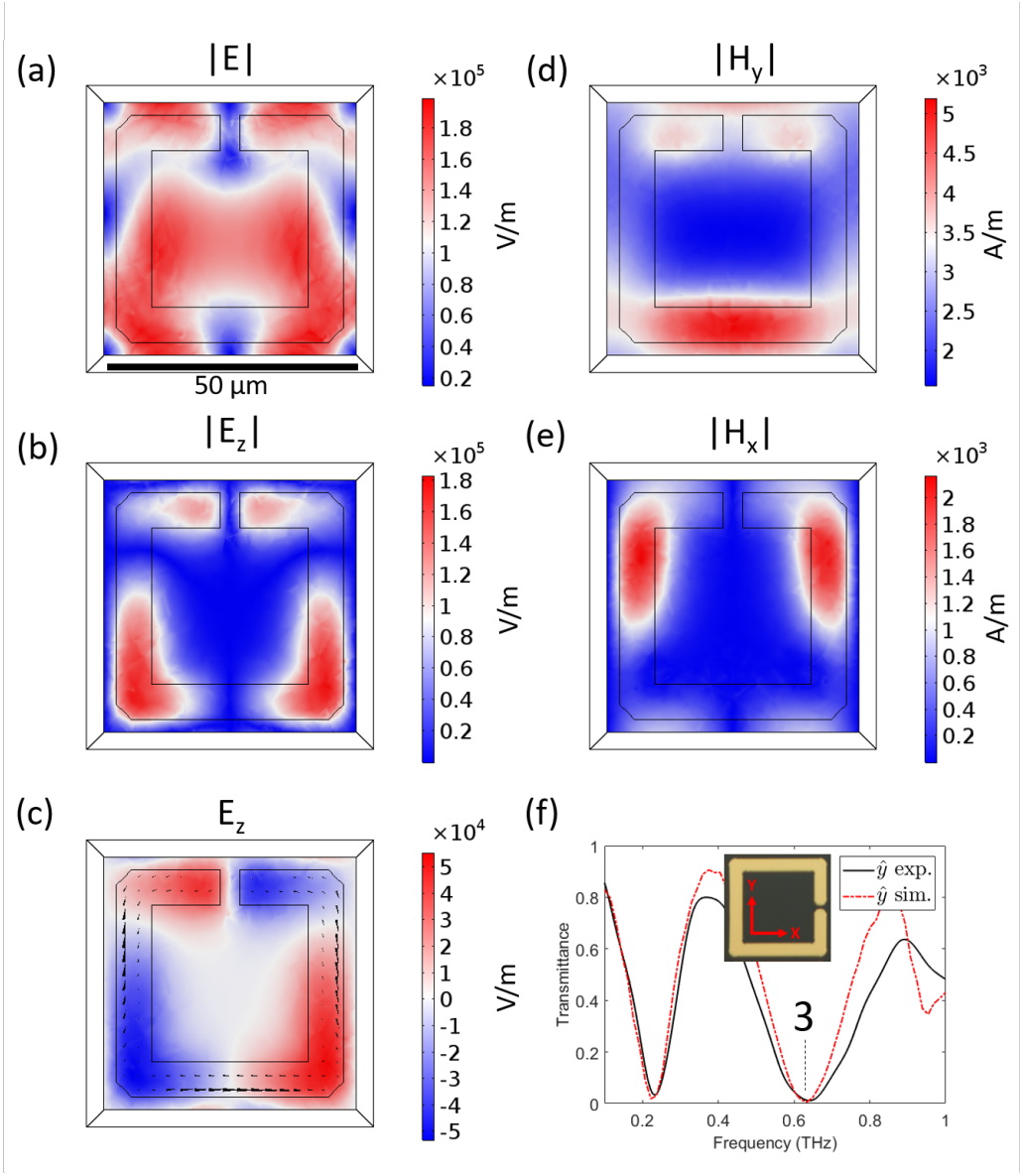

Figure 3.10: ***(a-e)*** *Simulated field maps for resonance* ***2*** *in* $\hat{x}$ *orientation at 0.48 THz which reveal three regions of high charge density connected by two regions of current, therefore demonstrating the second order resonance mode.* ***(f)*** *Experimental and simulated resonance spectra.*

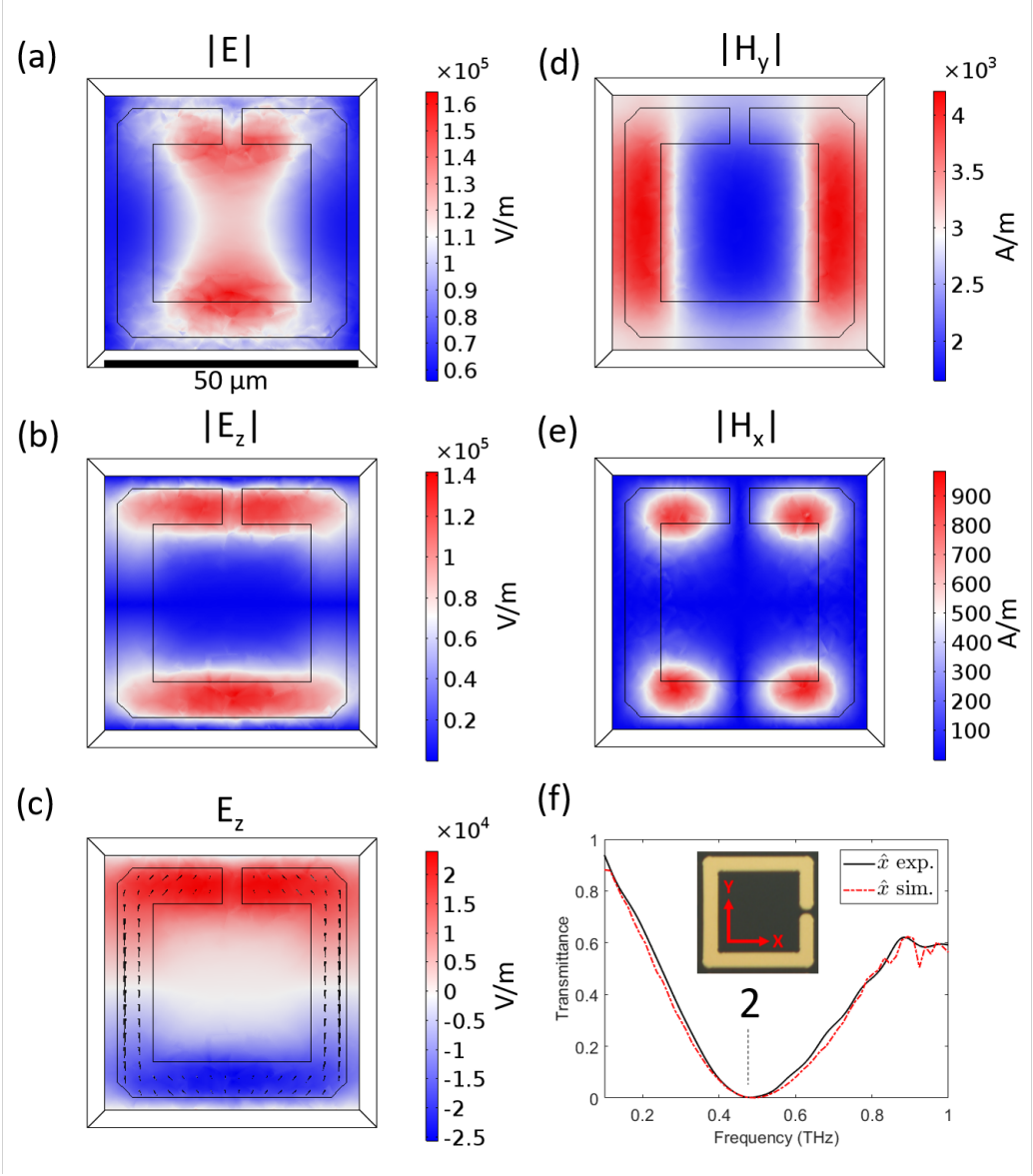

Figure 3.11: ***(a-e)*** *Simulated field maps for resonance* ***3*** *in* $\hat{y}$ *orientation at 0.64 THz which reveal four regions of high charge density connected by three regions of current, therefore demonstrating the third order resonance mode.* ***(f)*** *Experimental and simulated resonance spectra.*

Metasurface With Graphene:

In Figure 3.12 I plot the transmittance spectra measured in the $\hat{y}$ and $\hat{x}$ orientations for the metasurface before and after the transfer of graphene. In all cases it can be seen that once the metasurface is covered with graphene the resonance peaks are strongly damped, becoming weaker and wider. It is also noticed that the resonance peaks appear to become red-shifted to lower frequencies with the transfer of graphene. For the simulated spectra the Fermi level of the graphene is modified to achieve a good agreement with the experimental data. For the $\hat{y}$ orientation the Fermi level is set to 0.175 eV while for the $\hat{x}$ orientation the Fermi level is set to 0.170 eV.

The simulated data are fitted to the experimental results by use of a Mean Squared Error (MSE) approach in which the square of the difference between experimental and simulated results is summed over the frequency domain and divided by the number of discrete frequency elements to quantify the quality of the fit, and define which initial Fermi level provides the best fit to experimental data. In Figure 3.13 the MSE is plotted against graphene Fermi level, where the inferred initial Fermi level is obtained at the minimum MSE value.

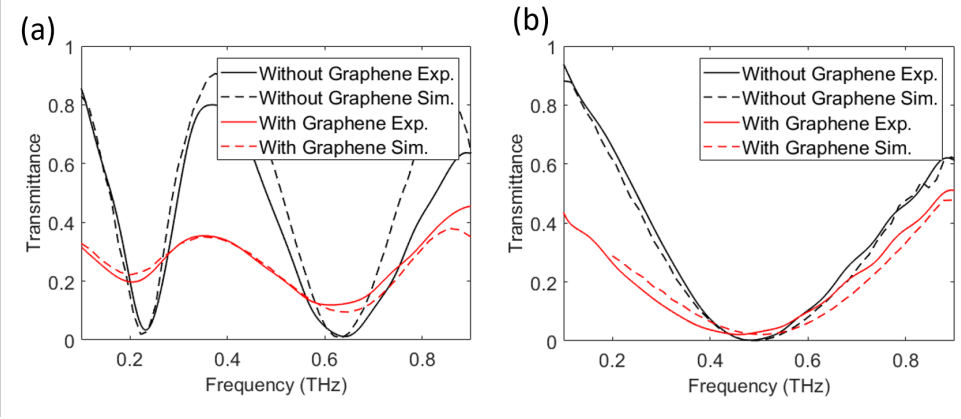

Figure 3.12: *(a) Experimental and simulated transmittance spectra of metasurface with and without graphene in $\hat{y}$ orientation for resonances **1** and **3**. **(b)** Experimental and simulated transmittance spectra of metasurface with and without graphene in $\hat{x}$ orientation for resonance **2**.*

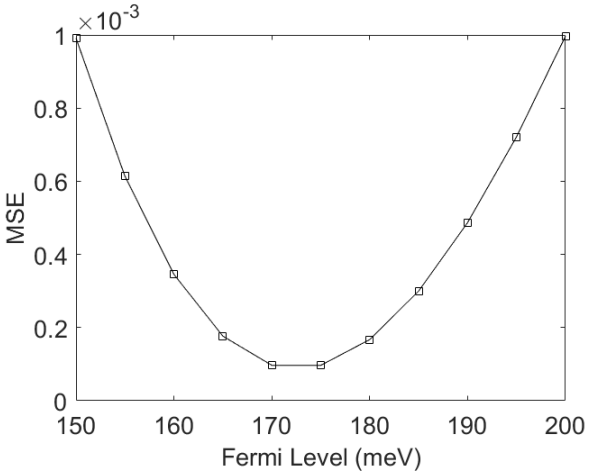

Figure 3.13: *Mean Squared Error (MSE) between simulated and experimental results plotted against varying graphene Fermi level for the $\hat{y}$ orientation suggests the graphene has an initial Fermi level of 0.175 eV.*

3.4.2 Photorefractive Changes to Resonators in $\hat{y}$ Orientation with Graphene

Figure 3.14 shows experimental and simulated spectra for the graphene covered device measure in the $\hat{y}$ orientation in the dark and then after illuminated with the 462 nm laser source which reveals photo-induced changes to the resonance spectra.

Figure 3.14(a) plots the normalised transmittance before and after illumination. The resonance peaks are fitted with Lorentzian functions to extract the corresponding linewidth, resonance frequency, and Q factor. Upon illumination there is damping of the resonant peaks where the FWHM of the peak at the fundamental resonance **1** (at 0.22 THz) is increased from 228 to 253 GHz, resulting in a Q factor decrease from 0.85 to 0.72, while at the third order resonance **3** the FWHM increased from 358 to 387 GHz resulting in the Q factor decreasing from 1.75 to 1.61 as the Ohmic losses are increased due to the optical doping effect induced by the substrate. Overlayed to Figure 3.14(a) are simulated transmission spectra, where the graphene Fermi level is modified from 0.175 to 0.195 eV. There is generally a good agreement between the shape of the experiment and simulation except for the low and high frequencies in which there is some deviation; low frequencies are

very sensitive to phase errors in the THz TDS and diffraction due to the large wavelength, while high frequencies suffer from low signal to noise ratios. Figure 3.14(b) plots the same experimental data set where the spectra have been normalised to transmittance before illumination. Two peaks can be observed which correspond to the resonant absorption frequencies at 0.22 and 0.65 THz, where the maximum increase in transmittance reaches up to 15%.

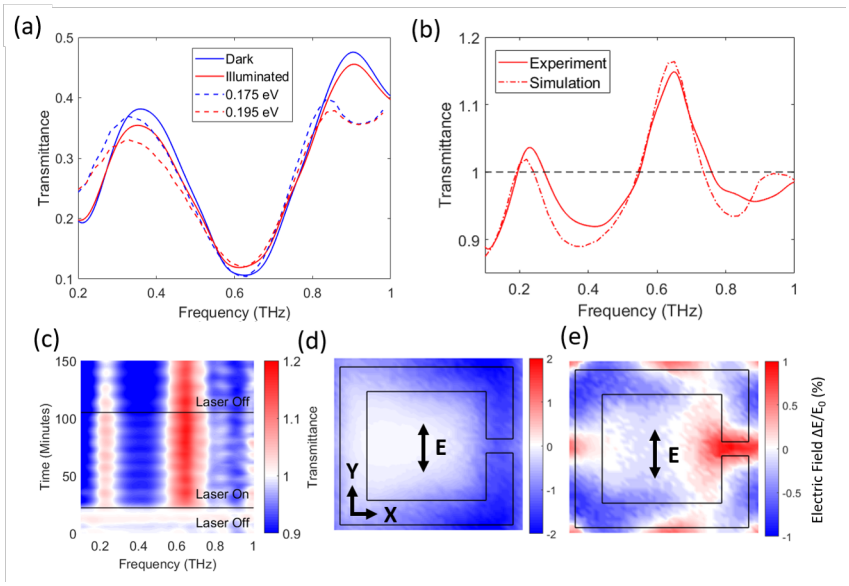

Figure 3.14: ***(a)*** *Transmittance for vertically polarized ($\vec{E} \parallel \hat{y}$) THz before (blue) and after (red) illumination (solid lines) overlayed with simulated results (dashed lines) for graphene Fermi levels of 0.175 eV (blue) and 0.195 eV (red). The experimental spectra are averaged over the "Laser On" and "Laser Off" periods (see panel (c)).* ***(b)*** *Experimental (solid) and simulated (dashed) relative transmittance normalised to the transmittance before illumination.* ***(c)*** *Transmittance as a function of frequency and time. The transmittance is constant before illumination, however once illuminated there is a rapid change in transmission spectra which remains once the illumination source is removed.* ***(d** & **e)*** *Simulated change in electric field after illumination due to photoinduced change of graphene Fermi level at 0.22 (d) and 0.65 THz (e).*

In Figure 3.14(c) frequency dependent transmittance values are plotted

in a colour map as a function of time (on the y axis). All transmission values are normalised with respect to the "dark" values. The colour map shows that in the first 20 minutes, while the laser is off, the THz transmittance through the device is stable in dark ambient conditions, however once the 462 nm laser source is switched on there is sudden change in transmission localised to two distinct frequency bands around 0.2 and 0.6 THz. After the laser is switched off however it can be seen from the graph that these optically induced effects persist even in the absence of illumination highlighting the non-volatile nature of the mechanism.

Figures 3.14(d) & (e) plot the simulated change in electric field in a plane situated 5 μm above the resonator surface for the fundamental (0.22 THz) and third order (0.65 THz) resonance, where the absolute values of electric field after illumination are subtracted from before illumination, and presented as a percentage of the absolute incident electric field. It can be seen that for the fundamental resonance at 0.22 THz there is a decrease in the electric field by ~ 1 % located in the gap of the ring. For the third order resonance at 0.65 THz there is a localised increase in the electric field in the gap while the field maxima at the two opposite corners show a decrease in electric field, consistent with an increased loss in the system.

3.4.3 Photorefractive Changes to Resonators in $\hat{x}$ Orientation with Graphene

Figure 3.15 presents the spectral response of the hybrid graphene metasurface measured in the $\hat{x}$ orientation which corresponds to a ring resonator configuration.

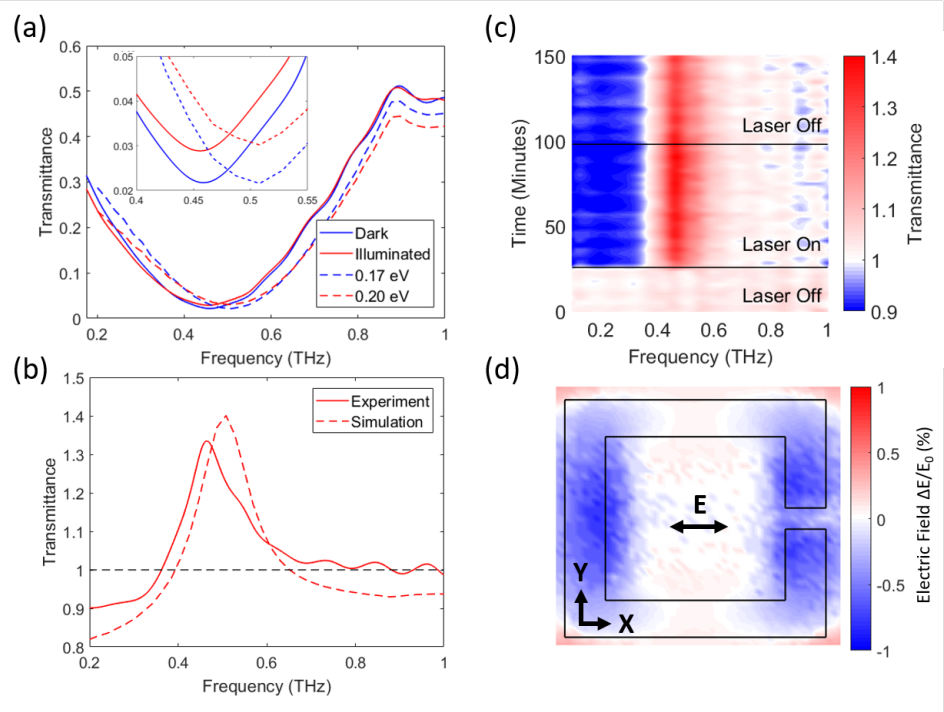

Figure 3.15: *Transmittance measured with horizontally polarized ($\vec{E} \parallel \hat{x}$) THz before and after illumination (solid lines) overlaid with simulated results (dashed lines) where graphene Fermi level is modified from 0.175 to 0.195 eV.* ***(b)*** *Experimental and simulated transmittance normalised to the spectra before illumination.* ***(c)*** *Transmittance versus time colour map.* ***(d)*** *Simulated change in electric field after illumination due to photoinduced change of graphene Fermi level.*

In Figure 3.15(a) it can be seen that the absorption peak centred around 0.45 THz is dampened after illumination of the device, where the FWHM (obtained by Lorentzian fitting) of the resonance peak increases from 590 to 630 GHz, resulting in a Q factor decrease from 0.78 to 0.73. For use in

a practical device it is important to investigate the absolute transmittance change (non-normalised) which can be achieved by this tuning mechanism. At 0.45 THz the transmittance change is relatively low as the largest effect occurs at the resonance frequency where transmittance is at a minimum, and therefore the modulation depth at 0.45 THz is 1% in response to incident optical energy of $\sim$20 J/cm^2, as shown in Figure 3.15(a). Figure 3.15b presents relative transmittance changes where it can be seen that at the resonance peak around 0.45 THz the optical doping effect results in a transmittance increase of 35 %. Simulated data is fitted to the transmission spectra where a graphene Fermi level change from 0.175 to 0.195 eV provides a good agreement with experimental data, which relates to a charge carrier modulation of $8.2 \times 10^{11}/cm^2$. The simulated spectra shows a similar shape to the experimentally measured resonance however the central frequency of the resonance peak is offset by $\sim$ 45 GHz, which may be attributed to differences between the modelled resonator and the actual fabricated geometry, and differences in the refractive index of the deposited gold layer. It is interesting to note here the carrier numbers calculated are around 10 times smaller than reported in Chapter 2, which may correspond with the 10 times lower iron doping content in the lithium niobate crystals used here.

The colour map in Figure 3.15c plots frequency dependent transmittance against time, normalised to the transmittance before illumination. From the figure it can be seen that the system is initially stable in the dark however once illuminated there is an abrupt change in transmittance centred around the resonance frequency at 0.45 THz, while at larger wavelengths there is negligible change. Furthermore the figure shows that once the illumination source is removed the effect remains in the dark which highlights the non-volatilty of the photorefractive doping effect.

The electric field map in Figure 3.15(d) presents change in electric field, where the absolute electric field values after illumination are subtracted from field values before illumination, and normalised as a percentage of the field incident on the sample. It can be seen from the electric field map that as the graphene Fermi level is increased there is a drop in the electric field magnitude at each end of the resonator as would be expected from the direction of the electric dipole.

3.4.4 Device Repeatability

Multiple cycles of illumination followed by thermal annealing of the device are presented in Figure 3.16, where the transmittance at two frequencies (on resonance, and off resonance) are plotted against time. All transmittance values are normalised with respect to transmittance before illumination. As the device is illuminated the transmittance at 0.45 THz (at resonance) increases with an exponential type trend, however far from the resonance (0.80 THz) there is negligible change in transmittance. After the 22 minute illumination period the device is thermally reset to restore the device to a uniform charge distribution. This cycle of illumination followed by thermal annealing is repeated a total of three times. An inverse exponential trend is fitted to each cycle. The graph highlights there is some degree of degradation of the device over the repeat cycles. This may be caused by atmospheric doping of the graphene where either charged particles from the atmosphere or moisture are attracted to the graphene surface and cause a doping effect. This could be avoided by either holding the device in a vacuum or inert environment, or by encapsulation of the graphene with an insulator such as hexagonal boron nitride.

3.4.5 Investigating the role of $LiNbO_3$ Ferroelectric Dipole in Photodoping Mechanism

Figure 3.17 presents experimental results for two devices (graphene covered metasurface on -z substrate and +z substrate) measured in the $\hat{x}$ orientation to investigate effects of lithium niobate ferroelectric axis direction. All scans during the illumination period are averaged and divided by the spectra before illumination to normalise the transmittance values. It can be seen that for the -z device there is a transmittance peak around 0.5 THz with a trough centred around 0.2 THz, both changing transmittance by around $\pm 10\%$, however for the +z device it can be seen there is a peak around 0.2 THz and a trough around 0.55 THz. The peaks and troughs are of opposite sign yet of nearly equal magnitude for the plus and minus z devices. It can be reasoned that if the graphene layer around the resonators increases its conductivity the resonance peak would be expected to becomes broader and shallower, while if the graphene conductivity decreases the resonance peak would be expected to become sharper and deeper. Therefore it can be argued that when graphene of the +z face of the substrate is illuminated the graphene conductivity is

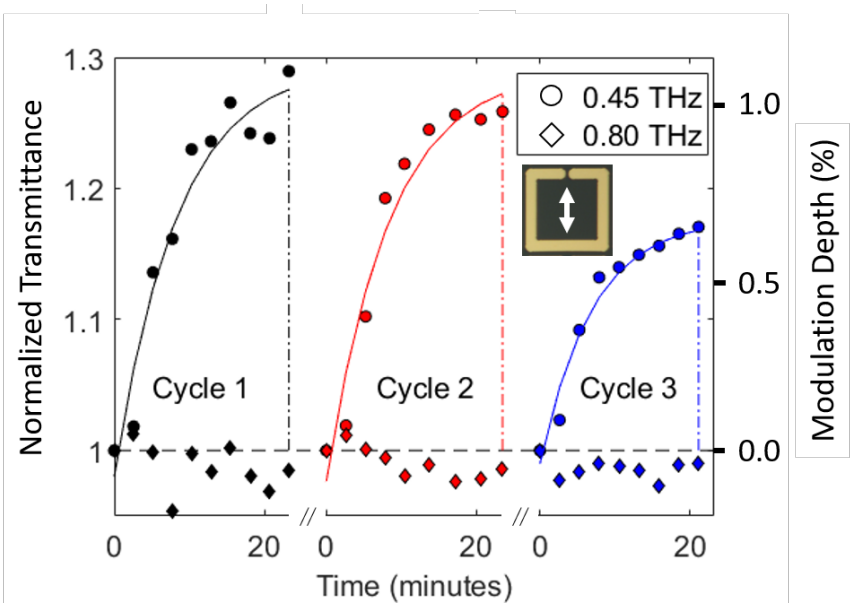

Figure 3.16: *Transmittance (and modulation depth) at 0.45 THz (circles) and 0.80 THz (diamonds) measured in the $\hat{x}$ orientation are plotted against time while illuminated for three repeat cycles of illumination followed by thermal annealing.*

decreased, while for the -z face the graphene conductivity is increased. These results suggest that with the competing mechanisms of photoconductivity it is the drift effect (which excites electrons preferentially along the +z axis) which is making the main contribution compared to diffusion (migration from regions of high to low illumination intensity).

3.4.6 Control Experiment Without Graphene

The results of a control experiment are provided in Figure 3.18 where the transmission through a device consisting of resonators measured in the $\hat{x}$ orientation without graphene is presented. The colourmap in Figure 3.18(a) reveals that although there is some variation in transmission there is no discernible relation to the laser illumination. It can be seen that at the resonance peak frequency around 0.46 THz there is some amount of transmission decrease however again this process is present from before the laser illumination and may be attributed to drift in the system. In Figure 3.18(b) I

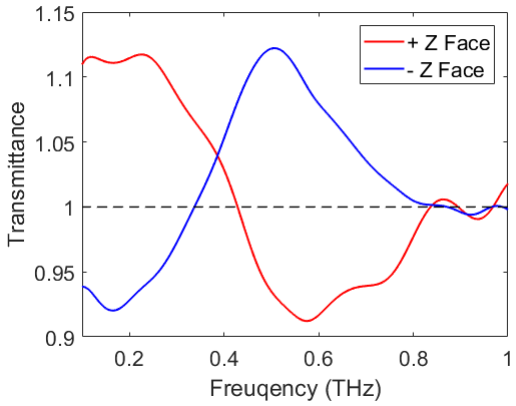

Figure 3.17: *Optically induced transmittance changes for two devices measured under illumination with horizontally polarized ($\vec{E} \parallel \hat{x}$) THz ; one with array patterned on the +z face, and one device patterned on the -z face. Results show the change in transmittance is of equal yet opposite magnitude for the ±z faces, suggesting the graphene conductivity change is dependent* on the polarity of the ±z faces of the substrate.

plot the transmission spectra averaged for before, during, and after laser illumination normalised to the transmission through a sample of unpatterned lithium niobate. From this figure there is no noticeable behaviour however when normalised to the transmission before illumination (as shown in Figure 3.18c) it can be clearly seen that there is some degree of transmission change around the resonance frequency. Far from the resonance frequency it appears as if the transmission decreases uniformly over time which may be attributed to a drift in laser power. By comparing the result in panel (c) to that in panel (a) it can be seen that this transmission change at resonance frequency is not related to laser illumination. Although the photoconductive effects of the substrate creates free electrons within the Fe:$LiNbO_3$ crystal these are of such low numbers due to the low illumination intensity that they have no measurable effect on the transmission. Furthermore if any change was observed it would be a transient effect which would disappear once the illumination source was removed [42]. It could also be argued that due to the non-volatile electron migration associated with the photoconductive effect that an optically induced change in electron distribution may (through the generation of internal electric field and subsequent change in refractive index) result in a change of transmission, however again if this effect is present it is

certainly far below the measurable reaches of my spectroscopy setup.

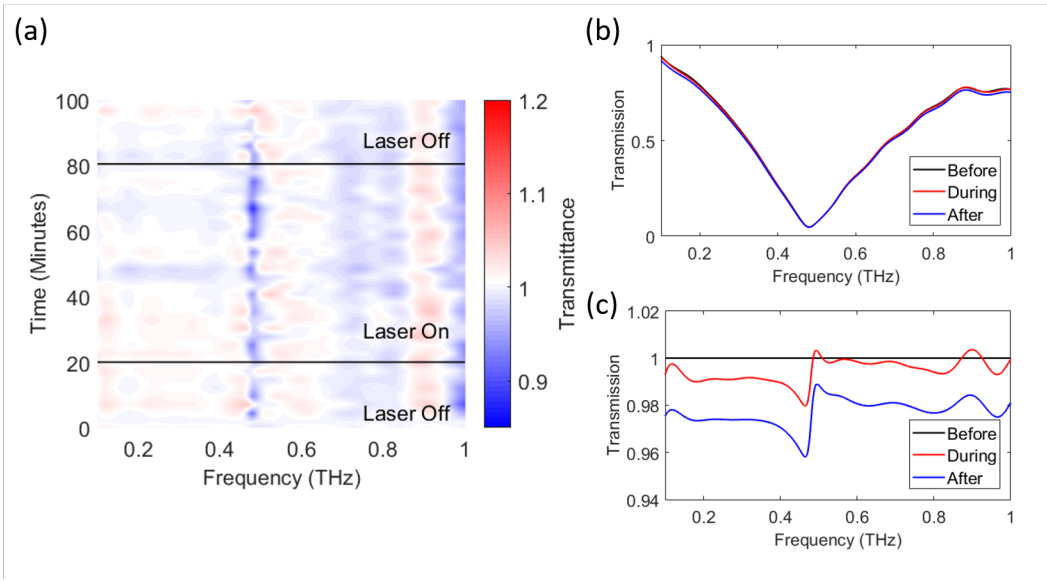

Figure 3.18: *THz transmittance spectra for ring resonators on -z Fe:LiNbO$_3$ without graphene as a control experiment.* ***(a)*** *The colour map shows that despite some drift in the system there is no relation to the laser on/off times.* ***(b)*** *Transmission spectra normalised to lithium niobate substrate.* ***(c)*** *Transmission spectra normalised to resonator device before illumination.*

3.4.7 Error Analysis

To determine the errors involved in a THZ TDS result is a rather complicated issue as there are many components involved in the spectrometer system such as the photoconductive antenna (PCA), lock-in amplifier, delay stage, etc, all of which will introduce various levels of uncertainty into the system.

The strength of the THz electric field can be calculated by Electro-Optic Sampling (EOS) [43, 44] in which the THz beam and an optical probe beam both pass co-linearly through an electro-optic crystal such as zinc telluride; this crystal is generally favoured for electro-optic detection of THz pulses as it exhibits a strong electro-optic coefficient while also achieving a low velocity mismatch between the THz pulse and optical probe pulse, which allows the two pulses to propagate in the crystal together [45]. With accurate knowledge of the electro-optic coefficient on the crystal (e.g. zinc telluride) the

strength of the incident THz electric field can therefore be deduced. However, in the experiments performed here the absolute energy at the detector was not calculated, and instead all measurements are quoted in reference to normalisation scans taken through air. To assess the errors involved here I will aim to describe the experimental limitations of the relevant pieces of hardware which contribution to variations in the system.

Time Domain Step Size: The minimum step distance used determines the range of frequency features which are able to be calculated from the time domain data. As the mechanical delay stage oscillates data is continually collected and split into 1024 bins over a 50 ps range which gives a time step of 0.049 ps. The spatial resolution of the equipment quoted by the manufacturer is ± 4 fs which is one order of magnitude smaller than the bin size. By multiplying the bin size by the number of spatial points used in the Fourier transform and taking the reciprocal I obtain the step in frequency which is achieved which is 0.32 GHz. To put this number into perspective the width (FWHM) of the smallest resonance line measured is ~ 0.1 THz which would provide over 300 data points to plot the shape of the feature in the frequency domain, which is therefore more than adequate.

Laser Stability: By far the largest source of uncertainty in the THz TDS is the fluctuation of the Ti:Sapphire laser which has been measured in my group to vary by $\pm 5\%$ over a period of several minutes. This effect is especially a problem if an air reference is taken and then sample measurements are taken over a long period of time, as is the case here. To investigate this effect one should refer to Figure 3.16 in which the transmittance at 0.45 and 0.80 THz is plotted for the ring resonator configuration, where 0.45 THz corresponds to the resonant frequency of the plasmonic system, while 0.80 THz is far from the resonance, where it is expected that there should be negligible transmittance change in response to optical illumination. By analysing the average transmittance value off-resonance it is seen the average transmittance is 0.989 ± 0.013, as calculated by taking the mean of the 28 data points and the standard deviation. This analysis method can also be applied to the control experiment presented in Figure 3.18 which measures transmittance in an illuminated sample without graphene over a 100 minute period, collecting over 400,000 data points which reveals an average normalised transmittance value of 1.013 ± 0.023. Therefore I can set a lower limit on the transmittance value accuracy of ± 0.023, which is around one order of magnitude smaller than that of the changes measured via the optically induced effects.

Finite Element Analysis: Quantifying the errors associated in the fi-

nite element analysis would be a rather convoluted problem to address however it could be assumed that the most uncertain part of the process happens when the simulated results with varying graphene Fermi level are compared to the experimental results. The process was performed by overlaying the experimental and simulated transmittance spectra for a range of Fermi level values on the same graph and visually determining the best match, especially looking for matching spectra around the resonance frequencies. The Fermi level was swept in steps of 10 meV, where the inferred changes in the graphene were 20 meV for the $\hat{y}$ orientation and 30 meV for the $\hat{x}$ orientation. The inferring of the Fermi level values is therefore rather vague and the values should not be relied upon, however what can be clearly realised from the simulations is the direction of the Fermi level change.

3.5 Conclusion

In this chapter I have demonstrated non-volatile optical tuning of terahertz frequency transmittance through a metasurface device. The device consists of a metallic resonator array sandwiched between monolayer graphene and a photoresponsive Fe:$LiNbO_3$ substrate. By illuminating the device with a 462 nm laser the lithium niobate substrate undergoes a photorefractive effect in which electrons migrate within the crystal creating regions of non-uniform charge density. In response to these electrostatic fields created by the substrate the graphene will experience a modulation of charge carrier numbers which alters the graphene electrical conductivity and therefore alters the losses in the metasurface. The effect is capable of producing up to $\sim$35% relative transmittance changes in the device at the plasmonic resonance peak in an effect which is non-volatile yet reversible under thermal annealing. By simulating the device with a finite element method and matching experimental to simulated results I determine the photoresponsive substrate is capable of shifting the Fermi level of the graphene monolayer corresponding to a charge carrier injection of 8.2×10^{11} cm^{-2}, which corresponds to a resistivity decrease from 780 to 660 Ohms/sq.

To further investigate this effect it would be advantageous to incorporate an electrical topgate which could bring the graphene close to its Dirac point where the Fermi level is most sensitive to changes in carrier density. Further, by insulating the graphene with hexagonal boron nitride it may be possible to enhance the graphene mobility which could allow for sharper resonances and

therefore larger photoinduced changes to transmission spectra. The boron nitride encapsulation could also reduce degradation of the graphene by preventing atmospheric adsorption. Another route of investigation here would be to attempt optical erasure of photo-induced doping effects which could allow for faster operation of the device, taking the erasure time from hours down to minutes or even seconds if the power can be scaled sufficiently high.

Bibliography

[1] Markelz, A.; Roitberg, A.; Heilweil, E. Pulsed Terahertz Spectroscopy Of DNA, Bovine Serum Albumin And Collagen Between 0.1 And 2.0 THz. *Chemical Physics Letters* **2000**, *320*, 42 – 48.

[2] Ebbinghaus, S.; Kim, S. J.; Heyden, M.; Yu, X.; Heugen, U.; Gruebele, M.; Leitner, D. M.; Havenith, M. An Extended Dynamical Hydration Shell Around Proteins. *Proceedings of the National Academy of Sciences* **2007**, *104*, 20749–20752.

[3] Walther, M.; Fischer, B.; Schall, M.; Helm, H.; Jepsen, P. Far-Infrared Vibrational Spectra Of All-Trans, 9-Cis And 13-Cis Retinal Measured By THz Time-Domain Spectroscopy. *Chemical Physics Letters* **2000**, *332*, 389–395.

[4] Woodward, R. M.; Wallace, V. P.; Pye, R. J.; Cole, B. E.; Arnone, D. D.; Linfield, E. H.; Pepper, M. Terahertz Pulse Imaging of ex vivo Basal Cell Carcinoma. *Journal of Investigative Dermatology* **2003**, *120*, 72–78.

[5] Federici, J. F.; Schulkin, B.; Huang, F.; Gary, D.; Barat, R.; Oliveira, F.; Zimdars, D. THz Imaging And Sensing For Security Applications - Explosives, Weapons And Drugs. *Semiconductor Science and Technology* **2005**, *20*, S266–S280.

[6] Appleby, R.; Wallace, H. B. Standoff Detection of Weapons and Contraband in the 100 GHz to 1 THz Region. *IEEE Transactions on Antennas and Propagation* **2007**, *55*, 2944–2956.

[7] Chen, J.; Chen, Y.; Zhao, H.; Bastiaans, G. J.; Zhang, X.-C. Absorption Coefficients Of Selected Explosives And Related Compounds In The Range Of 0.1-2.8 THz. *Optics Express* **2007**, *15*, 12060.

[8] Wei, J.; Olaya, D.; Karasik, B. S.; Pereverzev, S. V.; Sergeev, A. V.; Gershenson, M. E. Ultrasensitive Hot-Electron Nanobolometers For Terahertz Astrophysics. *Nature Nanotechnology* **2008**, *3*, 496–500.

[9] Negrello, M. et al. The Detection Of A Population Of Submillimeter-Bright, Strongly Lensed Galaxies. *Science* **2010**, *330*, 800–804.

[10] Nagai, N.; Sumitomo, M.; Imaizumi, M.; Fukasawa, R. Characterization Of Electron- Or Proton-Irradiated Si Space Solar Cells By Thz Spectroscopy. *Semiconductor Science and Technology* **2006**, *21*, 201–209.

[11] Ahi, K.; Shahbazmohamadi, S.; Asadizanjani, N. Quality Control And Authentication Of Packaged Integrated Circuits Using Enhanced-Spatial-Resolution Terahertz Time-Domain Spectroscopy And Imaging. *Optics and Lasers in Engineering* **2018**, *104*, 274–284.

[12] Jornet, J. M.; Akyildiz, I. F. Graphene-Based Plasmonic Nano-Antenna For Terahertz Band Communication In Nanonetworks. *IEEE Journal on Selected Areas in Communications* **2013**, *31*, 685–694.

[13] Seeds, A. J.; Shams, H.; Fice, M. J.; Renaud, C. C. TeraHertz Photonics for Wireless Communications. *Journal of Lightwave Technology* **2015**, *33*, 579–587.

[14] Alius, H.; Dodel, G. Amplitude-Modulation, Phase-Modulation, And Frequency-Modulation Of Far-Infrared Radiation By Optical-Excitation Of Silicon. *Infrared Physics* **1991**, *32*, 1–11.

[15] Vogel, T.; Dodel, G.; Holzhauer, E.; Salzmann, H.; Theurer, A. High-Speed Switching Of Far-Infrared Radiation By Photoionization In A Semiconductor. *Applied Optics* **1992**, *31*, 329–337.

[16] Nozokido, T.; Minamide, H.; Mizuno, K. Modulation Of Submillimeter Wave Radiation By Laser-Produced Free Carriers In Semiconductors. *Electronics and Communications in Japan Part II-Electronics* **1997**, *80*, 1–9.

[17] Rivas, J. G.; Kuttge, M.; Kurz, H.; Bolivar, P. H.; Sánchez-Gil, J. A. Low-Frequency Active Surface Plasmon Optics On Semiconductors. *Applied Physics Letters* **2006**, *88*, 082106.

[18] Han, J.; Lakhtakia, A. Semiconductor Split-Ring Resonators For Thermally Tunable Terahertz Metamaterials. *Journal of Modern Optics* **2009**, *56*, 554–557.

[19] Chen, H.-T.; Padilla, W. J.; Cich, M. J.; Azad, A. K.; Averitt, R. D.; Taylor, A. J. A Metamaterial Solid-State Terahertz Phase Modulator. *Nature Photonics* **2009**, *3*, 148–151.

[20] Kleine-Ostmann, T.; Dawson, P.; Pierz, K.; Hein, G.; Koch, M. Room-Temperature Operation Of An Electrically Driven Terahertz Modulator. *Applied Physics Letters* **2004**, *84*, 3555–3557.

[21] Chen, H.-T.; Padilla, W. J.; Zide, J. M. O.; Gossard, A. C.; Taylor, A. J.; Averitt, R. D. Active Terahertz Metamaterial Devices. *Nature* **2006**, *444*, 597–600.

[22] Han, Z.; Kohno, K.; Fujita, H.; Hirakawa, K.; Toshiyoshi, H. MEMs Reconfigurable Metamaterial For Terahertz Switchable Filter And Modulator. *Optics Express* **2014**, *22*, 21326.

[23] Tao, H.; Strikwerda, A. C.; Fan, K.; Padilla, W. J.; Zhang, X.; Averitt, R. D. Reconfigurable Terahertz Metamaterials. *Physical Review Letters* **2009**, *103*, 147401.

[24] Busch, S.; Scherger, B.; Scheller, M.; Koch, M. Optically Controlled Terahertz Beam Steering And Imaging. *Optics Letters* **2012**, *37*, 1391–1393.

[25] Okada, T.; Tanaka, K. Photo-Designed Terahertz Devices. *Scientific Reports* **2011**, *1*, 5.

[26] Weis, P.; Garcia-Pomar, J. L.; Höh, M.; Reinhard, B.; Brodyanski, A.; Rahm, M. Spectrally Wide-Band Terahertz Wave Modulator Based on Optically Tuned Graphene. *ACS Nano* **2012**, *6*, 9118–9124.

[27] Chen, S.; Fan, F.; Miao, Y.; He, X.; Zhang, K.; Chang, S. Ultrasensitive Terahertz Modulation By Silicon-Grown MoS_2 Nanosheets. *Nanoscale* **2016**, *8*, 4713–4719.

[28] Padilla, W. J.; Taylor, A. J.; Highstrete, C.; Lee, M.; Averitt, R. D. Dynamical Electric And Magnetic Metamaterial Response At Terahertz Frequencies. *Physical Review Letters* **2006**, *96*, 107401.

[29] Manceau, J. M.; Shen, N. H.; Kafesaki, M.; Soukoulis, C. M.; Tzortzakis, S. Dynamic Response Of Metamaterials In The Terahertz Regime: Blueshift Tunability And Broadband Phase Modulation. *Applied Physics Letters* **2010**, *96*, 021111.

[30] Chowdhury, D. R.; Singh, R.; O'Hara, J. F.; Chen, H. T.; Taylor, A. J.; Azad, A. K. Dynamically Reconfigurable Terahertz Metamaterial Through Photo-Doped Semiconductor. *Applied Physics Letters* **2011**, *99*, 231101.

[31] Chen, H. T.; O'Hara, J. F.; Azad, A. K.; Taylor, A. J.; Averitt, R. D.; Shrekenhamer, D. B.; Padilla, W. J. Experimental Demonstration Of Frequency-Agile Terahertz Metamaterials. *Nature Photonics* **2008**, *2*, 295–298.

[32] Gu, J. Q.; Singh, R.; Liu, X. J.; Zhang, X. Q.; Ma, Y. F.; Zhang, S.; Maier, S. A.; Tian, Z.; Azad, A. K.; Chen, H. T.; Taylor, A. J.; Han, J. G.; Zhang, W. L. Active Control Of Electromagnetically Induced Transparency Analogue In Terahertz Metamaterials. *Nature Communications* **2012**, *3*, 6.

[33] Hendry, E.; Lockyear, M. J.; Rivas, J. G.; Kuipers, L.; Bonn, M. Ultrafast Optical Switching Of The Thz Transmission Through Metallic Subwavelength Hole Arrays. *Physical Review B* **2007**, *75*, 235305.

[34] Janke, C.; Rivas, J. G.; Bolivar, P. H.; Kurz, H. All-Optical Switching Of The Transmission Of Electromagnetic Radiation Through Subwavelength Apertures. *Optics Letters* **2005**, *30*, 2357–2359.

[35] Chen, H. T.; Padilla, W. J.; Zide, J. M. O.; Bank, S. R.; Gossard, A. C.; Taylor, A. J.; Averitt, R. D. Ultrafast Optical Switching Of Terahertz Metamaterials Fabricated On ErAs/GaAs Nanoisland Superlattices. *Optics Letters* **2007**, *32*, 1620–1622.

[36] Zheng, W.; Fan, F.; Chen, M.; Chen, S.; Chang, S. J. Optically Pumped Terahertz Wave Modulation In MoS_2-Si Heterostructure Metasurface. *AIP Advances* **2016**, *6*, 075105.

[37] Arezoomandan, S.; Gopalan, P.; Tian, K.; Chanana, A.; Nahata, A.; Tiwari, A.; Sensale-Rodriguez, B. Tunable Terahertz Metamaterials Employing Layered 2-D Materials Beyond Graphene. *Ieee Journal of Selected Topics in Quantum Electronics* **2017**, *23*, 7.

[38] Wang, Q.; Rogers, E. T.; Gholipour, B.; Wang, C.-M.; Yuan, G.; Teng, J.; Zheludev, N. I. Optically Reconfigurable Metasurfaces And

Photonic Devices Based On Phase Change Materials. *Nature Photonics* **2016**, *10*, 60–65.

[39] Gholipour, B.; Zhang, J.; MacDonald, K. F.; Hewak, D. W.; Zheludev, N. I. An All-Optical, Non-volatile, Bidirectional, Phase-Change Meta-Switch. *Advanced Materials* **2013**, *25*, 3050–3054.

[40] Palik, E. D. *Handbook of Optical Constants of Solids*; Academic Press, 1997.

[41] Jabbarzadeh, F.; Heydari, M.; Habibzadeh-Sharif, A. A Comparative Analysis Of The Accuracy Of Kubo Formulations For Graphene Plasmonics. *Materials Research Express* **2019**, *6*, 086209.

[42] Blundell, S.; Gorecki, J.; Papasimakis, N.; Mailis, S.; Apostolopoulos, V. THz Spectroscopy of Photogenerated Carriers in Fe:$LiNbO_3$ for Optical Control of 2D Materials. *2019 Conference on Lasers and Electro-Optics Europe & European Quantum Electronics Conference (CLEO/Europe-EQEC)* **2019**,

[43] Auston, D.; Nuss, M. Electrooptical generation and detection of femtosecond electrical transients. *IEEE Journal of Quantum Electronics* **1988**, *24*, 184–197.

[44] Sitnikov, D. S.; Romashevskiy, S. A.; Ovchinnikov, A. V.; Chefonov, O. V.; Savel'ev, A. B.; Agranat, M. B. Estimation of THz field strength by an electro-optic sampling technique using arbitrary long gating pulses. *Laser Physics Letters* **2019**, *16*, 115302.

[45] Dexheimer, S. L., Ed. *Terahertz Spectroscopy*; CRC Press, Chapter 2, Page 57, 2017.

Chapter 4

Optically Defined Graphene Plasmonics

4.1 Introduction

Graphene plasmonic devices show great potential for a wide range of applications where the inherent ultra-high mobility values [1], extreme plasmon confinement [2, 3], and tuneable Fermi level [4] render graphene to be a highly adaptive platform for plasmonic resonance devices [5]. The dependency of plasmonic resonance frequency on Fermi level can be derived from a Drude model, where due to the massless nature of the charge carriers the plasma frequency depends not on the effective mass but instead on the Fermi level, and has been shown to be tuned by controlling the Fermi level through gating the graphene [6]. Due to high mobility values of graphene plasmonic resonances can reach into terahertz frequencies [6] and beyond into infra-red [7, 8] frequencies.

Graphene plasmonic device with patterning of the graphene have been fairly well investigated and demonstrate some degree of tuning, however such devices are not truly reconfigurable as they rely on permanent structuring of the graphene into resonator geometries. On the road towards reconfigurable devices there have been several theoretical investigations which suggest that continuous graphene sheets with periodic carrier density modulation are capable of sustaining plasmonic resonances however there are limited platforms to achieve such doping profiles in a reconfigurable fashion.

Here I propose that graphene on photorefractive lithium niobate could act as the necessary modulation method by optically defining charge distributions within the lithium niobate to spatially modulate graphene carrier density. If such a device can be realised experimentally it would enable resonator geometries to be patterned simply by structured optical illumination of the device, creating non-volatile doping of the graphene which could be reversed by uniform illumination of the substrate, allowing resonator structures to be created and redefined at will.

4.2 Graphene Plasmonics

There are generally two paths taken when employing plasmonic resonances in graphene, where the graphene can be patterned into a structure such as a ribbon or split ring to sustain a plasmonic resonance [6], or the less explored case where a continuous graphene layer can be periodically doped in order to sustain a resonance mode. The first route mentioned has been

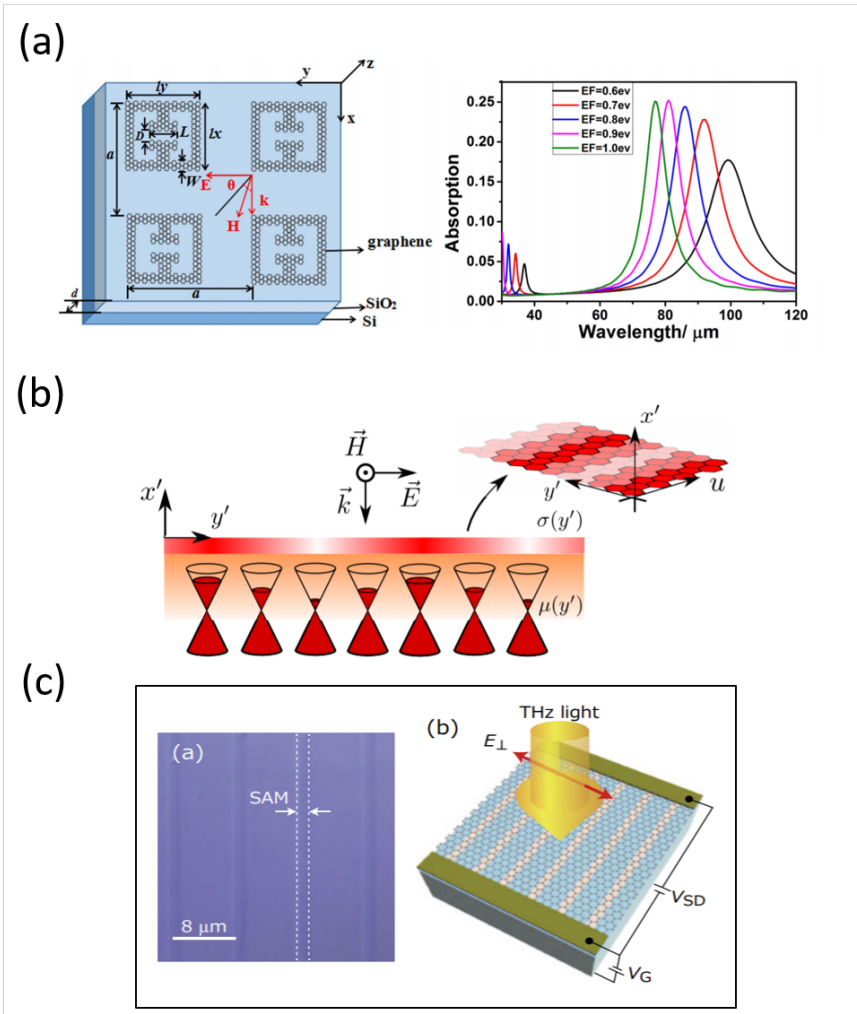

Figure 4.1: ***(a)*** *Tuneable resonance frequency in patterned graphene structure through electrostatic back-grating with Si/SiO_2 substrate allows for gate dependent shifting of resonance frequency and strength [9].* ***(b)*** *Periodic variation in graphene Fermi level shown via simulations to create ribbon resonator type structure to sustain plasmonic resonances [10].* ***(c)*** *Graphene plasmonics by spatially selective gating by patterning organic gate to periodic ribbon structures. By application of the electric back-gate the plasmonic resonance can be switched "on" or "off" by switching between periodic and uniform Fermi level pattern in the graphene with the back-gate [11].*

demonstrated for; graphene ribbons on top of a silicon on insulator substrate to tune the plasmonic resonance absorption strength and frequency by gating the graphene with an ionic gel [6]; by chemical doping of graphene patterned into disk arrays [12], and for graphene patterned into split ring resonators [9, 13, 14, 15] (see Figure 4.1a).

The less explored second route towards graphene plasmonics utilises periodic variations in the Fermi level of a continuous graphene sheet to confine resonance modes. A theoretical analysis of graphene with a periodic variation in Fermi level has been presented for ribbons [10] (see Figure 4.1b) and disks [16] in which it is shown by patterning graphene with a suitable Fermi level geometry that plasmonic resonances can indeed be sustained at terahertz frequencies. However, the question from this research remains as to how such a periodic Fermi level contrast can be realised practically. One route suggested is to deposit graphene on trenched silicon substrates which introduce Fermi level variations which were shown to create wave guiding conditions [17]. Another approach is based on graphene sandwiched between two periodically poled ferroelectric substrates, which is shown via simulations to create a ribbon type structured Fermi level profile within the graphene due to electrostatic interactions with the substrates which is capable of sustaining plasmonic resonances [18]. Such doping techniques have been demonstrated experimentally on lithium niobate, where spatially resolved Raman spectroscopy was used to show a periodic Fermi level shift in graphene on poled lithium niobate [19] however plasmonic resonances were not investigated. Recently there have been demonstrations of terahertz frequency plasmonics in devices consisting of a graphene layer on top of transparent metal oxide or organic gates by Tu et. al in 2018 [11] (Figure 4.1c) and 2020 [20]. The gates are patterned into ribbons with periods of several microns which allow for spatial control of the graphene electronic properties. The authors mention that the use of metal oxide or organic gates allows for high transmission of terahertz radiation, while also minimising coupling between the graphene plasmon and the gate.

It should be noted here that such structures (graphene on trenched silicon, periodically poled lithium niobate, or metal oxide gates), while being able to induce Fermi level profiles in graphene, are not reconfigurable as the fabrication is permanent. Despite the clear advantages of such reconfigurable platforms, the art of tuning graphene Fermi level in a spatially defined yet adaptive and non-volatile manner is still in its infancy. Here I address this matter by investigating whether photorefractive charge distributions within

lithium niobate are suitable to create periodic tuning of a graphene layer to sustain plasmonic resonances. The lithium niobate is an attractive substrate for this application due to the spatially resolved micron scale charge distributions which can be imprinted on the crystal in response to optical illumination in a non-volatile yet optically rewritable fashion [21, 22], which I have been shown to be able to optically tune the electronic properties of graphene [23].

4.3 Routes of Investigation

I provide four routes of investigation via simulations, where for the discrete case I consider graphene patterned with two Fermi level values (high and low E_F), while for the continuous case I calculate the continuously varying Fermi level profile of graphene induced by space charge densities in the substrate. An example of the Fermi level profiles is depicted in Figure 4.2.

- Discrete 1D E_F Profile (Ribbon)
- Discrete 2D E_F Profile (Split Ring)
- Continuous 1D E_F Profile (Ribbon)
- Continuous 2D E_F Profile (Split Ring)

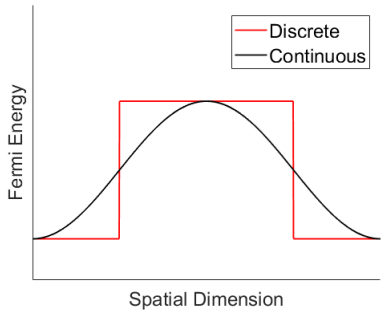

Figure 4.2: *Example of discrete and continuous Fermi level profiles for a ribbon structure.*

The results presented in this chapter were produced in close collaboration with Adnane Noual, who has provided the simulations of the electrostatic

environments in lithium niobate to determine the Fermi level profiles created in graphene layers. From these Fermi level profiles I have investigated the plasmonic resonances of the system which can be achieved.

4.4 Parameter Space

Here I outline the various parameters which are available to play with in the search for plasmonic devices (Figure 4.3), and discuss practical limitations to the available parameter values.

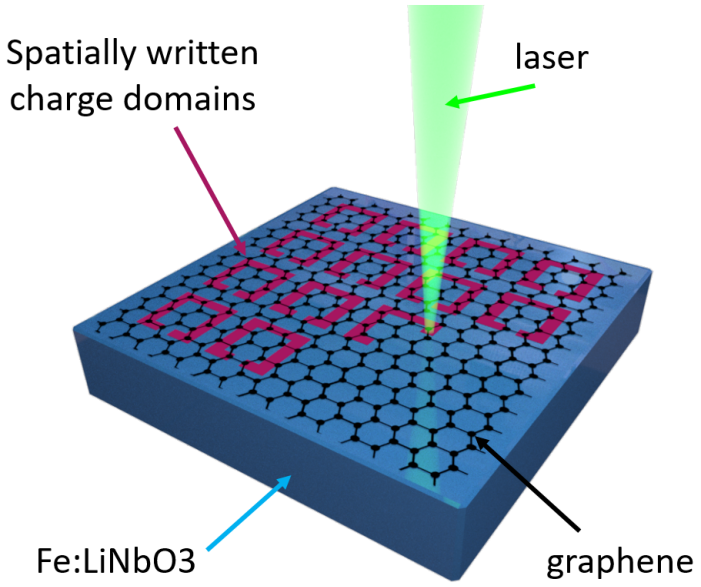

Figure 4.3: *Schematic of plasmonic device consisting of monolayer graphene on Fe:$LiNbO_3$ substrate. In response to structured illumination (depicted here as laser writing) the photorefractive effect in lithium niobate will create non-uniform charge distributions which will electrostatically dope the graphene. By creating structures of high/low conductivity graphene it is possible to confine plasmonic resonances in the graphene.*

Device Size: One of the first limitations on the device comes from the size requirements; due to the large wavelength of THz frequencies the minimum active area of the device should be on the scale of several square millime-

ters going up to several tens of square centimeters. This limitation requires the use of CVD graphene which can reach several tens of centimeters square even up to square meters [24]. For comparison exfoilated graphene single crystals are on the order of several microns in diameter [4].

Grating Periodicity: Due to the optical nature of the photorefractive effect there is a lower size limitation on the period of the optical grating as it is not possible to structure the illumination pattern at scales smaller than the wavelength of the illumination source. The photorefractive effect is responsive in the visible blue/green region of the spectrum [25], and with the use of a 462 nm laser source it would be difficult to resolve features below 1 micron. At length scales of a few microns it is believed that diffusion is the main driving force for electron migration, however as the length scales increase the drift mechanism tends to dominate [26], which has been demonstrated to create surface charges over large areas of square centimeters and is believed to not have an upper limit on the length scale of the illuminated area [27].

Mobility: The mobility of the graphene is an important consideration as the time period of THz radiation is relatively large (picoseconds) the mobility of the graphene must be high enough to sustain coherent electron motion over such timescales. The largest mobility values in graphene can be obtained by suspended single crystal exfoliated sheets [1], however this is not particularly practical for a large area device. There are currently many advances in CVD graphene production methods however for commercially available large area CVD films purchased from Graphenea the stated mobility values are somewhere in the region of 2,000 - 4,000 cm^2/Vs on SiO_2/Si, and increased to around 7,000 cm^2/Vs on aluminium oxide. This is generally in-line with reported values of CVD graphene mobility [28, 29], however can be increased to many tens of thousands by encapsulation with hexagonal boron nitride monolayers [30].

Fermi level: Based on the experimental findings in Chapter 2 I showed the photorefractive effect in lithium niobate could alter the charge carrier density by ~ 5.5 x10^{12} cm^{-2} which equated to a Fermi level change of 0.3 eV in graphene.

Photorefractive Charge Density: To gauge the electrostatic behaviour of lithium niobate I look to the reported large electric fields ranging from several tens up to hundred of kV/cm [31, 27, 32, 33], which equate to surface charge densities in the range from 10^{-3} up to 10^{-2} C/m^2. In my simulations I utilise a volume charge density to represent the photorefractive effect in

lithium niobate, where the required surface charge density range is achieved with volume densities of in the range of hundreds up to a few thousand C/m^3. Indeed, the charge carrier migration lengths in doped lithium niobate can be shown to determine the magnitude of the photorefractive charge densities which correspond to the above quoted values [34, 35].

4.5 Discrete 1D E_F Profile

In this section I create a simple starting point for this investigation where the graphene Fermi level distribution is considered as a discrete variation, defined as regions of high and low Fermi level. From Chapter 3.5.3 I estimated that the photorefractive doping effect in graphene had created a 0.3 eV shift in the Fermi level, and therefore in this section I investigate whether this Fermi level shift is capable of creating structures to sustain plasmonic modes. I begin here with a 2D simulation to investigate ribbon type structures.

4.5.1 Methods for discrete 1D E_F Profile

A finite element analysis method is used (Comsol) to investigate the electromagnetic response of the system. The 2D unit cell show in Figure 4.4(a) shows an air slab of width w (taken as 50 μm) with depth 300 μm on top of a lithium niobate slab of depth 200 μm. At the air / lithium niobate interface is a graphene monolayer modelled as a transition boundary. The graphene is split into 3 sections consisting of a region of high conductivity graphene in the centre of width 25 μm with Fermi level E_{F1} surrounded by graphene at low conductivity with Fermi level E_{F2}. It should be noted here that a transition boundary is used in order to negate the meshing of a 2 dimensional thin layer of graphene which would heavily increase the computational time. In order to justify this choice I have compared the two methods and found they both converge to provide a negligible difference in electromagnetic interaction, however the transition boundary is far quicker to solve.

The lithium niobate slab is modelled with frequency dependent values of complex refractive index which I have measured via THz TDS, where these values are presented in Appendix B. The graphene conductivity (σ) and scattering time (τ) are calculated from the Kubo formulations [36] in Equations 4.1 and 4.2 respectively,

$$\sigma = \frac{ie^2 E_F}{t\pi\hbar^2(\omega + i/\tau)} \tag{4.1}$$

$$\tau = \frac{E_F \mu}{e v_F^2} \tag{4.2}$$

where e is the electron charge; t is the graphene thickness (1 nm), ω is the radial frequency, μ is the graphene charge carrier mobility, and v_F is the Fermi velocity (10^8 cm/s).

4.5.2 Results of Discrete 1D E_F Profile

The transmission spectra in Figure 4.4(b) show THz transmission where E_{F2} is held at 0.01 eV, which corresponds to low conductivity graphene, while E_{F1} is varied up to 0.3 eV. The mobility is held constant at 10,000 cm^2/Vs. The results show that initially when E_{F1} is at low conductivity there is near complete transmission however as E_{F1} is increased there appears to be the presence of a transmission dip centered around 0.3 - 0.4 THz which grows in strength as E_{F1} is increased, reaching a maximum absorption of 7 %. Further, as E_{F1} is increased the resonance peak appears to blue-shift towards higher frequencies.

To confirm the presence of the fundamental resonance mode I plot the magnetic and electric fields at a plane 5 microns above the graphene layer in Figure 4.4(c). The absolute magnetic field out of plane shows a bell shaped curve with a maximum located at the centre of the ribbon (0 $\mu m\ \hat{x}$) which decays further from the centre. The absolute magnetic field can be interpreted as an indication of the electric current strength, as the moving electric charges will create a magnetic field in the direction perpendicular to the direction of current flow. I also plot the real part of the electric field in the vertical direction which can be interpreted as an indicator of the charge density, where high densities of charge will radiate electric field lines in the vertical direction. From the electric field we can interpret that at the ends of the resonator strip (at $\pm 12.5\ \mu m$) there is a large localisation of charges of opposite magnitude, which will create an electric potential difference between these two points (at $\pm 12.5\ \mu m$) which drives the electric current. Both the magnetic and electric fields presented here are consistent with the fundamental resonance mode.

In Figure 4.4 (d) the mobility of the graphene is investigated to find the optimum parameters for plasmonic resonance strength. Here the graphene Fermi energies are set to $E_{F1} = 0.3$ eV, and $E_{F2} = 0.01$ eV. The mobility is varied from 1,000 to 50,000 cm^2/Vs. A color map is presented in Figure 4.4(d) where the color bar represents the transmission value as a fraction (normalised to transmission through air/lithium niobate). From this color map we see that initially at low mobility values there is no noticeable plasmonic effect however even with modest mobility values of 4,000 cm^2/Vs the

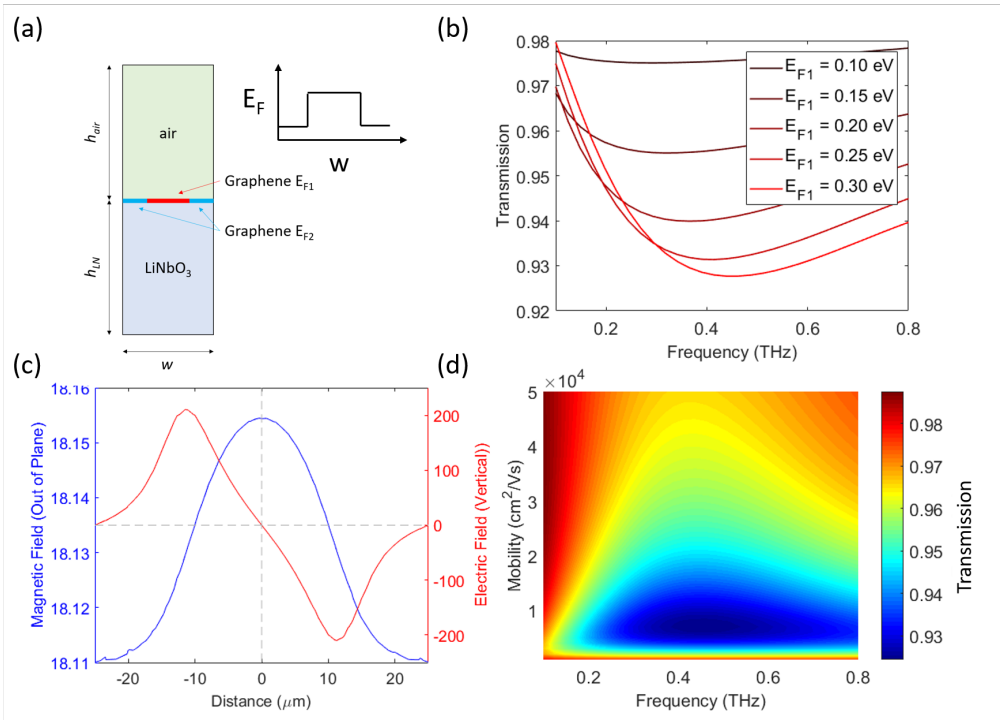

Figure 4.4: ***(a)*** *Schematic of unit cell consisting of air and lithium niobate slab, with graphene transition boundary at material interface.* ***(b)*** *Transmission spectra varying E_{F1} with E_{F2} held at 0.01 eV.* ***(c)*** *Magnetic field (out of plane) and electric field (vertical) plotted at a plane 5 microns above the graphene layer.* ***(d)*** *Transmission spectra with E_{F1} and E_{F2} at 0.3 and 0.01 eV respectively with varying mobility, where color scale corresponds to fractional transmission.*

plasmonic effect becomes noticeable. The resonance strength grows as the mobility is increased up to 7,000 cm^2/Vs, however this appears to be a tipping point, at which the resonance strength reverses trend and begins to diminish again as mobility is increased.

4.5.3 Discussion of Discrete 1D E_F Profile

In this section I have demonstrated that a 1D structure of graphene with a discrete variation in Fermi level is capable of sustaining plasmonic resonances at terahertz frequencies with a ribbon type resonator structure.

The length of the ribbon resonator here is set to 25 microns inside a 50 micron wide unit cell which results in a resonance peak around 0.4 THz which provides a useful starting point for the next section in indicating the perimeter length that I should use for a split ring resonator. The length of 25 microns is easy to access optically in a 1D grating structure, however to create a similar size split ring structure in 2 dimensions may encounter issues as the side length of 6 microns will be near the optical resolution limit which would likely be achieved by a spatial light modulator with a blue laser. It of course would be possible to scale up the geometry size of a resonator in which case the resonance peak frequency should decrease, however from practical considerations it would be beneficial for the resonance peak to stay within 0.1 to 1.0 THz as this is the frequency range which allows for strong transmission of terahertz frequency radiation through the lithium niobate substrate.

This section has investigated the effects of varying carrier mobility, where a 'sweet-spot' is found around 7,000 cm^2/Vs. It may appear slightly unexpected that as the graphene mobility is further increased the plasmonic resonance strength decreases, however this effect could be caused by the increased losses which the system will likely incur at high mobilities, which will dampen the plasmonic mode. In any case, this parameter window is rather fortunate as it sits in line with the typical mobility values which can be expected from large area CVD graphene which are typically from 1,000 to 10,000 cm^2/Vs.

4.6 Discrete 2D E_F Profile

In this section I extend the concept of a discrete 1D variation in graphene Fermi level into a discrete 2D geometry to create a split ring resonator. I show that it is again possible to create structures sustaining plasmonic resonances in the split ring resonator configuration, however the resonance strength appears to be severely diminished here as compared to the ribbon structure.

4.6.1 Methods for Discrete 2D E_F Profile

A 3D Comsol model is used to investigate the split ring resonator structures. Unless otherwise stated here, the modelling methods used are identical to those mentioned in the previous section. A top view of the unit cell is provided in Figure 4.5(a) where a unit cell of width w (15 μm) is covered with graphene. A split ring resonator geometry (shown in blue) defined with high conductivity graphene (E_{F1} = 0.3 eV) is surrounded by low conductivity graphene (shown in green) with Fermi level E_{F2} = 0.01 eV. The mobility is set to 7,000 cm^2/Vs as this was determined in the previous section to provide the strongest resonance peak. The outer resonator width (a) is set to 10 microns, with the inner width (b) set to 6 microns. The model is solved in two orientations (as depicted by the $\hat{x}$ and $\hat{y}$ arrows) where the THz electric field polarised along the $\hat{x}$ direction corresponds to a split ring resonator configuration, while the THz electric field polarised along the $\hat{y}$ direction corresponds to a ring resonator configuration.

4.6.2 Results of Discrete 2D E_F Profile

Figure 4.5(b) shows the transmission spectra measured in two orientations which correspond to the split ring and ring resonator configurations. It can be seen that both orientations display a resonance dip between 0.4 - 0.5 THz. For the split ring resonator the resonance peak is centered around 0.5 THz while for the ring resonator the resonance peak is red-shifted to 0.4 THz. Both resonance peaks observed here a fairly weak in strength, for the split ring resonator strength reaches nearly 2 % while for the ring resonator this is increased to 3 %.

To investigate the mode profiles of the resonances for the split ring I plot the real part of the electric field in the vertical direction ($\hat{z}$) in Figure 4.5(c)

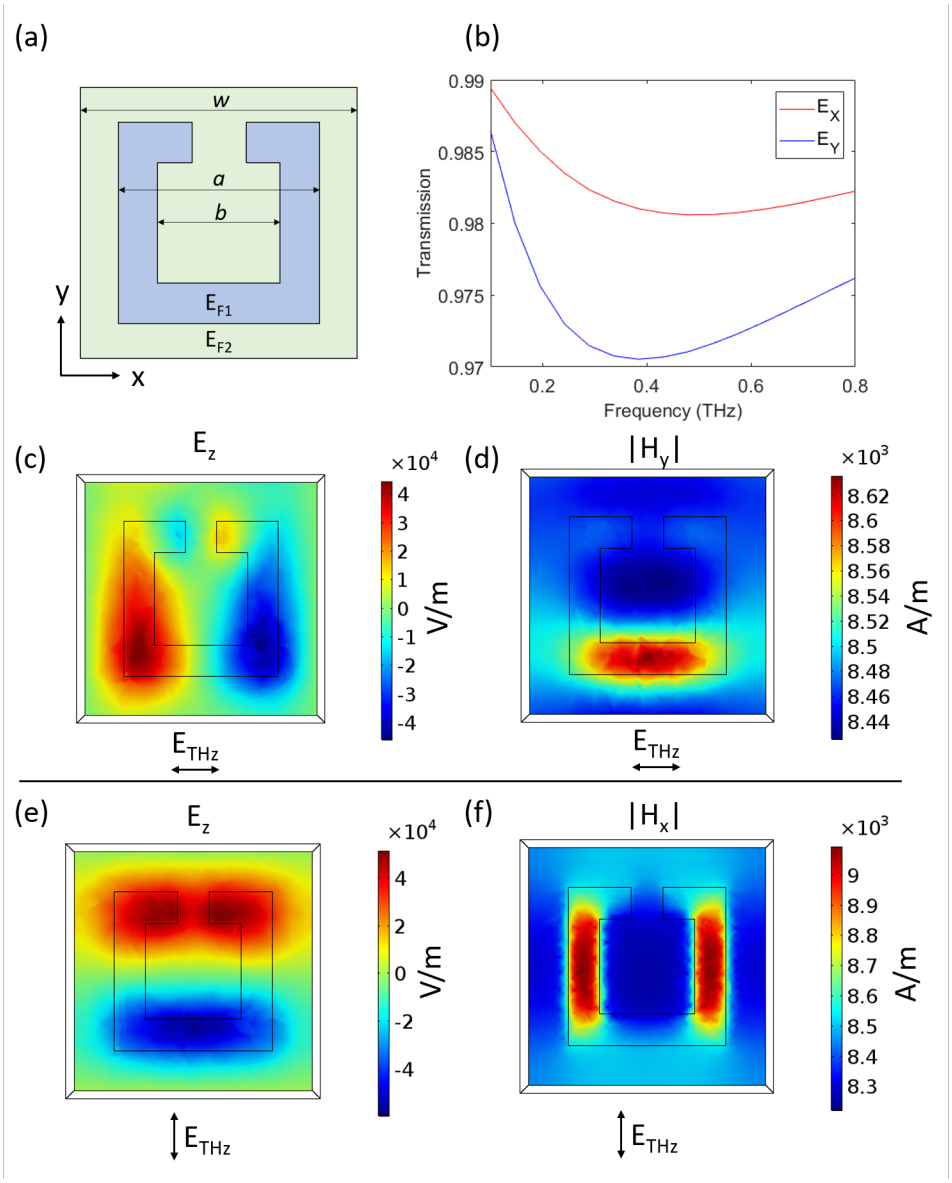

Figure 4.5: ***(a)*** *Schematic top view of unit cell.* ***(b)*** *Transmission spectra for incident THz wave polarised in $\hat{x}$ (split ring) and $\hat{y}$ (ring) orientations.* ***(c)*** *Electric field at 0.5 THz for $E_{THz} = \hat{x}$.* ***(d)*** *Magnetic field at 0.5 THz for $E_{THz} = \hat{x}$.* ***(e)*** *Electric field at 0.4 THz for $E_{THz} = \hat{y}$.* ***(f)*** *Magnetic field at 0.4 THz for $E_{THz} = \hat{y}$.*

and the absolute part of the magnetic field in the $\hat{y}$ direction in Figure 4.5(d). From the electric field profile we see two localised lobes of electric field with opposite magnitude at each side of the ring resonator, which corresponds to regions of high charge density. Due to the opposite magnitude of the charge density regions this will create an electric potential across the lower strip of the resonator which would drive a current along the path of electric potential. The magnetic fields confirm this behaviour, where a region of strong magnetic field along the lower strip of the resonator can be seen, which corresponds to a region of electric current moving the in $\hat{x}$ direction.

Figures 4.5(e & f) present mode profiles for the structure excited in the ring resonator configuration (E_{THz} in the $\hat{y}$ direction) at 0.4 THz, where Figures 4.5(e) plots the electric field in the vertical direction ($\hat{z}$) and Figures 4.5(f) plots the magnetic field in the $\hat{x}$ direction. From the electric field plots it can be seen there is a positively charged electric field region along the top of the resonator, with a mirror image of negatively charged charge region at the bottom of the resonator. These two oppositely charge regions will create an electric potential between them which will drive an electric current along the path of electric potential. This view is confirmed by the magnetic field plot which shows two regions of strong magnetic field along each of the side arms of the resonator structure, where magnetic field in the $\hat{x}$ direction corresponds to electric currents along the $\hat{y}$ direction. From the plots of electric and magnetic field it can therefore be concluded that regions of oppositely charged electric potential at the top and bottom of the structure drive electric currents along the side arms of the resonator along the $\hat{y}$ direction.

4.6.3 Discussion of Discrete 2D E_F Profile

This section has demonstrated that by patterning a 2D surface of graphene with a discrete variation in Fermi level a spilt ring resonator structure can be designed which sustains plasmonic resonances at terahertz frequencies. The response of the system is probed at two orientations of incident terahertz electric field, corresponding to a ring and split ring resonator geometry.

The transmission spectra have shown the presence of two resonance peaks in the region of 0.4 to 0.5 THz (one for the ring, and one for the split ring resonator). The strength of both these peaks in fairly weak, reaching only a few percent in absorption. In comparison the 1D discrete structure reached 7 % absorption, however in this section there was no optimisation performed

with the graphene mobility which may provide further improvements to the response of the system.

By assessing the field maps of the electric and magnetic fields at a plane 5 microns above the surface of the graphene it can be concluded that the split ring resonator is sustaining the fundamental resonance mode with a region of high current density located at the bottom arm of the ring, while for the ring resonator configuration we see two symmetric regions of high current density on each of the side arms of the structure.

The Fermi level profiles presented here are fairly simplistic in their view of a discrete variation in Fermi level, as in reality one would expect a gradual change in Fermi level instead of a step function. Nevertheless, from this simple starting point I have gained useful information on the parameter space in which plasmonic resonances may be sustained. In the next section I assess the more realistic case of smooth spatially varying carrier densities in graphene created in response to volume charge densities in lithium niobate.

4.7 Continuous 1D E_F Profile

In this section I move beyond discrete variations in graphene Fermi level, and instead calculate a spatially varying Fermi level profile by modelling the surface charge density on lithium niobate which can be achieved by creating volume charge densities in the substrate. I utilise a 2D model to investigate a ribbon resonator structure, which reveals a fundamental plasmonic resonance mode around 0.3 THz. Further, I investigate the effects of mobility and unit cell size on the resonance peak, and a discussion of the various results.

4.7.1 Methods for Continuous 1D E_F Profile

To determine the surface charge profiles created in lithium niobate due to the photorefractive effect an electrostatic simulation is used. The model assumes that lithium niobate is capable of producing volume charge densities of several kC/m^3 in response to non-uniform optical illumination. A schematic diagram of the 2D Comsol model is presented in Figure 4.6(a) which shows a unit cell of 50 micron width. At the top of the unit cell is a slab of air, with an incoming port bounding the top surface. Below is a slab of lithium niobate cut into two sections, where the left section is given a volume charge density of $+\rho$ while the right hand side of the slab is given a volume charge density of $-\rho$. The bottom surface of the lithium niobate is grounded. The electrostatics module in Comsol is solved to obtain the charge density at the top surface of the lithium nioabate.

Charge Density Profile of Continuous 1D E_F Profile

The charge density profile calculated in Comsol at the top surface of the lithium niobate is converted into an electron number density per cm^2 in order to determine the number of electrons which will be injected into the graphene sheet in response to the electrostatic interaction with the substrate (assuming a one to one correlation). Figure 4.6(b) presents the number of carriers injected into the graphene as a function of spatial dimension $\hat{x}$ along the 50 micron wide unit cell for several values of volume charge density ρ. It can be seen the carrier density displays a sinusoidal profile across the $\hat{x}$ dimension, and that by increasing the value of ρ the magnitude of the sinusoidal profile can be increased. In the inset figure in the top left the magnitude of the sinusoidal profile (Δn) is plotted against ρ revealing a

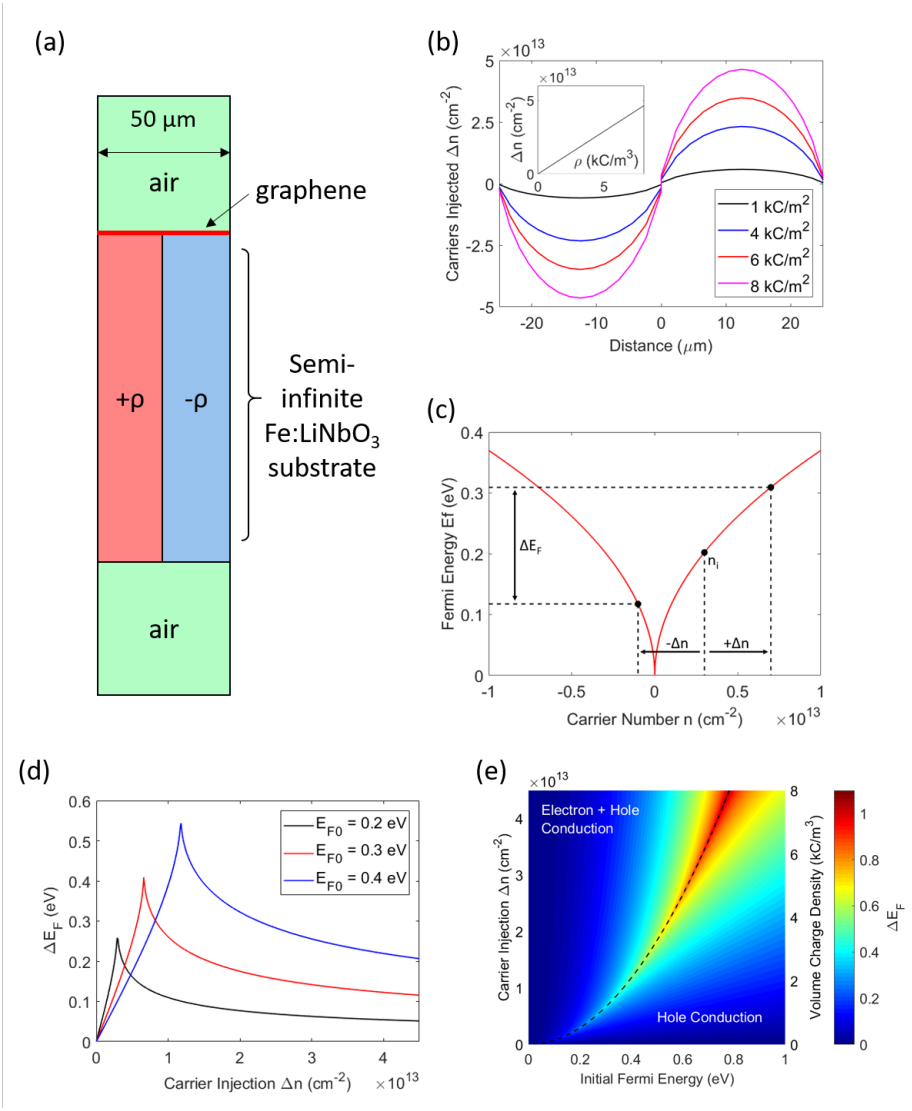

Figure 4.6: *(a) Schematic of 2D unit cell, consisting of air slab followed by lithium niobate split into two regions of positive and negative space charge density. A graphene monolayer covers the top surface of the lithium niobate. (b) Spatially varying induced carrier density change in graphene sheet. (c) Relation of Fermi level to carrier density. (d) Fermi level change as a function of carrier density. (e) Color map of Fermi level changes.*

linear relation, where a volume charge density of several kC/m^3 is capable of injecting $\sim 10^{13}$/cm^2 carriers, which for graphene constitutes a significant carrier injection.

Fermi level from Carrier Numbers of continuous 1D E_F Profile

Figure 4.6(c) presents an example graph showing the relation of Fermi level to charge carrier numbers, where the Fermi level has a minimum value at zero carriers and increases sub-linearly with increasing absolute number of carriers (either electrons or holes). Typical values of Fermi level and carrier densities for graphene are energies up to 1.0 eV, and carrier densities up to 10^{13}/cm^2. The graph shows the example of a graphene sheet starting with n carriers which experiences an injection/ejection of Δn carriers, which results in the creation of two new Fermi level values. The difference in Fermi level values is termed ΔE_F.

Fermi level Line Profiles of Continuous 1D E_F Profile

Figure 4.6(d) presents the Fermi level differences (ΔE_F) plotted against carrier injection number which can be achieved for various initial values of E_F. It can be seen for all three lines that initially as carrier numbers increase the Fermi level difference also increases (almost linearly), however there is a maximum Fermi level difference which can be reached before there is an abrupt reversal in the trend. This point corresponds to passing over the point of minimum Fermi level where the carrier type changes from holes to electrons and the Fermi level once again increases. It can be seen from Figure 4.6(d) that by increasing the initial Fermi level the maximum ΔE_F which can be reached increases, however the sensitivity to Δn is decreased (depicted by the decrease in gradient).

Fermi level Map of Continuous 1D E_F Profile

Figure 4.6(e) develops the idea of Fermi level line profiles further by presenting a color map of Fermi level difference (ΔE_F) plotted against initial Fermi level, and carrier injection (Δn). It can be seen that for all initial Fermi energies with zero carrier injection begin in the hole conduction regime, however as carriers are injected the ΔE_F increases, and can pass into the regime where one portion of the graphene is conducting with holes, and one portion of the graphene is conducting with electrons.

4.7.2 Results of Continuous 1D E_F Profile

Graphene Fermi level for Continuous 1D E_F Profile

Figure 4.7(a) presents the graphene carrier number injection (Δn) and Fermi level as a function of spatial dimension $\hat{x}$ in response to the electrostatic interaction with a lithium niobate substrate, where the substrate in the central $\pm$12.5 micron region is held at a volume charge density of $+\rho$ while the outside region is held at -ρ, where ρ is set to 1,500 C/m^3. It can be seen from the carrier injection (left hand $\hat{y}$ axis in red) that in the centre (0 micron) the graphene experiences carrier injections of 1×10^{13}/cm^2 holes while at the edges this behaviour is reversed and there is carrier ejection of 1×10^{13}/cm^2. In blue I plot the Fermi level of the graphene, where it can be seen that the addition of holes in the central region raises the Fermi level to near 0.5 eV while at the edges the Fermi level falls to around 0.05 eV, corresponding to a central ribbon of conducting graphene surrounded by low conductivity graphene on each side.

Resonance Spectra Varying Δn of Continuous 1D E_F Profile

In Figure 4.7(b) I present THz transmission through periodically doped graphene on lithium niobate, where the graphene doping is calculated from the surface charge density created on the lithium niobate surface. The transmission values are normalised against transmission through an identical air / lithium niobate unit cell in the absence of graphene. The initial Fermi level is set of 0.4 eV and the mobility at 10,000 cm^2/Vs. Transmission plots are provided for various values of Δn. It can be seen from the figure that as Δn is increased the transmission through the unit cell increases, and at a Δn value of 1.2 $\times10^{13}$/cm^2 a clear resonance peak can be observed around 0.25 THz.

Resonance Mode Profile of Continuous 1D E_F Profile

In Figure 4.7(c) I investigate the resonance mode by plotting the electric and magnetic fields at a plane 5 microns above the graphene layer. The electric field is the real part of the field in the $\hat{y}$ axis (vertical) which relates to regions of localised charges in the graphene. It can be seen from the electric field that there is a localisation of negative charge at the left side, and a localisation of positive charge at the right hand side which will create an electric potential

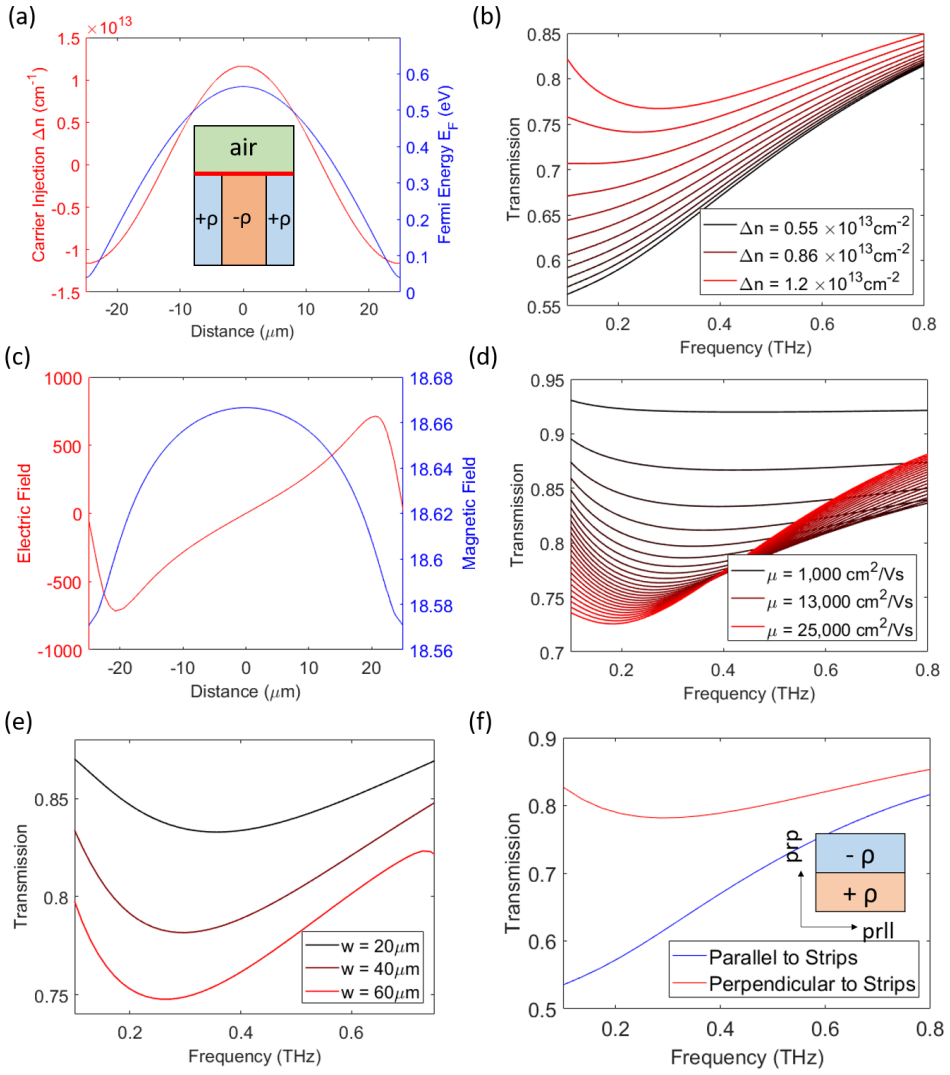

Figure 4.7: *(a) Charge density and Fermi level profile of graphene sheet, with schematic of unit cell where graphene is indicated by red line. (b) Transmission spectra with varying Δn. (c) Electric and magnetic fields highlighting fundamental resonance mode. (d) Transmission spectra for varying mobility values. (e) Transmission spectra for varying unit cell size. (f) Transmission spectra for incident electric field parallel and perpendicular to plasmonic grating direction.*

between these two regions. The magnetic field is the absolute part in the out of plane direction, which relates to electric current passing in the $\hat{x}$ direction. The figure shows magnetic fields are concentrated in the central region of the unit cell, which suggests electric currents passing along the $\hat{x}$ direction. The single central maxima of magnetic field, and the two electric field localisations suggest a this is indeed the profile of the fundamental resonance mode for a ribbon structure.

Resonance Spectra Varying Mobility of Continuous 1D $\mathbf{E}_F$ Profile

Figure 4.7(d) presents THz transmission spectra for a range of carrier mobility values, from 1,000 to 25,000 $\mathrm{cm}^2/\mathrm{Vs}$. In this simulation the initial Fermi level is set to 0.4 eV while the carrier injection value (Δn is set to 1.2 $\times 10^{13}/\mathrm{cm}^2$, which renders the minimum Fermi level near zero. It can be seen that as the mobility increases the strength of the resonance is increased and is also red-shifted to lower frequencies, reaching a maximum peak strength around 25 % at 0.2 THz when the mobility is a maximum at 25,000 $\mathrm{cm}^2/\mathrm{Vs}$.

Investigating Unit Cell Size of Continuous 1D $\mathbf{E}_F$ Profile

Figure 4.7(e) investigates the effect of unit cell size on the resonance profiles. In this simulation the initial Fermi level is set to 0.4 eV while the carrier injection value (Δn) is set to 1.2 $\times 10^{13}/\mathrm{cm}^2$ and mobility at 10,000 $\mathrm{cm}^2/\mathrm{Vs}$. It can be seen that as the unit cell size increases the resonance peak grows in strength and is also red-shifted to lower frequencies. It should be noted here that in order to increase the unit cell size while maintaining a constant value of Δn that the space charge density ρ would also have to be increased.

Polarisation Dependent Resonance Response of Continuous 1D $\mathbf{E}_F$ Profile

Figure 4.7(f) investigates the polarisation response of the graphene resonator. To achieve this the model is adapted to a 3D simulation so that the response parallel and perpendicular to the ribbon direction can be investigated. The inset figure shows a top down view of the unit cell with two regions of lithium niobate at high and low space charge density (ρ), with the parallel ($\overrightarrow{prll}$) and perpendicular ($\overrightarrow{prp}$) orientations denoted in the diagram. In the parallel orientation there is no resonance mode excited, while in the perpendicular orientation there resonance mode is excited. For the perpendicular orientation

where the resonance mode exists it can be seen there is higher transmission, and the presence of a resonance peak around 0.3 THz. For the parallel configuration where no resonance mode exists it can be seen the transmission is far lower, and that no resonance peak is observed.

4.7.3 Discussion of Continuous 1D E_F Profile

In this section, using the knowledge that iron doped lithium niobate can exhibit volume charge distributions of several kC/m^3, I have demonstrated that periodic regions of volume charge distributions with alternating magnitudes within lithium niobate are capable of creating surface charge densities on the order $10^{13}/cm^2$ carriers. It is shown that a graphene sheet on the surface of the lithium niobate would therefore would display a sinusoidal variation in Fermi level which is capable of sustaining a fundamental mode plasmonic resonance around 0.2 THz.

From Figure 4.7(b) it can be seen that as Δn increases the transmission also increases, and the presence of a resonance peak appears. This behaviour is slightly unusual as it would be expected that adding more free carriers would decrease the transmission as the free carriers absorb the radiation, however it should be noted that the graphene begins with a uniform charge density n (corresponding to Fermi level 0.4 eV) and that some portions of the graphene experience an injection of Δn carriers, while come portions of the graphene experience a Δn decrease in carrier numbers, so the total number of carriers in the graphene in this scenario is actually unchanged. In fact, as carrier numbers do not scale linearly with Fermi level it can be seen that if one were to start with two regions of graphene both at 0.4 eV, and inject Δn carriers from one region and eject Δn carriers from the other region, that the average Fermi level would actually decrease (as long as Δn is not sufficient to pass over the Dirac point). From this understanding we can therefore see that as Δn increases the average Fermi level decreases, and as this has a linear relation to the conductivity it is therefore not surprising that the transmission increases.

Furthermore, it could be hypothesised that initially when the graphene has a low carrier injection (and therefore a low Fermi level contrast) there is no plasmonic resonance mode. In this scenario the graphene absorbs the THz radiation due to free carrier absorption where the energy is lost to the surroundings. As the number of free carriers increases the plasmonic resonance appears and the graphene resonantly absorbs and re-emits the

incident radiation, and therefore the transmission is higher for the case of the plasmonic resonator.

Additional insight into this process can be gained from Figure 4.7(f) in which the ribbon resonator is excited with THz radiation both parallel and perpendicular to the ribbon direction, where it is expected that the parallel orientation should show no plasmonic mode. It can be seen in this figure that when excited non-resonantly the transmission is far lower than for the resonant case, and the spectra is very similar to those shown in Figure 4.7(b) for low values of Δn. From this evidence it therefore suggests that the main cause of the transmission increasing as Δn increases is not due to the average conductivity decreasing, but because of the resonant re-emission of the absorbed radiation.

4.8 Continuous 2D E_F Profile

In this section I show how a two dimensional pattern of space charge density in lithium niobate can create a split ring resonator in graphene, and investigate the effects of varying graphene mobility on the resonance strength.

4.8.1 Methods for Continuous 2D E_F Profile

A 3D model is created in Comsol which consists of a slab of air 300 microns deep, with a square unit cell size of 50 microns. Below the air is a slab of lithium niobate also of 300 microns depth. At the air-lithium niobate interface is a sheet of graphene defined as a two dimensional transition boundary. The lithium niobate is split into two sections of positive and negative charge density, as shown in Figure 4.8(a) which creates a split ring geometry. The top and bottom faces of the lithium niobate are grounded, and the charge volume density used here is 1,500 C/m^3 inside the ring, while the volume outside the ring is at 1580 C/m^3. This subtle balance of the two values of space charge density is essential to achieve the correct Fermi level profile in the graphene to create a resonator structure which is electrically 'isolated' from its surroundings.

The first stage of the simulation uses an electrostatics module which solves for the surface charge density which is created on the lithium niobate - air interface. The surface charge density is then divided by the electron charge to determine the number of carriers ($\Delta n(x, y)$) which will be injected into the graphene. The initial graphene Fermi level is set to 0.4 eV and the electrostatics simulation is solved to find the resultant Fermi level distribution in the graphene.

The second stage of the simulations solves the frequency dependent transmission of the THz wave for a range of mobility values. All transmission spectra are normalised against a similar unit cell in the absence of the graphene layer.

4.8.2 Results of Continuous 2D E_F Profile

Figure 4.8(b) shows a surface map of the graphene Fermi level which is created in response to the electrostatic charge distributions within the lithium niobate substrate. The split ring geometry of the lithium niobate is overlaid in black outlines. Although the graphene initially starts at 0.4 eV it can be

seen that all regions of the graphene exhibit a reduced value of Fermi level, where the highest value is 0.18 eV. This global reduction can be understood by assessing the charge distribution geometry within the lithium niobate, where an imbalance in the volume of regions at $+\rho$ and $-\rho$ will result in a net non-zero change to the graphene Fermi level. From the figure it can also be seen there is a region of high conductivity (shown in red) which follows a split ring shape, bounded outside by lower conductivity graphene.

Figure 4.8(c) presents transmission spectra at terahertz frequencies for varying values of graphene mobility. It can be seen that with a moderate value of 10,000 cm^2/Vs there is the presence of a resonance absorption centred around 0.3 THz, however this is a fairly weak resonance reaching only a few percent absorption. As the mobility is increased it can be seen that the resonance increases in strength and also red-shifts to lower frequencies.

Mobility values are further investigated in Figure 4.8(d) where mobility is swept from 5,000 to 50,000 cm^2/Vs. In the color map I plot the absolute differential of transmission with respect to frequency which highlights the location of the resonance frequency (which I have emphasised with the white dotted line). It can be seen that as the mobility increases there is a near linear decrease in the location of the resonant frequency, which disappears from within the available frequency window by a mobility value of 30,000 cm^2/Vs.

To investigate whether this is indeed the fundamental resonance mode I analyse the electric and magnetic fields at a plane 5 microns above the graphene for the resonance frequency at a mobility value of 10,000 cm^2/Vs. In Figure 4.8(e) I plot the real part of the electric field in the $\hat{z}$ direction which is related to accumulation of charges on the graphene surface. It can be seen that there are two regions of localised electric field, one positive and one negative, at each side of the ring of equal but opposite magnitude. This can be understood as localised regions of charge density within the graphene of opposite magnitude, where a potential voltage will exist between these two regions. As this plot shows the real part of the complex electric field it should be noted that this is a 'snap-shot' in time and that the regions of charge density will oscillate between positive and negative.

In response to the potential voltage created between the two regions of charge density there should exist a flow of current, as charges move in response to the potential voltage. To analyse this current flow in Figure 4.8(f) I plot the magnetic field in the $\hat{y}$ direction, which should be proportional to current flow in the $\hat{x}$ direction. it can be seen from this figure that there is a

region of high magnetic field localised to a horizontal band across the middle of the unit cell. This could be understood as a current which is flowing from horizontally across the unit cell (in the $\hat{x}$ direction).

4.8.3 Discussion of Continuous 2D E_F Profile

The transmission spectra presented in Figure 4.8(c) shows that as the mobility of the graphene is increased the plasmonic resonance grows in strength but also is red-shifted to lower frequencies. It could be possible here to simply decrease the dimensions of the resonator geometry however the geometry presented here is near the lower limit of what could be achieved with optical illumination of the substrate. Due to the need for illumination at blue and green wavelengths this sets a lower limit on the resolution which could be achieved, with a 'pixel' size around 1 micron, and therefore to achieve a split ring pattern comprising of a few pixels would require a unit cell minimum size at around 10 microns wide.

The achievable modulation depth with this scheme, as shown in Figure 4.8c, is able to reach 6% at resonance frequency with a graphene mobility value of 20,000 cm^2/Vs. It is shown in the figure that the modulation depth increases as the graphene mobility increases, where mobility values are plotted in the range 5,000 – 20,000 cm^2/Vs. To provide context in practical terms, the value of 20,000 cm^2/Vs is at the upper end of what is currently achievable with CVD graphene however it may be possible to utilise large area exfoliated flakes to extend this upper limit to higher mobility values.

From the map of electric field presented in Figure 4.8(e) it could be inferred that this is a fundamental resonance mode of a split ring resonator. The maps show an electric potential exist between the two sides of the ring where the presence of an electric current between these two sides is suggested by the magnetic field map in Figure 4.8(g). The mode is, however, rather spread out and lacking in confinement which is presumably due to the fact that graphene is covering the entire surface area of the unit cell. Through future optimisation of the substrate charge density pattern it may be possible to further confine this plasmonic mode and in-turn enhance the modulation depth which is achieved with this tuning mechanism.

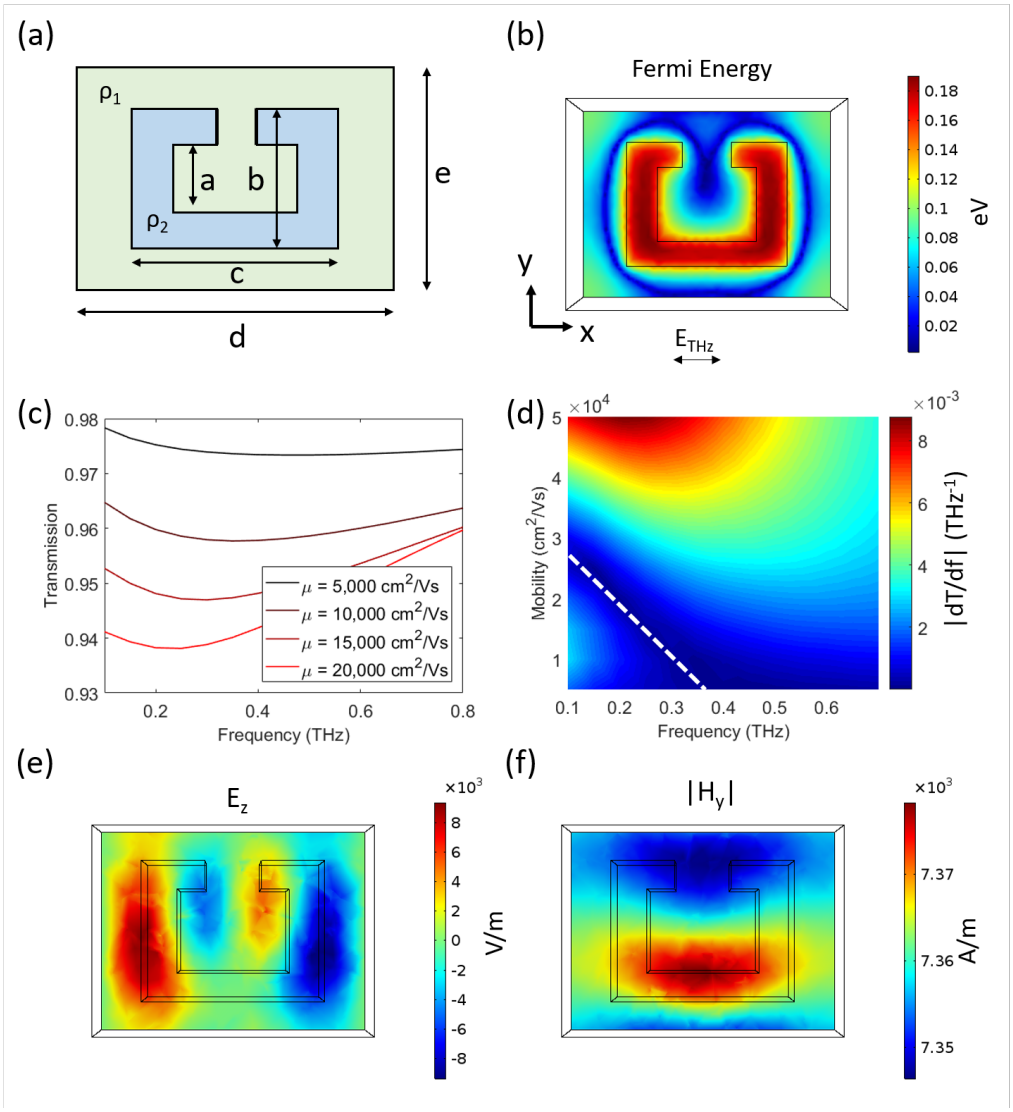

Figure 4.8: ***(a)*** *Geometry of spatial charge densities in lithium niobate where $a = 6\ \mu m$, $b = 10\ \mu m$, $c = 13\ \mu m$, $d = 20\ \mu m$, $e = 15\ \mu m$, $\rho_1 = 1{,}580\ C/m^3$ and $\rho_2 = 1{,}500\ C/m^3$.* ***(b)*** *Fermi level profile of graphene sheet in eV.* ***(c)*** *Transmission spectra for varying mobility values.* ***(d)*** *Color-map of transmission against frequency and mobility, with red dotted line indicating location of resonant frequencies.* ***(e)*** *Map of real part of electric field ($E_{\hat{z}}$) at resonant frequency.* ***(f)*** *Absolute part of magnetic field ($H_{\hat{y}}$) at resonant frequency.*

4.9 Conclusions

In this chapter I have demonstrated via simulations that it is possible to utilise the photorefractive effect in iron doped lithium niobate to realise graphene plasmonics by spatially modulating the graphene charge carrier density. Starting with the assumption that lithium niobate can introduce a 0.3 eV shift in the graphene Fermi level, I present a simple assumption of discrete Fermi level profiles (two distinct values of Fermi level) and show that periodic patterns of high and low conductivity graphene can sustain plasmonic resonances in ribbon and split ring geometries. I develop this idea further by modelling regions of volume charge density in lithium niobate via an electrostatics simulation to determine charge profiles at the surface of the lithium niobate - graphene interface to infer the spatially varying Fermi level distributions, and show that such situations are capable of sustaining plasmonic resonances in ribbon and split ring geometries.

If such devices can be realised experimentally this would open the doors to a new generation of truly reconfigurable plasmonic devices without the need for permanent patterning of structures and instead relying on optically defined carrier density modulations which can be created and redefined at will simply by structured illumination. To further develop this work the natural next step would be an experimental verification of the simulated results, however to obtain high mobility and therefore large scattering times the quality and encapsulation the of the graphene must be investigated.

Bibliography

[1] Bolotin, K.; Sikes, K.; Jiang, Z.; Klima, M.; Fudenberg, G.; Hone, J.; Kim, P.; Stormer, H. Ultrahigh electron mobility in suspended graphene. *Solid State Communications* **2008**, *146*, 351–355.

[2] Principi, A.; van Loon, E.; Polini, M.; Katsnelson, M. I. Confining graphene plasmons to the ultimate limit. *Physical Review B* **2018**, *98*, 035427.

[3] Iranzo, D. A.; Nanot, S.; Dias, E. J. C.; Epstein, I.; Peng, C.; Efetov, D. K.; Lundeberg, M. B.; Parret, R.; Osmond, J.; Hong, J.-Y.; Kong, J.; Englund, D. R.; Peres, N. M. R.; Koppens, F. H. L. Probing the ultimate plasmon confinement limits with a van der Waals heterostructure. *Science* **2018**, *360*, 291–295.

[4] Novoselov, K. S. Electric Field Effect in Atomically Thin Carbon Films. *Science* **2004**, *306*, 666–669.

[5] Grigorenko, A. N.; Polini, M.; Novoselov, K. S. Graphene plasmonics. *Nature Photonics* **2012**, *6*, 749–758.

[6] Ju, L.; Geng, B.; Horng, J.; Girit, C.; Martin, M.; Hao, Z.; Bechtel, H. A.; Liang, X.; Zettl, A.; Shen, Y. R.; Wang, F. Graphene plasmonics for tunable terahertz metamaterials. *Nature Nanotechnology* **2011**, *6*, 630–634.

[7] Zhou, W.; Lee, J.; Nanda, J.; Pantelides, S. T.; Pennycook, S. J.; Idrobo, J.-C. Atomically localized plasmon enhancement in monolayer graphene. *Nature Nanotechnology* **2012**, *7*, 161–165.

[8] Yan, H.; Low, T.; Zhu, W.; Wu, Y.; Freitag, M.; Li, X.; Guinea, F.; Avouris, P.; Xia, F. Damping pathways of mid-infrared plasmons in graphene nanostructures. *Nature Photonics* **2013**, *7*, 394–399.

[9] Liu, L.; Chen, J.; Zhou, Z.; Yi, Z.; Ye, X. Tunable absorption enhancement in electric split-ring resonators-shaped graphene arrays. *Materials Research Express* **2018**, *5*, 045802.

[10] Galiffi, E.; Pendry, J. B.; Huidobro, P. A. Broadband Tunable THz Absorption with Singular Graphene Metasurfaces. *ACS Nano* **2018**, *12*, 1006–1013.

[11] Tu, N. H.; Takamura, M.; Ogawa, Y.; Suzuki, S.; Kumada, N. Plasmon confinement by carrier density modulation in graphene. *Japanese Journal of Applied Physics* **2018**, *57*, 110307.

[12] Yan, H.; Li, X.; Chandra, B.; Tulevski, G.; Wu, Y.; Freitag, M.; Zhu, W.; Avouris, P.; Xia, F. Tunable infrared plasmonic devices using graphene/insulator stacks. *Nature Nanotechnology* **2012**, *7*, 330–334.

[13] Papasimakis, N.; Thongrattanasiri, S.; Zheludev, N. I.; de Abajo, F. G. The magnetic response of graphene split-ring metamaterials. *Light: Science & Applications* **2013**, *2*, e78–e78.

[14] Chen, D.; Yang, J.; Huang, J.; Bai, W.; Zhang, J.; Zhang, Z.; Xu, S.; Xie, W. The novel graphene metasurfaces based on split-ring resonators for tunable polarization switching and beam steering at terahertz frequencies. *Carbon* **2019**, *154*, 350–356.

[15] Tang, W.; Wang, L.; Chen, X.; Liu, C.; Yu, A.; Lu, W. Dynamic metamaterial based on the graphene split ring high-Q Fano-resonnator for sensing applications. *Nanoscale* **2016**, *8*, 15196–15204.

[16] Silveiro, I.; Manjavacas, A.; Thongrattanasiri, S.; de Abajo, F. J. G. Plasmonic energy transfer in periodically doped graphene. *New Journal of Physics* **2013**, *15*, 033042.

[17] Zheng, J.; Yu, L.; He, S.; Dai, D. Tunable pattern-free graphene nanoplasmonic waveguides on trenched silicon substrate. *Scientific Reports* **2015**, *5*, 7987.

[18] Jin, D.; Kumar, A.; Fung, K. H.; Xu, J.; Fang, N. X. Terahertz plasmonics in ferroelectric-gated graphene. *Applied Physics Letters* **2013**, *102*, 201118.

[19] Baeumer, C.; Saldana-Greco, D.; Martirez, J. M. P.; Rappe, A. M.; Shim, M.; Martin, L. W. Ferroelectrically driven spatial carrier density modulation in graphene. *Nature Communications* **2015**, *6*, 6136.

[20] Tu, N. H.; Yoshioka, K.; Sasaki, S.; Takamura, M.; Muraki, K.; Kumada, N. Active spatial control of terahertz plasmons in graphene. *Communications Materials* **2020**, *1*, 7.

[21] Buse, K. Light-induced charge transport processes in photorefractive crystals I: Models and experimental methods. *Applied Physics B: Lasers and Optics* **1997**, *64*, 273–291.

[22] Arizmendi, L.; Lopez-Barbera, F. J. Lifetime of Thermally Fixed Holograms in $LiNbO_3$ Crystals Doped with Mg and Fe. *Applied Physics B* **2007**, *86*, 105–109.

[23] Gorecki, J.; Apostolopoulos, V.; Ou, J.-Y.; Mailis, S.; Papasimakis, N. Optical Gating of Graphene on Photoconductive Fe:$LiNbO_3$. *ACS Nano* **2018**, *12*, 5940–5945.

[24] Xin, H.; Li, W. A review on high throughput roll-to-roll manufacturing of chemical vapor deposition graphene. *Applied Physics Reviews* **2018**, *5*, 031105.

[25] Furukawa, Y.; Kitamura, K.; Ji, Y.; Montemezzani, G.; Zgonik, M.; Medrano, C.; Günter, P. Photorefractive properties of iron-doped stoichiometric lithium niobate. *Optics Letters* **1997**, *22*, 501.

[26] Gunter, P., Huignard, J.-P., Eds. *Photorefractive Materials and Their Applications 2*; Springer New York, 2007.

[27] Puerto, A.; Muñoz-Martín, J. F.; Méndez, A.; Arizmendi, L.; García-Cabañes, A.; Agulló-López, F.; Carrascosa, M. Synergy between pyroelectric and photovoltaic effects for optoelectronic nanoparticle manipulation. *Optics Express* **2019**, *27*, 804.

[28] Chen, X.; Zhang, L.; Chen, S. Large area CVD growth of graphene. *Synthetic Metals* **2015**, *210*, 95–108.

[29] Mattevi, C.; Kim, H.; Chhowalla, M. A review of chemical vapour deposition of graphene on copper. *Journal of Materials Chemistry* **2011**, *21*, 3324–3334.

[30] Tang, S.; Wang, H.; Wang, H. S.; Sun, Q.; Zhang, X.; Cong, C.; Xie, H.; Liu, X.; Zhou, X.; Huang, F.; Chen, X.; Yu, T.; Ding, F.;

Xie, X.; Jiang, M. Silane-catalysed fast growth of large single-crystalline graphene on hexagonal boron nitride. *Nature Communications* **2015**, *6*, 6499.

[31] de Miguel, E. M.; Limeres, J.; Carrascosa, M.; Arizmendi, L. Study of developing thermal fixed holograms in lithium niobate. *Journal of the Optical Society of America B* **2000**, *17*, 1140.

[32] Kalkum, F.; Peithmann, K.; Buse, K. Dynamics of holographic recording with focused beams in iron-doped lithium niobate crystals. *Optics Express* **2009**, *17*, 1321.

[33] Calamiotou, M.; Chrysanthakopoulos, N.; Papaioannou, G.; Baruchel, J. Dynamics of photodeformations and space charge field in photorefractive Fe:$LiNbO_3$ studied with synchrotron area diffractometry. *Journal of Applied Physics* **2007**, *102*, 083527.

[34] Dong, Q.; Liu, L.; Liu, D.; Dai, C. Grating spacing dependence of nonvolatile holographic recording with arbitrary charge transport lengths. *Optik* **2004**, *115*, 427–431.

[35] Wang, X.; Yan, A.; Liu, L.; Liu, D.; Zhi, Y.; Hu, Z. Influence of recording conditions on crossed-beam photorefractive gratings in doubly doped LiNbO_3 crystals. *Applied Optics* **2006**, *45*, 5942.

[36] Jabbarzadeh, F.; Heydari, M.; Habibzadeh-Sharif, A. A comparative analysis of the accuracy of Kubo formulations for graphene plasmonics. *Materials Research Express* **2019**, *6*, 086209.

Chapter 5

Conclusions

5.1 Summary

Two dimensional materials offer exciting prospects in optoelectronic devices such as photodetection and plasmonics however there currently exist a lack of platforms to control the electronic properties of two dimensional materials in spatially resolved, and non-volatile methods. To this end this thesis has presented experimental and simulated investigations into the use of photorefractive lithium niobate as a platform to optically control two dimensional materials via optically defined non-volatile charge distributions within the crystal substrate. Here I have performed investigations with graphene however this platform is not limited simply to use with graphene and should be applicable to a whole range of two dimensional materials.

In Chapter 2 I demonstrated how the photorefractive effect could be used to tune the DC electrical conductivity of a graphene sheet in response to optical illumination. The effect was capable of inducing a 2.6 fold increase in the graphene resisitvity which was shown to be reversible under thermal annealing which returns the lithium niobate substrate to its initial pre-illuminated conditions with a uniform charge distribution. From these measurements I calculated the doping effect altered the graphene Fermi level by 0.3 eV which corresponded to a change injection of $5.5 \times 10^{12} cm^{-2}$.

In Chapter 3 I created a hybrid metamaterial device consisting of a metallic resonator array sandwiched between monolayer graphene and iron doped lithium niobate. I demonstrated through terahertz transmission measurements how the photorefractive tuning of the graphene resisitivity is able to alter the losses in the plasmonic resonance system which tunes the transmissive properties of the device. It is shown that this effect is optically induced however is non-volatile under dark conditions. Further, I create devices on opposite polar faces of z cut lithium niobate in order to investigate which charge migration mechanism may be responsible for the photorefractive migration of electrons, which suggests that the photogalvanic effect is dominant over the diffusion mechanism.

In Chapter 4 I investigate through use of simulations whether the photorefractive effect in lithium niobate could be used to create optically defined resonator structures in a un-patterned sheet of monolayer graphene. Using the results from Chapter 2 in which I determined the Fermi level shift induced by the lithium niobate substrate I show that by patterning lithium niobate charge distributions to the correct dimensions indeed results in a graphene

doping profile which can sustain plasmonic resonances at terahertz frequencies. If such structures can be realised experimentally this would open the doors to a new platform for truly reconfigurable plasmonic systems defined by light without the need for permanent patterning of structures.

5.2 Outlook

5.2.1 Optically Controlled Electronics

Throughout the investigations presented in Chapter 2 there remain several unanswered questions which are essential to probe in order to realise the full potential of lithium niobate as a platform for optical control of 2D materials.

Firstly, there must be an accurate determination of the Fermi level changes induced in the graphene sheet in response to the optical illumination. To accurately determine the Fermi level changes induced, and therefore the change in carrier numbers in graphene, it would be necessary to combine the lithium niobate with an electrical gate to created a dual gated device. In this manner it would then be possible to compare the optical and electrical gates, and accurately determine the carrier mobility, and change in carrier numbers as a function of illumination. Over the course of the PhD many attempts were made at fabrication of electrical gates via a range of methods however the devices always appeared to suffer from leakage currents, which may be due to working with large area graphene sheets which increases the chances of incurring a defect in the gate dielectric. To overcome this issue therefore it would be appropriate the pattern the graphene into small channels via photographically techniques, thereby reducing the area of the active graphene device from several square millimeters to tens of square micrometers.

Another route of investigation would be to show an optical annealing of the optical doping effect. Optical annealing has been demonstrated in holographic experiments in many reports of lithium niobate, and therefore is known to be technically possible, however has not yet been demonstrated for reversible control over 2D materials. If this could be achieved here it would show proof-of-concept for an all-optical system which would dramatically enhance that capabilities of this platform. Finally, it would be advantageous to replace the graphene with other 2D materials such as MoS_2 which exhibits an electronic bandgap which could allow for the lithium niobate to effectively switch this semiconducting material from insulating to metallic, which would

allow for an optical transistor device with much higher on/off ratios than could be achieved with graphene.

The experiments here are conducted using broadband white light illumination however the writing speed could be improved using blue or green laser light, or even a pulsed source, as the response time of charge migration is a function of illumination intensity and can respond on sub-ps time scales under pulsed illumination. To further investigate the doping effect in graphene I propose the use of THz TDS to measure the electrical properties of graphene during illumination. This method has several benefits as the process is non-contact and therefore non-destructive to the sample, furthermore the electrical properties are averaged over a large area defined by the THz beam focal spot which may reduce errors caused by local variation in the properties of graphene.

5.2.2 Optically Controlled Metasurface

For future work it is advantageous to enhance the modulation strength of the effect which can be achieved in this configuration. In preliminary studies I see via simulations that the modulation strength can be increased by adjusting the geometry of the metallic resonators and tuning the initial Fermi level of the graphene. The geometric adjustment can be achieved through reducing the distance of the split ring gap which is simple enough by creating a new photomask. By the fabrication methods presented in Chapter 3 the use of UV photolithography allows for a split ring gap which could reach down to $\sim 0.5\mu m$ comfortably without extensive fabrication optimisation, however as the wavelength of the light is on the order of $0.2-0.3\mu m$ it would be difficult to create features less than $0.5\ \mu m$. For future work it would be advantageous to investigate thoroughly the modulation strength which could be achieved through optimisation of the resonator geometry and to experimentally verify this with a new set of devices.

Further, if additional reductions to the resonator dimensions are required it would be possible to replace UV photolithography with electron beam lithography or focused ion-beam milling which can reliably reproduce features with dimensions of tens of nanometers. In addition to this, the use of electron beam lithography could enable the reproduction of smaller resonator geometries with resonance frequencies at shorter wavelengths; it would be interesting to investigate how this modulation technique fairs at longer or shorter wavelengths, where the modulation depth may show a dependence

on resonance frequency, as it is known that graphene electrical properties are highly dependent on frequency.

The experiments presented in Chapter 3 utilised a large area uniform sheet of graphene covering the entirety of the active device, however it could be interesting to pattern the graphene, for example to achieve graphene sitting only in the split ring gaps of the resonator unit cells as this may allow for enhanced confinement of the plasmonic mode. Alternatively, the metallic resonators could be removed and replaced simply with graphene patterned into an array of resonators as depicted in Figure 5.1.

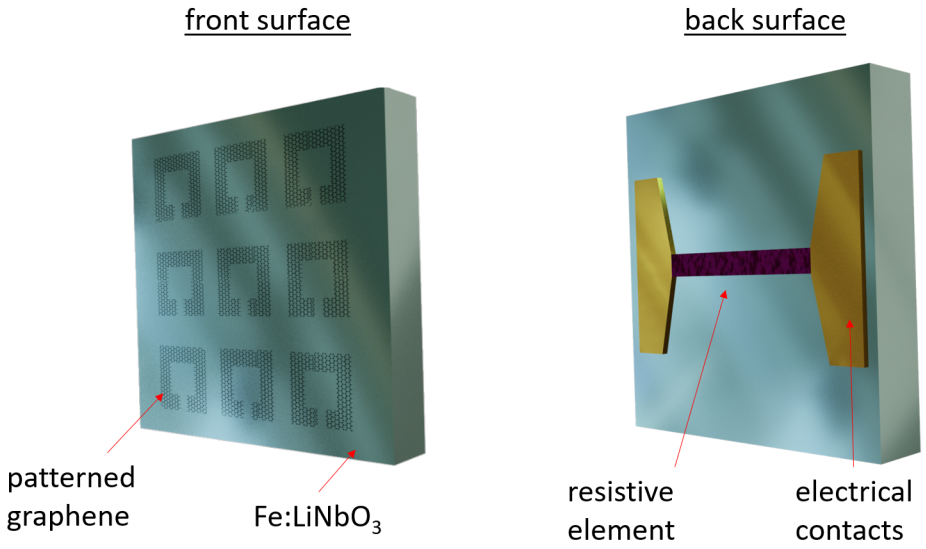

Figure 5.1: *Depiction of proposed sensing device incorporating a graphene resonator array on photorefractive lithium niobate attached to bolometric element. The device shown here could be fabricated in a large array to create a spatially resolved sensing grid with graphene-on-lithium-niobate used as optically controlled adaptive filtering elements over each 'pixel'.*

In Figure 5.1 I present a schematic diagram of a proposed device in which the optically controlled graphene metasurface acts as an adaptive filtering element in front of a bolometer sensor. The device would utilise patterned graphene resonators on the surface of iron doped lithium niobate to optically control the transmissive properties of radiation at Terahertz frequencies or perhaps into the infra-red region. A bolometric sensor is fabricated on the

reverse side of the substrate which consists simply of electrical contacts and a thin strip of material which changes its electrical resistivity in response to heating effects from incident photons. By considering the device shown in Figure 5.1 as a single 'pixel' it could be possible to create a large array of sensing elements with individually addressable filtering elements to adaptively control the radiation frequencies which are measured.

5.2.3 Optically Defined Plasmonics

The results presented in Chapter 4 reveal that optically defined plasmonic devices of graphene on lithium niobate may well be possible however one important issue to overcome is the charge carrier mobility of the graphene monolayer. Currently through the use of commercially available CVD sheets the achievable mobility values are at the lower end of the required parameter-space; manufacturers are continually striving for higher mobility values through reducing the graphene defect density however these improved crystals may be a long time to reach market. To overcome this issue of low mobility values I propose the use of exfoliated graphene flakes instead of a CVD graphene layer as shown in Figure 5.2. One important issue to note here is that the grating period of the illumination must be significantly smaller than the diameter of the exfoliated graphene crystals so that plasmonic resonances can occur. In this configuration I propose that plasmonic resonances can be sustained in exfoliated graphene sheets with high values of charge carrier mobility which will allow optically defined plasmonic devices.

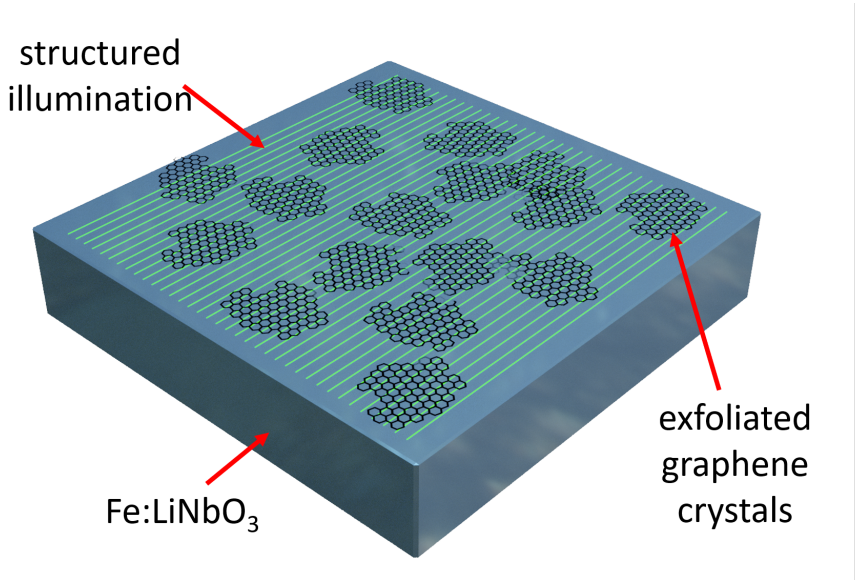

Figure 5.2: *Depiction of proposed plasmonic gratings with exfoliated graphene on lithium niobate. Structured periodic illumination is projected onto the lithium niobate substrate to induce spatially resolved charge densities. Exfoliated graphene flakes on the surface of the substrate experienced a electrostatic doping effect which creates a periodic variation in graphene Fermi level.*

List of Publications

5.3 Journal Papers

Optically Reconfigurable Graphene/Metal Metasurface on Fe:$LiNbO_3$ for Adaptive THz Optics
J. Gorecki, L. Piper, A. Noual, S. Mailis, N. Papasimakis, V. Apostolopoulos
ACS Applied Nano Materials
DOI: 10.1021/acsanm.0c02243
Awaiting Volume and Issue number (2020)

High-precision THz-TDS via self-referenced transmission echo method
J. Gorecki, N. Klokkou, L. Piper, S. Mailis, N. Papasimakis, V. Apostolopoulos
Applied Optics
DOI: 10.1364/AO.391103
Vol. 59, Issue 22, Pages 6744-6750 (2020)

Optical Gating of Graphene on Photoconductive Fe:$LiNbO_3$
J. Gorecki, V. Apostolopoulos, J-Y. Ou, S. Malis, N. Papasimakis
ACS Nano
DOI: 10.1021/acsnano.8b02161
Vol. 12, Issue 6, Pages 5940–5945 (2018)

5.4 Conference Presentations

THz Spectroscopy of Photogenerated Carriers in Fe:$LiNbO_3$ for Optical Control of 2D Materials
S. Blundell, J. Gorecki, N. Papasimakis, S. Malis, V. Apostolopoulos
CLEO EU (Oral Presentation)
DOI: 10.1109/CLEOE-EQEC.2019.8871708
2019

Optical Tuning of Graphene Electronics and Plasmonics on Iron Doped Lithium Niobate
J. Gorecki, L. K. Piper, V. Apostolopoulos, S. Mailis, N. Papasimakis
CLEO US (Oral Presentation)
DOI: 10.23919/CLEO.2019.8750291
2019

Optical Gating of Graphene
J. Gorecki, V. Apostolopoulos, S. Mailis, N. Papasimakis
Graphene Week (Poster)
2018

Light Controlled Conductivity of Graphene on Photorefractive Lithium Niobate
J. Gorecki, N. Papasimakis, S. Mailis, V. Apostolopoulos
Nanophotonics and Micro/Nano Optics International Conference (Oral Presentation)
2017

5.5 Collaborative Works

Singlemoded THz guidance in bendable TOPAS suspended-core fiber directly drawn from a 3D printer
W. Talataisong, J. Gorecki, R. Ismaeel, M. Beresna, D. Schwendemann, V. Apostolopoulos, G. Brambilla
Scientific Reports
DOI: 10.1038/s41598-020-68079-y
Vol. 10, Article Number 11045, (2020)

3D-printed polymer antiresonant waveguides for short-reach terahertz applications
L. D. van Putten, J. Gorecki, E. Numkam Fokoua, V. Apostolopoulos, F. Poletti
Applied Optics
DOI: 10.1364/AO.57.003953
Vol. 57, Issue 14, Pages 3953-3958 (2018)

Appendix A - THz TDS Echo Referencing

Introduction

Terahertz time domain spectroscopy (THz TDS) is a powerful analytical technique for investigating a wide range of materials such as spectroscopy of biological samples [1, 2, 3, 4], detection of concealed drugs and explosives [5, 6, 7], imaging of astronomical objects [8, 9], and industrial quality control of semiconductor manufacturing [10, 11]. The THz TDS method relies on taking a suitable reference scan by which the sample scans are normalised, however if the THz pulse is not correctly referenced or the spectrometer has drifted since the reference scan this can lead to errors in the measured refractive index.

Here, I address the issue of reference stability by presenting a method to determine frequency dependent complex refractive index of a sample without an air reference in transmission mode. The method relies on internal reflections within the sample to produce echo pulses which can be normalised to each other, therefore requiring only one measurement scan to obtain all necessary data. I derive the relevant parameter extraction equations for referencing the echo pulse to the first transmitted pulse, and present a comparative study in which a lithium niobate sample is measured repeatedly over a 50 minute period and complex refractive index values are compared for the two extraction methods. It is demonstrated that the echo reference method can reduce the variation between repeated measurements for the real part of the refractive index up to 67% at frequencies below 1 THz.

Requirements of Referencing

The THz TDS method relies on taking a suitable reference scan by which the sample scans are normalised, which is usually achieved by measuring the THz pulse transmitted through air, and then placing a sample in the beam path and measuring the THz pulse through the sample. If the THz pulse is not correctly referenced, or the spectrometer has drifted since the reference scan, this can lead to errors in the complex refractive index. There are many practical issues to address when referencing a THz scan such as temporal drift in the spectrometer power, mechanical drift in the delay stage, atmospheric moisture, and access to samples to easily insert/remove them from the beam path. Despite the myriad of THz referencing and extraction methods there are still issues to overcome in an effort to increase the reliability of TDS data.

Drift: One major issue to highlight is from the air referencing method is that a THz spectrometer may experience drift in the laser power between taking an air measurement and a sample measurement. This effect is especially compounded when it is required to take repeat measurements of samples over a long time period such as several hours to investigate a temporally changing system.

Access: Furthermore, when taking an air reference measurement the sample must be added/removed to the optical system which may not be physically possible in some situations, for example with a sample held in a sealed chamber or other enclosed space.

Moisture: When taking a measurement with an air reference it is generally assumed the complex refractive index of the air is 1 + 0i, ie. the air has identical refractive index as that of a vacuum, however in practical cases there is often atmospheric moisture which can cause absorption of the THz pulse. After the air reference is taken and the sample is placed in the spectrometer the beam is then passing through less water vapour which can skew the values of imaginary refractive index register in the system as an artificial gain in intensity.

Echo Reference Method

Here, I address the issue of air referencing by presenting a method to determine complex refractive index of a sample without an air reference. The method relies on internal reflections within the sample to produce echo pulses which can be normalised to each other, requiring only one measurement scan to obtain all necessary data. This method has a number of advantages over the traditional air referencing method as both measurements can be taken in a single time domain trace which reduces the drift in the spectrometer between measurements. Secondly this method allows for the sample to be held securely in the optical setup at all times which reduces chances of misalignment between repeated sample mountings, and can allow for samples to be held in difficult-to-access places such as sealed chambers and thermal stages. Thirdly this 'echo referencing' method reduces the need for dry inert gas which is often used to displace atmospheric moisture however requires a spectrometer system to be fully enclosed which can be costly and difficult to achieve.

Theory of Extraction with Separable Solutions

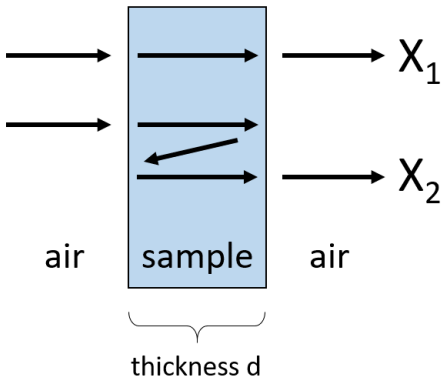

Figure 5.3: *Pulse propagation paths are shown for the first transmitted pulse (X_1) and the first internally reflected, or 'echo' pulse (X_2) travelling from air, through a sample, and re-emerging to air.*

Figure 5.3 depicts the optical paths for the first transmitted pulse and the echo pulse within the crystal sample. By measuring the THz time domain the two pulses can be separated and individually converted into the frequency domain by a Fourier transform. The first pulse enters from air into the sample in a transformation which can be described by the Fresnel transmission function. The pulse then propagates through a length d of the sample, which can be described by a complex Beer Lambert exponential attenuation equation, and finally passes out of the sample into air which can be described by a further Fresnel transmission equation. The total combination of these functions describes the transmitted wave termed X_1 as shown in Equation 5.1, where A is the arbitrary power of the incoming pulse, T_{ij} is the complex Fresnel transmission coefficient passing from material i into j, and P_d is the exponential attenuation from passing through length d of material with form $P_d = exp(-i\tilde{n}\omega d/c)$, where d is the length of material passing through, and c is the speed of light.

$$X_1 = A \cdot T_{ab} \cdot P_d \cdot T_{ba} \tag{5.1}$$

The echo pulse termed X_2 is descirbed by Equation 5.2 where where R_{ij} is the complex Fresnel reflection coefficient from inside material i bounding material j, with form $R_{ij} = (\tilde{n_i} - \tilde{n_j})/(\tilde{n_i} + \tilde{n_j})$.

$$X_2 = A \cdot T_{ab} \cdot P_d \cdot R_{ba} \cdot P_d \cdot R_{ba} \cdot P_d \cdot T_{ba} \tag{5.2}$$

By dividing the two pulses the arbitrary power of the emitter A is removed, along with the transmission coefficients, leaving the complex transfer function termed H. This transfer function H can be equated to the experimental data for the complex Fourier transform presented in unwrapped polar coordinates as $|\mathrm{Y}(\omega)| \cdot \mathrm{e}^{i\phi(\omega)}$, where $|Y(\omega)|$ is the magnitude, and $\phi(\omega)$ is the unwrapped angle of the the complex Fourier transform.

$$H = P_d^2 \cdot R_{ba}^2 = |Y(\omega)| \cdot e^{i\phi(\omega)} \tag{5.3}$$

With the assumption that n>>k then the Fresnel coefficients can be assumed to be real valued which allows for the real and imaginary parts of the equations to be solved separately by rewriting the propagation constant in real and imaginary parts where $\tilde{n} = n + ik$. Firstly the real values of n can be calculated from Equation 5.4, and then plugged into Equation 5.5 to obtain the imaginary k components. For the case of an air referenced sample a similar deviation is used to calculate n and k as described in literature [12].

$$e^{-2in\omega d/c} = e^{i\phi(\omega)} \tag{5.4}$$

$$e^{2k\omega d/c} \cdot (\frac{n_a - n_b}{n_a + n_b})^2 = |Y(\omega)| \tag{5.5}$$

Theory of Extraction with Non-Separable Solutions

In the case that n and k are of a similar order of magnitude it is no longer possible to assume the Fresnel coefficients are completely real. In this case the real and imaginary parts of the refractive index must be solved simultaneously. For this task a Newton Raphson method may be used, which is an analytical technique to minimise the difference between two functions, where the two functions are the experimental transfer function, and the theoretical transfer function. The Newton Raphson iteratively adjusts the theoretical

transfer function until the difference between theoretical and experimental falls to an arbitrarily small number (10^{-7} in this case).

To perform the Newton Raphson method it is desirable to use the natural logarithm of the transfer function H, as this separates the real and imaginary parts of H, defined as G = ln(H) shown in in Equation 5.6. The method also requires an analytical expression for the derivative of G with respect to $\tilde{n}$, as shown in Equation 5.7. I present these equations here for completeness, however for the rest of this chapter I proceed with the separable solutions method.

$$G = ln(H) = ln(\frac{\tilde{n}_2 - \tilde{n}_1}{\tilde{n}_2 + \tilde{n}_1})^2 - 2i\tilde{n}_2\omega d/c \tag{5.6}$$

$$dG/d\tilde{n}_2 = \frac{4\tilde{n}_1}{\tilde{n}_2^2 - \tilde{n}_1^2} - 2i\omega d/c \tag{5.7}$$

Experimental Method

A z-cut crystal of congruent lithium niobate of 0.5 mm thickness is mounted on top of a metallic aperture of 10 mm diameter and placed in the beam path of a collimated THz source. The THz spectrometer is a commercially available Zomega spectrometer which detects THz radiation via femtosecond pulse interaction in a non-linear crystal. A reference scan is first taken in absence of the lithium niobate crystal through the metallic aperture, the lithium niobate is then mounted in the aperture and THz spectra are recording with an averaging period of 2 minutes, recording a total of 24 spectra over a 50 minute period.

Results

Time Domain of Pulses

Figure 5.4 shows the time domain of the THz radiation passing through the lithium niobate sample, where the first (red) pulse corresponds to the pulse which passes once through the sample, while the second (blue) pulse corresponds to the echo pulse which is delayed in time due to the internal reflections within the sample. It can be seen the echo pulse amplitude is attenuated in comparison to the first transmitted pulse due to the additional material interaction of the THz radiation with the sample due to the internal reflections. The two pulses are separated from each other by multiplying the time domain by an exponentially damped window, as shown by the dashed lines, and then converting into the frequency domain by performing a Fourier transform on each data set. Once the Fourier transforms are performed the magnitude of the echo pulse is divided by that of the first pulse to obtain $|Y(\omega)|$ while the unwrapped phase of the echo pulse is subtracted from that of the first pulse to obtain $\phi(\omega)$. The complex refractive index is calculated with the echo method for separable solutions.

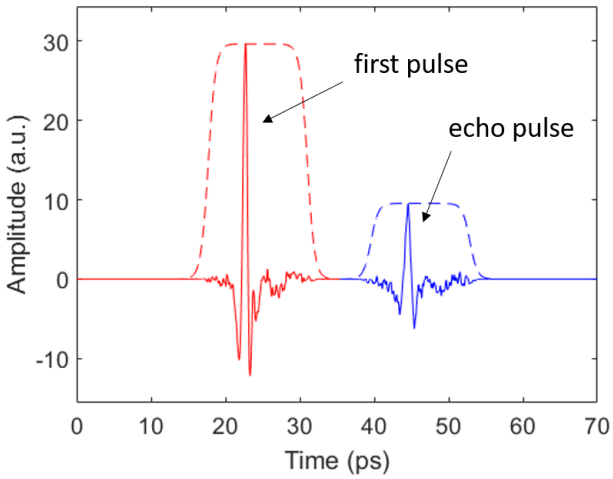

Figure 5.4: *THz Time domain of first pulse and echo pulse through lithium niobate sample with window functions (in dashed lines) overlayed on top of the pulses.*

Complex Refractive Index

Figure 5.5(a) displays the real part of the refractive index z-cut lithium niobate averaged for 24 measurements taken over a 50 minute period, with the standard deviation shown as the shaded regions. The data is extracted with two different methods; in the first method labelled 'air reference' a reference measurement of THz propogation through air is taken before sample measurements and all subsequent lithium niobate measurements are normalised to this single air reference. In the second method labelled 'Echo Reference' the data is extracted by referencing the echo pulse to the first transmitted pulse as described in the theory section. It can be seen from the graph that the air reference method is capable of providing trustworthy values up to 1.5 THz, while the echo pulse method suffers from large noise above 1 THz, however in the region of 0.1 to 1 THz it is clear that the echo pulse method has a much lower standard deviation than the air reference method.

Figure 5.5(b) shows the imaginary refractive index extracted by the air reference and echo reference methods for 24 repeat measurements of lithium niobate where mean values are plotted as solid lines with standard deviation plotted as colored error bars. It can be seen that for frequencies below 1 THz both methods give similar readings however above 1 THz the echo reference results become unstable. Both extraction methods provide values which are in general accordance with reported literature [13, 14, 15].

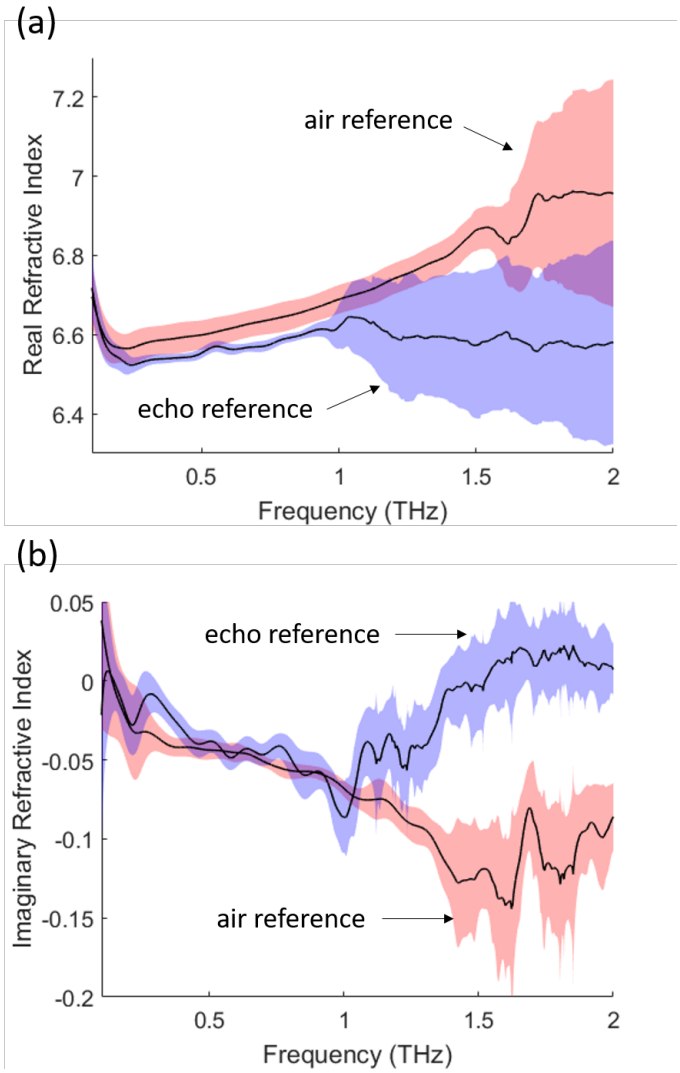

Figure 5.5: *Real and imaginary refractive index averaged for 24 measurements of lithium niobate over a 50 minute period, where the error bars are given by the standard deviation of the repeat measurements. The red datasets shows the refractive index calculated by referencing to a measurement in air, while the blue datasets use the echo referencing method. It can be seen for the real refractive index the echo method achieves a lower standard deviation as compared to the air reference method at frequencies below 1 THz, however the echo method values become unreliable above 1 THz while the air reference results are stable up to 1.5 THz.*

Standard Deviation Comparison

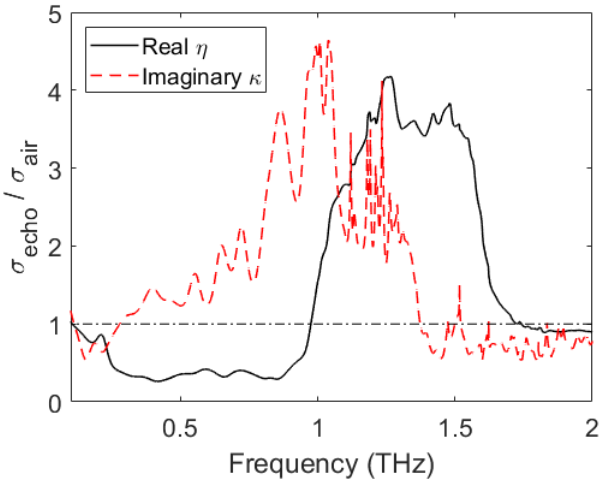

Figure 5.6: *Fractional change in standard deviation of n and k for 24 measurements of lithium niobate as calculated by air reference and echo reference methods.*

Figure 5.6 presents a comparison of the variation between the two referencing methods. The standard deviation of n and k for the echo method is divided by the deviation calculated using the air reference method. It can be seen that for values of n below 1 THz there is a reduced standard deviation, achieving around 67 % lower standard deviation than the air reference method. The imaginary part however suffers from greater variation compared to the air method at all frequencies, which is perhaps due to the lower signal-to-noise ratio of the echo pulse as compared to the first transmitted pulse.

Material Suitability

The method presented here requires a suitably strong echo pulse in order to obtain useable data from the THz measurements. The strength of the echo pulse can be estimated from Fresnel coefficients. Figure 5.7 plots the echo pulse power obtained from Equation 5.2 against varying real refractive index n (where the arbitrary power A is set to 1, and the attenuation coefficients are ignored). It can be seen that as the refractive index increases from 1 the

echo power increases (plotted in red). This is understood as the reflection coefficient (blue) growing from zero when n equals 1. At a value around 6 the echo power reaches a maximum before starting to decrease. This decrease comes from the fact that as n increases the transmission coefficient (black) decreases, and so there is a sweet-spot around n = 6. This is a rather fortunate value as it coincides nicely with the refractive index of lithium niobate.

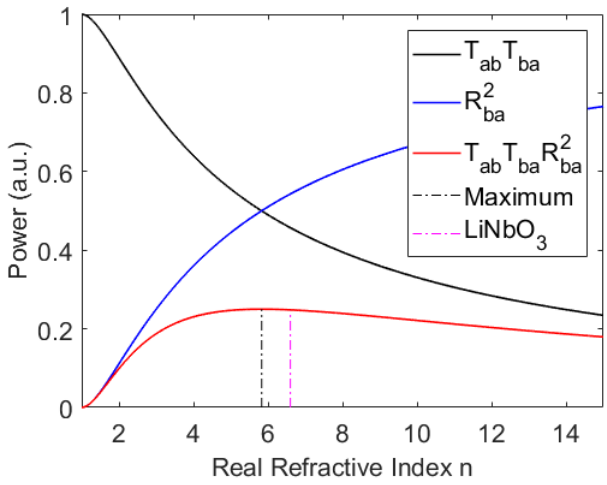

Figure 5.7: *Transmission, Reflection, and Echo coefficients plotted against refractive index.*

Conclusions

In conclusion I have presented a novel 'echo reference' method to determine complex refractive index from THz TDS data in absence of an air reference measurement. I present a benchmark test in which a test sample of lithium niobate is measured 24 times over a 50 minute period and the data extracted for by both echo reference, and air reference methods. It is shown that for frequencies below 1 THz the echo reference measurements achieve 67 % lower standard deviation in real refractive index values as compared to the air reference method, however the useable frequency bandwidth for the echo reference is lower than that of the air reference method. I argue the

echo reference method has a number of advantages over a traditional air referencing method such as reduced effects of power drift, reduces the need for purging of the spectrometer chamber with inert gas, and allows the sample to be held securely in the optics setup without the need for removing the sample between measurements which reduces chances of optical misalignment.

Bibliography

[1] Markelz, A.; Roitberg, A.; Heilweil, E. Pulsed terahertz spectroscopy of DNA, bovine serum albumin and collagen between 0.1 and 2.0 THz. *Chemical Physics Letters* **2000**, *320*, 42 – 48.

[2] Ebbinghaus, S.; Kim, S. J.; Heyden, M.; Yu, X.; Heugen, U.; Gruebele, M.; Leitner, D. M.; Havenith, M. An extended dynamical hydration shell around proteins. *Proceedings of the National Academy of Sciences* **2007**, *104*, 20749–20752.

[3] Walther, M.; Fischer, B.; Schall, M.; Helm, H.; Jepsen, P. Far-infrared vibrational spectra of all-trans, 9-cis and 13-cis retinal measured by THz time-domain spectroscopy. *Chemical Physics Letters* **2000**, *332*, 389–395.

[4] Woodward, R. M.; Wallace, V. P.; Pye, R. J.; Cole, B. E.; Arnone, D. D.; Linfield, E. H.; Pepper, M. Terahertz Pulse Imaging of ex vivo Basal Cell Carcinoma. *Journal of Investigative Dermatology* **2003**, *120*, 72–78.

[5] Federici, J. F.; Schulkin, B.; Huang, F.; Gary, D.; Barat, R.; Oliveira, F.; Zimdars, D. THz imaging and sensing for security applications—explosives, weapons and drugs. *Semiconductor Science and Technology* **2005**, *20*, S266–S280.

[6] Appleby, R.; Wallace, H. B. Standoff Detection of Weapons and Contraband in the 100 GHz to 1 THz Region. *IEEE Transactions on Antennas and Propagation* **2007**, *55*, 2944–2956.

[7] Chen, J.; Chen, Y.; Zhao, H.; Bastiaans, G. J.; Zhang, X.-C. Absorption coefficients of selected explosives and related compounds in the range of 0.1-2.8 THz. *Optics Express* **2007**, *15*, 12060.

[8] Wei, J.; Olaya, D.; Karasik, B. S.; Pereverzev, S. V.; Sergeev, A. V.; Gershenson, M. E. Ultrasensitive hot-electron nanobolometers for terahertz astrophysics. *Nature Nanotechnology* **2008**, *3*, 496–500.

[9] Negrello, M. et al. The Detection of a Population of Submillimeter-Bright, Strongly Lensed Galaxies. *Science* **2010**, *330*, 800–804.

[10] Nagai, N.; Sumitomo, M.; Imaizumi, M.; Fukasawa, R. Characterization of electron- or proton-irradiated Si space solar cells by THz spectroscopy. *Semiconductor Science and Technology* **2006**, *21*, 201–209.

[11] Ahi, K.; Shahbazmohamadi, S.; Asadizanjani, N. Quality control and authentication of packaged integrated circuits using enhanced-spatial-resolution terahertz time-domain spectroscopy and imaging. *Optics and Lasers in Engineering* **2018**, *104*, 274–284.

[12] Jepsen, P.; Cooke, D.; Koch, M. Terahertz spectroscopy and imaging - Modern techniques and applications. *Laser & Photonics Reviews* **2010**, *5*, 124–166.

[13] Unferdorben, M.; Szaller, Z.; Hajdara, I.; Hebling, J.; Palfalvi, L. Measurement of Refractive Index and Absorption Coefficient of Congruent and Stoichiometric Lithium Niobate in the Terahertz Range. *Journal of Infrared, Millimeter, and Terahertz Waves* **2015**, *36*, 1203–1209.

[14] Wu, X.; Zhou, C.; Huang, W. R.; Ahr, F.; Kärtner, F. X. Temperature dependent refractive index and absorption coefficient of congruent lithium niobate crystals in the terahertz range. *Optics Express* **2015**, *23*, 29729.

[15] Yi-Min, S.; Zong-Liang, M.; Bi-Hui, H.; Guo-Qing, L.; Li, W. Giant Birefringence of Lithium Niobate Crystals in the Terahertz Region. *Chinese Physics Letters* **2007**, *24*, 414–417.

Appendix B - Refractive Index of $LiNbO_3$

Introduction

The refractive index of lithium niobate at terahertz frequencies is measured via THz TDS in transmission mode. A reference measurement through air is taken with an empty metallic aperture mounted into the spectrometer. A sample of undoped z cut lithium niobate with 0.3 mm thickness is mounted into the metallic aperture and placed into the spectrometer beam path. Transmission scans are averaged over a 2 minute period, with the delay stage scanning at $\sim$ 2 Hz. After the two minute period the scan data is saved, and the scan process repeated a total of 24 times over a 50 minute period.

Results

Each of the 24 THz scans is used to extract a complex refractive index for the sample, and the mean values for real and imaginary index are plotted in Figure 5.8. The standard deviation obtained over the 24 measurements is plotted as the shaded region. The data are untrusted outside the frequency range of 0.2 to 1.5 THz as the signal to noise ratio drops to unusable levels.

The real part of the refractive index is measured to be around 6.6 at low frequencies (0.2 THz) and increases superlinearly to around 6.9 at 1.5 THz. The imaginary part of the refractive index begins near 0 at 0.15 THz, and decreases to near -1.25 at 1.5 THz. These values are in line with previously reported values of the refractive index [1, 2, 3].

Discussion

Similar measurements were performed with iron doped lithium niobate at 0.1 and 0.01 weight %, which obtained identical refractive indexes within experimental error. In other words, the THz transmission properties through lithium niobate appear unaltered by the iron doping within the sensitivity of the spectrometer.

It can be seen from the real part of the refractive index that there appears to be a sudden increase below 0.2 THz, which may highlight the presence of a phonon resonance mode of some other physical phenomena. Unfortunately the frequency range below 0.2 THz is subject to high levels of error due to

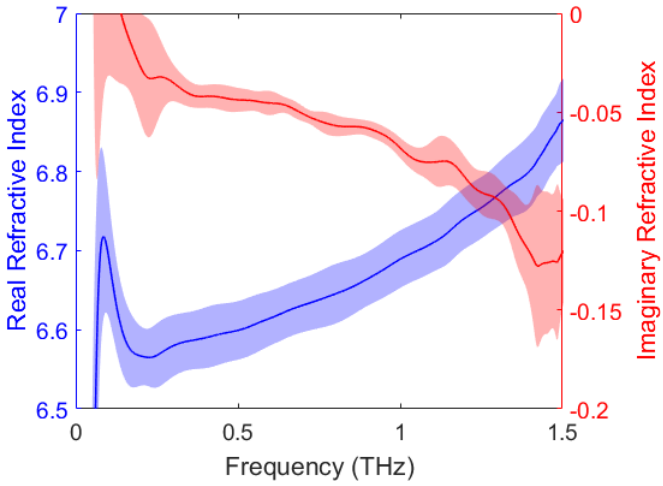

Figure 5.8: *Frequency dependent refractive index of lithium niobate at terahertz frequencies.*

.

diffraction as the free-space wavelength of the radiation becomes on a similar order of magnitude as the size of the sample and the detector, and so no conclusion can be drawn from this data. It would be useful here to refer to previous reports of the refractive index in this region to look for similar peaks at low frequencies, however many reports of refractive index of lithium niobate cut the frequencies below 0.5 THz to avoid spurious looking results [1, 2, 3].

Bibliography

[1] Wu, X.; Zhou, C.; Huang, W. R.; Ahr, F.; Kartner, F. X. Temperature dependent refractive index and absorption coefficient of congruent lithium niobate crystals in the terahertz range. *Optics Express* **2015**, *23*, 29729.

[2] Shao, G.; jun Ge, S.; chao Shi, Y.; Hu, W.; qing Lu, Y. Extended Cauchy equations of congruent $LiNbO_3$ in the terahertz band and their applications. *Optical Materials Express* **2016**, *6*, 3766.

[3] Unferdorben, M.; Szaller, Z.; Hajdara, I.; Hebling, J.; Palfalvi, L. Measurement of Refractive Index and Absorption Coefficient of Congruent

and Stoichiometric Lithium Niobate in the Terahertz Range. *Journal of Infrared, Millimeter, and Terahertz Waves* **2015**, *36*, 1203–1209.

Appendix C - Optically Tuned Refractive Index of $LiNbO_3$

Introduction

In this section I present changes in the refractive index of doped lithium niobate due to optical illumination of the crystal with a 462 nm laser source. The initial motivation for this set of measurements was to use the optical illumination to excite free carriers within the crystal to attenuate the THz transmission, and by fitting to a Drude model thereby calculate the total number of optically excited carriers within the lithium niobate. During analysis of the measurements it became clear that I could not fit the data to a Drude model for free carriers, which I now believe is due to the existence of strong phonon mode peaks which dominate the materials transmission properties at terahertz frequencies. Regardless of this shortcoming, the results are presented in this appendix as reference material for future work. The measurements were performed by Sophie Blundell during a summer internship in her undergraduate degree, and I have performed the analysis.

Results

In Figure 1(a) I present frequency dependent transmission through 1 mm thick crystal of iron doped lithium niobate (0.1 weight %) under five illumination conditions. Transmission is measured via the THz TDS setup in transmission mode. All transmission values are normalised with respect to the transmission measured through the crystal in dark conditions. It can be seen from the figure that as the crystal is illuminated the transmission decreases, where this effect is especially pronounced at higher frequencies, while at low frequencies below 0.2 THz there is negligible transmission change. Further, the figure shows that as the illumination intensity is increased the transmission decreases more strongly.

In Figure 1(b) I plot the transmission values at five select frequencies against the illumination power incident on the crystal from the blue 462 nm laser source. It can be seen that for each frequency there is generally a linear relation with transmission and illumination power, so I have therefore fitted each data set with a linear line. Further, the absolute value of the gradients appear to increase as the THz frequencies increase.

In Figure 1(c) I plot the gradient of the linear fit of transmission against power for each frequency from 0.1 to 1.0 THz for three crystals (0.1% doped $LiNbO_3$, 0.01% doped $LiNbO_3$, and undoped $LiNbO_3$), where the shaded

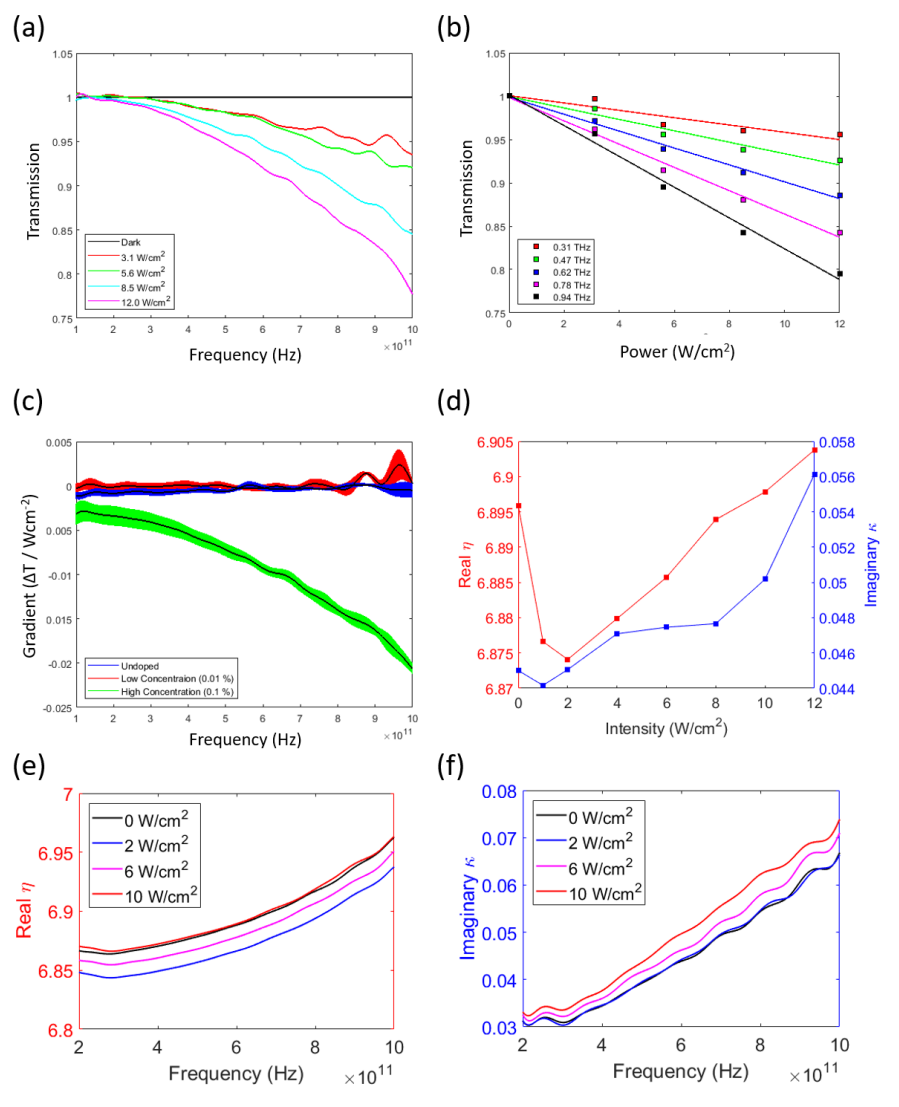

Figure 5.9: ***(a)*** *Frequency dependent transmission through Fe:$LiNbO_3$ (0.1 wt %) crystal for 5 illumination conditions.* ***(b)*** *Transmission plotted against illumination intensity for five select frequencies with linear fits.* ***(c)*** *Transmission vs illumination power gradients are plotted against frequency, with the error bars given as the standard error of the fitted gradients.* ***(d)*** *The complex refractive index for Fe:$LiNbO_3$ (0.1 wt %) plotted against illumination intensity.* ***(e)*** *Real refractive index for Fe:$LiNbO_3$ (0.1 wt %).* ***(f)*** *Imaginary refractive index for Fe:$LiNbO_3$ (0.1 wt %).*

error bars come from the standard error in the fitted gradient. It can be seen in the green line (for highly doped crystal) that indeed the transmission effect is especially pronounced at high frequencies, and the effect is far larger than the systematic error, however for the case of the low doped and undoped crystal the results reveal no transmission change in response to illumination.

In Figure 1(d) I extract the complex refractive index for the highly doped crystal as a function of illumination intensity. The complex refractive index values presented are taken at a frequency of 0.4 THz. It can be seen that the real part of the refractive index (n) begins around 6.9 however as the illumination is applied there is a sudden drop to around 6.87 (0.4 %), yet with further illumination intensity this trend reverses and n begins to increase again, ending slightly higher than it start point at 6.905. For the imaginary part of the refractive index the trend is slightly different as the effect appears to be generally linear with illumination intensity, however it the data is slightly noisy so it is difficult from these few data points to draw a precise conclusion. Regardless, we can see that the imaginary part (k) experiences a roughly 25 % increase in response to illumination at 12 W/cm^2.

Discussion

The results presented in this section reveal that optical illumination can alter the complex refractive index of lithium niobate, however the effect is only measurable for the highly doped crystal. It could be expected that the lower concentration doped crystal would also show a similar effect however with a 10 times smaller magnitude due to the difference in doping concentration. For the highly doped crystal there is a 30 % drop in transmission so for the lower concentration doped crystal this would scale to 3 % (assuming a linear correlation with doping concentration) however 3 % transmission changes are difficult to measure with THz TDS due to power fluctuations of the system, so it is highly likely that if they are present they would not be detected.

In an effort to find whether the low concentration doped substrate does exhibit an optically induced effect is may be possible to enhance the sensitivity of the measurement by performing a lock-in technique, where the blue laser is modulated with a beam chopper, and the mechanical delay stage held at the maximum peak of the terahertz pulse. This may be able to show optical modulation of average transmission, however would not retrieve any frequency dependent information.

The method of actuation here is not fully understood as is was not possible to fit the complex conductivity to a model for free carrier absorption such as the Drude model. A key issue here is that the real refractive index decreases and then increases, which when interpreted by the Drude model would suggest that one had moved over the resonance frequency, however the refractive index (and conductivity) both show a monotonic relation to frequency, and no resonance peak is measured in the available frequency range.

Similar trend reversal behaviour has been observed in Mg and Ce doped lithium niobate samples, in which optical illumination has been shown to create a refractive index change which decreases and then increases, where the turning point happens at similar levels of light intensity to those mentioned here [1, 2, 3]. In these publications (all from the same group) it is argued that the trend reversal is attributed to a light induced domain reversal in the crystal, however there arguments for this process are rather vague and the illumination intensities seem extremely low to allow for a domain reversal.

Therefore, I hypothesise that the effects observed here cannot be (fully) attributed to absorption by optically excited free carriers, and perhaps may be a thermal effect due to heating of the crystal by the laser source. This hypothesis is investigated in the next appendix section.

Bibliography

[1] Zuo, Z.-G.; Ling, F.-R.; Ma, D.-C.; Wu, L.; Liu, J.-S.; Yao, J.-Q. The effect of an optical pump on the absorption coefficient of magnesium-doped near-stoichiometric lithium niobate in terahertz range. *Chinese Physics B* **2013**, *22*, 107802.

[2] Wu, L.; Ling, F.; Zuo, Z.; Liu, J.; Yao, J. Far-infrared dispersion of the complex dielectric constant in ferroelectric near-stoichiometric $LiNbO_3$:Ce. *Journal of Optics* **2011**, *13*, 105501.

[3] Li, D.; Liu, Y.; Wang, H.; Yao, J.; Ling, F. Investigation of optical pumping on the dielectric properties of near-stoichiometric $LiNbO_3$: Mg in terahertz range. *Optik* **2015**, *126*, 4896–4898.

Appendix D - Thermally Tuned Refractive Index of $LiNbO_3$

Introduction

In this section I investigate the degree to which thermal effects may tune the refractive index of lithium niobate. This study is motivated on the back of the previous section (Appendix B) in which I show optical illumination is capable of tuning the refractive index of lithium niobate, however there appears to be more than one mechanism responsible as the real part of the refractive index first decreases, then increases with illumination intensity.

During the optical illumination with the 462 nm laser source I measured temperature increases up to 12 °C via a thermocouple mounted to the surface of the crystal. In the experiment presented here I mount a crystal of iron doped lithium niobate onto a temperature controlled ceramic heating element which has a 5 mm diameter hole in the centre for which a THz pulse may pass through allowing transmission measurements. The crystal starts at room temperature and is slowly heated, taking measurements at a range of temperatures up to 32 °C.

Results

In Figure 1(a) I present transmission through 1 mm thick iron doped lithium niobate crystal (0.1 weight %) measured at increasing temperatures. The transmission measurements are normalised to the transmission measured at room temperature. It can be seen from the graph that as the temperature is increased the transmission decreases at all frequencies, where the effect is most pronounced at higher frequencies. At a maximum temperature increase of 12 °C the transmission drops by around 10 % at 1 THz, while at 0.1 THz there is negligible change measured.

In Figure 1(b) I present the phase of the pulse travelling through the crystal, measured at various temperatures, where the phase is subtracted from the phase of the pulse travelling through the crystal at room temperature. From this graph it can be seen that initially at low temperatures the phase increases with heating for the first few degrees, however this trend then reverses and the phase drops for higher temperatures.

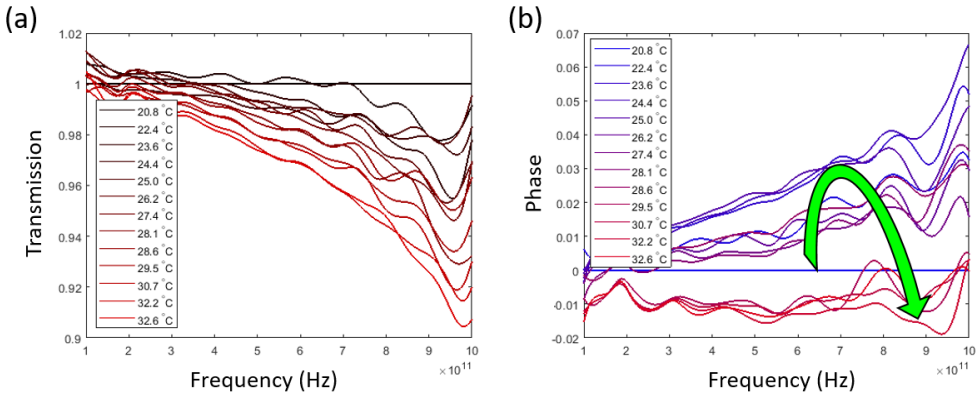

Figure 5.10: *Thermally induced changes in $LiNbO_3$ crystal **(a)** transmission and **(b)** phase. The green arrow highlights the trend reversal where the phase initially increases at low temperatures and then begins to decrease at higher temperatures.*

Discussion

The behaviour of the transmission and phase in response to thermal heating (transmission decreases at higher frequencies, and trend reversal in phase) are consistent with the results obtained by optical illumination of the crystal.

It is known that the refractive index of lithium niobate can be tuned thermally. This effect has been demonstrated to monotonically increase the refractive index, and no trend reversal was reported [1, 2], however both investigations were performed with undoped crystals whereas here I use iron doped lithium niobate which may exhibit additional behaviours.

It should be noted here however that this does not provide a conclusion to the actuation mechanism as it is known that thermal energy delivered to the Fe:$LiNbO_3$ crystal can release electrons from Fe trap sites in the photorefractive effect similar to optical illumination. To investigate further it would be advantageous to reproduce the experiment presented here with an undoped crystal as this may reveal that the trend reversal in refractive index is caused by the iron content in the crystal.

Bibliography

[1] Wu, X.; Zhou, C.; Huang, W. R.; Ahr, F.; Kartner, F. X. Temperature dependent refractive index and absorption coefficient of congruent lithium niobate crystals in the terahertz range. *Optics Express* **2015**, *23*, 29729.

[2] Shao, G.; jun Ge, S.; chao Shi, Y.; Hu, W.; qing Lu, Y. Extended Cauchy equations of congruent $LiNbO_3$ in the terahertz band and their applications. *Optical Materials Express* **2016**, *6*, 3766.

Appendix E - Published Articles

Optical Gating of Graphene on Photoconductive Fe:$LiNbO_3$

ACS NANO
Cite This: ACS Nano 2018, 12, 5940−5945
www.acsnano.org

ARTICLE

Optical Gating of Graphene on Photoconductive Fe:$LiNbO_3$

Jon Gorecki,*,† Vasilis Apostolopoulos,‡ Jun-Yu Ou,† Sakellaris Mailis,† and Nikitas Papasimakis†

†Optoelectronics Research Centre, University of Southampton, Southampton SO17 1BJ, U.K.
‡Department of Physics, University of Southampton, Southampton SO17 1BJ, U.K.

Supporting Information

ABSTRACT: We demonstrate experimentally nonvolatile, all-optical control of graphene's charge transport properties by virtue of an Fe:$LiNbO_3$ photoconductive substrate. The substrate can register and sustain photoinduced charge distributions which modify locally the electrostatic environment of the graphene monolayer and allow spatial control of graphene resistivity. We present light-induced changes of graphene sheet resistivity as high as ∼370 Ω/sq (∼2.6-fold increase) under spatially nonuniform light illumination. The light-induced modifications in the sheet resistivity are stable at room temperature but can be reversed by uniform illumination or thermal annealing (100 °C for 4 h), thus restoring graphene's electrical properties to their initial, preillumination values. The process can be subsequently repeated by further spatially nonuniform illumination.

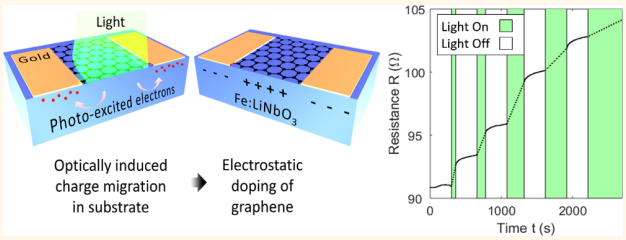

KEYWORDS: *graphene, two-dimensional materials, reconfigurable electronics, field-effect, photoconductive, lithium niobate*

Graphene, demonstrated to be the world's first truly two-dimensional monolayer material in 2004 by Novoselov and Geim,[1] has attracted intense research interest owing to its unique electrical and optical properties. Consisting of carbon atoms arranged in a two-dimensional hexagonal lattice, graphene exhibits a linear dispersion for electrons with the density of states vanishing at the Dirac point. This allows altering significantly graphene's electronic properties by injecting relatively small numbers of charge carriers.[2] In combination with the inherent high values of charge carrier mobility, these properties render graphene an appealing material for applications such as microelectromechanical systems (MEMS),[3] flexible touch-screen electrodes,[4,5] chemical sensing,[6,7] membranes,[8] and especially optoelectronic applications,[9] including photodetection.[10] Graphene has been shown to support strongly confined plasmonic excitations in the terahertz (THz)/infrared spectral (IR) range,[11] which allows the realization of miniaturized tunable devices.[12−14]

The charge transport properties of graphene are typically controlled through chemical doping,[15] by electrostatic gating[1] or by structuring. In the latter case, for example it is possible to create a band gap in graphene nanoribbons by patterning or unzipping of carbon nanotubes[16−18] or by combination with other 2D lattices[19] such as hexagonal boron nitride (hBN)[20] and transition metal dichalcogenides (TMDs).[21,22] In the case of electrostatic gating, a field-effect transistor (FET) configuration is usually employed, where graphene is placed on a Si/SiO_2 substrate acting as an insulated electrical backgate; the current transmitted through the device can then be altered by applying a gate voltage, which regulates the number of available charge carriers into graphene, thus modifying the sheet resistivity. However, such doping mechanisms require additional processing steps and/or do not provide substantial control over the spatial distribution of charge carriers. To this end, a number of light-assisted approaches have been put forward including photochemical effects,[23−25] where irradiation leads to exchange of dopants between the atmosphere and graphene, and photo-oxidation of organic layers, resulting in nonreversible charge transfer.[26] In addition, it has been shown that combining light illumination with an electrostatic gate can lead to charge exchange between graphene and the substrate.[27−29] Finally, depositing graphene on substrates with ferroelectric and pyroelectric properties allows control either through local electrostatic fields[30,31] or laser heating,[32] respectively. Here we present an approach toward spatially resolved control of the charge transport properties of monolayer graphene that is both reversible and nonvolatile, allowing for electrostatic charge distributions to be written or erased in an all-optical fashion.

Our approach is based on an Fe-doped lithium niobate (Fe:$LiNbO_3$) substrate, an electro-optic photoconductor that has been studied extensively in the past as a holographic storage medium.[33] $LiNbO_3$ is an artificial dielectric crystal that has found a multitude of uses in optoelectronics due to its combination of ferroelectric, pyroelectric, piezoelectric, electro-

Received: March 22, 2018
Accepted: May 17, 2018
Published: May 17, 2018

DOI: 10.1021/acsnano.8b02161
ACS Nano 2018, 12, 5940−5945

optic (Pockels), photovoltaic, and photoelastic effects.[34] $LiNbO_3$ exhibits a photorefraction effect;[35] Fe ion impurities in the crystal act as photoexcited charge centers, supplying electrons to the conduction band, which are free to migrate in the lattice. Depending on their valence state, these impurities can act as donors or acceptors; thus by nonuniform illumination of the substrate photoexcited electrons diffuse away from the irradiated area to dark regions, where they become trapped in acceptor Fe^{3+} sites, creating a nonuniform charge distribution that is stable at room temperature over long periods of time (years).[36] This ability to store photoinduced charge distributions locally, combined with the electro-optic effect that is inherent to the material, enabled the use of $Fe:LiNbO_3$ for the nonvolatile recording of holograms,[33] optoelectronic tweezers for manipulating nano-objects,[37] and optically aligned liquid crystal devices.[38] Here, we employ the photorefractive properties of $Fe:LiNbO_3$ to define the local electrostatic environment at the substrate surface using light. The schematic in Figure 1(a) illustrates the optical doping mechanism; nonuniform illumination of the substrate causes electron migration away from illuminated regions, creating a nonuniform surface charge distribution. This effect is capable of producing nonvolatile charge distributions of arbitrary shape, which can however be erased by uniform illumination or thermal annealing, which redistributes evenly the separated charge carriers. A graphene sheet on the surface of the substrate will experience an injection of charge carriers in response to the electrostatic environment of the $Fe:LiNbO_3$; as the charge carriers are injected, the Fermi level of the graphene is significantly altered, modifying its electrical properties. Here, we demonstrate a nonvolatile ~2.6× increase of the sheet resistivity of chemical vapor deposition (CVD)-grown monolayer graphene, which is subjected to the electric field of the substrate's local charge distributions. We show that the changes in the electrical properties of graphene are reversed by thermal annealing, and in fact literature suggests this behavior of $Fe:LiNbO_3$ can be repeated indefinitely.[33] We propose that the optical doping mechanism demonstrated here will enhance the potential of graphene for remote sensing applications and rewritable electrical interconnects and will allow the realization of plasmonic devices defined by structured illumination, removing the need for lithographic patterning of graphene. Moreover, the doping method demonstrated here is expected to be compatible with a wide range of TMDs and other 2D materials and hence will be of interest for numerous electronics and optoelectronics applications, including light emission and detection, optically controlled FETs, and sensing.[39−42]

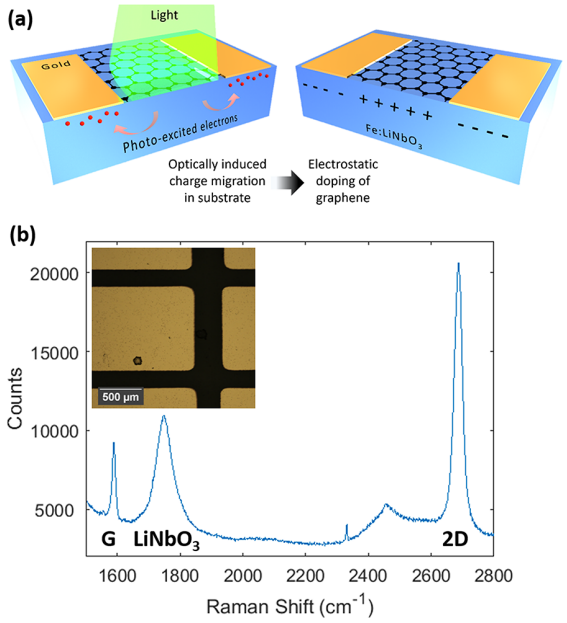

Figure 1. (a) Schematic illustration of the electrostatic environment in a graphene/$Fe:LiNbO_3$ composite under illumination. In the substrate, electrons photoexcited from Fe^{2+} centers to the conduction band are free to migrate in the lattice until being trapped by Fe^{3+} centers in the dark regions. This results in a nonuniform charge distribution in the substrate and subsequently in a spatially inhomogeneous electrostatic environment for the graphene layer, which in turn leads to inhomogeneous doping of the graphene layer. (b) Raman spectrum of graphene on a $Fe:LiNbO_3$ substrate exhibiting the graphene G peak at ~1580 cm^{-1} corresponding to an in-plane vibrational mode, the 2D peak at ~2700 cm^{-1} attributed to an overtone of the defect activated D peak (not pictured here), and the 2E lithium niobate peak at ~1750 cm^{-1}. Inset: Reflection mode optical microscopy image of the sample surface with deposited metallic electrodes. The dark regions between the electrodes correspond to the exposed parts of the (nonreflecting) graphene layer.

RESULTS AND DISCUSSION

For the purpose of our investigation we fabricated devices that consist of a uniform monolayer of CVD graphene, transferred to one of the polar surfaces ($-z$) of $Fe:LiNbO_3$ substrates. An array of gold metallic electrode pairs with varying spacing between them (see Methods) was fabricated on the graphene film. An optical microscopy image of the electrode arrangement is shown in the inset of Figure 1(b). Raman spectroscopy was used to characterize the graphene layer. The (~2:1) 2D/G peak ratio, observed in a Raman spectrum (Figure 1(b)), which has been obtained in a position between the electrodes, indicates the presence of a single graphene monolayer.

To illustrate the optical gating of graphene on $Fe:LiNbO_3$, the device was illuminated intermittently with alternating "bright" and "dark" periods (corresponding to "on" and "off" intervals in Figure 2, respectively). The resistance was measured at the end of each "bright" period and was monitored continuously during "dark" periods. The graphene-on-$Fe:LiNbO_3$ devices were illuminated uniformly using a low-intensity broadband light source (1 mW/cm^2). However, the metallic electrodes are opaque, leading to a nonuniform irradiation of the $Fe:LiNbO_3$ substrate. Here the area between electrodes was irradiated while the area under the electrodes remained dark. Current was not measured during illumination periods to avoid the applied potential voltage difference from influencing the migration of photoexcited electrons in the substrate (see Figure 2). During the measurement, a voltage of 0.1 V was applied across the electrodes and the current was recorded over a 300 s period while the device was kept in a light-proof box. The shaded areas of the graph correspond to the "bright" irradiation periods, while the clear sections correspond to "dark" periods. The graph shows that the resistance increases after each illumination period, and eventually, the effect reaches saturation with additional illumination producing negligible changes in the resistance as the photoelectron donor sites in $Fe:LiNbO_3$ are being depleted. Over the "dark" periods we observe negligible resistance changes (<1% or 2 Ω). After saturation the device is

DOI: 10.1021/acsnano.8b02161
ACS Nano 2018, 12, 5940−5945

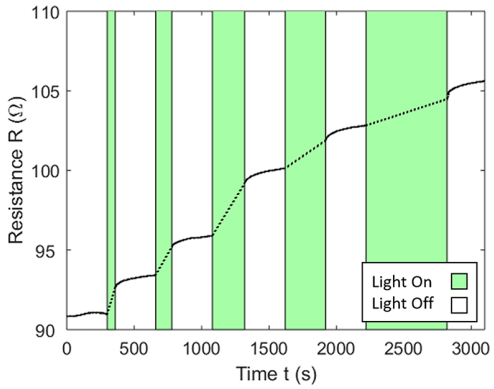

Figure 2. Light-induced changes in the charge transport properties of graphene on Fe:$LiNbO_3$. The sample is intermittently illuminated by a white light source with illumination periods of varying duration (shaded regions) being interrupted by 300 s periods (nonshaded regions) over which the device is stored in the dark. Measurements are obtained only during the latter periods, when the sample is not illuminated (solid black lines). Dashed lines over the illumination periods serve as a guide to the eye.

thermally annealed in a convection oven at 100 °C for 4 h to reset it to its initial state.

The observed light-induced resistance changes can be associated with changes in the graphene layer, but also to changes in the contact resistance between the electrode pads and the measurement probe tips. To evaluate the effect of illumination on the graphene resistivity and decouple it from the contact resistance, we employed the transmission line method (TLM),[43−45] where measurements are taken between electrodes with varying interelectrode spacing (see Methods). The measured resistance is plotted against the interelectrode spacing, and a straight line is fitted to the data, as shown in Figure 3(a). The slope of each line is used to calculate the resistivity of graphene, while the intercept with the vertical axis corresponds to the contact resistance. The TLM measurements were performed in the dark following irradiation. Successive irradiation/measurement steps were taken to generate a family of lines, as shown in Figure 3(a), each corresponding to a specific irradiation fluence. The graph shows that with each successive illumination period the gradient of the line is increased, which suggests an increase of graphene resistivity, while the vertical axis intercept is close to the zero point for each fitted line, suggesting the contact resistance is small and unchanged by illumination. The average contact resistance is determined to be 1.7 Ω. Thermal annealing of the device (100 °C for 4 h) resets the device to its initial state, and the resistivity measurement sequence can be performed again. We repeated the illumination/annealing cycle three times.

The resistivity change as a function of the illumination fluence is shown in the plot of Figure 3(b). The sheet resistivity values in Figure 3 were calculated from the slope of the linear fits, shown in Figure 3(a), where the standard error of the linear fitting is used to calculate the errors in resistivity values. Data from all three cycles showed similar behavior, and each time resistivity returned to initial preillumination values after annealing (see Supporting Information Figure S1, where three individual cycles are shown). Average resistivity of the three illumination cycles is taken for each fluence dose and the errors propagated forward as shown by the error bars in Figure 3(b). The resistivity, ρ, follows an exponential increase as a function of illumination fluence, F, which can be fitted by $\rho = a(1 - \exp^{(-F/F_0)}) + c$, where a = 373 Ω/sq, F_0 = 6318 mJ/cm^2, and c = 231 Ω/sq. This dependence suggests that the effect saturates to a resistivity value of 604 Ω/sq (~2.6-fold increase from initial preillumination values), reaching e^{-1} of saturation value at a fluence of 6318 mJ/cm^2. The secondary vertical axis, to the right, in the plot of Figure 3(b) provides the

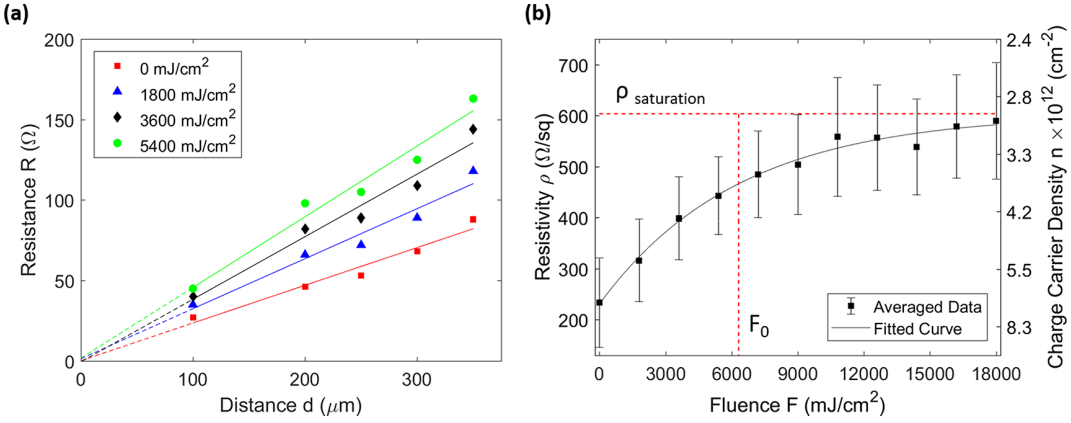

Figure 3. (a) Resistance measured across electrode pairs with varying interelectrode distance d, for four different values of irradiation fluence. Red squares: nonilluminated; blue triangles: 1800 mJ/cm^2; black diamonds: 3600 mJ/cm^2; green circles: 5400 mJ/cm^2. Error bars are omitted because the standard error was 4 orders of magnitude smaller than the resistance. The straight lines in the plot correspond to linear regression fits. The slope of the lines is used to calculate the sheet resistivity, while the vertical axis intercept corresponds to 2 times the contact resistance. Standard error of the gradient is used to quantify the error in the calculated resistivity value. (b) Graphene sheet resistvity is measured *via* the TLM method as a function of illumination fluence for three independent illumination cycles. Each illumination cycle provides the device with a total fluence dose of 18 000 mJ/cm^2, at which point further changes in resistivity are negligible. The sample is then reset *via* the thermal annealing process. The average resistivities of the three cycles are plotted against fluence, showing an inverse exponential trend. An inverse exponential curve is fitted *via* a regression method, revealing the effect saturates at a final resistivity of 604 Ω/sq, reaching e^{-1} of saturation value after a fluence dose of 6318 mJ/cm^2. Errors in resistivty at each fluence value are calculated using the standard error of the fitted gradient, as illustrated in (a) for each illumination cycle and propagated forward to account for averaging between the three illumination cycles.

DOI: 10.1021/acsnano.8b02161
ACS Nano 2018, 12, 5940−5945

corresponding values for charge carrier density calculated from the measured resistivity values, electron charge, and using a mobility value of 3760 $cm^2\ V^{-1}\ s^{-1}$, as characterized by the supplier of the graphene monolayer. The graph indicates that the carrier density decreases by a factor of ~3 (corresponding to a modulation of carrier density ~5.5×10^{12} cm^{-2}) with increasing illumination. A control device consisting of graphene on a Si/SiO_2 substrate with an identical (to the $Fe:LiNbO_3$ sample) electrode array was used to confirm that the changes in graphene resistivity are substrate-specific (see Supporting Information Figure S3), as a negligible increase of the resistivity was observed in the control sample as a function of irradiating fluence.

The experimental errors in resistivity values as plotted in Figure 3(b) are due in part to the TLM method, which combines measurements across different pairs of electrodes in different areas of the sample and therefore assumes identical contact resistance across the whole array of contacts and a uniform graphene sheet resistivity. However, we expect that both factors are subjected to spatial variation across the substrate, especially with polycrystalline CVD graphene. Furthermore, the deposition of electrodes and electrical probing can be detrimental to the graphene layer. Literature suggests accurate measurements of graphene sheet resistivity and charge carrier mobility can be obtained *via* terahertz time domain spectroscopy,[46] and the process is noncontact and therefore nondestructive to the sample.

The observed change in the resistance as a function of nonuniform illumination is attributed to photoexcited electrons in $Fe:LiNbO_3$, which diffuse and become trapped in the dark, nonilluminated, regions (see schematic illustration of Figure 1(a)). This charge migration effect is well documented in $Fe:LiNbO_3$ and can produce space charge distributions that are stable in the dark for long periods of time (years).[36] The response time of charge migration is a function of illumination intensity[47] and can reach sub-picosecond time scales under pulsed illumination.[48,49] Furthermore, the charge migration effect can create charge distributions of sub-micrometer dimensions.[36] In particular, as we illuminate the $Fe:LiNbO_3$ crystal, we are moving electrons away from the illuminated area and under the electrodes where they become trapped. When the illumination stops, this process creates a positive region underneath graphene, which due to its metallic behavior draws electrons from the electrodes. Because CVD graphene generally exhibits residual hole doping due to the fabrication process,[50,51] the injection of electrons due to the illumination will result in a net decrease in charge carrier density, and therefore the resistivity is expected to increase with increasing fluence. Assuming the graphene sheet follows a typical behavior where resistivity reaches a maximal value when charge carrier concentration is zero and decreases as carriers are injected,[1] then starting with hole-doped graphene and a sufficiently strong optical doping effect, it may be possible to pass over the point of maximum resistivity and therefore begin to decrease the resistivity. The experimental results presented here suggest the optical doping method was not of sufficient strength to shift the graphene entirely from the hole to the electron-doped region. Practically this may be achieved by the use of an electrical top-gate as an additional method to control the charge carrier density of the device and bring the graphene sheet closer to its charge neutrality point. A top-gate could also be used to bring the graphene to the point of maximum rate of change of resistivity with respect to charge carrier concentration, thereby allowing the optical gating effect on resistivity to exhibit maximum responsivity. The photorefractive sensitivity of $Fe:LiNbO_3$ increases in blue and green regions of the visible spectrum, so it is reasonable to assume that if repeated with blue laser irradiation the experiment would achieve lower F_0 values than with broadband white light. Furthermore, the response time of the effect could be reduced by increasing the intensity of the irradiation, i.e., using a pulsed source.

The optical method to locally control the graphene doping that is introduced in this work can be readily extended to the control of graphene plasmons. Indeed, our results indicate that illumination can be employed to change the charge carrier concentration of graphene by a factor of 5.5×10^{12} cm^{-2}, which in the absence of intrinsic doping corresponds to a change in the graphene Fermi level of 0.3 eV. Such effects are sufficient to practically switch "on" and "off" plasmonic excitations in graphene microstructures over the microwave and THz spectral ranges.[11,52] Moreover, the optical control of the graphene spatial doping profile could allow the definition of graphene plasmonic resonators simply through nonuniform illumination of continuous graphene layers, alleviating thus the requirement for patterning.

We propose that the optical doping mechanism presented here is not limited to application with only graphene and would be a versatile tool for investigating doping effects in a wide range of emerging 2D materials. Since the initial identification of graphene by Geim and Novoselov, the study of 2D materials has grown rapidly into its own field,[53,54] yielding materials with unique properties especially of interest in optoelectronics[55] such as molybdenum disulfide,[56] silicene,[57] and black phosphorus,[58] where a primary motivation for moving to 2D materials beyond graphene is to find materials that exhibit a band gap while still maintaining high values of charge carrier mobility. We expect that our approach will enable sensing applications, rewritable electrical interconnects, and the possibility of reconfigurable plasmonic structures defined by structured illumination.

CONCLUSIONS

We have demonstrated nonvolatile control of graphene electrical resistivity by virtue of optically driven charge redistribution in iron-doped lithium niobate. Graphene on $Fe:LiNbO_3$ was illuminated *via* a broadband white light source, achieving a maximum increase in resistivity of ~370 Ω/sq (~2.6-fold increase), while a control sample of graphene on Si/SiO_2 showed a negligible change in electrical properties after illumination. For graphene on $Fe:LiNbO_3$ we calculated that the charge migration within the substrate can induce charge carrier density modulation on the order of $5.5 \times 10^{12}/cm^2$ in the graphene sheet. We have conducted our experiments using broadband white light illumination; however the writing speed could be improved using blue or green laser light. The ability to optically control the electrical resistivity of graphene in a spatially resolved, nonvolatile, reversible manner will enable the investigation of the electronic properties of graphene and other emerging 2D materials.

METHODS

Fabrication. Monolayer CVD graphene grown on a copper substrate (obtained commercially from Graphenea) was transferred *via* a sacrificial polymer layer onto *z* cut $Fe:LiNbO_3$ (0.1 wt %). Metallic electrodes were created *via* thermal resistance evaporation of a Cr/Au layer (5/100 nm) with a shadow mask to partially obscure sections of

DOI: 10.1021/acsnano.8b02161
ACS Nano 2018, 12, 5940−5945

the substrate to create an array of electrode pads. The metallic electrodes were patterned with a varying interelectrode distance as required by TLM to decouple the contact and sheet resistivities. A similar procedure was followed for the fabrication of a control sample consisting of a graphene monolayer deposited on a Si/SiO_2substrate.

Raman Characterization. Raman spectroscopy is used to characterize the graphene layer after deposition onto the substrate, using a 632 nm laser source to probe the graphene with a 50× objective lens. The Raman spectrum is shown in Figure 1(b), where the high ratio of heights of the 2D:G peak is a characteristic sign of monolayer graphene.[59] The broad peak centered around 1750 cm^{-1} is due to luminescence of the $Fe:LiNbO_3$ substrate.

Electrical Characterization. An Agilent 4155c electrical parameter analyzer is used in a two-probe configuration to pass a voltage (sweeping from −0.1 V to +0.1 V with a step of 1 mV) while measuring the current passing through the circuit. The transition line method is used to determine sheet resistivity; the method requires an array of electrodes with varying interelectrode spacing, and each is assumed to have identical contact resistance. By measuring resistance across a pair of electrodes the total resistance is the sum of two contact resistances and a graphene resistance equal to the sheet resistivity multiplied by electrode width divided by electrode gap. By plotting the total resistance against electrode gap the sheet and contact resistances can be decoupled, where contact resistance is half the value of the *y* axis intercept and sheet resistivity is the gradient multiplied by channel width divided by electrode length. A linear regression analysis is used to calculate the line of best fit; the standard error of the gradient is used as an estimate of the error in the sheet resistivity. All measurements are performed in a cleanroom environment to ensure stable control over temperature and humidity conditions. A broadband white light source is used for illumination of the substrate, delivering a power of 1 mW/cm^2 as measured at the surface of the sample, in the wavelength range 400−800 nm.

Thermal Annealing. After illumination devices are thermally annealed in a convection oven (100 °C for 4 h) to restore the $Fe:LiNbO_3$ substrate to a state of uniform charge distribution.

ASSOCIATED CONTENT

Supporting Information

The Supporting Information is available free of charge on the ACS Publications website at DOI: 10.1021/acsnano.8b02161.

Sheet resistivity measurements for three independent illumination cycles, contact resistance characterization, and control device measurements (PDF)

AUTHOR INFORMATION

Corresponding Author

*E-mail: j.gorecki@soton.ac.uk.

ORCID

Jon Gorecki: 0000-0001-9205-2294

Jun-Yu Ou: 0000-0001-8028-6130

Notes

The authors declare no competing financial interest.

ACKNOWLEDGMENTS

The authors thank F. Javier Garcia de Abajo for stimulating discussions. We acknowledge financial support from the UK's Engineering and Physical Sciences Council through the Teranet network (grant EP/M00306X/1). All data supporting this study are openly available from the University of Southampton repository at https://doi.org/10.5258/SOTON/D0521.

REFERENCES

(1) Novoselov, K.; Geim, A.; Morozov, S.; Jiang, D.; Zhang, Y.; Dubonos, S.; Grigorieva, I.; Firsov, A. Electric Field Effect in Atomically Thin Carbon Films. *Science* **2004**, *306*, 666−669.

(2) Castro Neto, A. H.; Guinea, F.; Peres, N. M. R.; Novoselov, K. S.; Geim, A. K. The Electronic Properties of Graphene. *Rev. Mod. Phys.* **2009**, *81*, 109−162.

(3) Zang, X.; Zhou, Q.; Chang, J.; Liu, Y.; Lin, L. Graphene and Carbon Nanotube (CNT) in MEMS/NEMS Applications. *Microelectron. Eng.* **2015**, *132*, 192−206.

(4) Huang, X.; Zeng, Z.; Fan, Z.; Liu, J.; Zhang, H. Graphene-Based Electrodes. *Adv. Mater.* **2012**, *24*, 5979−6004.

(5) Bae, S.; Kim, H.; Lee, Y.; Xu, X.; Park, J.-S.; Zheng, Y.; Balakrishnan, J.; Lei, T.; Kim, H. R.; Song, Y. I.; Kim, Y.-J.; Kim, K. S.; Ozyilmaz, B.; Ahn, J.-H.; Hong, B. H.; Iijima, S. Roll-to-Roll Production of 30-Inch Graphene Films for Transparent Electrodes. *Nat. Nanotechnol.* **2010**, *5*, 574−578.

(6) Schedin, F.; Geim, A. K.; Morozov, S. V.; Hill, E. W.; Blake, P.; Katsnelson, M. I.; Novoselov, K. S. Detection of Individual Gas Molecules Adsorbed on Graphene. *Nat. Mater.* **2007**, *6*, 652−655.

(7) Shao, Y.; Wang, J.; Wu, H.; Liu, J.; Aksay, I. A.; Lin, Y. Graphene Based Electrochemical Sensors and Biosensors: A Review. *Electroanalysis* **2010**, *22*, 1027−1036.

(8) Liu, G.; Jin, W.; Xu, N. Graphene-Based Membranes. *Chem. Soc. Rev.* **2015**, *44*, 5016−5030.

(9) Bonaccorso, F.; Sun, Z.; Hasan, T.; Ferrari, A. C. Graphene Photonics and Optoelectronics. *Nat. Photonics* **2010**, *4*, 611−622.

(10) Liu, C.-H.; Chang, Y.-C.; Norris, T. B.; Zhong, Z. Graphene Photodetectors with Ultra-Broadband and High Responsivity at Room Temperature. *Nat. Nanotechnol.* **2014**, *9*, 273−278.

(11) Jablan, M.; Buljan, H.; Soljacic, M. Plasmonics in Graphene at Infrared Frequencies. *Phys. Rev. B: Condens. Matter Mater. Phys.* **2009**, *80*, in press.

(12) Grigorenko, A. N.; Polini, M.; Novoselov, K. S. Graphene Plasmonics. *Nat. Photonics* **2012**, *6*, 749−758.

(13) Fei, Z.; Rodin, A. S.; Andreev, G. O.; Bao, W.; McLeod, A. S.; Wagner, M.; Zhang, L. M.; Zhao, Z.; Thiemens, M.; Dominguez, G.; Fogler, M. M.; Castro Neto, A. H.; Lau, C. N.; Keilmann, F.; Basov, D. N. Gate-Tuning of Graphene Plasmons Revealed by Infrared Nano-Imaging. *Nature* **2012**, *487*, 82−85.

(14) Chen, J.; Badioli, M.; Alonso-Gonzalez, P.; Thongrattanasiri, S.; Huth, F.; Osmond, J.; Spasenovic, M.; Centeno, A.; Pesquera, A.; Godignon, P.; Zurutuza Elorza, A.; Camara, N.; Javier Garcia de Abajo, F.; Hillenbrand, R.; Koppens, F. H. L. Optical Nano-Imaging of Gate-Tunable Graphene Plasmons. *Nature* **2012**, *487*, 77−81.

(15) Wang, X.; Li, X.; Zhang, L.; Yoon, Y.; Weber, P. K.; Wang, H.; Guo, J.; Dai, H. N-Doping of Graphene Through Electrothermal Reactions with Ammonia. *Science* **2009**, *324*, 768−771.

(16) Han, M. Y.; Oezyilmaz, B.; Zhang, Y.; Kim, P. Energy Band-Gap Engineering of Graphene Nanoribbons. *Phys. Rev. Lett.* **2007**, *98*, in press DOI: 10.1103/PhysRevLett.98.206805.

(17) Son, Y.-W.; Cohen, M. L.; Louie, S. G. Energy Gaps in Graphene Nanoribbons. *Phys. Rev. Lett.* **2006**, *97*, in press DOI: 10.1103/PhysRevLett.97.216803.

(18) Kosynkin, D. V.; Higginbotham, A. L.; Sinitskii, A.; Lomeda, J. R.; Dimiev, A.; Price, B. K.; Tour, J. M. Longitudinal Unzipping of Carbon Nanotubes to form Graphene Nanoribbons. *Nature* **2009**, *458*, 872−876.

(19) Das Sarma, S.; Adam, S.; Hwang, E. H.; Rossi, E. Electronic Transport in Two-Dimensional Graphene. *Rev. Mod. Phys.* **2011**, *83*, 407−470.

(20) Dean, C. R.; Young, A. F.; Meric, I.; Lee, C.; Wang, L.; Sorgenfrei, S.; Watanabe, K.; Taniguchi, T.; Kim, P.; Shepard, K. L.; Hone, J. Boron Nitride Substrates for High-Quality Graphene Electronics. *Nat. Nanotechnol.* **2010**, *5*, 722−726.

(21) Britnell, L.; Ribeiro, R. M.; Eckmann, A.; Jalil, R.; Belle, B. D.; Mishchenko, A.; Kim, Y. J.; Gorbachev, R. V.; Georgiou, T.; Morozov, S. V.; Grigorenko, A. N.; Geim, A. K.; Casiraghi, C.; Castro Neto, A.

H.; Novoselov, K. S. Strong Light-Matter Interactions in Heterostructures of Atomically Thin Films. *Science* **2013**, *340*, 1311−1314.
(22) Geim, A. K.; Grigorieva, I. V. Van der Waals Heterostructures. *Nature* **2013**, *499*, 419−425.
(23) Iqbal, M. Z.; Iqbal, M. W.; Khan, M. F.; Eom, J. Ultraviolet-Light-Driven Doping Modulation in Chemical Vapor Deposition Grown Graphene. *Phys. Chem. Chem. Phys.* **2015**, *17*, 20551−20556.
(24) Wang, H. I.; Braatz, M.-L.; Richter, N.; Tielrooij, K.-J.; Mics, Z.; Lu, H.; Weber, N.-E.; Muellen, K.; Turchinovich, D.; Klaeui, M.; Bonn, M. Reversible Photochemical Control of Doping Levels in Supported Graphene. *J. Phys. Chem. C* **2017**, *121*, 4083−4091.
(25) Tiberj, A.; Rubio-Roy, M.; Paillet, M.; Huntzinger, J. R.; Landois, P.; Mikolasek, M.; Contreras, S.; Sauvajol, J. L.; Dujardin, E.; Zahab, A. A. Reversible Optical Doping of Graphene. *Sci. Rep.* **2013**, *3*, in press DOI: 10.1038/srep02355.
(26) Seo, B. H.; Youn, J.; Shim, M. Direct Laser Writing of Air-Stable p-n Junctions in Graphene. *ACS Nano* **2014**, *8*, 8831−8836.
(27) Wang, X.-J.; Zou, L.; Li, D.; Zhang, Q.; Wang, F.; Zhang, Z. Photo-Induced Doping in Graphene/Silicon Heterostructures. *J. Phys. Chem. C* **2015**, *119*, 1061−1066.
(28) Ho, P.-H.; Chen, C.-H.; Shih, F.-Y.; Chang, Y.-R.; Li, S.-S.; Wang, W.-H.; Shih, M.-C.; Chen, W.-T.; Chiu, Y.-P.; Li, M.-K.; Shih, Y.-S.; Chen, C.-W. Precisely Controlled Ultrastrong Photoinduced Doping at Graphene-Heterostructures Assisted by Trap-State-Mediated Charge Transfer. *Adv. Mater.* **2015**, *27*, 7809−7815.
(29) Jun, L.; Velasco, J., Jr.; Huang, E.; Kahn, S.; Nosiglia, C.; Tsai, H.-Z.; Yang, W.; Taniguchi, T.; Watanabe, K.; Zhang, Y.; Zhang, G.; Crommie, M.; Zettl, A.; Wang, F. Photoinduced Doping in Heterostructures of Graphene and Boron Nitride. *Nat. Nanotechnol.* **2014**, *9*, 348−352.
(30) Yusuf, M. H.; Gura, A.; Du, X.; Dawber, M. Local Control of the Resistivity of Graphene Through Mechanically Induced Switching of a Ferroelectric Superlattice. *2D Mater.* **2017**, *4*, 021022.
(31) Papasimakis, N.; Mailis, S.; Huang, C. C.; Al-Saab, F.; Hewak, D. W.; Luo, Z.; Shen, Z. X. Strain Engineering in Graphene by Laser Irradiation. *Appl. Phys. Lett.* **2015**, *106*, 061904.
(32) Gopalan, K. K.; Janner, D.; Nanot, S.; Parret, R.; Lundeberg, M. B.; Koppens, F. H. L.; Pruneri, V. Mid-Infrared Pyroresistive Graphene Detector on $LiNbO_3$. *Adv. Opt. Mater.* **2017**, *5*, in press DOI: 10.1002/adom.201770025.
(33) Buse, K.; Adibi, A.; Psaltis, D. Non-Volatile Holographic Storage in Doubly Doped Lithium Niobate Crystals. *Nature* **1998**, *393*, 665−668.
(34) Weis, R. S.; Gaylord, T. K. Lithium-Niobate - Summary of Physical Properties and Crystal Structure. *Appl. Phys. A: Solids Surf.* **1985**, *37*, 191−203.
(35) Buse, K.; Imbrock, J.; Kratzig, E.; Peithmann, K. In *Photorefractive Materials and Their Applications 2: Applications*; Gunter, P., Huignard, J., Eds.; Springer: New York, 2007; pp 83−86.
(36) Arizmendi, L.; Lopez-Barbera, F. J. Lifetime of Thermally Fixed Holograms in $LiNbO_3$ Crystals Doped with Mg and Fe. *Appl. Phys. B: Lasers Opt.* **2007**, *86*, 105−109.
(37) Carrascosa, M.; Garcia-Cabanes, A.; Jubera, M.; Ramiro, J. B.; Agullo-Lopez, F. $LiNbO_3$: A Photovoltaic Substrate for Massive Parallel Manipulation and Patterning of Nano-Objects. *Appl. Phys. Rev.* **2015**, *2*, 040605.
(38) Lucchetti, L.; Kushnir, K.; Reshetnyak, V.; Ciciulla, F.; Zaltron, A.; Sada, C.; Simoni, F. Light-Induced Electric Field Generated by Photovoltaic Substrates Investigated Through Liquid Crystal Reorientation. *Opt. Mater.* **2017**, *73*, 64−69.
(39) Bhimanapati, G. R.; Lin, Z.; Meunier, V.; Jung, Y.; Cha, J.; Das, S.; Xiao, D.; Son, Y.; Strano, M. S.; Cooper, V. R.; Liang, L.; Louie, S. G.; Ringe, E.; Zhou, W.; Kim, S. S.; Naik, R. R.; Sumpter, B. G.; Terrones, H.; Xia, F.; Wang, Y.; et al. Recent Advances in Two-Dimensional Materials beyond Graphene. *ACS Nano* **2015**, *9*, 11509−11539.
(40) Liu, Y.; Weiss, N. O.; Duan, X.; Cheng, H.-C.; Huang, Y.; Duan, X. Van der Waals Heterostructures and Devices. *Nat. Rev. Mater.* **2016**, *1*, 16042.
(41) Novoselov, K. S.; Mishchenko, A.; Carvalho, A.; Castro Neto, A. H. 2D Materials and van der Waals Heterostructures. *Science* **2016**, *353*, aac9439.
(42) Manzeli, S.; Ovchinnikov, D.; Pasquier, D.; Yazyev, O. V.; Kis, A. 2D Transition Metal Dichalcogenides. *Nat. Rev. Mater.* **2017**, *2*, 17033.
(43) Xia, F.; Perebeinos, V.; Lin, Y.-m.; Wu, Y.; Avouris, P. The Origins and Limits of Metal-Graphene Junction Resistance. *Nat. Nanotechnol.* **2011**, *6*, 179−184.
(44) Venugopal, A.; Colombo, L.; Vogel, E. M. Contact Resistance in Few and Multilayer Graphene Devices. *Appl. Phys. Lett.* **2010**, *96*, 013512.
(45) Smith, J. T.; Franklin, A. D.; Farmer, D. B.; Dimitrakopoulos, C. D. Reducing Contact Resistance in Graphene Devices through Contact Area Patterning. *ACS Nano* **2013**, *7*, 3661−3667.
(46) Boggild, P.; Mackenzie, D. M. A.; Whelan, P. R.; Petersen, D. H.; Buron, J. D.; Zurutuza, A.; Gallop, J.; Hao, L.; Jepsen, P. U. Mapping the Electrical Properties of Large-Area Graphene. *2D Mater.* **2017**, *4*, 042003.
(47) Chen, F. S. Optically Induced Change of Refractive Indices in $LiNbO_3$ and $LiTaO_3$. *J. Appl. Phys.* **1969**, *40*, 3389−3396.
(48) Hsieh, H.; Psaltis, D.; Beyer, O.; Maxein, D.; von Korff Schmising, C.; Buse, K.; Sturman, B. Femtosecond Holography in Lithium Niobate Crystals. *Opt. Lett.* **2005**, *30*, 2233−2235.
(49) Paipulas, D.; Buivydas, R.; Juodkazis, S.; Mizeikis, V. Local Photorefractive Modification in Lithium Niobate Using Ultrafast Direct Laser Write Technique. *J. Laser Micro/Nanoeng.* **2016**, *11*, 246−252.
(50) Chan, J.; Venugopal, A.; Pirkle, A.; McDonnell, S.; Hinojos, D.; Magnuson, C. W.; Ruoff, R. S.; Colombo, L.; Wallace, R. M.; Vogel, E. M. Reducing Extrinsic Performance-Limiting Factors in Graphene Grown by Chemical Vapor Deposition. *ACS Nano* **2012**, *6*, 3224−3229.
(51) Pirkle, A.; Chan, J.; Venugopal, A.; Hinojos, D.; Magnuson, C. W.; McDonnell, S.; Colombo, L.; Vogel, E. M.; Ruoff, R. S.; Wallace, R. M. The Effect of Chemical Residues on the Physical and Electrical Properties of Chemical Vapor Deposited Graphene Transferred to SiO_2. *Appl. Phys. Lett.* **2011**, *99*, 122108.
(52) Thongrattanasiri, S.; Silveiro, I.; Javier Garcia de Abajo, F. Plasmons in Electrostatically Doped Graphene. *Appl. Phys. Lett.* **2012**, *100*, 201105.
(53) Miro, P.; Audiffred, M.; Heine, T. An Atlas of Two-Dimensional Materials. *Chem. Soc. Rev.* **2014**, *43*, 6537−6554.
(54) Mas-Balleste, R.; Gomez-Navarro, C.; Gomez-Herrero, J.; Zamora, F. 2D Materials: to Graphene and Beyond. *Nanoscale* **2011**, *3*, 20−30.
(55) Ponraj, J. S.; Xu, Z.-Q.; Dhanabalan, S. C.; Mu, H.; Wang, Y.; Yuan, J.; Li, P.; Thakur, S.; Ashrafi, M.; Mccoubrey, K.; Zhang, Y.; Li, S.; Zhang, H.; Bao, Q. Photonics and Optoelectronics of Two-Dimensional Materials Beyond Graphene. *Nanotechnology* **2016**, *27*, 462001.
(56) Mak, K. F.; Lee, C.; Hone, J.; Shan, J.; Heinz, T. F. Atomically Thin MoS_2: A New Direct-Gap Semiconductor. *Phys. Rev. Lett.* **2010**, *105*, in press DOI: 10.1103/PhysRevLett.105.136805.
(57) Vogt, P.; De Padova, P.; Quaresima, C.; Avila, J.; Frantzeskakis, E.; Asensio, M. C.; Resta, A.; Ealet, B.; Le Lay, G. Silicene: Compelling Experimental Evidence for Graphene like Two-Dimensional Silicon. *Phys. Rev. Lett.* **2012**, *108*. DOI: 10.1103/PhysRevLett.108.155501
(58) Liu, H.; Neal, A. T.; Zhu, Z.; Luo, Z.; Xu, X.; Tomanek, D.; Ye, P. D. Phosphorene: An Unexplored 2D Semiconductor with a High Hole Mobility. *ACS Nano* **2014**, *8*, 4033−4041.
(59) Ferrari, A. C.; Basko, D. M. Raman Spectroscopy as a Versatile Tool for Studying the Properties of Graphene. *Nat. Nanotechnol.* **2013**, *8*, 235−246.

DOI: 10.1021/acsnano.8b02161
ACS Nano 2018, 12, 5940−5945

Optically Reconfigurable Graphene/Metal Metasurface on Fe:$LiNbO_3$ for Adaptive THz Optics

ACS APPLIED NANO MATERIALS

www.acsanm.org Article

Optically Reconfigurable Graphene/Metal Metasurface on Fe:$LiNbO_3$ for Adaptive THz Optics

Jon Gorecki,* Lewis Piper, Adnane Noual, Sakellaris Mailis, Nikitas Papasimakis, and Vasilis Apostolopoulos

Cite This: *ACS Appl. Nano Mater.* 2020, 3, 9494−9501 Read Online

ACCESS | Metrics & More | Article Recommendations | Supporting Information

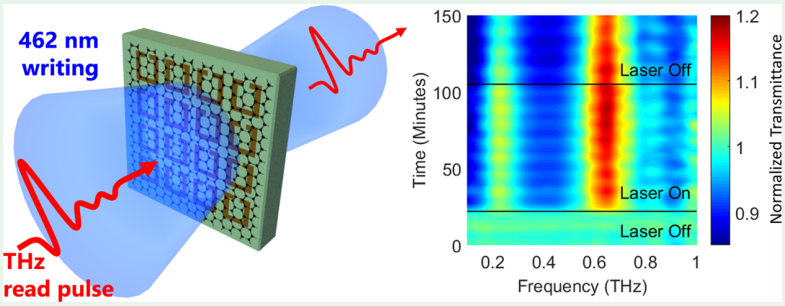

ABSTRACT: We demonstrate, experimentally, nonvolatile optical control of terahertz metasurfaces composed of a metallic split-ring resonator array sandwiched between monolayer graphene and a photoconductive Fe:$LiNbO_3$ substrate. We demonstrate frequency-selective tuning of THz transmission amplitude, and our results pave the way toward spatially resolved control of THZ metasurfaces for beam steering, imaging, and sensing applications. The substrate (Fe:$LiNbO_3$) supports nonvolatile yet reversible photoinduced charge distributions, which locally modify the electrostatic environment of the nano-thickness graphene monolayer, altering the graphene electrical conductivity and therefore changing the resonance spectra of the metamaterial array. We present light-induced normalized transmittance changes up to 35% that are nonvolatile and persist after the illumination source is removed yet can be reversed by thermal annealing.

KEYWORDS: *tunable, metamaterials, plasmonic, lithium niobate, terahertz, 2D materials, nonvolatile*

1. INTRODUCTION

Terahertz frequencies show potential for technological applications in a wide range of areas, such as spectroscopy of biological samples,[1−4] detection of concealed drugs and explosives,[5−7] imaging of astronomical objects,[8,9] industrial quality control of semiconductor manufacturing,[10,11] and broad bandwidth telecommunication systems.[12,13] Despite this wide array of applications, there is a lack of optoelectronic devices for the tuning of phase, amplitude, and polarization of terahertz radiation. To this end, a variety of tuning techniques based on optical,[14−16] thermal,[17,18] electronic,[19−21] and mechanical[22,23] actuation methods have been developed. Optical actuation methods generally offer an advantage over other approaches in that they readily allow for large areas of the tuning device to be addressed in parallel and with micron-scale spatial resolution, although such mechanisms are typically volatile. Early demonstrations relied on optically excited charge carriers in bulk semiconductors.[14−16,24] Under illumination with a pump laser, electrons are excited from the valence to the conduction band and consequently act as a free-carrier plasma interacting strongly with THz radiation. Optical tuning by this method has been demonstrated in silicon[14−16] and GaAs[16] where the resultant amplitude tuning is a broad band effect, which decays on the order of the charge recombination time of the semiconductor material (τ_{Si} ∼100 ns, τ_{GaAs} ∼ 1 ns). The effect has also been employed in combination with structured illumination for wavefront shaping[24] and tunable plasmonic gratings.[25] Semiconductors have been combined with two-dimensional (2D) materials to enhance the photoabsorption effects, where photoexcited carriers within the semiconductor diffuse into the 2D material where they experience a significantly higher mobility and therefore interact more strongly to absorb the THz radiation.[26,27] To implement further functionality into tuning devices, it can be desirable to incorporate metamaterials as they have been demonstrated to allow for strong absorption with highly frequency selective spectra.[28−32] Metamaterials fabricated on semi-insulating

Received: August 19, 2020
Accepted: August 26, 2020
Published: September 7, 2020

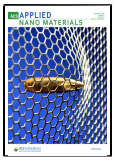

GaAs,[33,34] silicon,[35−39] and ErAs/GaAs[40] have been demonstrated where tuning of the substrate dielectric properties affects the plasmonic resonance of the metamaterial array. Further, the combination of 2D materials with metamaterials and semiconductors allows us to tune metamaterial resonance through optical doping of the 2D material by the semiconductor substrate.[41,42] Such mechanisms based on photoexcited charge carriers are volatile and do not persist once the illumination source is removed; it is therefore advantageous to look toward optically actuated mechanisms that are nonvolatile. Phase-change materials have been demonstrated as a platform for tunable nonvolatile plasmonic devices, where the crystalline-to-amorphous transition results in substantial refractive index changes. However, optical control of phase-change media requires typically complex configurations based on pulsed, high-intensity laser systems.[43−47] The crystalline-to-amorphous transition of a phase-change material results in a substantial refractive index change, which can tune a resonant structure by controlling its electromagnetic environment. This mechanism does not involve electrical doping and therefore cannot control in a direct manner the properties of a 2D material, and furthermore phase-change materials are notoriously difficult to combine with metals as they suffer from interdiffusion, which can destroy plasmonic resonant systems.[48] The mechanism proposed here can allow a platform for nonvolatile control of other semiconducting 2D materials beyond graphene to enable devices with tunable frequency and strength of emission.

Here, we present a nonvolatile optical doping mechanism for 2D and few-atomic-layer nanomaterials based on iron-doped lithium niobate (Fe:$LiNbO_3$). Fe:$LiNbO_3$ exhibits a photorefractive effect,[49−51] where Fe impurities act as photoexcited donor/acceptor sites for electrons, allowing the formation of optically defined charge domains within the crystal. Upon illumination, electrons are excited from Fe^{+2} donor sites to the conduction band within which they are free to migrate in the crystal lattice. Under nonuniform illumination, electrons will migrate from areas of high to low illumination intensity due to diffusion, becoming trapped at Fe^{+3} acceptor sites in dark regions. Along with diffusion, there is also a drift mechanism in which the photoexcited electrons are released from the donor sites with a directional preference along the direction of the +z crystal axis.[51,52] There is an interplay between the two mechanisms with the drift mechanism dominating at length scales above a few microns.[53,54] Nonuniform illumination results in an optically written spatial charge distribution of arbitrary shape that depends on the illumination pattern. The spatial charge distribution is nonvolatile at room temperature for long periods of time (years);[55] however, it can be reversed by either thermal annealing or uniform illumination, which evenly redistributes the charges within the crystal. The photoresponsive mechanism in lithium niobate is extremely versatile to implement as it is responsive to a wide frequency range in the visible spectrum (depending on the choice of dopant[56]) and can be actuated by both incoherent and coherent, pulsed or continuous wave light sources. Further, the speed of the photorefractive effect scales with illumination intensity[49] and can reach sub-picosecond time scales.[57,58] The ability to create photoinduced nonvolatile charge distributions has led to the use of Fe:$LiNbO_3$ for recording of holograms,[59] optoelectronic tweezers for nano-objects,[60] and optical alignment of liquid crystals.[61] Recently, we suggested that iron-doped lithium niobate can be employed as an optically responsive substrate for the tuning of the electrical properties of monolayer graphene[62] and demonstrated a nonvolatile and reversible 2.6-fold increase of graphene resistivity under white light illumination. Here, we use this material platform to demonstrate optical control of the properties of monolayer graphene at terahertz frequencies. The system under study consists of a hybrid graphene−metal metasurface comprising an array of split-ring resonators (SRR) on an Fe:$LiNbO_3$ substrate (see Figure 1a). We optically define charge

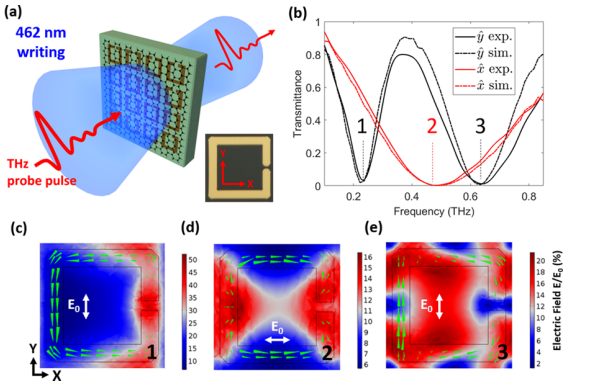

Figure 1. (a) Schematic of an Fe:$LiNbO_3$ substrate patterned with a gold resonator array and covered in graphene. Upon illumination, electrons within the substrate are excited into the conduction band, which are then free to migrate in the crystal, thus creating nonuniform charge distributions. In response to the electrostatic field created in the substrate, the graphene becomes electrostatically doped, altering the Ohmic losses in the metamaterial system, altering the resonance spectra. (b) Experimental and simulated transmittance spectra of metallic resonators at two orientations without graphene. (c−e) Simulated electric field maps at 0.22, and 0.65 THz for the y orientation and at 0.45 THz for the x orientation. The electric field is normalized to the amplitude of the incident field. Green arrows represent the current density in the metallic split rings.

distributions in the substrate to locally tune the conductivity of the graphene monolayer, which controls the damping of the resonator system and thereby tunes the metamaterial resonance strength. We observe nonvolatile light-induced changes in the metasurface spectral response, which are reversed by thermal annealing of the substrate. By fitting finite element calculations to the experimental results, we estimate an optically induced change in graphene charge carrier density of the order of 8×10^{11} cm^{-2}. We propose that the spatially addressed frequency-dependent transmission through such a device could be an invaluable tool for a reconfigurable control of THz optics in applications such as wavefront shaping of beam steering. Further, we propose that the photoconductive lithium niobate platform presented here can allow for nonvolatile control of a range of low-dimensional semiconducting materials such as transition-metal dichalcogenides, which exhibit gate-dependent electrical conduction and emission.[63]

2. RESULTS AND DISCUSSION

The hybrid graphene−metal metasurface is fabricated on a z-cut iron-doped lithium niobate (Fe:$LiNbO_3$) single crystal substrate, and a resonator array is photolithographically defined by deposition of a 5/100 nm Cr/Au film and the subsequent lift-off process. The resonance behavior of the metallic structure can be described well by analogy with an

https://dx.doi.org/10.1021/acsanm.0c02243
ACS Appl. Nano Mater. 2020, 3, 9494−9501

inductor−capacitor electrical circuit.[64] In broad terms, the capacitance is inversely proportional to the split-ring gap, while the inductance is related to the square of the resonator width. The device (depicted in Figure 1a) is illuminated from the top surface using a 462 nm laser source to create a nonuniform illumination within the Fe:$LiNbO_3$ substrate, which results in optically induced space−charge distributions. THz transmittance through the device is measured by time domain spectroscopy (TDS) before, during, and after illumination to investigate the optical tuning of the plasmonic resonances. Figure 1b shows the transmittance spectrum of the device before the transfer of graphene on top of the metasurface, measured for different polarizations of the THz wave, either parallel (y) or perpendicular (x) to the split-ring gap. The transmittance values are divided by transmittance through a lithium niobate substrate without metal or graphene. In the former case, we observe a pronounced resonance dip at 0.22 THz followed by a broader dip at around 0.65 THz, which correspond to the fundamental and third-order resonances, respectively, while in the case of perpendicular to the gap polarization (x), the metasurface presents a broad resonance dip centered at 0.45 THz, which is the second-order resonance. Experimental measurements are in good agreement with finite element simulations for both polarizations (see dashed lines in Figure. 1b). Overlaid on the plot are dashed lines showing simulated transmittance spectra corresponding to a similar metamaterial unit cell on the lithium niobate substrate. There is a deviation between the simulated and measured transmittance at higher frequencies, which is attributed to fabrication imperfections. Figure 1c,e shows simulated electric field maps (without graphene) at a plane 5 μm above the metamaterial surface for the parallel to the gap polarization (y) at 0.22 and 0.65 THz, indicating magnetic dipole and electric quadrupole field configurations, with the electric field presented as a percentage of the absolute electric field propagating through air (in the absence of substrate and metal). Figure 1(d) presents similar data for 0.45 THz for the perpendicular to the gap polarization (x), where the system supports an electric dipole resonance.

Figure 2 shows experimental and simulated spectra revealing photoinduced changes in the response of the hybrid graphene−metal metasurface measured with polarized THz along the y-axis (y) radiation. Figure 2a plots the transmittance before and after illumination. The resonant transmittance dips at 0.22 and 0.65 THz show significant damping as compared to the spectra in the absence of the graphene layer (shown in Figure 1b). The resonance dips are fitted with Lorentzian functions to extract the corresponding line width, resonance frequency, and Q factor. Upon illumination, there is additional damping of the resonant dips where the full width at half-maximum (FWHM) of the fundamental resonance (at 0.22 THz) is increased from 228 to 253 GHz. To assess the shape of a resonance feature, the Q factor is commonly quoted, which is defined by the central frequency divided by the resonance width ($Q = f_0/\Delta f$), where the FWHM of the resonance peak is used for the resonance width Δf. As the resonance width increases at the fundamental resonance, the Q factor decreases from 0.85 to 0.72, while at the third-order resonance, the FWHM increases from 358 to 387 GHz, resulting in the Q factor decreasing from 1.75 to 1.61 as the Ohmic losses are increased due to the optically induced gating effect induced by the substrate. Overlaid in Figure 2a are simulated transmittance spectra, where the graphene Fermi

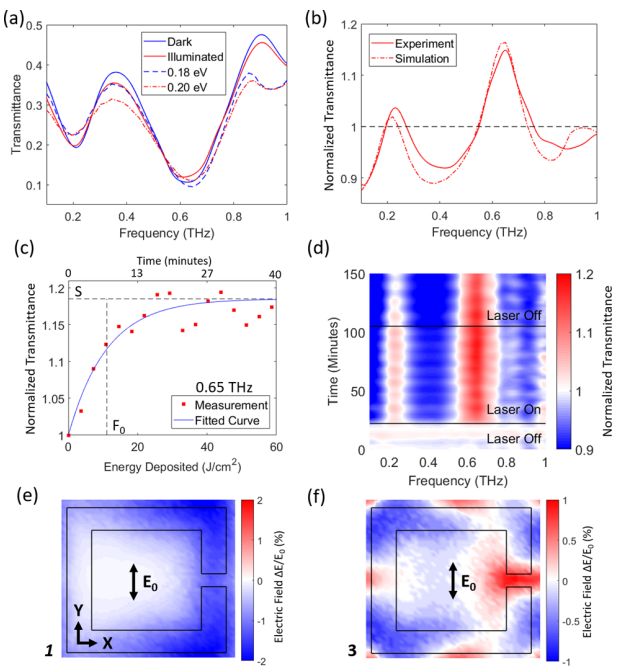

Figure 2. (a) Transmittance for THz radiation polarized in the y-axis (y) before (blue) and after (red) illumination (solid lines) overlayed with simulated results (dashed lines) for graphene Fermi levels of 0.18 eV (blue) and 0.20 eV (red). The experimental spectra are averaged over the "Laser On" and "Laser Off" periods. (b) Experimental (solid) and simulated (dashed) transmittance normalized to the transmittance before illumination. (c) Normalized transmittance measured at 3rd resonance mode (0.65 THz) during illumination, fitted with the inverse exponential equation. (d) Normalized transmittance as a function of frequency and time. The transmittance is constant before illumination; however, once illuminated, there is a rapid change in transmittance spectra, which persists once the illumination source is removed. (e, f) Simulated change in electric field $|E|$ after illumination due to photoinduced change of the graphene Fermi level at 0.22 (d) and 0.65 THz (e).

level is modified from 0.18 to 0.20 eV. There is good agreement between the experiment and simulation except at the low frequencies, where transmittance measurements in the THz TDS become sensitive to phase errors and diffraction, and high frequencies, which suffer from low signal-to-noise ratio. Figure 2b presents the transmittance spectra of Figure 2a normalized to transmittance before illumination. Two peaks can be observed that correspond to the resonant frequencies of 0.22 and 0.65 THz, where the maximum increase in normalized transmittance reaches up to 15%. Figure 2c plots the normalized transmittance at the third-order resonance mode (0.65 THz) while the device is under illumination. The transmittance values are normalized to transmittance before illumination, and the data points are fitted with an inverse exponential equation[51] of form $T = a(1 - e^{-F/F_0}) + 1$, where T is the normalized transmittance value, a is the scaling factor = 0.19, F is the energy deposited, and F_0 is the energy required to reach to 67 % of saturation value, which here is equal to 11.1 J/cm^2. The saturation value $s = a + 1$, which therefore reveals the saturated normalized transmittance change of 1.19. In Figure 2d, frequency-dependent normalized transmittance values are plotted in a color map as a function of time (on the y-axis). All transmittance values are normalized with respect to the "dark" values. The color map shows that in the first 20 min, while the

https://dx.doi.org/10.1021/acsanm.0c02243
ACS Appl. Nano Mater. 2020, 3, 9494−9501

laser is off, the THz transmittance through the device is stable in dark ambient conditions. However, once the 462 nm laser source is switched on, sudden changes in transmittance occur, which are localized to two distinct frequency bands at 0.22 and 0.65 THz. After the laser is switched off, the optically induced effects persist, in the absence of illumination, highlighting the nonvolatile nature of the mechanism. Figures 2e,f presents the corresponding simulated change of the electric field ($|\overrightarrow{E_{0.2\ eV}}| - |\overrightarrow{E_{0.18\ eV}}|)/|\overrightarrow{E_0}|$ above the metasurface for the first (0.22 THz) and second (0.65 THz) resonance. At the fundamental resonance (0.22 THz), the main change takes place in the vicinity of the split-ring gap, where the electric field decreases by ~1%. At the third-order resonance (0.65 THz), in Figure 2f, the electric field minimum in the gap increases, while the field maxima at the two opposite corners show a decrease in electric field, which shows a reduced contrast in electric field values. The field maps presented in Figure 2e,f can be understood in the following manner: as the Fermi level of the graphene is increased, the graphene conductivity also increases, which leads to a decrease in confinement and increase in Ohmic loss. Electric fields in regions that were previously high will be decreased, while fields in regions which were low will be increased as the plasmonic mode loses confinement. Therefore, Figures 2e,f shows almost the inverse color profile to Figures 1c and e (which display the electric field maps without graphene).

Figure 3 presents the spectral response of the hybrid graphene metasurface measured with polarized THz along the *x*-axis (*x*). Here, the resonance centered at 0.45 THz is damped after illumination of the device, which leads to an increase of the FWHM (obtained by Lorentzian fitting) from 590 to 630 GHz and results in a *Q* factor decrease from 0.78 to 0.73. The corresponding normalized transmittance change (see Figure 3b) presents a resonance peak at around 0.45 THz, where the optical doping effect results in an increase of 35%. Simulated data are fitted to the transmittance spectra where a graphene Fermi level change from 0.17 to 0.20 eV provides a good agreement with experimental data. The simulated spectra show a similar shape to the experimentally measured transmittance. However, the central frequency of the resonance peak is offset by ~45 GHz, which may be attributed to differences between the modeled resonator and the actual fabricated geometry and differences in the refractive index of the deposited gold layer. The color map in Figure 3c indicates that the normalized transmittance change is localized at around 0.45 THz and that once the illumination is removed the effect persists, while the device is held in the dark. The simulated electric field change ($|\overrightarrow{E_{0.2\ eV}}| - |\overrightarrow{E_{0.17\ eV}}|)/|\overrightarrow{E_0}|$ in Figure 3d indicates that as the graphene Fermi level is increased, the electric field magnitude decreases at each end of the resonator as would be expected from the direction of the electric dipole.

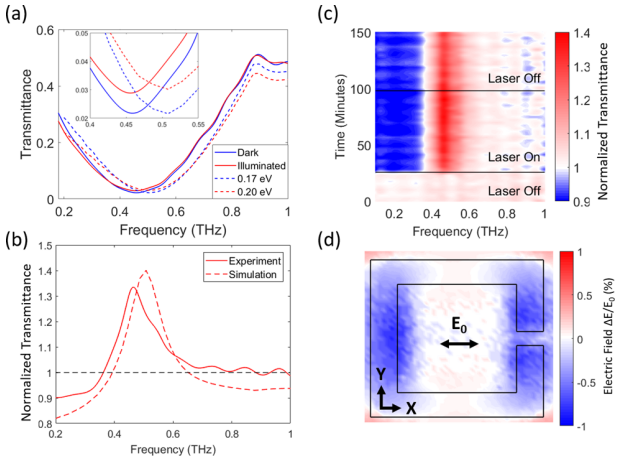

Figure 3. (a) Transmittance measured with THz radiation polarized in the *x*-axis (*x*) before and after laser illumination (solid lines) overlayed with simulated results (dashed lines) where the graphene Fermi level is modified from 0.17 to 0.20 eV. (b) Experimental and simulated transmittance normalized to the spectra before illumination. (c) Normalized transmittance versus time color map. (d) Simulated change in electric field after illumination due to photoinduced change of the graphene Fermi level. The electric field map is obtained by simulating the resonator covered with graphene at 0.20 and 0.17 eV, calculating the absolute value of the electric field $|\vec{E}|$, subtracting the electric field before the change (0.17 eV) from the electric fields after the change (0.20 eV), and then normalizing all values with respect to the incident electric field.

The results presented in Figures 2b and 3b show that when measured with *x* and *y* polarized THz (corresponding to electric dipole and magnetic dipole configurations) the illumination creates distinct peaks of increased transmittance, which correspond to the resonant reflectance peaks of the metasurface. Therefore, it can be understood that upon illumination the reflection resonance becomes weaker, which relates to an increase in transmittance. The normalized transmittance change is highest for THz polarization in the *x*-axis (*x*), which is perhaps unexpected as it could be presumed that small changes in the graphene conductivity would result in large changes to the capacitance of the resonator gap, therefore altering the *y* polarization by a greater degree. Our simulations indicate that the change in doping is significantly larger for the former case, which can be attributed to adsorption of atmospheric particles and moisture that can screen the electrostatic field of the substrate and dope the graphene. The measurements at different orientations are separated by several days and several thermal annealing cycles, which are likely to induce changes to the graphene layer, which is responsible for the different initial Fermi levels between the two polarizations measured here. When repeat cycles of illumination followed by thermal annealing are investigated (Supporting Information, Figure S1), we find that the normalized transmittance changes decrease with repeat cycles. Since we know that $LiNbO_3$ can be reused without degradation,[60,61] this behavior suggests a possible degradation of the graphene layer, where changes to the electrical properties of graphene devices on ferroelectric substrates have previously been reported due to adsorption of charged atmospheric particles.[65] To overcome this issue, future experiments will involve encapsulating the graphene with a protective layer such as hexagonal boron nitride (hBN), which could increase the long-term stability of the device. Graphene covered with hBN has been demonstrated to allow for high values of charge carrier mobility[66] and provide isolation from atmospheric chemical doping.[67] Furthermore, in recent years, hBN monolayers of several square centimeters have become commercially available on sacrificial polymer substrates for routine transfer processes, which indeed makes hBN encapsulation compatible with the device we present here.

https://dx.doi.org/10.1021/acsanm.0c02243
ACS Appl. Nano Mater. 2020, 3, 9494−9501

Our experimental measurements (see Figures 2c and 3c) indicate that the change in resonance spectra occurs within the first few minutes of illumination. In fact, the speed of the photorefractive effect in Fe:$LiNbO_3$ is directly proportional to the intensity of the illumination source[49] and can reach sub-picosecond time scales.[57,58] However, the limiting factor for the speed of the process here is associated with the THz data collection system, which takes some minutes to collect accurate data, and as such, the device is illuminated at low intensity. Moreover, once the illumination source is removed, the spectral response does not revert back to pre-illumination conditions, highlighting the nonvolatility of the effect. Small variations in the resonance spectra in the absence of illumination can be attributed to the adsorption of atmospheric particles that compensate the electric field of the lithium niobate substrate. In Supporting Information Figure S4, we plot normalized transmittance during the illumination period and for a subsequent period of 3 h in the dark, which demonstrates the nonvolatility of the mechanism. There are visible fluctuations in transmittance; however, when a moving average is overlaid (blue line) on the figure, we see that the moving average in the post-illumination period for the two frequencies follows largely the same behavior, suggesting that this effect is due to the spectrometer.

A control experiment is performed in which a device consisting of Fe:$LiNbO_3$ with a metallic metasurface array without graphene is illuminated while the THz transmittance properties are measured. The results of this control experiment (provided in Supporting Information Figure S2) reveal that in the absence of graphene there are no optically induced transmittance changes. Further, the standard deviation of the control experiment normalized transmittance is ±0.023, which demonstrates that the spectrometer fluctuations are lower than the measured normalized transmittance changes in the graphene−metal metasurface devices. Finally, our results indicate that there is a significant contribution to the observed photoinduced effects from the drift mechanism in the substrate.[51,52] This is illustrated in Supporting Information Figure S3, where we show reversal of the effects in metasurfaces on oppositely charged ±z Fe:$LiNbO_3$ faces. The magnitude of the transmittance changes presented here is currently limited by the design of the metallic resonator structure (which could be optimized to produce a higher Q factor resonance) and the quality of the graphene. Further, by use of an independent electrical top gate, we propose that the graphene could be brought toward the Dirac point where the graphene electrical resistivity is most sensitive to changes in charge carrier numbers. To investigate the potential for device optimization, we perform finite element simulations in which the split-ring gap is reduced to 0.5 μm and the initial Fermi level is reduced to 0.03 eV. By injection of 8×10^{11} cm^{-2} charge carriers into the graphene, it is shown in Supporting Information Figure S5 that the optically induced normalized transmittance changes reach ∼90% for the $\hat{y}$ polarization and up to 80% for the $\hat{x}$ polarization. We see that in the optimized device the largest transmittance changes that can be achieved for the y orientation are at 0.3 THz where the transmittance decreases from 0.26 in dark conditions to 0.16 when illuminated.

3. CONCLUSIONS

We have demonstrated nonvolatile optical tuning of a plasmonic resonator array sandwiched between monolayer graphene and a photoresponsive Fe:$LiNbO_3$ substrate. The effect is capable of producing normalized transmittance changes up to ∼35% in the device at the plasmonic resonance peak in a nonvolatile manner and reversible under thermal annealing. Finite element method simulations determine that the photorefractive effect results in a charge carrier injection of 8×10^{11} cm^{-2} into the graphene. In subsequent work, optical erasure methods will be investigated to remove the reliance on thermal annealing. To improve the switching capabilities of this device, we propose future optimization of the resonator geometry and the fabrication of an electrical top gate to bring the graphene near to the Dirac point where it is most sensitive to electrostatic gating. The ability to locally control the electrical loss in a plasmonic resonator array *via* optical illumination can allow for reconfigurable sensing and tuning applications in graphene. Further, we propose that the ability to locally tune the graphene Fermi level will allow for nonvolatile, yet reversible, optically defined plasmonic resonators of a graphene/Fe:$LiNbO_3$ device by optically patterning regions of high and low conductivity graphene, removing the need for permanent lithographic patterning of metallic structures. Finally, we propose that the Fe:$LiNbO_3$ substrate is not limited to use only with graphene but will be applicable to tuning of a wide range of 2D or low-dimensional nanomaterials such as transition-metal dichalcogenides, which exhibit electronic band gaps to allow for high on−off ratio tuning of electronic conductivities.

4. METHODS

4.1. Fabrication. Devices are fabricated on iron-doped lithium niobate (Fe:$LiNbO_3$) crystal substrates. An array of metallic SRRs is defined by photolithography of an S1813 photoresist followed by electron beam evaporation deposition of a Cr/Au stack (5/100 nm). Excess material is removed in a lift-off process in acetone to remove any metal deposited on top of the photoresist. Commercially supplied chemical vapor deposition (CVD) graphene (grown on copper foil) is transferred *via* a sacrificial polymer substrate and layered on top of the SRRs in a wet-transfer process. After transfer of the graphene, the device is held under vacuum (10^{-3} mBar) for 24 hours to remove moisture under the graphene layer and promote adhesion before the removal of the protective poly(methyl methacrylate) (PMMA) layer *via* washing in acetone followed by isopropyl alcohol. Due to the photoresponsive nature of the substrate, the devices are thermally annealed in a convection oven at 100°C for 24 h prior to any measurements to thermally redistribute any nonuniform charge distributions within the substrate.

4.2. THz Time Domain Spectroscopy. THz TDS is used to characterize the transmittance spectrum of the devices in the frequency range 0.1−1 THz. THz pulses are created by the optical excitation of a voltage-biased photoconductive antenna (PCA) via a pulsed femtosecond laser at 800 nm. The devices are measured before, during, and after illumination, and then the frequency domain spectra are divided by a reference spectrum that was obtained before illumination. The division removes the effects of frequency-dependent emission, propagation in air, propagation in lithium niobate, and Fresnel reflections from the air/Fe:$LiNbO_3$ interface.

4.3. Illumination. The devices are illuminated from the top surface, which is covered with the resonator array and graphene by a 462 nm fiber-coupled diode laser at 25 mW cm^{-2}, collimated at the fiber output by an aspheric lens, resulting in a 10 mm beam diameter as shown in Figure 1a. The laser is aligned on the device to ensure that the beam completely covers the region of the focused THz pulse; this is achieved using a metallic aperture of diameter 3 mm at the rear surface of the device, which is placed at the THz focus and visually overlapping the laser beam with the aperture. For the duration of all experiments, the emitter, detector, and SRR device are held in a light-

https://dx.doi.org/10.1021/acsanm.0c02243
ACS Appl. Nano Mater. 2020, 3, 9494−9501

proof box to avoid ambient illumination of the device. Before illumination, THz scans are taken over a 20 min period to gauge the drift in the THz system. The device is then illuminated continuously for a 70 min period while measuring the THz transmittance. The illumination source is then switched off, and the scans continue in the dark to observe whether any optically induced transmittance change is nonvolatile. As the optical beam is larger than the device, we assume that the illumination intensity of the area of the device is uniform; therefore, the photorefractive effect will be driven by drift (along the z-axis) and diffusion (to dark areas under the metallic resonators).

4.4. Charge Carrier Calculations. Charge carrier numbers can be extracted from the Fermi level values,[68] where the frequency-dependent conductivity is calculated from the Fermi level and the DC conductivity is obtained by multiplying by $(1 - i\omega\tau)$. The carrier number n is then simply given by dividing the DC conductivity by electron charge and mobility. From this calculation, we find that for a Fermi level change from 0.17 to 0.20 eV there is a carrier injection of 8×10^{11} cm^{-2} in response to the optical gating effect of the substrate under illumination.

4.5. Finite Element Analysis. A finite element analysis method is performed to show the effect of varying graphene Fermi levels on the transmittance spectrum of the resonator structures. The model consists of a unit cell 50 × 50 μm^2 in the x−y direction; linearly polarized electromagnetic radiation is excited from a port on the upper plane of the unit cell propagating downward through 300 μm of air and then into a 1 mm deep slab of lithium niobate. Experimental values of the frequency-dependent complex refractive index of the $LiNbO_3$ substrate are measured in our THz TDS. A gold resonator structure is created on the air/lithium niobate interface and modeled to the two-dimensional geometry of the photolithography mask. The permittivity values of gold are taken from a Drude model.[69] Graphene is modeled as a 3D sheet covering the entire unit cell on top of the gold resonator, which is identical to the fabricated structure. Graphene permittivity and conductivity are dependent on the Fermi level and frequency, and mobility is taken as 3760 cm^2 V^{-1} s^{-1} as quoted by the graphene manufacturer. Transmitted power is normalized against a simulation in the absence of graphene and gold through a $LiNbO_3$ slab. The simulation is first performed in the absence of the graphene layer to compare to experimental spectra before graphene transfer. The graphene layer is then added to the simulated model, and the Fermi level of the graphene is modified in a parametric sweep to find convergence with experimental results.

■ ASSOCIATED CONTENT

Supporting Information

The Supporting Information is available free of charge at https://pubs.acs.org/doi/10.1021/acsanm.0c02243.

Repeatability investigation; multiple cycles of write, read, and erasure; control experiment with metallic metasurface on a lithium niobate substrate without graphene; metasurfaces fabricated on plus and minus z faces on lithium niobate to investigate effects of the ferroelectric axis (PDF)

■ AUTHOR INFORMATION

Corresponding Author

Jon Gorecki − *Optoelectronics Research Centre, University of Southampton, Southampton SO17 1BJ, U.K.*; orcid.org/0000-0001-9205-2294; Email: J.Gorecki@soton.ac.uk

Authors

Lewis Piper − *School of Physics and Astronomy, University of Southampton, Southampton SO17 1BJ, U.K.*

Adnane Noual − *LPMR, Department of Physics, FPN, University Mohammed Premier, Oujda 60000, Morocco*

Sakellaris Mailis − *Skolkovo Institute of Science and Technology, Moscow 143026, Russia*; orcid.org/0000-0002-3067-5311

Nikitas Papasimakis − *Optoelectronics Research Centre, University of Southampton, Southampton SO17 1BJ, U.K.*

Vasilis Apostolopoulos − *School of Physics and Astronomy, University of Southampton, Southampton SO17 1BJ, U.K.*

Complete contact information is available at: https://pubs.acs.org/10.1021/acsanm.0c02243

Notes

The authors declare no competing financial interest.

■ ACKNOWLEDGMENTS

We acknowledge financial support from the U.K.'s Engineering and Physical Sciences Council through the Teranet network (grant EP/M00306X/q) and from the Quantum Hub of Sensing and Timing (EP/T001046/1). All data supporting this study are openly available from the University of Southampton repository.

■ REFERENCES

(1) Markelz, A.; Roitberg, A.; Heilweil, E. Pulsed Terahertz Spectroscopy of DNA, Bovine Serum Albumin and Collagen between 0.1 and 2.0 THz. *Chem. Phys. Lett.* **2000**, *320*, 42−48.

(2) Ebbinghaus, S.; Kim, S. J.; Heyden, M.; Yu, X.; Heugen, U.; Gruebele, M.; Leitner, D. M.; Havenith, M. An Extended Dynamical Hydration Shell around Proteins. *Proc. Natl. Acad. Sci. U.S.A.* **2007**, *104*, 20749−20752.

(3) Walther, M.; Fischer, B.; Schall, M.; Helm, H.; Jepsen, P. Far-Infrared Vibrational Spectra of all-Trans, 9-cis and 13-cis Retinal Measured by THz Time-Domain Spectroscopy. *Chem. Phys. Lett.* **2000**, *332*, 389−395.

(4) Woodward, R. M.; Wallace, V. P.; Pye, R. J.; Cole, B. E.; Arnone, D. D.; Linfield, E. H.; Pepper, M. Terahertz Pulse Imaging of ex vivo Basal Cell Carcinoma. *J. Invest. Dermatol.* **2003**, *120*, 72−78.

(5) Federici, J. F.; Schulkin, B.; Huang, F.; Gary, D.; Barat, R.; Oliveira, F.; Zimdars, D. THz Imaging and Sensing for Security Applications - Explosives, Weapons and Drugs. *Semicond. Sci. Technol* **2005**, *20*, S266−S280.

(6) Appleby, R.; Wallace, H. B. Standoff Detection of Weapons and Contraband in the 100 GHz to 1 THz Region. *IEEE Trans. Antennas Propag.* **2007**, *55*, 2944−2956.

(7) Chen, J.; Chen, Y.; Zhao, H.; Bastiaans, G. J.; Zhang, X.-C. Absorption Coefficients of Selected Explosives and Related Compounds in the Range of 0.1-2.8 THz. *Opt. Express* **2007**, *15*, 12060−12067.

(8) Wei, J.; Olaya, D.; Karasik, B. S.; Pereverzev, S. V.; Sergeev, A. V.; Gershenson, M. E. Ultrasensitive Hot-Electron Nanobolometers for Terahertz Astrophysics. *Nat. Nanotechnol* **2008**, *3*, 496−500.

(9) Negrello, M.; Hopwood, R.; Zotti, G. D.; Cooray, A.; Verma, A.; Bock, J.; Frayer, D. T.; Gurwell, M. A.; Omont, A.; Neri, R.; Dannerbauer, H.; Leeuw, L. L.; Barton, E.; Cooke, J.; Kim, S.; da Cunha, E.; Rodighiero, G.; Cox, P.; Bonfield, D. G.; Jarvis, M. J.; Serjeant, S.; Ivison, R. J.; Dye, S.; Aretxaga, I.; Hughes, D. H.; Ibar, E.; Bertoldi, F.; Valtchanov, I.; Eales, S.; Dunne, L.; Driver, S. P.; Auld, R.; Buttiglione, S.; Cava, A.; Grady, C. A.; Clements, D. L.; Dariush, A.; Fritz, J.; Hill, D.; Hornbeck, J. B.; Kelvin, L.; Lagache, G.; Lopez-Caniego, M.; Gonzalez-Nuevo, J.; Maddox, S.; Pascale, E.; Pohlen, M.; Rigby, E. E.; Robotham, A.; Simpson, C.; Smith, D. J. B.; Temi, P.; Thompson, M. A.; Woodgate, B. E.; York, D. G.; Aguirre, J. E.; Beelen, A.; Blain, A.; Baker, A. J.; Birkinshaw, M.; Blundell, R.; Bradford, C. M.; Burgarella, D.; Danese, L.; Dunlop, J. S.; Fleuren, S.; Glenn, J.; Harris, A. I.; Kamenetzky, J.; Lupu, R. E.; Maddalena, R. J.; Madore, B. F.; Maloney, P. R.; Matsuhara, H.; Michaowski, M. J.; Murphy, E. J.; Naylor, B. J.; Nguyen, H.; Popescu, C.; Rawlings, S.; Rigopoulou, D.; Scott, D.; Scott, K. S.; Seibert, M.; Smail, I.; Tuffs, R. J.; Vieira, J. D.; van der Werf, P. P.; Zmuidzinas, J. The Detection of a Population of Submillimeter-Bright, Strongly Lensed Galaxies. *Science* **2010**, *330*, 800−804.

(10) Nagai, N.; Sumitomo, M.; Imaizumi, M.; Fukasawa, R. Characterization of Electron- or Proton-Irradiated Si Space Solar Cells by THz spectroscopy. *Semicond. Sci. Technol* **2006**, *21*, 201−209.
(11) Ahi, K.; Shahbazmohamadi, S.; Asadizanjani, N. Quality Control and Authentication of Packaged Integrated Circuits using Enhanced-Spatial-Resolution Terahertz Time-Domain Spectroscopy and Imaging. *Opt. Laser Eng.* **2018**, *104*, 274−284.
(12) Jornet, J. M.; Akyildiz, I. F. Graphene-based Plasmonic Nano-Antenna for Terahertz Band Communication in Nanonetworks. *IEEE J. Select. Areas Commun.* **2013**, *31*, 685−694.
(13) Seeds, A. J.; Shams, H.; Fice, M. J.; Renaud, C. C. TeraHertz Photonics for Wireless Communications. *J. Lightwave Technol.* **2015**, *33*, 579−587.
(14) Alius, H.; Dodel, G. Amplitude-, Phase-, and Frequency Modulation of Far-Infrared Radiation by Optical Excitation of Silicon. *Infrared Phys. Technol.* **1991**, *32*, 1−11.
(15) Vogel, T.; Dodel, G.; Holzhauer, E.; Salzmann, H.; Theurer, A. High-Speed Switching of Far-Infrared Radiation by Photoionization in a Semiconductor. *Appl. Opt.* **1992**, *31*, 329−337.
(16) Nozokido, T.; Minamide, H.; Mizuno, K. Modulation of Submillimeter Wave Radiation by Laser-Produced Free Carriers in Semiconductors. *Electr. Commun. JPN* **1997**, *80*, 1−9.
(17) Rivas, J. G.; Kuttge, M.; Kurz, H.; Bolivar, P. H.; Sánchez-Gil, J. A. Low-Frequency Active Surface Plasmon Optics on Semiconductors. *Appl. Phys. Lett.* **2006**, *88*, No. 082106.
(18) Han, J.; Lakhtakia, A. Semiconductor Split-Ring Resonators for Thermally Tunable Terahertz Metamaterials. *J. Mod. Opt.* **2009**, *56*, 554−557.
(19) Chen, H.-T.; Padilla, W. J.; Cich, M. J.; Azad, A. K.; Averitt, R. D.; Taylor, A. J. A Metamaterial Solid-State Terahertz Phase Modulator. *Nat. Photonics* **2009**, *3*, 148−151.
(20) Kleine-Ostmann, T.; Dawson, P.; Pierz, K.; Hein, G.; Koch, M. Room-Temperature Operation of an Electrically Driven Terahertz Modulator. *Appl. Phys. Lett.* **2004**, *84*, 3555−3557.
(21) Chen, H.-T.; Padilla, W. J.; Zide, J. M. O.; Gossard, A. C.; Taylor, A. J.; Averitt, R. D. Active Terahertz Metamaterial Devices. *Nature* **2006**, *444*, 597−600.
(22) Han, Z.; Kohno, K.; Fujita, H.; Hirakawa, K.; Toshiyoshi, H. MEMS Reconfigurable Metamaterial for Terahertz Switchable Filter and Modulator. *Opt. Express* **2014**, *22*, 21326−21339.
(23) Tao, H.; Strikwerda, A. C.; Fan, K.; Padilla, W. J.; Zhang, X.; Averitt, R. D. Reconfigurable Terahertz Metamaterials. *Phys. Rev. Lett.* **2009**, *103*, No. 147401.
(24) Busch, S.; Scherger, B.; Scheller, M.; Koch, M. Optically Controlled Terahertz Beam Steering and Imaging. *Opt. Lett.* **2012**, *37*, 1391−1393.
(25) Okada, T.; Tanaka, K. Photo-Designed Terahertz Devices. *Sci. Rep.* **2011**, *1*, No. 121.
(26) Weis, P.; Garcia-Pomar, J. L.; Höh, M.; Reinhard, B.; Brodyanski, A.; Rahm, M. Spectrally Wide-Band Terahertz Wave Modulator Based on Optically Tuned Graphene. *ACS Nano* **2012**, *6*, 9118−9124.
(27) Chen, S.; Fan, F.; Miao, Y.; He, X.; Zhang, K.; Chang, S. Ultrasensitive Terahertz Modulation by Silicon-Grown MoS_2 Nanosheets. *Nanoscale* **2016**, *8*, 4713−4719.
(28) Wu, P.; Zhang, C.; Tang, Y.; Liu, B.; Lv, L. A Perfect Absorber Based on Similar Fabry-Perot Four-Band in the Visible Range. *Nanomaterials* **2020**, *10*, 488.
(29) Wu, P.; Chen, Z.; Jile, H.; Zhang, C.; Xu, D.; Lv, L. An infrared perfect absorber based on metal-dielectric-metal multi-layer films with nanocircle holes arrays. *Results Phys.* **2020**, *16*, No. 102952.
(30) Li, J.; Chen, X.; Yi, Z.; Yang, H.; Tang, Y.; Yi, Y.; Yao, W.; Wang, J.; Yi, Y. Broadband solar energy absorber based on monolayer molybdenum disulfide using tungsten elliptical arrays. *Mater. Today* **2020**, *16*, No. 100390.
(31) Li, J.; Chen, Z.; Yang, H.; Yi, Z.; Chen, X.; Yao, W.; Duan, T.; Wu, P.; Li, G.; Yi, Y. Tunable Broadband Solar Energy Absorber Based on Monolayer Transition Metal Dichalcogenides Materials Using Au Nanocubes. *Nanomaterials* **2020**, *10*, 257.
(32) Qj, Y.; Zhang, Y.; Liu, C.; Zhang, T.; Zhang, B.; Wang, L.; Deng, X.; Wang, X.; Yu, Y. A Tunable Terahertz Metamaterial Absorber Composed of Hourglass-Shaped Graphene Arrays. *Nanomaterials* **2020**, *10*, 533.
(33) Padilla, W. J.; Taylor, A. J.; Highstrete, C.; Lee, M.; Averitt, R. D. Dynamical Electric and Magnetic Metamaterial Response at Terahertz Frequencies. *Phys. Rev. Lett.* **2006**, *96*, No. 107401.
(34) Manceau, J. M.; Shen, N. H.; Kafesaki, M.; Soukoulis, C. M.; Tzortzakis, S. Dynamic Response of Metamaterials in the Terahertz Regime: Blueshift Tunability and Broadband Phase Modulation. *Appl. Phys. Lett.* **2010**, *96*, No. 021111.
(35) Roy Chowdhury, D.; Singh, R.; O'Hara, J. F.; Chen, H. T.; Taylor, A. J.; Azad, A. K. Dynamically Reconfigurable Terahertz Metamaterial through Photo-Doped Semiconductor. *Appl. Phys. Lett.* **2011**, *99*, No. 231101.
(36) Chen, H. T.; O'Hara, J. F.; Azad, A. K.; Taylor, A. J.; Averitt, R. D.; Shrekenhamer, D. B.; Padilla, W. J. Experimental Demonstration of Frequency-Agile Terahertz Metamaterials. *Nat. Photonics* **2008**, *2*, 295−298.
(37) Gu, J. Q.; Singh, R.; Liu, X. J.; Zhang, X. Q.; Ma, Y. F.; Zhang, S.; Maier, S. A.; Tian, Z.; Azad, A. K.; Chen, H. T.; Taylor, A. J.; Han, J. G.; Zhang, W. L. Active Control of Electromagnetically Induced Transparency Analogue in Terahertz Metamaterials. *Nat. Commun.* **2012**, *3*, No. 1151.
(38) Hendry, E.; Lockyear, M. J.; Rivas, J. G.; Kuipers, L.; Bonn, M. Ultrafast Optical Switching of the THz Transmission through Metallic Subwavelength Hole Arrays. *Phys. Rev. B* **2007**, *75*, No. 235305.
(39) Janke, C.; Rivas, J. G.; Bolivar, P. H.; Kurz, H. All-Optical Switching of the Transmission of Electromagnetic Radiation through Subwavelength Apertures. *Opt. Lett.* **2005**, *30*, 2357−2359.
(40) Chen, H. T.; Padilla, W. J.; Zide, J. M. O.; Bank, S. R.; Gossard, A. C.; Taylor, A. J.; Averitt, R. D. Ultrafast Optical Switching of Terahertz Metamaterials Fabricated on ErAs/GaAs Nanoisland Superlattices. *Opt. Lett.* **2007**, *32*, 1620−1622.
(41) Zheng, W.; Fan, F.; Chen, M.; Chen, S.; Chang, S. J. Optically Pumped Terahertz Wave Modulation in MoS_2-Si Heterostructure Metasurface. *AIP Adv.* **2016**, *6*, No. 075105.
(42) Arezoomandan, S.; Gopalan, P.; Tian, K.; Chanana, A.; Nahata, A.; Tiwari, A.; Sensale-Rodriguez, B. Tunable Terahertz Metamaterials Employing Layered 2-D Materials Beyond Graphene. *J. Sel. Top. Quantum Electron* **2017**, *23*, 188−194.
(43) Gholipour, B.; Zhang, J.; MacDonald, K. F.; Hewak, D. W.; Zheludev, N. I. An All-Optical, Non-volatile, Bidirectional, Phase-Change Meta-Switch. *Adv. Mater* **2013**, *25*, 3050−3054.
(44) Wang, Q.; Rogers, E. T.; Gholipour, B.; Wang, C.-M.; Yuan, G.; Teng, J.; Zheludev, N. I. Optically Reconfigurable Metasurfaces and Photonic Devices based on Phase Change Materials. *Nat. Photonics* **2016**, *10*, 60−65.
(45) Wuttig, M.; Bhaskaran, H.; Taubner, T. Phase-Change Materials for Non-Volatile Photonic Applications. *Nat. Photonics* **2017**, *11*, 465−476.
(46) Pitchappa, P.; Kumar, A.; Prakash, S.; Jani, H.; Venkatesan, T.; Singh, R. Chalcogenide Phase Change Material for Active Terahertz Photonics. *Adv. Mater* **2019**, *31*, No. 1808157.
(47) Jeong, Y.-G.; Bahk, Y.-M.; Kim, D.-S. Dynamic Terahertz Plasmonics Enabled by Phase-Change Materials. *Adv. Opt. Mater* **2019**, *8*, No. 1900548.
(48) Lu, L.; Dong, W.; Behera, J. K.; Chew, L.; Simpson, R. E. Interdiffusion of plasmonic metals and phase change materials. *J. Mater. Sci.* **2019**, *54*, 2814−2823.
(49) Gunter, P.; Huignard, J. P. *Photorefractive Materials and Their Applications 1*; Springer, 2006.
(50) Weis, R. S.; Gaylord, T. K. Lithium Niobate - Summary of Physical Properties and Crystal Structure. *Appl. Phys. A* **1985**, *37*, 191−203.
(51) Puerto, A.; Munoz-Martin, J. F.; Mendez, A.; Arizmendi, L.; Garcia-Cabanes, A.; Agullo-Lopez, F.; Carrascosa, M. Synergy Between Pyroelectric and Photovoltaic Effects for Optoelectronic Nanoparticle Manipulation. *Opt. Express* **2019**, *27*, 804−815.

https://dx.doi.org/10.1021/acsanm.0c02243
ACS Appl. Nano Mater. 2020, 3, 9494−9501

(52) Buse, K. Light-Induced Charge Transport Processes in Photorefractive Crystals I: Models and Experimental Methods. *Appl. Phys. B* **1997**, *64*, 273−291.
(53) Prokhorov, A. M.; Kuzminov, Y. S. *Physics and Chemistry of Crystalline Lithium Niobate*; IOP Publishing, 1990.
(54) Ohmori, Y.; Yasojima, Y.; Inuishi, Y. Photoconduction, Thermally Stimulated Luminescence, and Optical Damage in Single Crystal of $LiNbO_3$. *Jpn. J. Appl. Phys* **1975**, *14*, 1291−1300.
(55) Arizmendi, L.; Lopez-Barbera, F. J. Lifetime of Thermally Fixed Holograms in $LiNbO_3$ Crystals Doped with Mg and Fe. *Appl. Phys. B* **2006**, *86*, 105−109.
(56) Furukawa, Y.; Kitamura, K.; Ji, Y.; Montemezzani, G.; Zgonik, M.; Medrano, C.; Günter, P. Photorefractive Properties of Iron-Doped Stoichiometric Lithium Niobate. *Opt. Lett.* **1997**, *22*, 501−503.
(57) Hsieh, H.-T.; Psaltis, D.; Beyer, O.; Maxein, D.; von Korff Schmising, C.; Buse, K.; Sturman, B. Femtosecond Holography in Lithium Niobate Crystals. *Opt. Lett.* **2005**, *30*, 2233−2235.
(58) Paipulas, D. Local Photorefractive Modification in Lithium Niobate Using Ultrafast Direct Laser Write Technique. *J. Laser Micro Nanoen.* **2016**, *11*, 246−252.
(59) Buse, K.; Adibi, A.; Psaltis, D. Non-Volatile Holographic Storage in Doubly Doped Lithium Niobate Crystals. *Nature* **1998**, *393*, 665−668.
(60) Carrascosa, M.; Garcia-Cabanes, A.; Jubera, M.; Ramiro, J. B.; Agullo-Lopez, F. $LiNbO_3$: A Photovoltaic Substrate for Massive Parallel Manipulation and Patterning of Nano-Objects. *Appl. Phys. Rev.* **2015**, *2*, No. 040605.
(61) Lucchetti, L.; Kushnir, K.; Reshetnyak, V.; Ciciulla, F.; Zaltron, A.; Sada, C.; Simoni, F. Light-Induced Electric Field Generated by Photovoltaic Substrates Investigated through Liquid Crystal Reorientation. *Opt. Mater.* **2017**, *73*, 64−69.
(62) Gorecki, J.; Apostolopoulos, V.; Ou, J. Y.; Mailis, S.; Papasimakis, N. Optical Gating of Graphene on Photoconductive Fe:$LiNbO_3$. *ACS Nano* **2018**, *12*, 5940−5945.
(63) Xiao, J.; Zhao, M.; Wang, Y.; Zhang, X. Excitons in atomically thin 2D semiconductors and their applications. *Nanophotonics* **2017**, *6*, 1309−1328.
(64) Jeppesen, C.; Mortensen, N. A.; Kristensen, A. Capacitance tuning of nanoscale split-ring resonators. *Appl. Phys. Lett.* **2009**, *95*, No. 193108.
(65) Rogers, S. P.; Xu, R.; Pandya, S.; Martin, L. W.; Shim, M. Slow Conductance Relaxation in Graphene−Ferroelectric Field-Effect Transistors. *J. Phys. Chem. C* **2017**, *121*, 7542−7548.
(66) Geim, A. K.; Grigorieva, I. V. Van der Waals heterostructures. *Nature* **2013**, *499*, 419−425.
(67) Mayorov, A. S.; Gorbachev, R. V.; Morozov, S. V.; Britnell, L.; Jalil, R.; Ponomarenko, L. A.; Blake, P.; Novoselov, K. S.; Watanabe, K.; Taniguchi, T.; Geim, A. K. Micrometer-Scale Ballistic Transport in Encapsulated Graphene at Room Temperature. *Nano Letters* **2011**, *11*, 2396−2399.
(68) Bøggild, P.; Mackenzie, D. M. A.; Whelan, P. R.; Petersen, D. H.; Due Buron, J.; Zurutuza, A.; Gallop, J.; Hao, L.; Jepsen, P. U. Mapping the Electrical Properties of Large-Area Graphene. *2D Mater.* **2017**, *4*, No. 042003.
(69) Palik, E. D. *Handbook of Optical Constants of Solids*; Academic Press, 1997.

https://dx.doi.org/10.1021/acsanm.0c02243
ACS Appl. Nano Mater. 2020, 3, 9494−9501

High-Precision THz-TDS via Self-Referenced Transmission Echo Method

applied optics

High-precision THz-TDS via self-referenced transmission echo method

Jon Gorecki,[1,*] Nicholas Klokkou,[1] Lewis Piper,[2] Sakellaris Mailis,[3] Nikitas Papasimakis,[1] and Vasilis Apostolopoulos[2]

[1]Optoelectronics Research Centre, University of Southampton, Southampton SO17 1BJ, UK
[2]School of Physics and Astronomy, University of Southampton, Southampton SO17 1BJ, UK
[3]Skolkovo Institute of Science and Technology, Moscow 143026, Russia
*Corresponding author: J.Gorecki@soton.ac.uk

Received 20 February 2020; revised 27 April 2020; accepted 28 April 2020; posted 28 April 2020 (Doc. ID 391103); published 30 July 2020

Terahertz time-domain spectroscopy (TDS) is a powerful characterization technique which allows for the frequency-dependent complex refractive index of a sample to be determined. This is achieved by comparing the time-domain of a pulse transmitted through air to a pulse transmitted through a material sample; however, the requirement for an independent reference scan can introduce errors due to laser fluctuations, mechanical drift, and atmospheric absorption. In this paper, we present a method for determining complex refractive index without an air reference, in which the first pulse transmitted through the sample is compared against the "echo", where the internal reflections delay the transmission of the echo pulse. We present a benchmarking experiment in which the echo reference method is compared to the traditional air method, and show that the echo method is able to reduce variation in real refractive index.

https://doi.org/10.1364/AO.391103

1. INTRODUCTION

Terahertz time-domain spectroscopy (THz-TDS) is a powerful analytical technique for investigating a wide range of materials such as spectroscopy of biological samples [1–4], detection of concealed drugs and explosives [5–7], imaging of astronomical objects [8,9], and industrial quality control of semiconductor manufacturing [10,11]. THz-TDS is unlike many spectroscopy methods, as it allows for both the real and imaginary parts of the refractive index to be determined due to the ability to measure the electric field in the time-domain at the sub-picosecond resolution [12]. The THz-TDS method relies on taking a suitable reference scan by which the sample scans are normalized, which is normally achieved by measuring the THz pulse transmitted through air, placing a sample in the beam path, and measuring the THz pulse through the sample. If the THz pulse is not correctly referenced, or the spectrometer has drifted since the reference scan, this can lead to errors in the complex refractive index which could, for example, cause the misidentification of an explosive security sample or failure to detect changes in a temporally evolving biological system.

There are many practical issues to address when referencing a THz scan in order to obtain reliable material characterization. One major issue to highlight from the air referencing method is that a THz spectrometer may experience fluctuations in the laser power between taking an air measurement and a sample measurement. This effect is especially compounded when it is required to take repeat measurements of samples over a long time period, such as several hours, to investigate a temporally changing system. Furthermore, when taking an air reference measurement, the sample must be removed/added to the optical system, which may not be physically possible in some situations; for example, with a sample held in a sealed chamber or other enclosed space. When taking a measurement with an air reference, it is generally assumed the complex refractive index of the air is $1 + 0i$, i.e., the air has identical refractive index to that of a vacuum; however, in practical cases, there is often atmospheric moisture, which can cause absorption of the THz pulse. After the air reference is taken and the sample is placed in the spectrometer, the beam then passes through less water vapor, which can skew the values of imaginary refractive index and register in the system as an artificial gain in intensity.

A self-referencing method to measure the strength of absorption peaks has been demonstrated in which a Fourier transform is applied to the time-domain signal with an ever-increasing window size [13]. In this manner, the frequency resolution of the data increases with the window size, allowing the strength of sharp absorption lines to be resolved. The method requires no independent reference scan, but is effective at measuring

absorption peaks with a sharp spectral width, and is not applicable to obtaining the real refractive index. To overcome some of these referencing issues, internally reflected pulses transmitted through the sample can be utilized to increase the sensitivity of spectroscopy devices. Various groups have demonstrated techniques where the first transmitted pulse and the internally reflected "echo" pulses are both compared to the air reference, where the echo pulses contain extra information due to increased interaction with the sample [14–16]. To negate the requirement for an air reference, an oblique reflection mode can be used where a sample is mounted against a quartz slide and the first THz pulse reflects off the face of the quartz, while the second pulse enters the quartz and reflects off the sample. By comparison of the two pulses, the complex refractive index of the sample can be determined [17,18]. A similar technique has been presented in transmission mode to determine refractive index, where the first pulse transmitted through the sample is compared to the echo pulse, which is internally reflected in the sample before being transmitted. However, this technique was only shown to produce the refractive index averaged over the THz pulse bandwidth instead of the frequency-dependent values [19,20]. Echo-based self-referencing has been demonstrated in reflection mode with a sample placed on a polished mirror, in which internally reflected THz pluses are delayed in time as compared to the pulse reflected on the top surface [21]. By comparing the first reflected and echo pulse, the refractive index can be obtained without an independent air reference. Such methods may be tricky to achieve, as the reflected echo is highly dependent on the sample–mirror interface, requiring alignment of two flat surfaces without an air gap. Further, the use of THz reflection setups can impose additional alignment issues as compared to transmission modes.

Here, we address the issue of air referencing by presenting a method to determine the frequency-dependent complex refractive index of a sample without an air reference in transmission-mode THz-TDS as shown in Fig. 1(a). The method relies on internal reflections within the sample to produce echo pulses which can be normalized to each other, requiring only one measurement scan to obtain all necessary data. This method has a number of advantages over the traditional air referencing method, as both measurements can be taken in a single time-domain trace, which reduces the chances of drift in the spectrometer between measurements. Second, this method allows for the sample to be held securely in the optical setup at all times, which reduces chances of misalignment between repeated sample mountings and can allow for samples to be held in difficult-to-access places such as sealed chambers and thermal stages. Third, we propose that this "echo referencing" method reduces the need for dry inert gas, as the sample does not need to be added/removed from the setup and therefore the volume of atmospheric gas is not decreased by inserting the sample. Dry inert gasses are often pumped into the THz spectrometer in order to displace atmospheric moisture, but this requires the system to be fully enclosed, which can be costly and difficult to achieve. In this paper, we derive the relevant parameter extraction equations for referencing the echo pulse to the first transmitted pulse, and present a comparative study in which a lithium niobate sample is measured repeatedly over a 50 minute period and complex refractive index values are compared for the two extraction methods: for the first transmitted pulse referenced to an air measurement, and for the first echo pulse referenced to the first transmitted pulse. We show that for the real refractive index, the echo reference method is able to reduce deviation between repeat measurements at frequencies below 1 THz; however, at higher frequencies, the echo method becomes unstable and ultimately has a lower usable bandwidth than the air reference method, which extends up to 1.5 THz.

2. REFRACTIVE INDEX EXTRACTION THEORY

Figure 1(b) depicts the optical paths for the first transmitted pulse and the echo pulse within the crystal sample. By measuring the THz time-domain, the two pulses can be separated and individually converted into the frequency domain by a Fourier transform. The first pulse enters from air into the sample in a transformation which can be described by the Fresnel transmission function. The pulse then propagates through a length d of the sample, which can be described by a complex Beer Lambert exponential attenuation equation, and finally passes out of the sample into air, which can be described by a further Fresnel transmission equation. The total combination of these functions describes the transmitted wave termed X_1 as shown in Eq. (1):

$$X_1 = A \cdot T_{ab} \cdot P_d \cdot T_{ba}, \tag{1}$$

where A is the arbitrary power of the incoming pulse, T_{ab} is the complex Fresnel transmission coefficient passing from material a into b, and P_d is the Beer Lambert term $P_d = \exp(-i\tilde{n}\omega d/c)$, where d is the thickness of material, and c is the speed of light. The echo pulse termed X_2 is described by Eq. (2):

$$X_2 = A \cdot T_{ab} \cdot P_d \cdot R_{ba} \cdot P_d \cdot R_{ba} \cdot P_d \cdot T_{ba}, \tag{2}$$

where R_{ba} is the complex Fresnel reflection coefficient from inside material b and bounding material a, with the form $R_{ba} = (\tilde{n}_b - \tilde{n}_a)/(\tilde{n}_b + \tilde{n}_a)$. By dividing the two pulses, the arbitrary power of the emitter A is removed, along with the transmission coefficients, leaving the complex transfer function termed H:

$$H = P_d^2 \cdot R_{ba}^2 = |Y(\omega)| \cdot e^{i\phi(\omega)}. \tag{3}$$

This transfer function H can be equated to the experimental data for the complex Fourier transform presented in unwrapped polar coordinates as $|Y(\omega)| \cdot e^{i\phi(\omega)}$, where $|Y(\omega)|$ is the magnitude and $\phi(\omega)$ is the unwrapped angle of the complex Fourier transform.

In the case in which $n \gg k$, then the Fresnel coefficients can be assumed to be real valued, which allows for the real and imaginary parts of the equations to be solved separately by rewriting the propagation constant in real and imaginary parts where $\tilde{n} = n + ik$. First, the real values of n can be calculated from

$$e^{-2in\omega d/c} = e^{i\phi(\omega)}, \tag{4}$$

and then plugged into

$$e^{2k\omega d/c} \cdot \left(\frac{n_a - n_b}{n_a + n_b}\right)^2 = |Y(\omega)| \tag{5}$$

to obtain the imaginary k components. For the case of an air-referenced sample, a similar extraction method is used

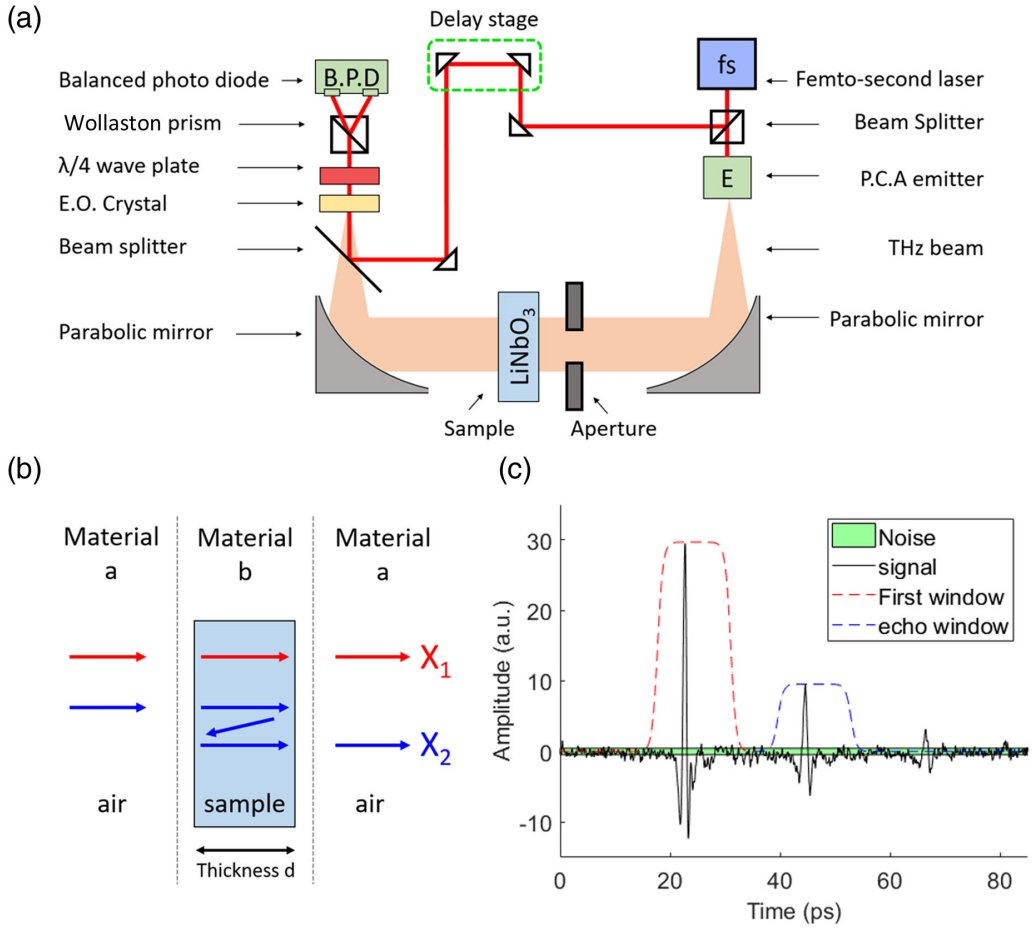

Fig. 1. (a) Schematic diagram of THz-TDS setup. The THz pulse is created by a photo-conductive antenna (P.C.A) which is collimated and transmitted through the $LiNbO_3$ sample. The pulse is detected via use of an electro-optic (E.O.) crystal and balanced photodiode. (b) Pulse propagation: Paths are shown for the first transmitted pulse (X_1) and the first internally reflected, or "echo" pulse (X_2) traveling from air, through a sample, and re-emerging to air. (c) Time-domain spectrum: The THz pulse passes through the $LiNbO_3$ sample, resulting in a peak around 20 ps. Due to internal reflections in the sample, subsequent echo-peaks can be seen, each with successively diminished intensities. Exponentially damped windows are applied to the first transmitted and first echo pulses. The noise of the detector (taking the standard deviation of the signal in the 30 ps period before the arrival of the first pulse) is highlighted by the green bar.

to calculate n and k as described in the literature [12]. The assumption of separable solutions for $n \gg k$ is valid in the case of lithium niobite, where the real part of the refractive index is over 100 times greater than the imaginary part. For the case where there is not such a large difference between n and k values, the real and complex solutions must be found simultaneously [12]. It should be noted that this method is not specific to use on the first transmitted and first echo pulse, and in fact any pair of subsequent echo pulses can be analyzed in this fashion without modification to the extraction equations presented here.

3. METHOD

A z-cut crystal of congruent lithium niobate is mounted on top of a metallic aperture of 10 mm diameter and placed in the beam path of a collimated THz source, as shown in Fig. 1(a). The sample thickness is measured with digital calipers to be 0.5 mm ($\pm$ 0.03 mm). The use of a collimated THz beam ensures normal incidence on the sample surface, which is required by the Fresnel equations we have used. The THz spectrometer is a commercially available Zomega spectrometer which detects THz radiation via femtosecond pulse interaction in a nonlinear crystal. A reference scan is first taken in the absence of the lithium niobate crystal through the metallic aperture; the lithium niobate is then mounted in the aperture and THz spectra are recorded with an averaging period of 2 min, recording a total of 24 spectra over a 50 min period. A fast-scan mechanism is employed in which the delay stage oscillates at 2 Hz, collecting multiple scans over a 2 min period. The use of the fast scan mechanism enables a large time-domain to be measured without significant increase in measurement time, although as the scan length increases the data resolution is correspondingly decreased. This effect is balanced, however, as in our case we obtain all data in a single trace instead of the usually obtained air trace and sample trace; therefore, we take one long measurement instead of two shorter measurements, and further do not need to account for time taken to add/remove the sample from the optics setup. All measurements are performed in an ambient air environment.

4. RESULTS

Figure 1(c) shows the time-domain of the THz radiation passing through the lithium niobate sample, where the first pulse (around 20 ps) corresponds to the pulse, which passes once through the sample, while the second pulse (around 45 ps) corresponds to the echo pulse, which is delayed in time due to the internal reflections within the sample. It can be seen that the echo pulse amplitude is attenuated in comparison to the first transmitted pulse due to the additional material interaction of the THz radiation with the sample due to the internal reflections. It can also be seen that there are additional echo pulses at 65 ps and 80 ps, but these are strongly attenuated and therefore we use only the first two peaks for the parameter extraction. The two pulses are separated from each other by multiplying the time-domain by an exponentially damped window, as shown by the dashed lines.

All pulses (measured through air or lithium niobate) are transformed with a window function. The window function is described by $W(t) = 1/(\exp((t - t0)/c) + 1)$, where c is 0.5 ps. An overlap between the first transmitted pulse and echo pulse always exists as the pulses extend infinitely in the time-domain. In the time-domain in Fig. 1(c), we highlight the standard deviation of the amplitude noise averaged over the 30 ps period before the arrival of the first pulse. From this figure it, can be seen that the signal of the first pulse descends into the noise level before the arrival of the echo pulse. The width of the windows is chosen to encompass fully the area in which the pulse signal is higher than the signal noise level. This process is not unimpeachable, but a full discussion of the windowing of time-domain pulses is far beyond the scope of this paper.

Figure 2(a) displays the amplitude of the frequency spectra obtained by Fourier transform for the pulse traveling through air, and the first pulse and echo pulse transmitted through lithium niobate. The transmission spectra reveal that the pulse through air has a usable bandwidth up to 3 THz, while lithium niobate has low transmission at frequencies above 1.5 THz for the first transmitted pulse, which is due to a phonon feature around 4 THz [22]. The echo pulse has a lower usable bandwidth than the first transmitted pulse, hitting the noise floor around 1 THz.

Once the Fourier transforms are performed, the magnitude of the echo pulse is divided by that of the first pulse to obtain $|Y(\omega)|$ while the unwrapped phase of the echo pulse is subtracted from that of the first pulse to obtain $\phi(\omega)$, and the complex refractive index is calculated. Figure 2(b) displays the real part of the refractive index of z-cut lithium niobate averaged for 24 measurements taken over a 50 min period, with the standard deviation shown as the shaded regions. The data is extracted with two different methods; in the first method, labeled "air reference," a reference measurement of THz propagation through air is taken before sample measurements and all subsequent lithium niobate measurements are normalized to this single air reference. In the second method, labeled "Echo Reference," the data is extracted by referencing the echo pulse to the first transmitted pulse, as described in the theory section.

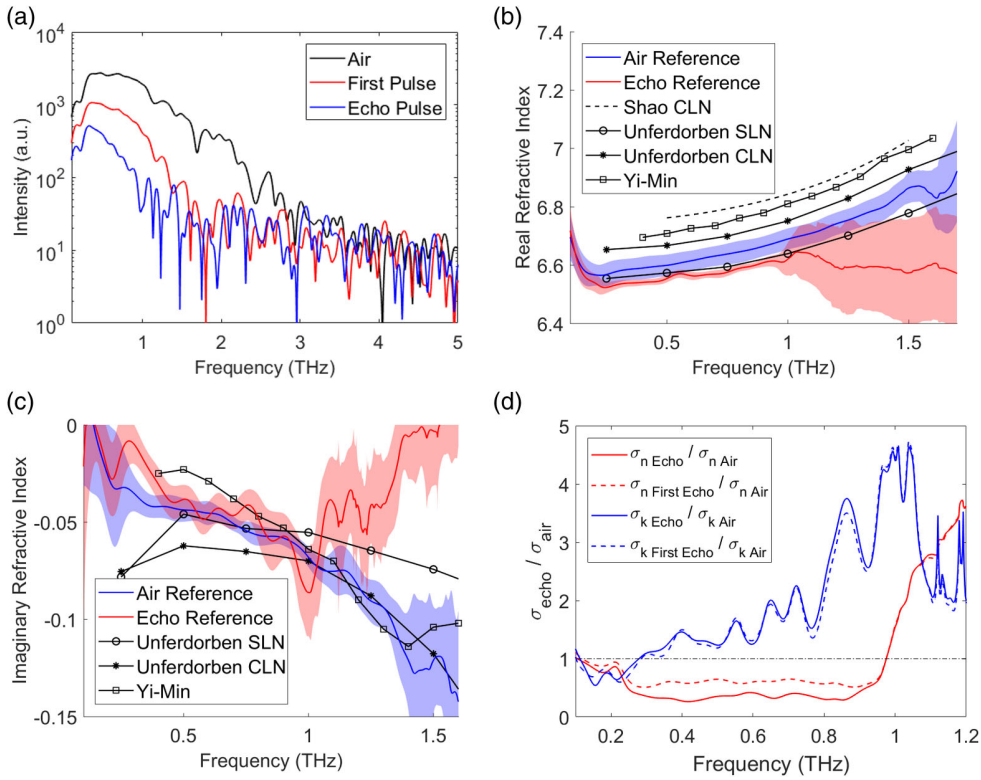

Fig. 2. (a) Frequency-domain spectra of pulse traveling through air and lithium niobate, and the first echo pulse. (b) and (c) Real and imaginary refractive index averaged for 24 measurements of lithium niobate over a 50 min period, where the error bars are given by the standard deviation of the repeat measurements. The blue datasets show the refractive index calculated by referencing to a measurement in air, while the red datasets use the echo referencing method. Previously reported values of refractive index are reproduced from the literature [23–25]. (d) Comparison of standard deviation from "air", "echo", and "first echo" methods showing ratio of echo methods to air method.

In the frequency range 0.1–1.0 THz, both methods result in similar values for real refractive index, where the echo method is on average 0.73% lower than for the air reference method. It can be seen from the graph that the air reference method is capable of providing trustworthy values up to 1.5 THz, while the echo pulse method suffers from large noise above 1 THz. However, in the region of 0.1 to 1 THz, it is clear that the echo pulse method has a much smaller standard deviation than the air reference method.

Overlaid to our experimental values of refractive index are those reported from Shao [23], Unferdorben [24], and Yi-Min [25]. There appears to be a relatively large variation in the reported values, which may be due to inherent differences in the crystal, measurement environments, or artificial differences—for example, from spectrometer alignment or extraction algorithms. The literature values reveal a large degree of variation, where the average range of literature values is 0.20 in this frequency region. Nevertheless, the value of refractive index we measure here are in general accordance with those reported from the literature. To compare all datasets, we look at the frequency range 0.5–1.0 THz, as this is the only range in which all datasets overlap. In this range, we find that the air reference method results in a real refractive index on average 1.06% lower than the average value from the literature, while the echo reference method is on average 1.89% lower.

Figure 2(c) shows imaginary refractive index extracted by the air and echo reference methods for 24 repeat measurements of lithium niobate where mean values are plotted as solid lines, with standard deviation plotted as colored error bars. Both extraction methods provide values which are in general accordance with the reported literature [23–25].

Figure 2(d) presents a comparison of the variation between the two referencing methods. The standard deviations of n and k for the echo method are divided by the deviation calculated using the air reference method. The echo method reduces the standard deviation for the real part of the refractive index between 0.1 and 1.0 THz, where the average value of the ratio is 0.35 in the frequency range 0.25–0.90 THz. The imaginary part, however, suffers from greater variation compared to the air method at all frequencies. This behavior is generally characteristic of THz-TDS where the imaginary components have greater variation than the real components; laser power fluctuations create variation in the imaginary components while the real components are affected by the drift of the mechanical delay stage, which is generally negligible in comparison.

It should be noted that we take 24 measurements through lithium niobate as compared to only one measurement through air; therefore, to compare the standard deviations of the air and echo methods may give a skewed impression of the statistical benefits. To further compare the two methods, we have also extracted data by the echo method in which every measurement of an echo pulse in lithium niobate is referenced to the first measurement of the first transmitted pulse which was taken at the beginning of the 50 min period (we will refer to this as the "first echo" method). In this manner, there is now a single reference scan for the air method and the "first echo" method. By division of the standard deviation of the "first echo" method by the air method, we see that the "first echo" method still achieves a reduction in the standard deviation for the real refractive index, while the imaginary components are relatively unchanged.

The large increase in standard deviation of the echo method above 1 THz is likely related to the echo pulse hitting the noise floor at this frequency [as shown in Fig. 2(a)]. To investigate whether this effect is indeed sample specific, we propose measuring silicon samples which display a relatively flat refractive index across 0.1–4.0 THz and should allow for the echo technique to be extended far beyond 1.0 THz.

5. SAMPLE COMPATIBILITY

The technique presented here imposes certain restrictions on the samples which can be measured. The thickness and refractive index of the sample must be large enough to effectively separate the multiply reflected pulses within the material so that they can be handled independently in the time-domain. By assessing the time-domain trace, we impose an exponential window on the pulses, by which we ensure span a time length sufficiently long to encompass the points at which the pulse descends into the noise level of the detector. From this, we can calculate the minimum separation of the first and echo peak, which ensures that the windows do no overlap at a level above the upper limit of the signal noise. The separation of the two pulse maxima is determined to be 16.9 ps. In Fig. 3(a), we plot the sample thickness d against refractive index n and highlight the region which allows for the necessary temporal separation of the two pulses, revealing a large region of material compatibility for samples.

To investigate the restrictions placed on the real part of the refractive index, we look towards the mathematical definition of the echo pulse presented in Eq. (2) (ignoring the Beer–Lambert propagation terms). By assessing the Fresnel terms of this equation, we see that the echo pulse is described by two transmission functions $T_{ab} \times T_{ba}$ and a squared reflection term R_{ab}^2. By plotting these two functions against refractive index n in Fig. 3(b), it can be seen that initially when $n = 1$, the transmission term is 1 while the reflection term is 0, which when multiplied together (red line) results in an echo pulse power of 0. As the refractive index increases, the transmission term decreases while the reflection term increases, which results in an echo power which initially increases and then tapers off, reaching a maximum around $n = 5.8$. For example, a measurement sample of silicon with refractive index $n = 3.4$ would exhibit an echo pulse power only 15% lower than for lithium niobate based on the Fresnel terms, demonstrating the wide range of material compatibility to the echo method.

The damping of the pulse as it propagates through a material is determined by the Beer–Lambert term, which increases exponentially with the imaginary part of the refractive index. The strength of the first transmitted pulse and echo pulse can be increased by choosing a sample material with a low k value, such as Si or GaAs, which are both around 40 times smaller in comparison to lithium niobate (at 1 THz, $k_{\mathrm{LiNbO_3}} = 0.07$ while $k_{si} \sim k_{\mathrm{GaAs}} \sim 0.0012$) [26]. Furthermore, the comparative benefits over the air referencing method will be dependent on the spectrometer hardware, such as the reliability of the mechanical delay stage, fluctuations in the laser power, and atmospheric humidity.

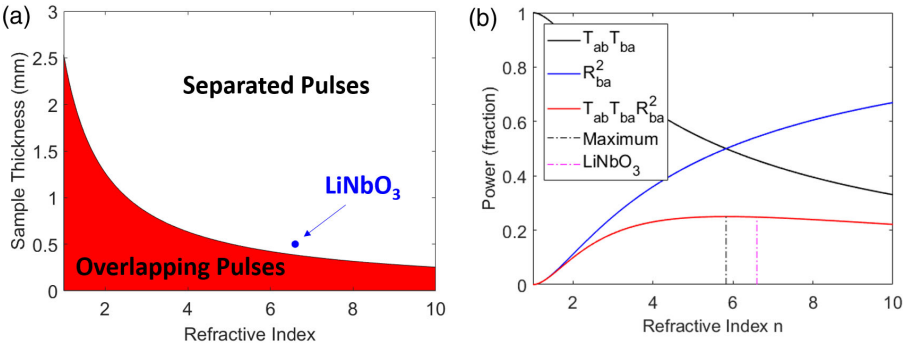

Fig. 3. (a) Theoretical power of echo pulse calculated by Fresnel coefficients reveals that the echo method is suitable for a broad range of refractive index values. (b) Diagram showing combination of sample thickness and refractive index which is capable of creating pulses separated in the time-domain. We plot the location of our 0.5 mm thickness lithium niobate sample, which reveals that even near the edge of the "separation" region, the method still functions adequately.

6. CONCLUSIONS

In conclusion, we have presented an "echo reference" method to determine complex refractive index from THz-TDS data in the absence of an air reference measurement. We present a benchmark test in which a test sample of lithium niobate is measured repeatedly over a 50 min period, and the data is extracted by both the echo reference and air reference methods. It is shown that for frequencies below 1 THz, the echo reference measurements achieve lower standard deviation in real refractive index values as compared to the air reference method, but the usable frequency bandwidth for the echo reference is lower than that of the air reference method. We argue the echo reference method has a number of advantages over a traditional air referencing method such as reduced effects of power drift, reduces the need for purging of the spectrometer chamber with inert gas, and allows the sample to be held securely in the optical setup without the need for removing the sample between measurements.

Funding. Engineering and Physical Sciences Research Council (EP/N509747/1).

Disclosures. The authors declare no conflicts of interest.

REFERENCES

1. A. Markelz, A. Roitberg, and E. Heilweil, "Pulsed terahertz spectroscopy of DNA, bovine serum albumin and collagen between 0.1 and 2.0 THz," Chem. Phys. Lett. **320**, 42–48 (2000).
2. S. Ebbinghaus, S. J. Kim, M. Heyden, X. Yu, U. Heugen, M. Gruebele, D. M. Leitner, and M. Havenith, "An extended dynamical hydration shell around proteins," Proc. Natl. Acad. Sci. USA **104**, 20749–20752 (2007).
3. M. Walther, B. Fischer, M. Schall, H. Helm, and P. Jepsen, "Far-infrared vibrational spectra of all-trans, 9-cis and 13-cis retinal measured by THz time-domain spectroscopy," Chem. Phys. Lett. **332**, 389–395 (2000).
4. R. M. Woodward, V. P. Wallace, R. J. Pye, B. E. Cole, D. D. Arnone, E. H. Linfield, and M. Pepper, "Terahertz pulse imaging of *ex vivo* basal cell carcinoma," J. Invest. Dermatol. **120**, 72–78 (2003).
5. J. F. Federici, B. Schulkin, F. Huang, D. Gary, R. Barat, F. Oliveira, and D. Zimdars, "THz imaging and sensing for security applications—explosives, weapons and drugs," Semicond. Sci. Technol. **20**, S266–S280 (2005).
6. R. Appleby and H. B. Wallace, "Standoff detection of weapons and contraband in the 100 GHz to 1 THz region," IEEE Trans. Antennas Propag. **55**, 2944–2956 (2007).
7. J. Chen, Y. Chen, H. Zhao, G. J. Bastiaans, and X.-C. Zhang, "Absorption coefficients of selected explosives and related compounds in the range of 0.1–2.8 THz," Opt. Express **15**, 12060–12067 (2007).
8. J. Wei, D. Olaya, B. S. Karasik, S. V. Pereverzev, A. V. Sergeev, and M. E. Gershenson, "Ultrasensitive hot-electron nanobolometers for terahertz astrophysics," Nat. Nanotechnol. **3**, 496–500 (2008).
9. M. Negrello, R. Hopwood, G. D. Zotti, A. Cooray, A. Verma, J. Bock, D. T. Frayer, M. A. Gurwell, A. Omont, R. Neri, H. Dannerbauer, L. L. Leeuw, E. Barton, J. Cooke, S. Kim, E. da Cunha, G. Rodighiero, P. Cox, D. G. Bonfield, M. J. Jarvis, S. Serjeant, R. J. Ivison, S. Dye, I. Aretxaga, D. H. Hughes, E. Ibar, F. Bertoldi, I. Valtchanov, S. Eales, L. Dunne, S. P. Driver, R. Auld, S. Buttiglione, A. Cava, C. A. Grady, D. L. Clements, A. Dariush, J. Fritz, D. Hill, J. B. Hornbeck, L. Kelvin, G. Lagache, M. Lopez-Caniego, J. Gonzalez-Nuevo, S. Maddox, E. Pascale, M. Pohlen, E. E. Rigby, A. Robotham, C. Simpson, D. J. B. Smith, P. Temi, M. A. Thompson, B. E. Woodgate, D. G. York, J. E. Aguirre, A. Beelen, A. Blain, A. J. Baker, M. Birkinshaw, R. Blundell, C. M. Bradford, D. Burgarella, L. Danese, J. S. Dunlop, S. Fleuren, J. Glenn, A. I. Harris, J. Kamenetzky, R. E. Lupu, R. J. Maddalena, B. F. Madore, P. R. Maloney, H. Matsuhara, M. J. Michaowski, E. J. Murphy, B. J. Naylor, H. Nguyen, C. Popescu, S. Rawlings, D. Rigopoulou, D. Scott, K. S. Scott, M. Seibert, I. Smail, R. J. Tuffs, J. D. Vieira, P. P. van der Werf, and J. Zmuidzinas, "The detection of a population of submillimeter-bright, strongly lensed galaxies," Science **330**, 800–804 (2010).
10. N. Nagai, M. Sumitomo, M. Imaizumi, and R. Fukasawa, "Characterization of electron- or proton-irradiated Si space solar cells by THz spectroscopy," Semicond. Sci. Technol. **21**, 201–209 (2006).
11. K. Ahi, S. Shahbazmohamadi, and N. Asadizanjani, "Quality control and authentication of packaged integrated circuits using enhanced-spatial-resolution terahertz time-domain spectroscopy and imaging," Opt. Lasers Eng. **104**, 274–284 (2018).
12. P. Jepsen, D. Cooke, and M. Koch, "Terahertz spectroscopy and imaging—modern techniques and applications," Laser Photon. Rev. **5**, 124–166 (2011).
13. A. Redo-Sanchez and X.-C. Zhang, "Self-referenced method for terahertz wave time-domain spectroscopy," Opt. Lett. **36**, 3308–3310 (2011).
14. P. R. Whelan, K. Iwaszczuk, R. Wang, S. Hofmann, P. Bøggild, and P. U. Jepsen, "Robust mapping of electrical properties of graphene from terahertz time-domain spectroscopy with timing jitter correction," Opt. Express **25**, 2725–2732 (2017).
15. J. Choi, W. S. Kwon, K.-S. Kim, and S. Kim, "Nondestructive material characterization in the terahertz band by selective extraction of sample-induced echo signals," J. Nondestruct. Eval. **34**, 269 (2014).

16. L. Duvillaret, F. Garet, and J.-L. Coutaz, "Highly precise determination of optical constants and sample thickness in terahertz time-domain spectroscopy," Appl. Opt. **38**, 409–415 (1999).
17. W. Lai, H. Cao, J. Yang, G. Deng, Z. Yin, Q. Zhang, B. Pelaz, and P. Del Pino, "Antireflection self-reference method based on ultrathin metallic nanofilms for improving terahertz reflection spectroscopy," Opt. Express **26**, 19470–19478 (2018).
18. S. Huang, P. C. Ashworth, K. W. Kan, Y. Chen, V. P. Wallace, Y. Ting Zhang, and E. Pickwell-MacPherson, "Improved sample characterization in terahertz reflection imaging and spectroscopy," Opt. Express **17**, 3848–3854 (2009).
19. F. Sanjuan, A. Bockelt, and B. Vidal, "Determination of refractive index and thickness of a multilayer structure with a single terahertz time domain spectroscopy measurement," Appl. Opt. **53**, 4910–4913 (2014).
20. F. Sanjuan and B. Vidal, "Refractive index calculation from echo interference in pulsed terahertz spectroscopy," Electron. Lett. **50**, 308–309 (2014).
21. F. Vandrevala and E. Einarsson, "Decoupling substrate thickness and refractive index measurement in THz time-domain spectroscopy," Opt. Express **26**, 1697–1702 (2018).
22. M. Dutta, C. Ellis, X. G. Peralta, A. Bhalla, and R. Guo, "Terahertz electrical and optical properties of $LiNbO_3$ single crystal thin films," Proc. SPIE **9586**, 958608 (2015).
23. G. Hao Shao, S. Jun Ge, Y. Chao Shi, W. Hu, and Y. Qing Lu, "Extended Cauchy equations of congruent LiNbO_3 in the terahertz band and their applications," Opt. Mater. Express **6**, 3766–3775 (2016).
24. M. Unferdorben, Z. Szaller, I. Hajdara, J. Hebling, and L. Pálfalvi, "Measurement of refractive index and absorption coefficient of congruent and stoichiometric lithium niobate in the terahertz range," J. Infrared Millim. Terahertz Waves **36**, 1203–1209 (2015).
25. S. Yi-Min, M. Zong-Liang, H. Bi-Hui, L. Guo-Qing, and W. Li, "Giant birefringence of lithium niobate crystals in the terahertz region," Chin. Phys. Lett. **24**, 414–417 (2007).
26. D. Grischkowsky, S. Keiding, M. van Exter, and C. Fattinger, "Far-infrared time-domain spectroscopy with terahertz beams of dielectrics and semiconductors," J. Opt. Soc. Am. B **7**, 2006–2015 (1990).

CLEO EU 2019

CLEO EU 2019
Sunday 23 June
Session: CE-1 “Opportunities for Advanced Nanostructured and Non-Linear Optical Materials”

UNIVERSITY OF Southampton

THz Spectroscopy of Fe:$LiNbO_3$ for Optical Control of 2D Materials


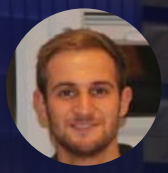


Sophie Blundell[1], Jon Gorecki[2*], Nikitas Papasimakis[2], Sakellaris Mailis[3], Vasilis Apostolopoulos[1]

[1]School of Physics and Astronomy, University of Southampton, UK

[2]Optoelectronics Research Centre, University of Southampton, UK

[3]Center for Photonics and Quantum Materials, Skoltech, RUS

Outline of the Talk

- Why optical control of 2D materials?
- How can Fe:$LiNbO_3$ be used?
- Examples of optical gating on Fe:$LiNbO_3$
- THz spectroscopy investigation
- Conclusions / Future Work

Why Use 2D Materials ?

Graphene

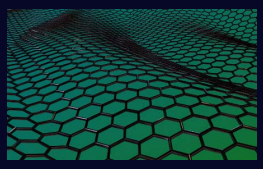

WS_2 $MoSe_2$ MoS_2

Transition Metal Dichalcogenides (TMDs)

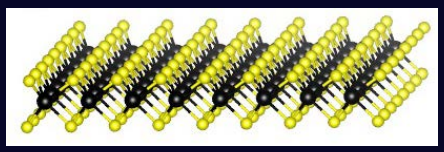

Perovskites

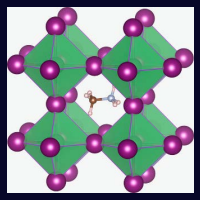

+ Many others

Controllable Electronic Properties

MEMs

Membranes

Flexible Touch-Screen Electrodes

Applications

Photodetection

Chemical Sensing

Plasmonics

Optoelectronics

Optical Tuning of Graphene

Linear dispersion relation

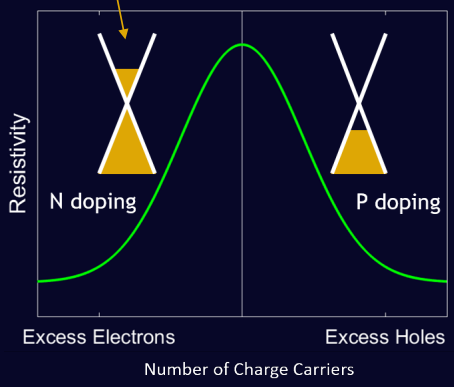

Small change in number of electrons = large change in conductivity

Reversible

Pyro-resistive substrate

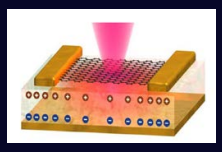

Gopalan et. al., **Adv. Opt. Mater**. 2017

Interfacial charge trap sites

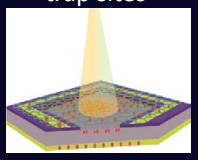

Wang et. al., **J. Phys. Chem. C**, 2015
Ho et. al., **Adv. Mater** 2015
Jun et. al., **Nat. Nanotechnol.,** 2014

Non-Volatile — **Volatile**

Chemical interactions with substrate/atmosphere

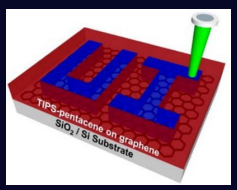

Seo et. al., **ACS Nano**, 2014
Wang et. al., **J. Phys. Chem. C** 2017
Iqbal et. al., **Phys. Chem. Chem. Phys**. 2015

Non-Reversible

Optical doping allows for:

- Non-contact
- Spatial resolution
- Complex doping patterns

Optical Tuning of Graphene

Linear dispersion relation

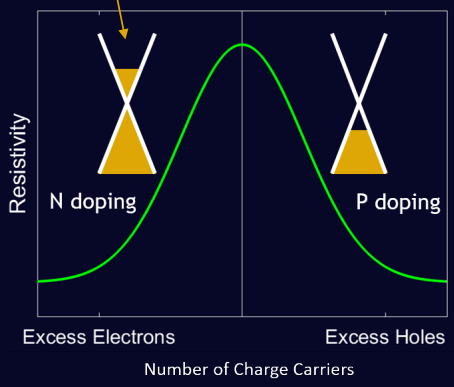

Small change in number of electrons = large change in conductivity

Reversible

Photoconductive Fe:$LiNbO_3$

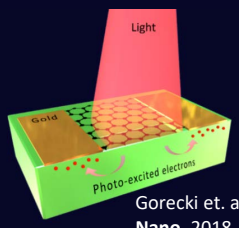

Gorecki et. al., **ACS Nano**. 2018

Pyro-resistive substrate

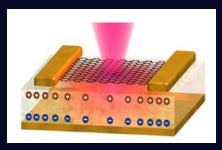

Gopalan et. al., **Adv. Opt. Mater**. 2017

Interfacial charge trap sites

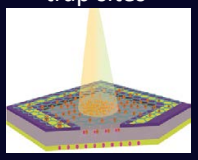

Wang et. al., **J. Phys. Chem. C**, 2015
Ho et. al., **Adv. Mater** 2015
Jun et. al., **Nat. Nanotechnol.,** 2014

Non-Volatile — **Volatile**

Chemical interactions with substrate/atmosphere

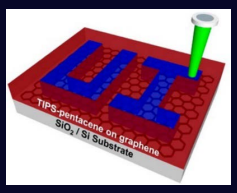

Seo et. al., **ACS Nano**, 2014
Wang et. al., **J. Phys. Chem. C** 2017
Iqbal et. al., **Phys. Chem. Chem. Phys**. 2015

Non-Reversible

Optical doping allows for:

- Non-contact
- Spatial resolution
- Complex doping patterns

Fe:$LiNbO_3$ for Optical Control of Graphene

Photorefractive damage = Optically induced charge migration

Photo-Refractive Mechanism

1. Photons absorbed by Fe ions
2. Electrons excited to conduction band
3. Electron migration in lattice
4. Electrons trapped at dark Fe ions

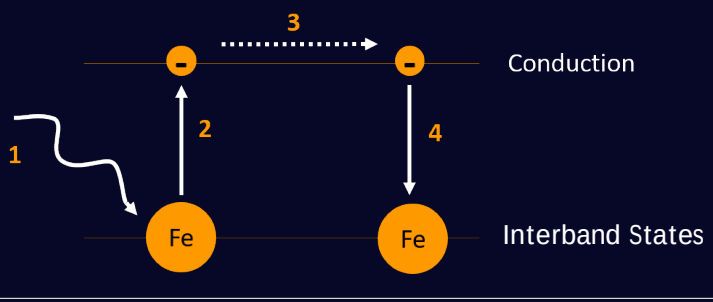

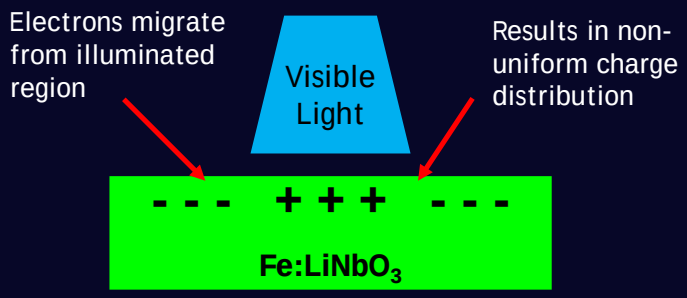

- Creates bulk charge distributions
- Remains in dark for years
- Fast optical erasing
- Spatial control
- Repeatable indefinitely
- Optically induced fields at surface 250 kV/cm
- Writing speed scales with intensity

Buse at. al., **Nature**, 1998
Arizmendi et. al., **Appl. Phys. B. Lasers. Opt.,** 2007
Puerto et. al., **Opt. Express**, 2019

$Fe:LiNbO_3$ for Optical Control of Graphene

Photorefractive damage = Optically induced charge migration

Photo-Refractive Mechanism

1. Photons absorbed by Fe ions
2. Electrons excited to conduction band
3. Electron migration in lattice
4. Electrons trapped at dark Fe ions

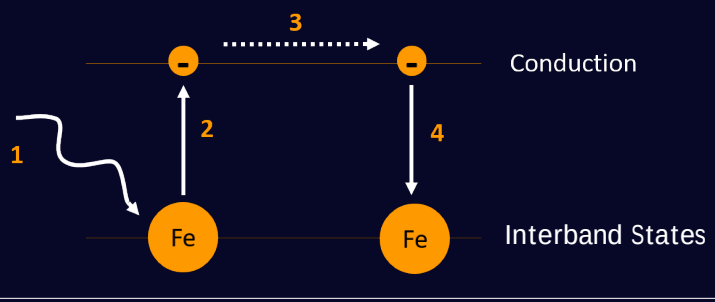

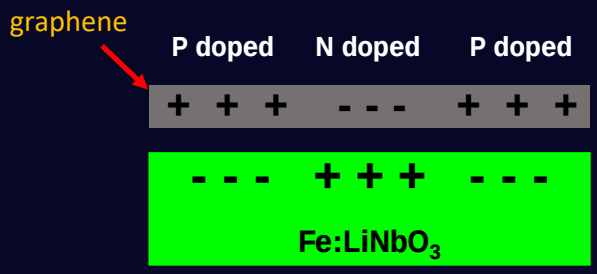

$Fe:LiNbO_3$ for electrostatic doping of graphene

- Electrostatic field created by substrate
- Electrons in graphene injected/removed to compensate
- Change in carrier number alters resistivity

Optical Control of Electronics

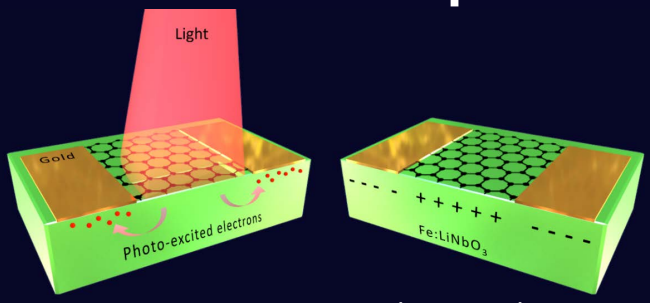

Optically induced charge migration in substrate → Electrostatic doping of graphene

Device fabrication details

- *$LiNbO_3$:Fe substrate*
- *CVD graphene on Z polar face*
- *Cr/Au electrodes by electron beam evaporation with shadow mask*

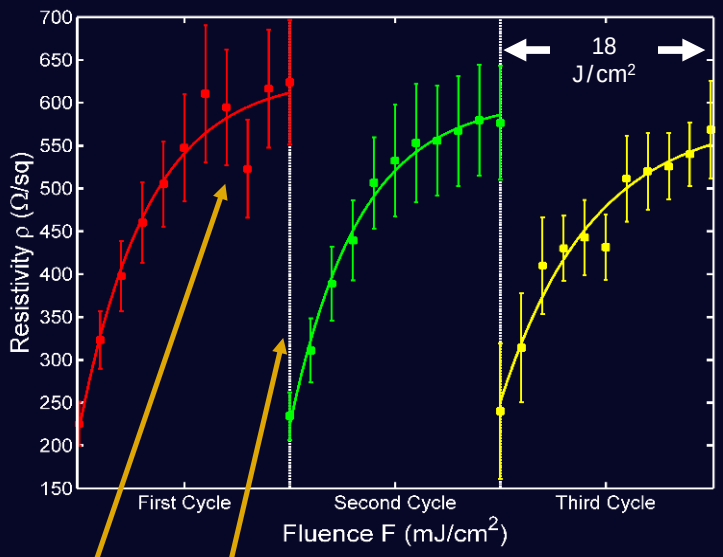

Saturation of substrate
After 18 J/cm² Δρ is negligible

Thermal reset
(4 hours in convection oven at 90°C)

Cycle is repeated
shows similar behaviour with each cycle

J. Gorecki, V. Apostolopoulos, J.Y. Ou, S. Mailis, N. Papasimakis, (2018) Optical gating of graphene on photoconductive Fe:$LiNbO_3$. ***ACS Nano***,

Optical Control of Plasmonics

Device Fabrication

- Z cut Fe:$LiNbO_3$
- gold split ring resonators (SRRs)
- Monolayer graphene top layer
- Designed for resonance peak ~ 0.46 THz

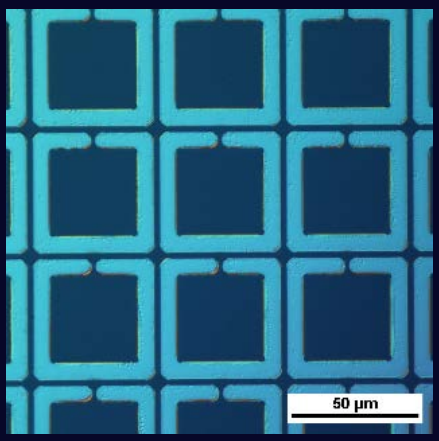

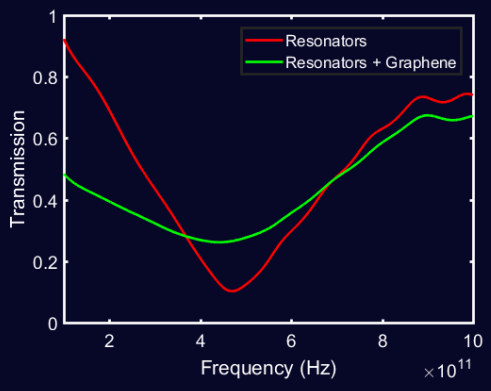

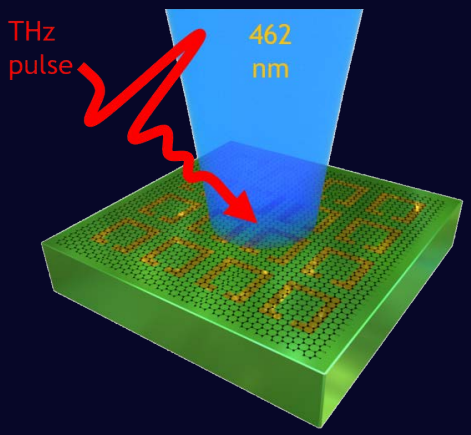

Experiment Procedure

- Device held in light proof box
- Illuminated with 462 nm source to induced photo-response
- Fe:$LiNbO_3$ shifts graphene conductivity, changing plasmonic spectra
- THz transmission measured while illuminated

Optical Control of Plasmonics

Dark Measurements

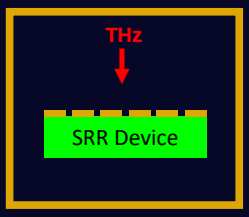

Illuminated Measurements

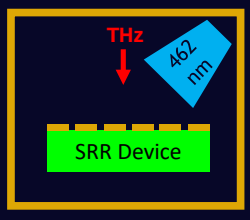

Dark Measurements

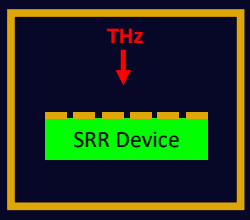

Illumination creates change in transmission spectra

Effect is non-volatile once laser source removed

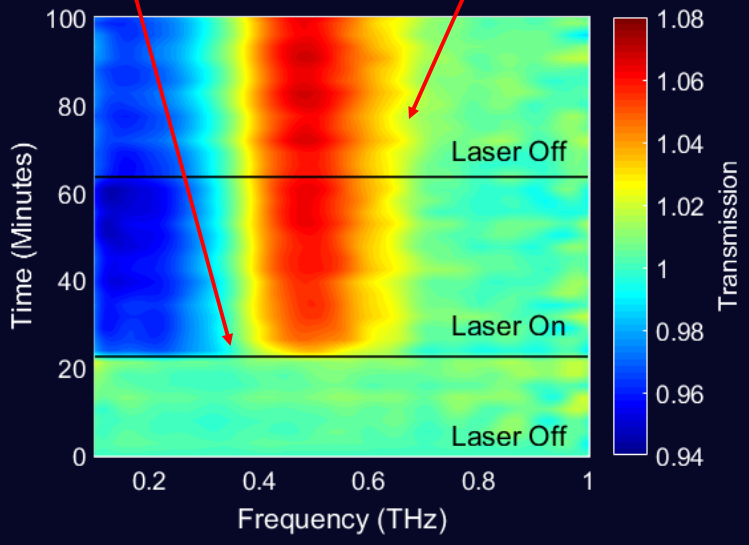

Modelled in comsol to gauge ΔE_F

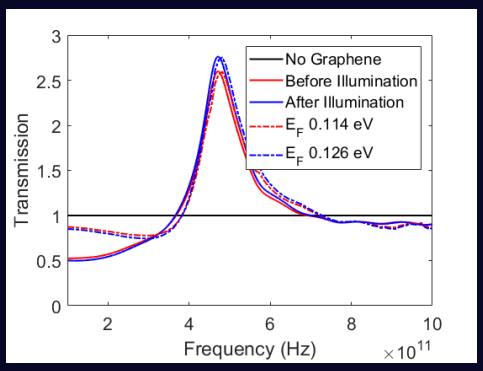

E_F change corresponds to carrier injection of $2.11 \times 10^{11}/cm^2$ into graphene from ground

THz Spectroscopy of Fe:$LiNbO_3$

Experimental Method

- Fe:$LiNbO_3$ sample illuminated by 462nm source to create free electrons
- THz transmission measured during illumination at various intensities
- Free electrons alter THz transmission (absorption and phase)
- Photo-excited carriers probed by THz time domain spectroscopy (TDS)

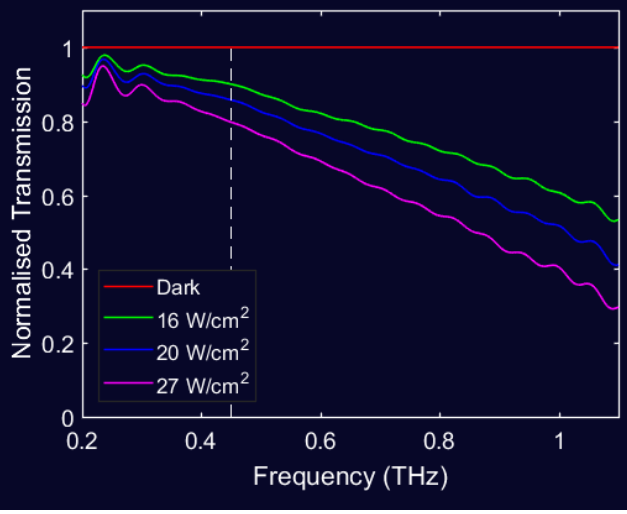

Initial dip then increase in **n**

k fairly linear with intensity

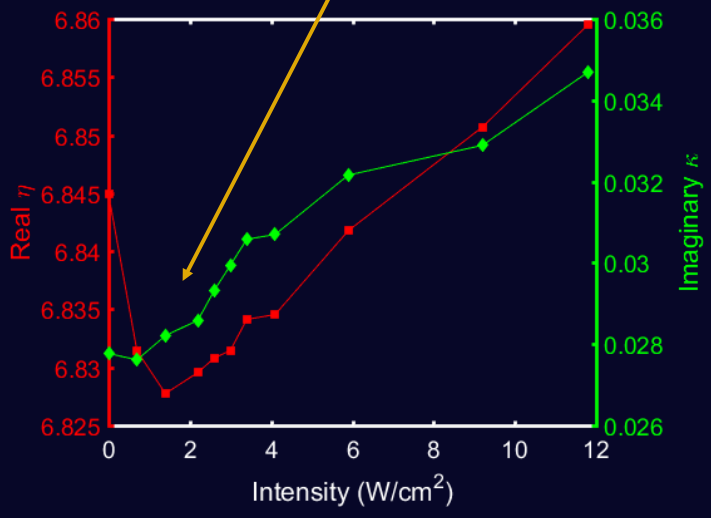

THz Spectroscopy of $Fe:LiNbO_3$

- THz TDS provides complex refractive index **n** and **k**
- **n** and **k** converted to complex conductivity
  - $\sigma_1 = \omega \varepsilon_0 (2nk)$
  - $\sigma_2 = \omega \varepsilon_0 (n^2 + k^2)$

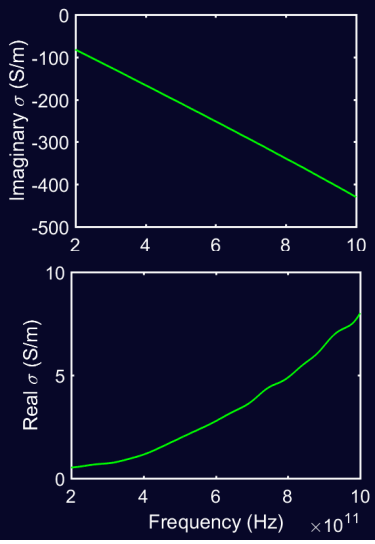

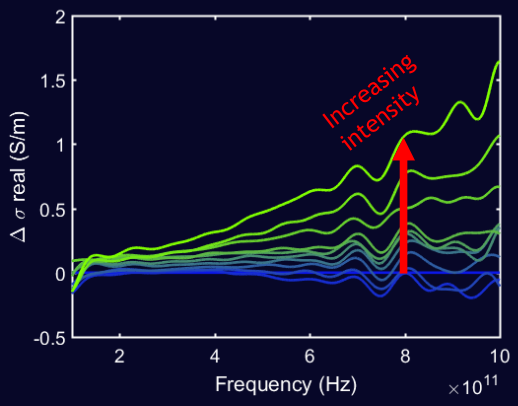

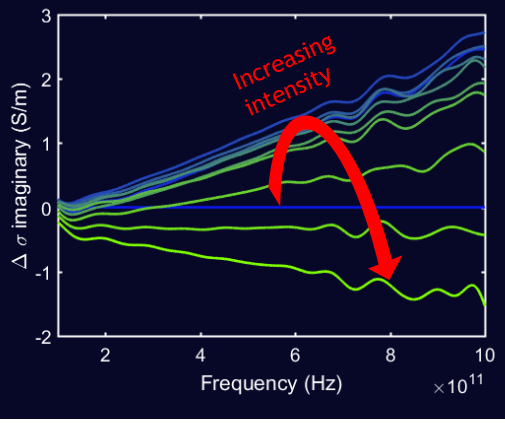

- Monotonic increase in real σ
- Imaginary σ has initial increase followed by decrease at higher illumination
- Look for model to fit to σ which may allow for carrier numbers to be calculated

Summary / Outlook

1. **Photorefractive Fe:$LiNbO_3$ can create charge distributions**

2. **Fe:$LiNbO_3$ allows for optical control of graphene conductivity**
   - spatially resolved
   - Non-volatile
   - Reversible
   - Repeatable

3. **We show optical gating of graphene on Fe:$LiNbO_3$**
   - Electronics
     - 2.6 fold increase in resistivity
   - Plasmonics
     - 8% transmission change
     - $2.11 \times 10^{11}/cm^2$ carrier injection in graphene

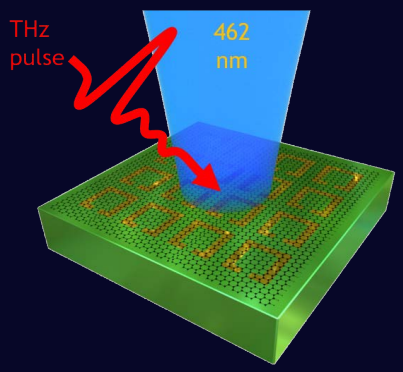

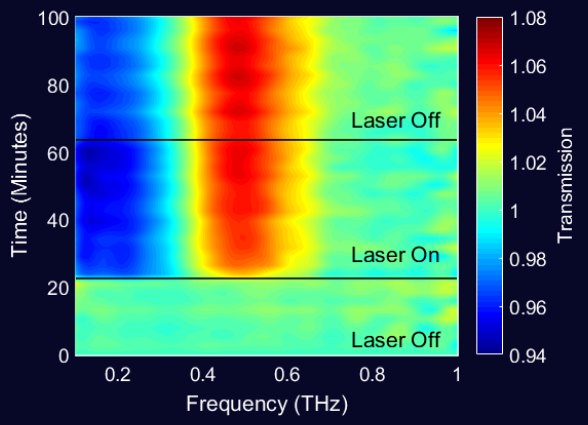

CLEO EU 2019
Sunday 23 June
Session: CE-1 “Opportunities for Advanced Nanostructured and Non-Linear Optical Materials”

UNIVERSITY OF Southampton

Thank You

Any Questions?


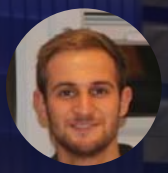


Sophie Blundell[1], Jon Gorecki[2*], Nikitas Papasimakis[2], Sakellaris Mailis[3], Vasilis Apostolopoulos[1]

j.gorecki@soton.ac.uk*

[1]School of Physics and Astronomy, University of Southampton, UK

[2]Optoelectronics Research Centre, University of Southampton, UK

[3]Center for Photonics and Quantum Materials, Skoltech, RUS

CLEO US 2019

UNIVERSITY OF Southampton

Optical Tuning of Graphene Electronics and Plasmonics on Fe:$LiNbO_3$

Jon Gorecki[1*], Vasilis Apostolopoulos[2] ,Sakellaris Mailis[3] , Nikitas Papasimakis[1]

j.gorecki@soton.ac.uk*

[1]Optoelectronics Research Centre, University of Southampton, UK

[2]School of Physics and Astronomy, University of Southampton, UK

[3]Center for Photonics and Quantum Materials, Skoltech, RUS

CLEO US 2019
Session: STh4H Optical Driven Photonics
Thursday 9th May

Who are we?

University of Southampton, UK

820 m^2 cleanroom facility

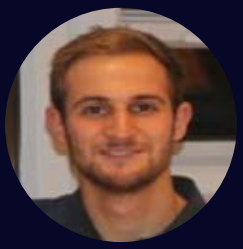

Jon Gorecki
PhD Student

Sakellaris Mailis
Photonics and Quantum Materials

Vasilis Apostolopoulos
Terahertz Laboratories

Nikitas Papasimakis
Metamaterials

Slide 3

Low Dimensional Materials

Graphene

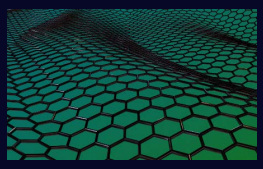

WS_2 $MoSe_2$ MoS_2

Transition Metal Dichalcogenides (TMDs)

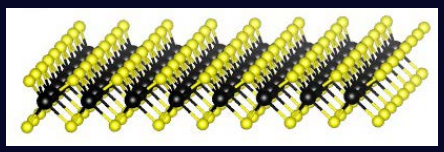

Perovskites

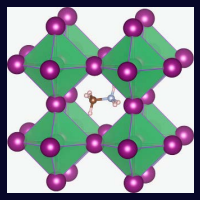

+ Many others

Controllable Electronic Properties

Applications

MEMs

Membranes

Flexible Touch-Screen Electrodes

Photodetection

Chemical Sensing

Plasmonics

Optoelectronics

Slide 4

Electronic Band Structure of Graphene

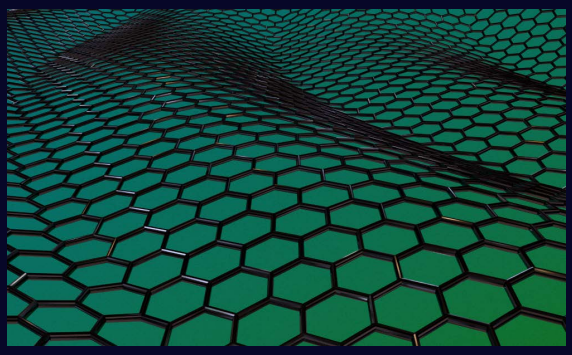

Hexagonal arrangement of carbon atoms

Electrons confined to 2D plane

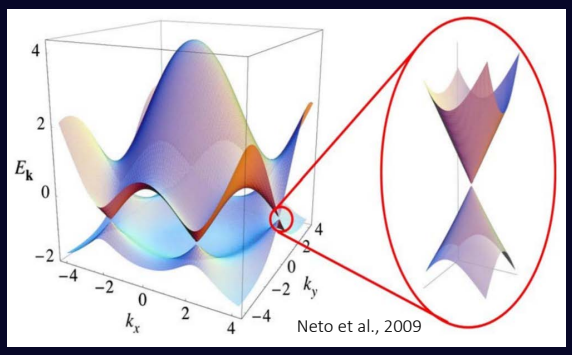

Neto et al., 2009

Linear dispersion relation

Density of states at Fermi Level -> 0

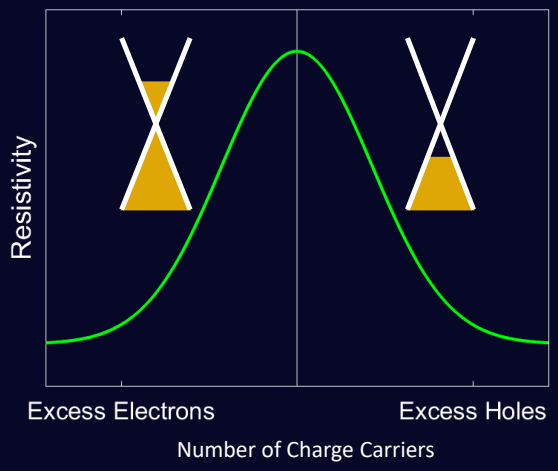

Small change in number of electrons results in large changes to conductivity

Slide 5

Electronic Band Structure of Graphene

Reversible

Pyro-resistive substrate

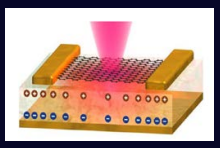

Gopalan et. Al., **Adv. Opt. Mater**. 2017

Interfacial charge trap sites

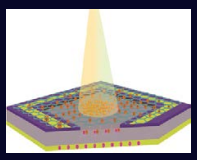

Wang et. Al., **J. Phys. Chem. C**, 2015
Ho et. Al., **Adv. Mater** 2015
Jun et. Al., **Nat. Nanotechnol.**, 2014

Non-Volatile — **Volatile**

Chemical interactions with substrate/atmosphere

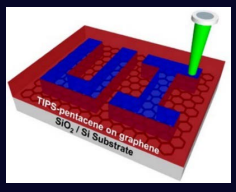

Seo et. Al., **ACS Nano**, 2014
Wang et. al., **J. Phys. Chem. C** 2017
Iqbal et. Al., **Phys. Chem. Chem. Phys**. 2015

Non-Reversible

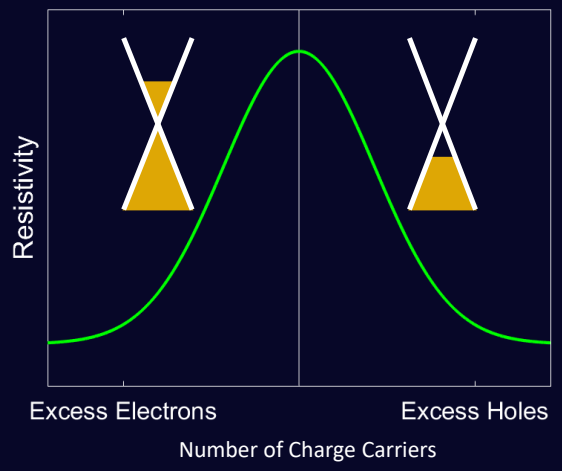

Small change in number of electrons results in large changes to conductivity

Slide 5

Electronic Band Structure of Graphene

Reversible

Pyro-resistive substrate

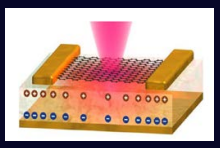

Gopalan et. Al., **Adv. Opt. Mater**. 2017

Interfacial charge trap sites

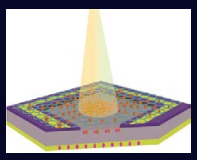

Wang et. Al., **J. Phys. Chem. C**, 2015
Ho et. Al., **Adv. Mater** 2015
Jun et. Al., **Nat. Nanotechnol.**, 2014

Photo conductive
Fe:$LiNbO_3$

Non-Volatile — **Volatile**

Chemical interactions with substrate/atmosphere

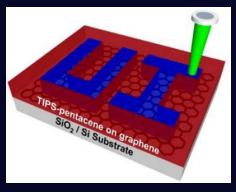

Seo et. Al., **ACS Nano**, 2014
Wang et. al., **J. Phys. Chem. C** 2017
Iqbal et. Al., **Phys. Chem. Chem. Phys**. 2015

Non-Reversible

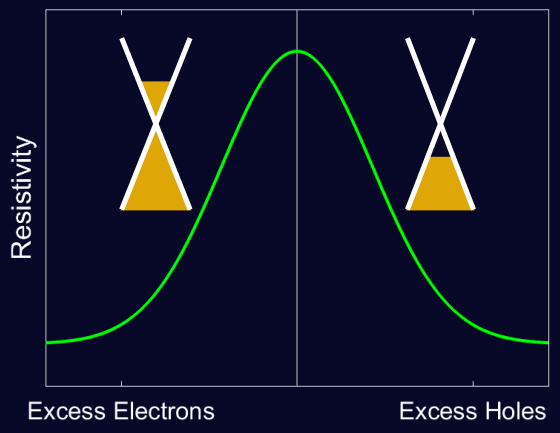

Small change in number of electrons results in large changes to conductivity

Photorefractive $Fe:LiNbO_3$

Photorefractive damage = Optically induced charge migration

Photo-Refractive Mechanism

1. Photons absorbed by Fe ions
2. Electrons excited to conduction band
3. Electron migration in lattice
4. Electrons trapped at dark Fe ions

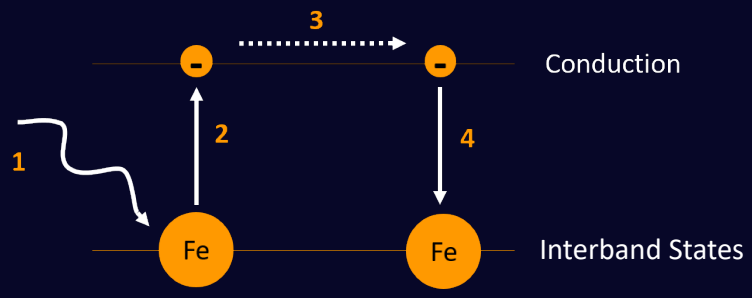

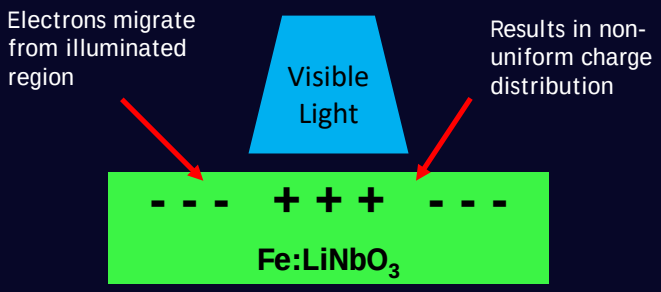

Effect used for holographic storage

- Creates bulk charge distributions
- Remains in dark for years
- Fast optical erasing
- Spatial control
- Repeatable indefinitely

Buse at. Al., **Nature**, 1998
Arizmendi et. Al., **Appl. Phys. B. Lasers. Opt.,** 2007

Slide 7

Optical Control of Electrical Properties - Device

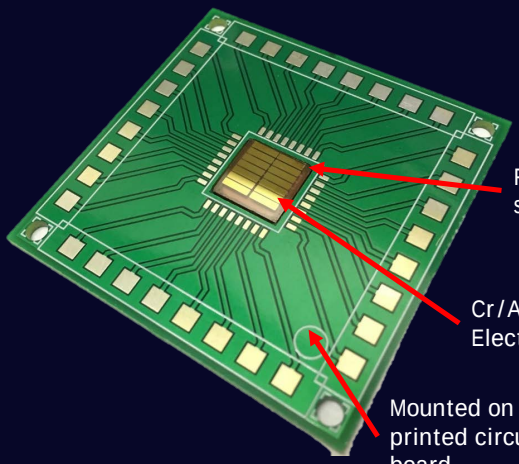

Device fabrication details

- *$LiNbO_3$:Fe substrate*
- *CVD graphene on Z polar face*
- *Cr/Au electrodes by electron beam evaporation with shadow mask*

Transmission Line Method

- Electrode pairs of varying spacing
- Plot Resistance against spacing
- Decouple contact and sheet resistance

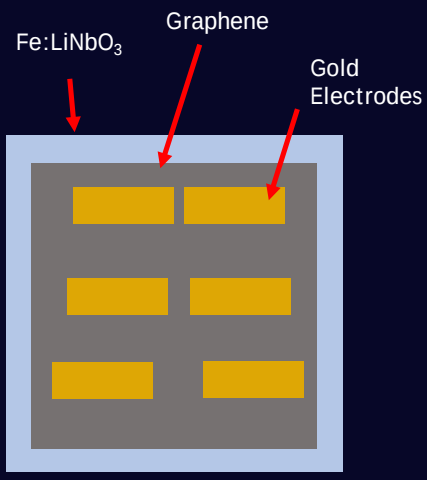

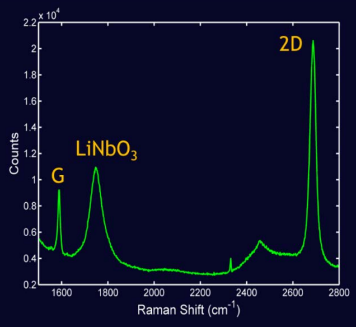

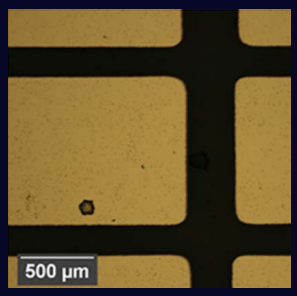

Optical reflection microscopy of electrode

Slide 8

Optical Control of Electrical Properties - Experiments

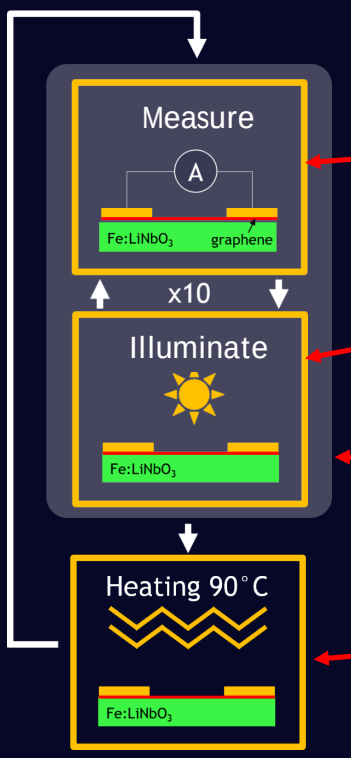

Electrical measurements performed in dark

illuminated for 30 minutes to induce a photorefractive effect (white light source)

Measurement and illumination is repeated 10 times

Device thermally annealed to return substrate to uniform charge distribution

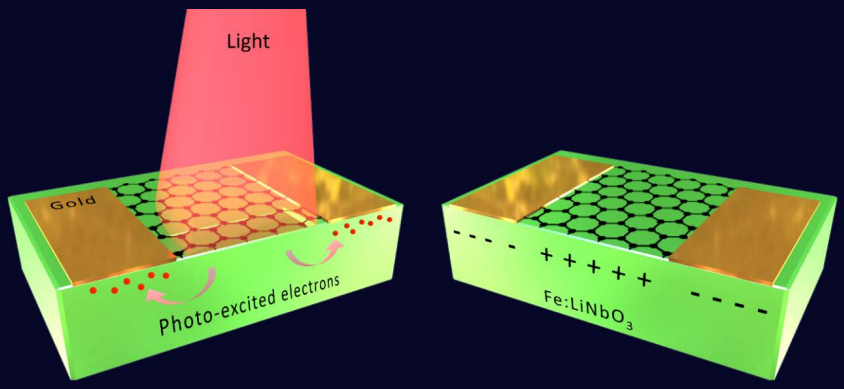

Optically induced charge migration in substrate

Electrostatic doping of graphene

Slide 9

Optical Control of Electrical Properties - Results

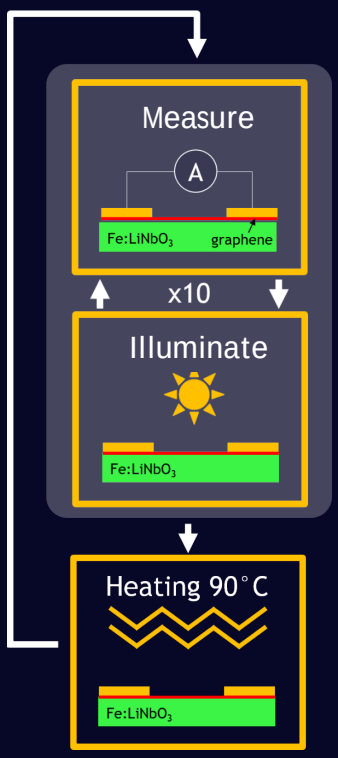

Resistance measurements

- Resistance plotted against electrode spacing
- Gradient provides sheet resistance ρ
- Y intercept equals contact resistance
- **Gradient increases with every illumination**

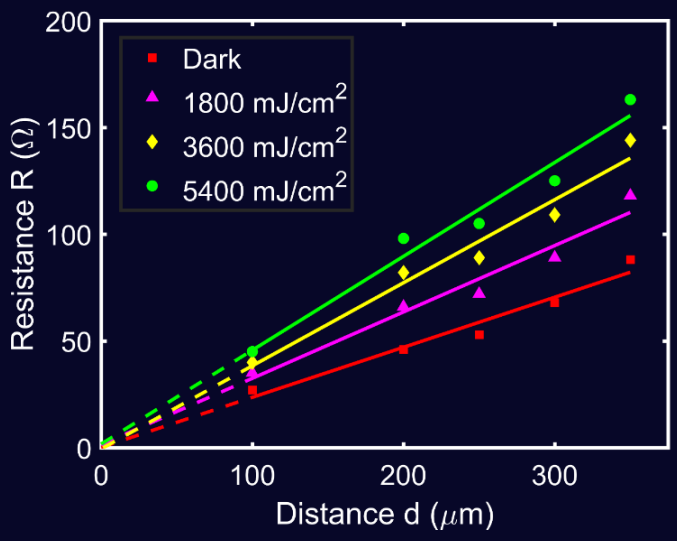

J. Gorecki, V. Apostolopoulos, J.Y. Ou, S. Mailis, N. Papasimakis, (2018) Optical gating of graphene on photoconductive Fe:$LiNbO_3$. ***ACS Nano***, 12 (6), 5940-5945.

Slide 10

Optical Control of Electrical Properties - Results

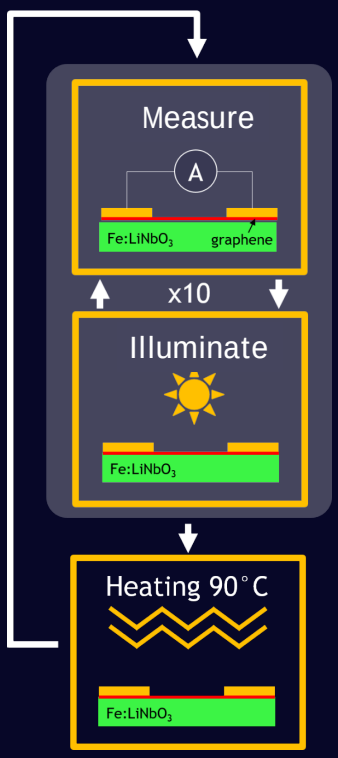

Resistivity ρ plotted against fluence

After 18 J/cm^2 Δ ρ is negligible

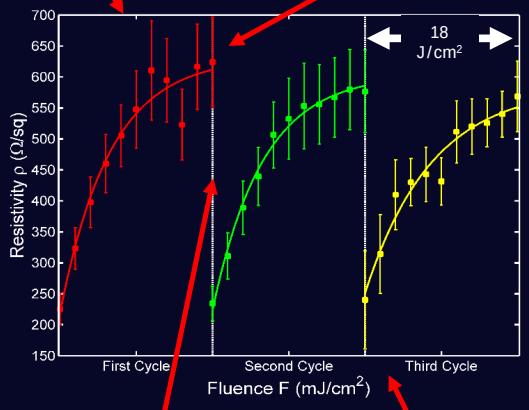

Thermal reset (4 hours in convection oven at 90°C)

Cycle is repeated showing similar behaviour

Results from 3 cycles averaged

- Fitted with inverse exponential
- Saturates with 2.6 fold increase in resistivity
- Reaches ~67% of saturation value after 6.3 J/cm^2

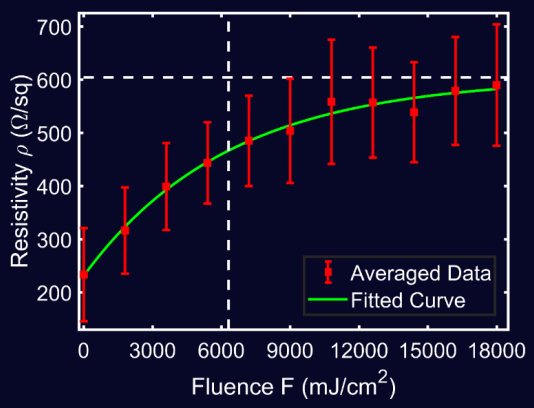

J. Gorecki, V. Apostolopoulos, J.Y. Ou, S. Mailis, N. Papasimakis, (2018) Optical gating of graphene on photoconductive Fe:$LiNbO_3$. ***ACS Nano***, 12 (6), 5940-5945.

Optical Control of Plasmonics – Device & Experiment

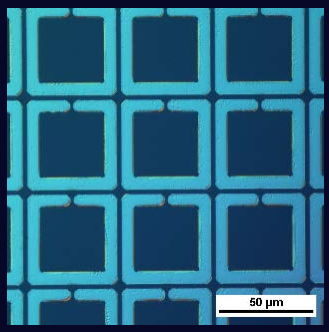

Device Fabrication

- Z cut Fe:$LiNbO_3$ patterned with split ring resonators (SRRs) with graphene top layer
- SRR dimension 45 µm squares
- Designed for resonance peak ~ 0.46 THz

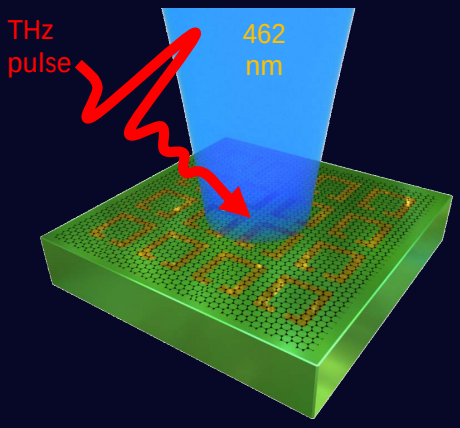

Experiment Procedure

- Device held in light proof box
- Illuminated with 462 nm source to induced photo-response in Fe:$LiNbO_3$
- THz transmission measured while illuminated

COMSOL Simulation

- Resistivity of graphene layer modified
- Alters electrical losses in plasmonic system
- Results in transmission changes without red-shifting of peak

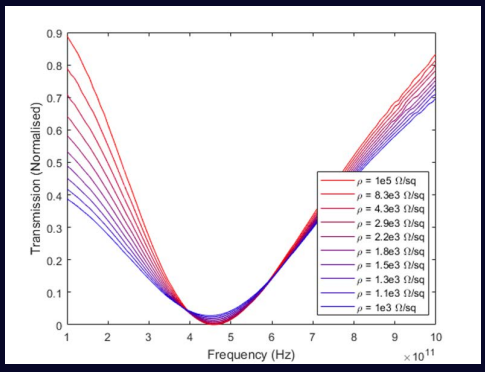

Slide 12

Optical Control of Plasmonics - Results

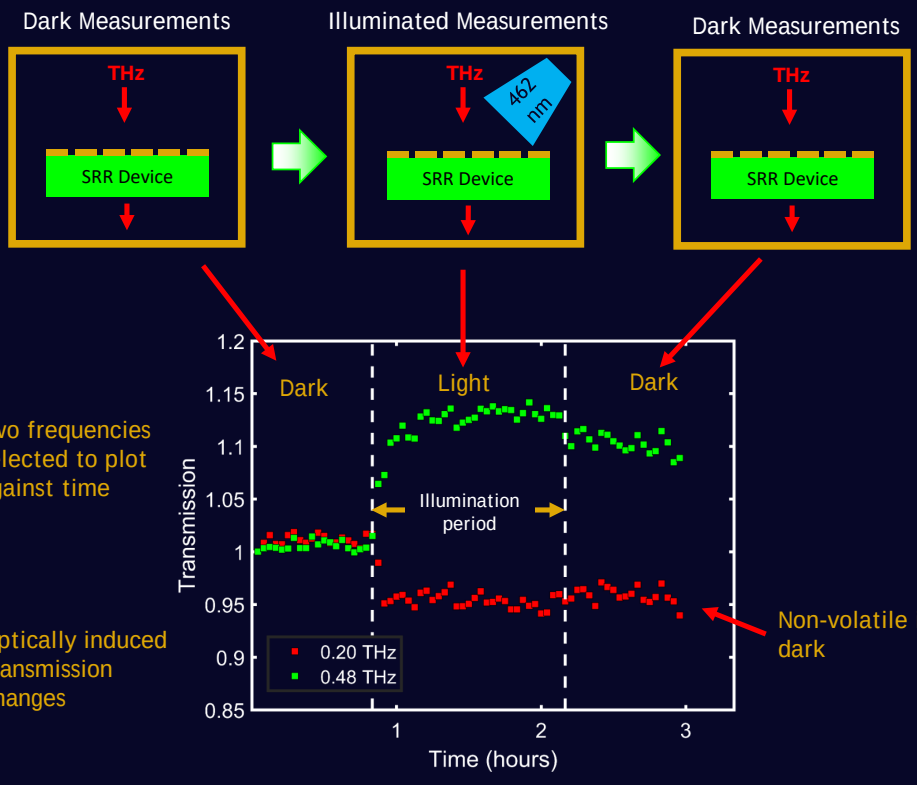

Two frequencies selected to plot against time

Optically induced transmission changes

Non-volatile in dark

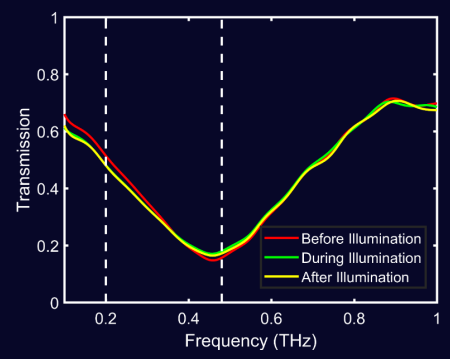

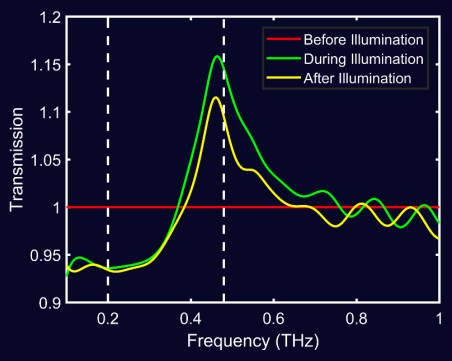

Summary / Outlook

1. **Fe:$LiNbO_3$ allows for optically written charge distributions**
   - Spatially resolved
   - Non-volatile
   - Reversible

2. **We show optical gating of graphene on Fe:$LiNbO_3$**
   - Electronics
   - Plasmonics

Questions for the Future

- How strong can the electrostatic effect be?
- Demonstrate spatial control
- Demonstrate optical annealing
- Apply to 2D materials with bandgap
- Plasmonic structures defined by structured illumination

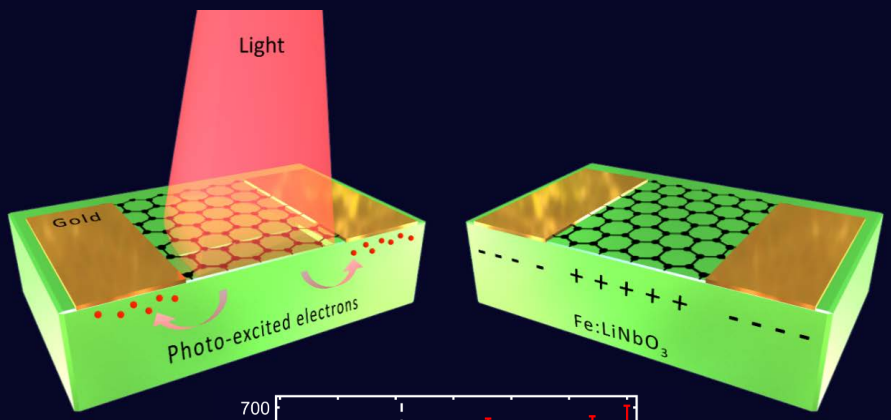

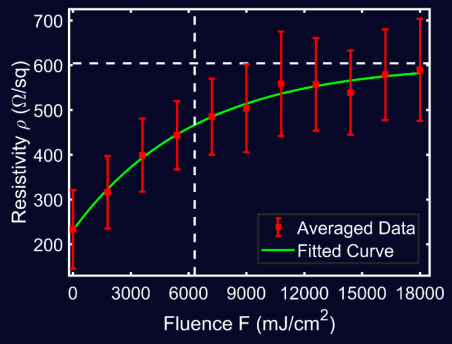

UNIVERSITY OF Southampton

Thank You

Any Questions?

Jon Gorecki[1*], Vasilis Apostolopoulos[2] ,Sakellaris Mailis[3] , Nikitas Papasimakis[1]

j.gorecki@soton.ac.uk*

CLEO US 2019
Session: STh4H Optical Driven Photonics
Thursday 9th May

Graphene Week 2018

Optical Gating of Graphene

J. Gorecki[1] *, V. Apostolopoulos[2], S. Mailis[1], N. Papasimakis[1]

[1] *Optoelectronics Research Centre & Centre for Photonic Metamaterials, University of Southampton, UK*

[2] *Department of Physics and Astronomy, University of Southampton, UK*

* *J.Gorecki@soton.ac.uk*

We demonstrate non-volatile optical tuning of the electronic charge transport properties of graphene by virtue of a photo-responsive iron doped lithium niobate substrate (Fe:$LiNbO_3$). The photo-responsive behaviour allows regions of non-uniform charge distribution to be defined within the substrate which are non-volatile, however can be erased by thermal annealing or subsequent illumination. This tuning mechanism enables the realisation of tuneable electronics and plasmonic devices.

Photorefractive Fe:$LiNbO_3$

$LiNbO_3$ exhibits a photorefractive effect in which non-volatile charge distributions can be optically written:

- Photon absorption by Fe ions
- Electrons excited to conduction band
- Electrons migrate by diffusion
- Electrons trapped by dark Fe ions
- Non-volatile charge distributions

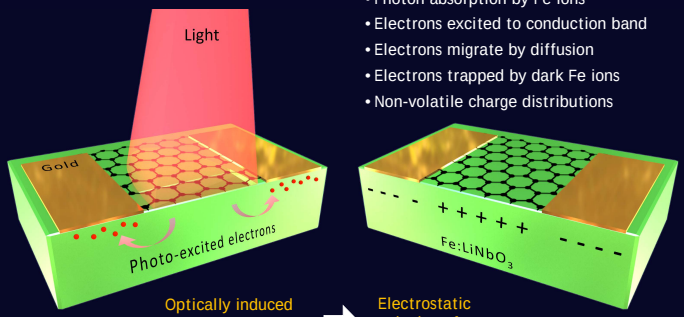

Optically induced charge migration in substrate → Electrostatic doping of graphene

Device Fabrication

Device fabrication details
- *$LiNbO_3$:Fe substrate*
- *CVD graphene on Z polar face*
- *Cr/Au electrodes by electron beam evaporation*

Array of electrode pairs with varying spacing for Transition Line Measurements (TLM) to decouple contact resistance and sheet resistance

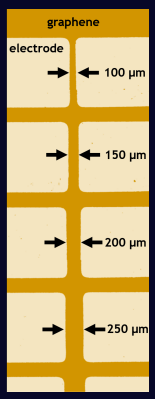

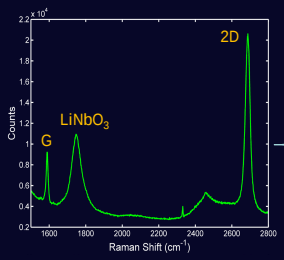

Raman spectrum from region between electrodes confirms presence of monolayer graphene from 2D:G peak height ratio, performed using 632 nm laser source with 50x objective lens

Optical Tuning of Electronic Charge Transport Properties

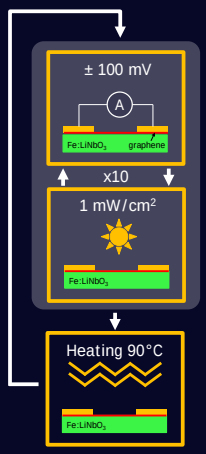

- Electrical measurements of graphene resistivity ρ performed in dark
- Device illuminated for 30 minutes to induce a photorefractive effect
- Measurement and illumination is repeated 10 times
- Device thermally annealed to return substrate to uniform charge distribution

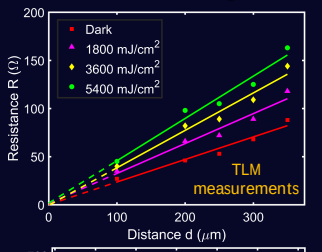

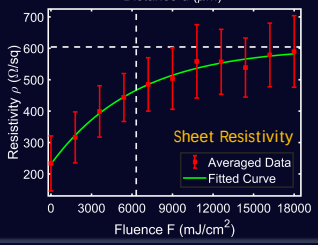

Effect is non-volatile, yet can be reset with thermal annealing (or uniform illumination)

Once thermally reset the doping effect is reproduced upon further illumination

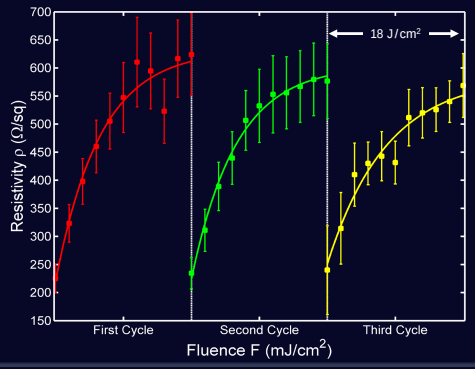

Optical Tuning of Terahertz Plasmonics

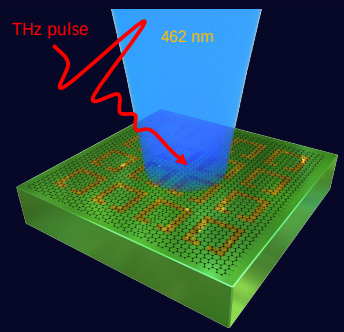

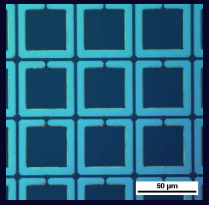

- Optical reflection microscopy of split ring resonators (SRRs)
- Side length 45 μm, 4 μm gap
- Resonance peak at 0.46 THz

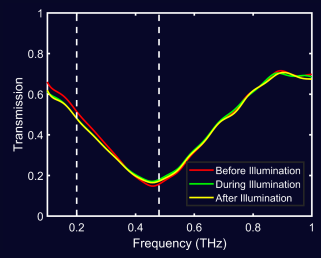

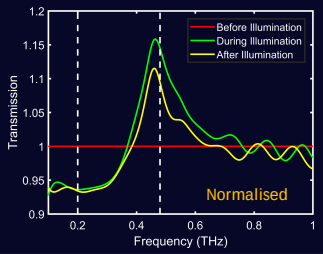

- Devices scanned in dark to gauge drift in THz setup
- Illumination with laser (0.8 mW/cm²)
- Illumination affects transmission spectra resulting in ~15% transmission change
- Device without graphene shows negligible effects with illumination

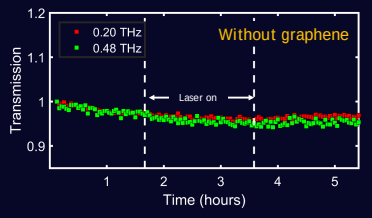

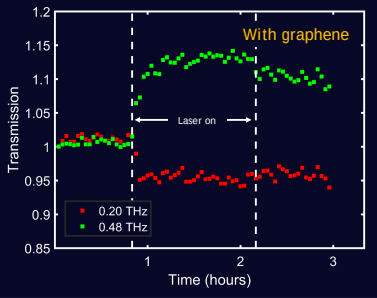

J. Gorecki, V. Apostolopoulos, J.Y. Ou, S. Mailis, N. Papasimakis, (2018) Optical gating of graphene on photoconductive Fe:$LiNbO_3$. ***ACS Nano***, 12 (6), 5940-5945.

NanoP 2017

UNIVERSITY OF Southampton

Optical Control of Graphene Conductivity

Jon Gorecki[1], Vasilis Apostolopoulos[2] ,Sakellaris Mailis[1] , Nikitas Papasimakis[1]

[1]Optoelectronics Research Centre, University of Southampton, UK

[2]School of Physics and Astronomy, University of Southampton, UK

Nano Photonics 2017
Session: OS3a Optical Properties of Nanostructures
Friday 15th September
Room 412

Optoelectronics Research Centre, University of Southampton

David Payne
Er doped fibres

Nikolay Zheludev
Metamaterials,
Nanophotonics

Graham Reed
Silicon Photonics

Nikitas Papasimakis
Metamaterials

Sakellaris Mailis
Nonlinear and Microstructured
Optical Materials

Vasilis Apostolopoulos
Terahertz Laboratories

Electronic Band Structure of Graphene

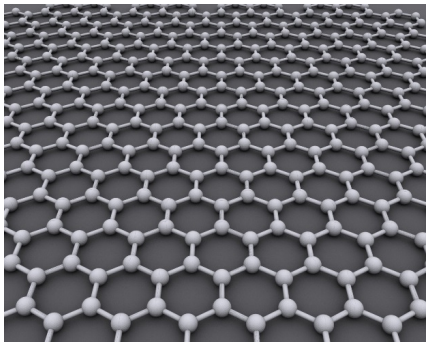

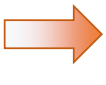

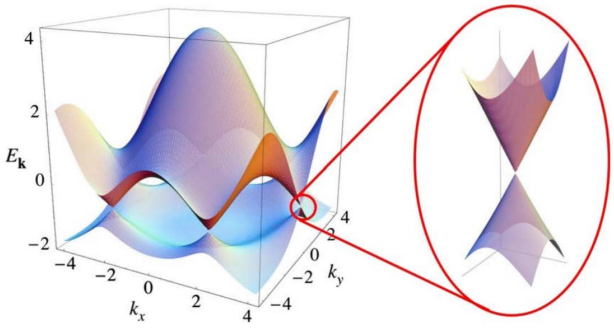

Density of states at Fermi Level -> 0

Neto et al., 2009

Electronic Band Structure of Graphene

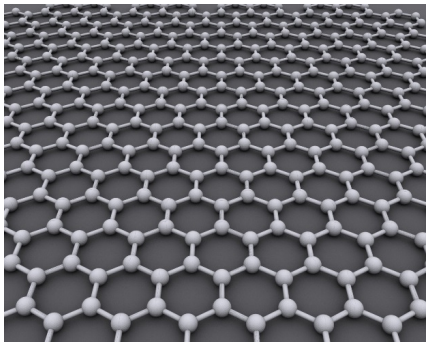

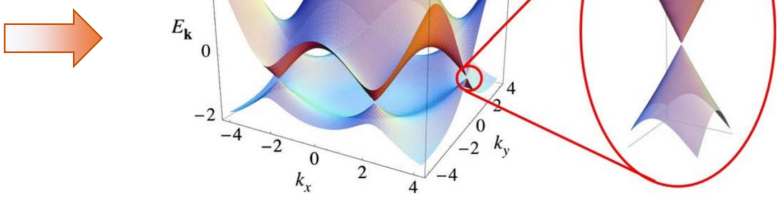

Density of states at Fermi Level -> 0

Neto et al., 2009

Electrical Resistivity

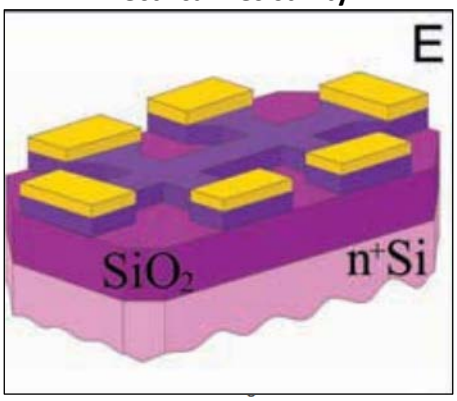

Geim et al., Science, 306, 2004

Plasmons

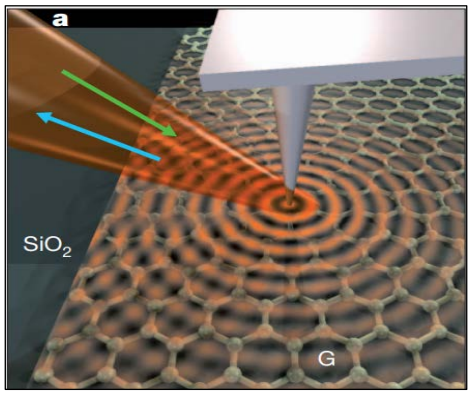

Basov et al., 2012
Koppens et al., Nature, 77, 2012

Radiative Transitions

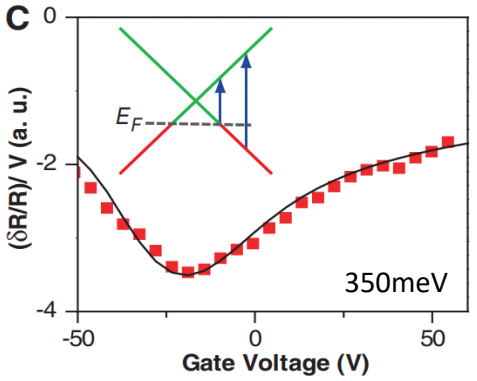

Wang et al., 2008

How can we control charge carrier concentration?

Controlling Graphene Charge Carrier Concentration

Volatile

Electrical Gating
Geim et al., 2004

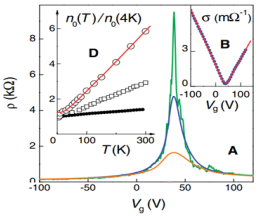

Chemical Doping
Jung et al., 2017

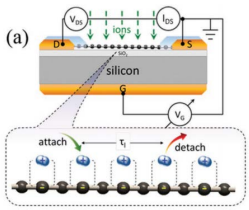

Pyroelectric Lithium Niobate
Pruneri et al., 2017

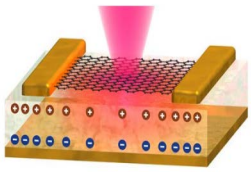

?

Non-Reversible

Reversible

Patterning (Ribbons etc)

Optical writing (doping from defects)

Heterostructures (MoS_2 etc)

Back-gated ferroelectric
Song et al., 2011

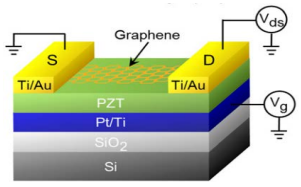

Non-Volatile

Can we have a doping mechanism which is…?

- Non-volatile
- Reversible
- Spatially Resolved
- Non-contact

Can we have a doping mechanism which is…?

- Non-volatile
- Reversible
- Spatially Resolved
- Non-contact

Optical Doping Mechanism with Lithium Niobate

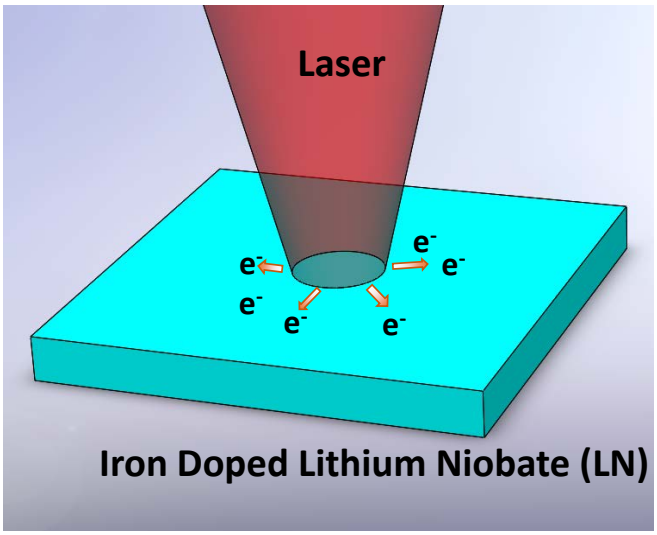

- **Fe ions absorb light (green, blue, UV)**
- **Electrons excited to conduction band (Photoconductive)**
- **Migration in lattice**
- **Trapped in dark regions**

Non-volatile, Reversible, Spatial resolution, Non-contact

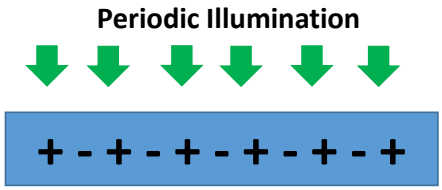

- Periodic charge distrib.

Optical Doping Mechanism with Lithium Niobate

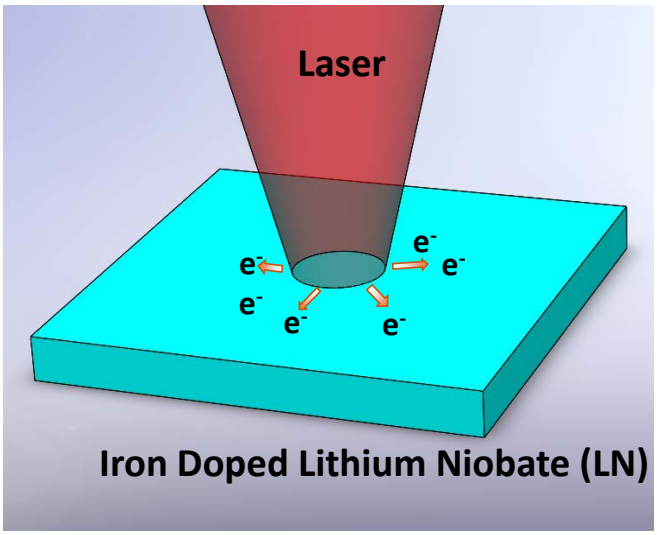

- **Fe ions absorb light (green, blue, UV)**
- **Electrons excited to conduction band (Photoconductive)**
- **Migration in lattice**
- **Trapped in dark regions**

Non-volatile, Reversible, Spatial resolution, Non-contact

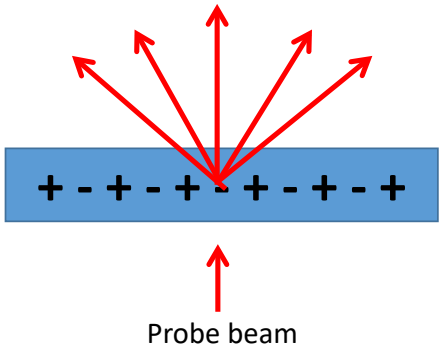

- Periodic charge distrib.
- Electro-optic Δn ∝ E
- Diffraction Grating

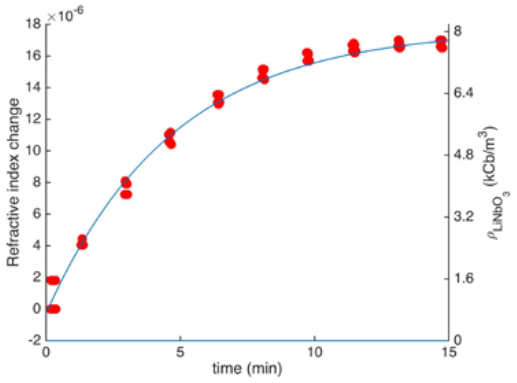

10 mW laser
~400nm
1.1um periodic grating

Optically induced changes in resistivity across graphene channel: transient and non-volatile effects

Device

- Iron doped lithium niobate
- CVD graphene
- Indium electrodes

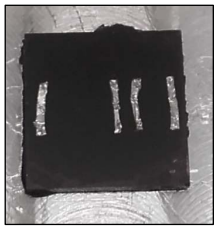

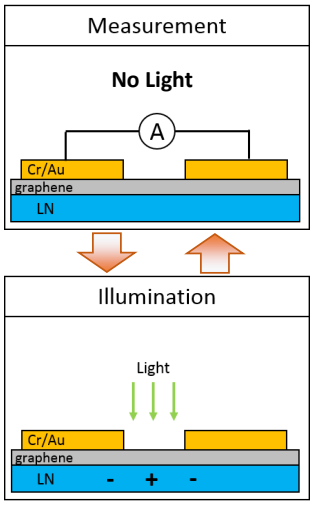

- Device placed into dark box
- Electrical resistance measured at t=0, t=120s, t=240s

- Device illuminated for 5 minutes (mW broadband source)

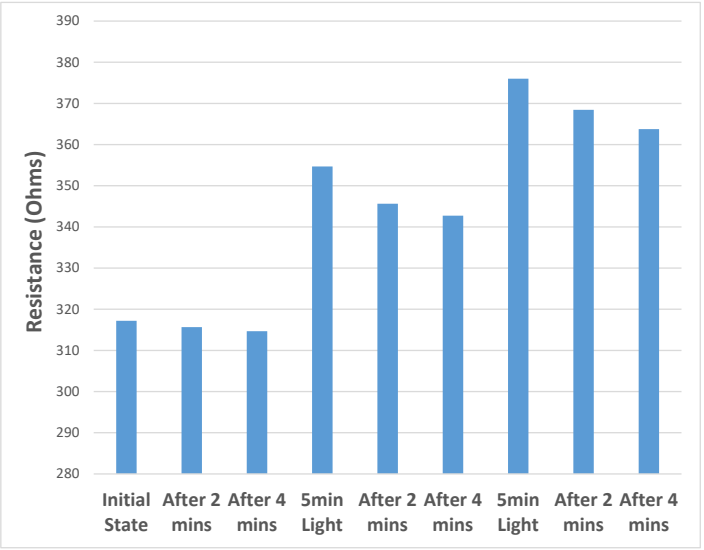

- Resistance increase after illumination
- Partial relaxation over few minutes
- Residual effect remains

Optically induced changes in resistivity across graphene channel: sheet resistance

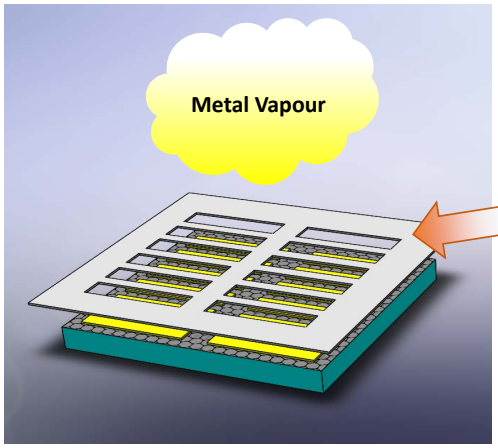

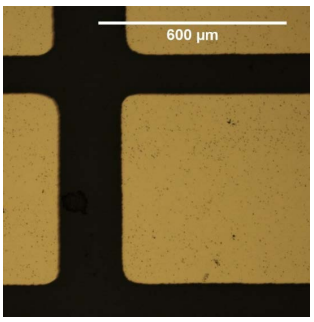

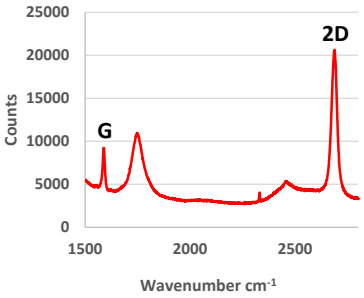

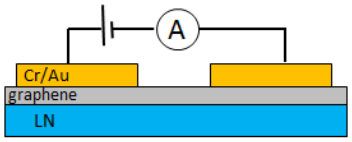

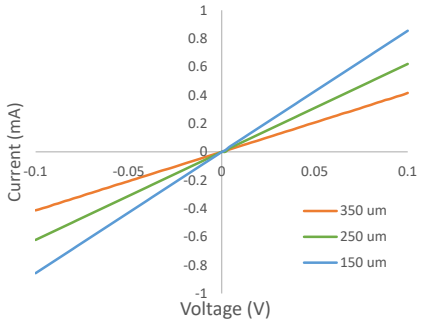

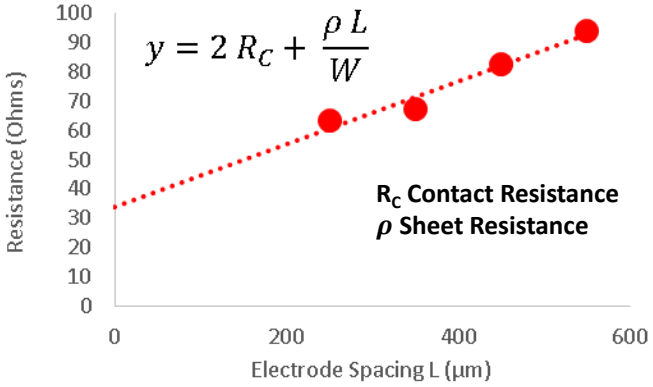

Optically Controlled Graphene Sheet Resistance

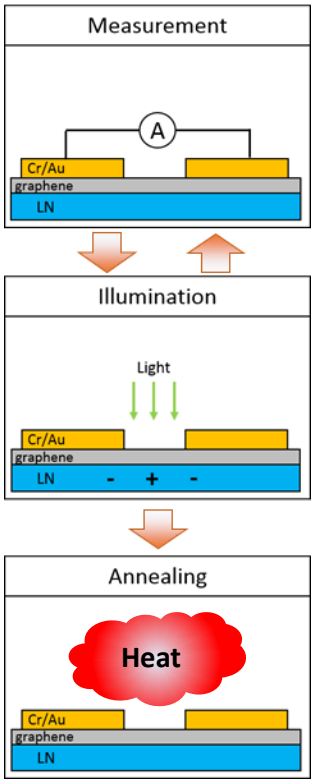

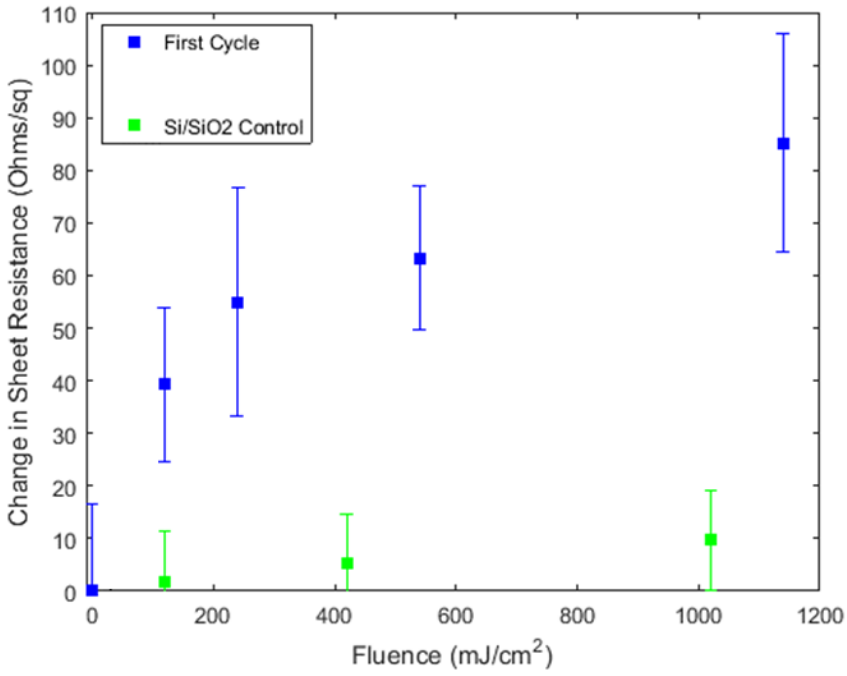

Optically Controlled Graphene Sheet Resistance

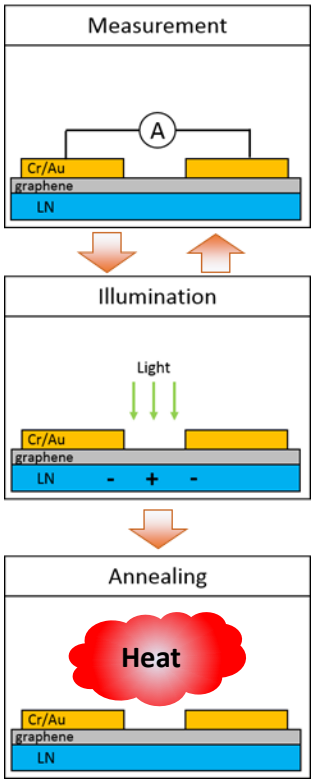

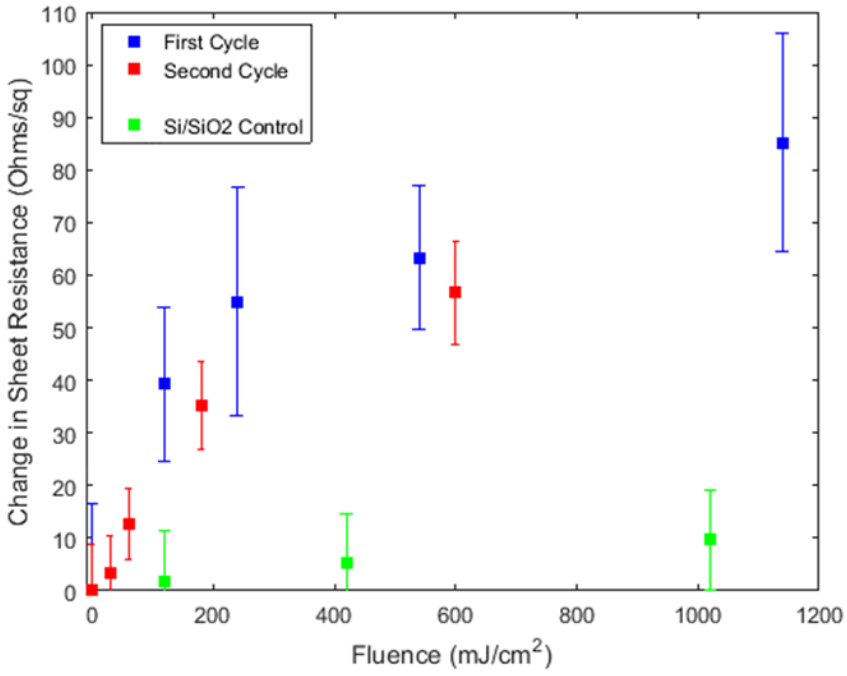

Optically Controlled Graphene Sheet Resistance

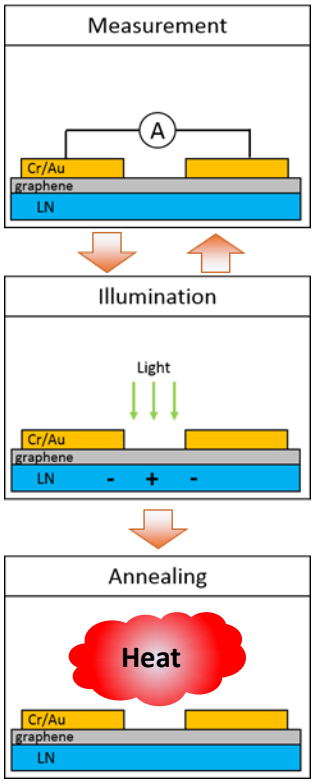

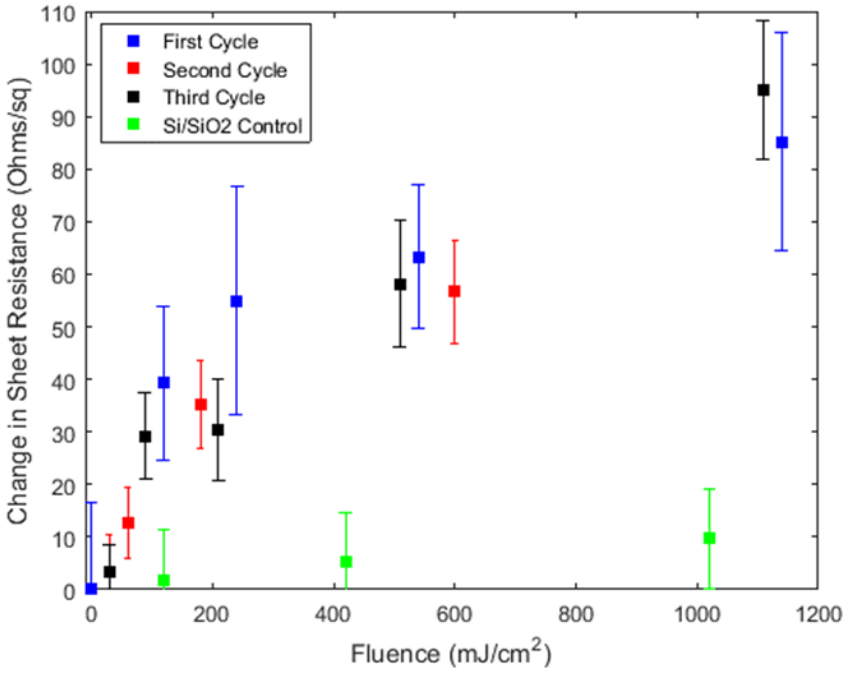

Optically Controlled Graphene Sheet Resistance

- **Change in sheet resistance**
- **Erasable by annealing**
- **Repeatable Behaviour**

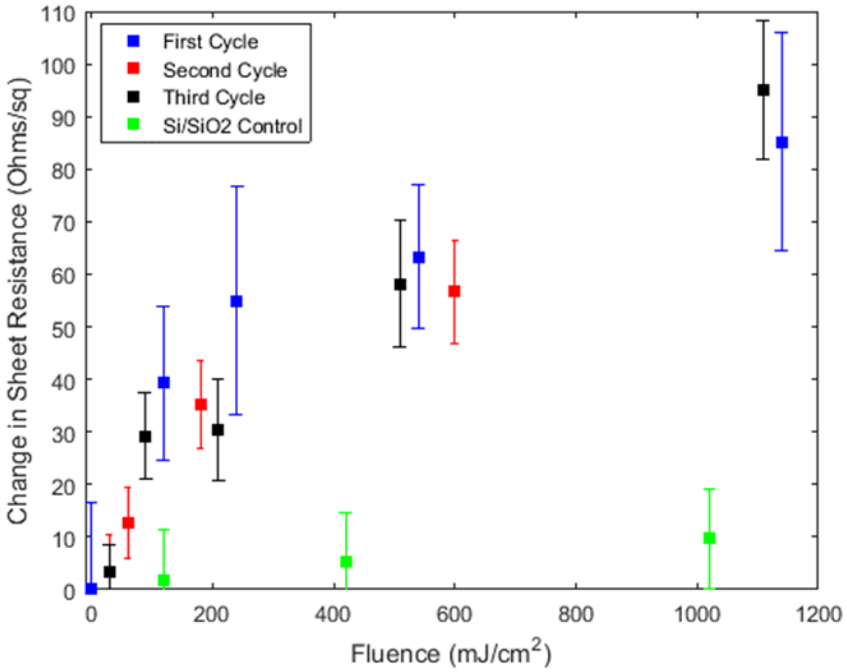

Optical Doping Mechanism with Lithium Niobate

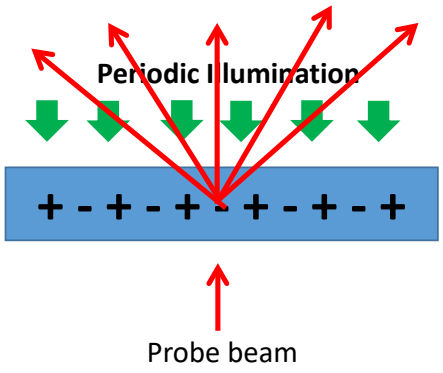

- Periodic charge distrib.
- Electro-optic Δn ∝ E
- Diffraction Grating

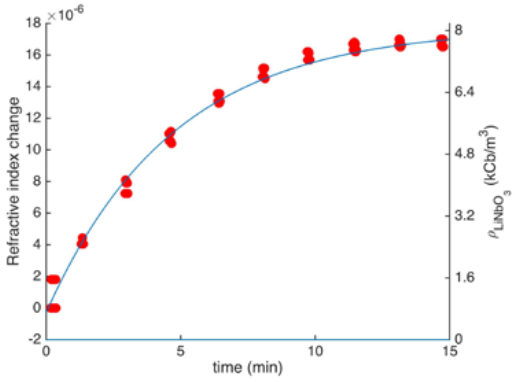

Reconfigurable plasmonics?

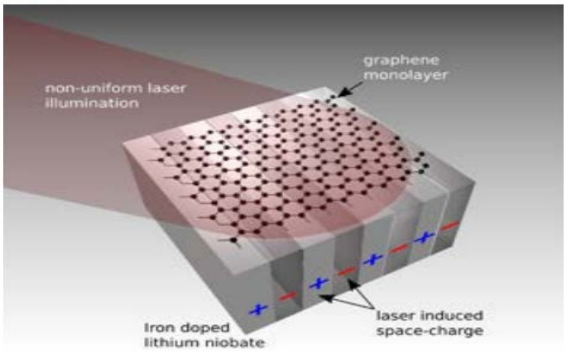

Illuminating lithium niobate with periodically structured pattern

max. realistic modulation of carriers:
$7 \times 10^{12}/cm^2$

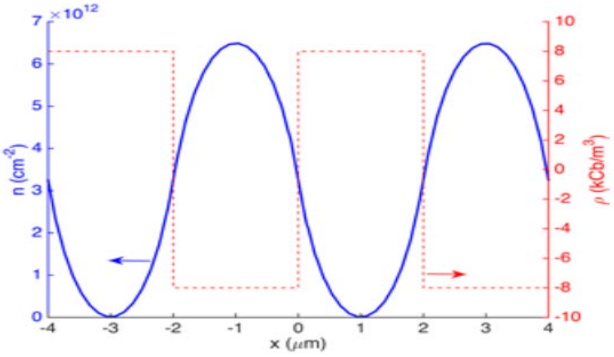

THz plasmons in graphene

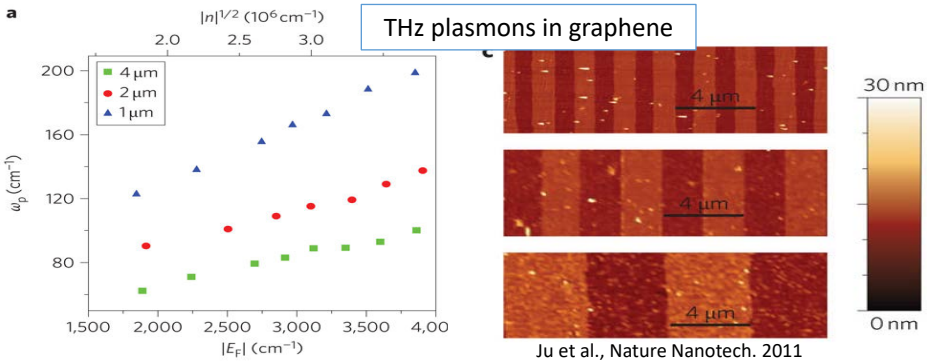

Ju et al., Nature Nanotech. 2011

Could lead to optically reconfigurable THz plasmonic structures in graphene

Summary

- A platform to optically control graphene electrical properties is demonstrated
- The mechanism is reversible, non-volatile, non-contact, and spatially resolved
- Arbitrary shape domains written on milisecond timescales, spatial resolution limited by Rayleigh limit
- Towards optically written, reconfigurable plasmonic structures
- Not limited to graphene – we have recently deposited few-layer MoS_2 onto lithium niobate substrate

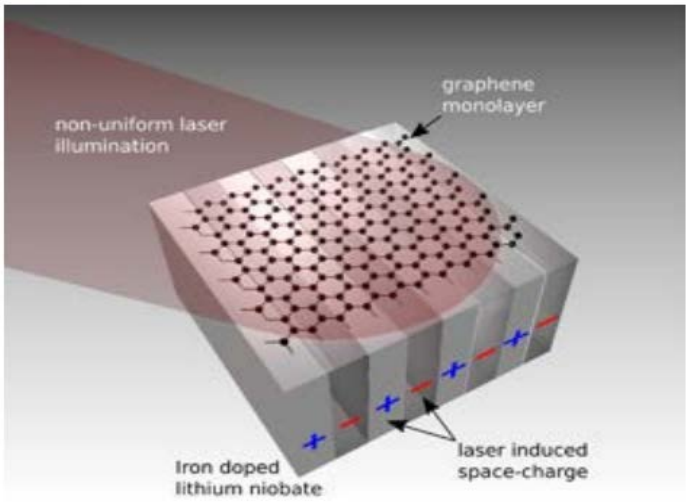

Thank You For Listening

The End :)